PSFC/RR-05-6 **DOE-ET-54512-352**

Edge Transport Barrier Studies On the Alcator C-Mod Tokamak

Jerry W. Hughes, Jr.

June 2005

Plasma Science and Fusion Center
Massachusetts Institute of Technology
Cambridge, Massachusetts 02139

This work was supported in part by the U.S. Department of Energy Contract No. DE-FC02-99ER54512. Reproduction, translation, publication, use and disposal, in whole or in part, by or for the United States government is permitted.

Edge Transport Barrier Studies On the Alcator C-Mod Tokamak

by

Jerry W. Hughes, Jr.

S.B. Mathematics (1997)
S.B. Nuclear Engineering (1998)
S.M. Nuclear Engineering (1999)
Massachusetts Institute of Technology

Submitted to the Department of Nuclear Science and Engineering
in partial fulfillment of the requirements for the degree of

Doctor of Philosophy in Nuclear Science and Engineering

at the

MASSACHUSETTS INSTITUTE OF TECHNOLOGY

September 2005

© Massachusetts Institute of Technology 2005. All rights reserved.

Author .....
Department of Nuclear Science and Engineering
June 24, 2005

Certified by .....
Dmitri Mossessian
former Research Scientist, Plasma Science and Fusion Center
Thesis Supervisor

Certified by .....
Ian H. Hutchinson
Professor of Nuclear Science and Engineering, Department Head
Thesis Reader

Accepted by .....
Professor Jeffery A. Coderre
Chairman, Department Committee on Graduate Students

Edge Transport Barrier Studies On the Alcator C-Mod Tokamak

by

Jerry W. Hughes, Jr.

Submitted to the Department of Nuclear Science and Engineering
on June 24, 2005, in partial fulfillment of the
requirements for the degree of
Doctor of Philosophy in Nuclear Science and Engineering

Abstract

Edge transport barriers (ETBs) in tokamak plasmas accompany transitions from low confinement (L-mode) to high confinement (H-mode) and exhibit large density and temperature gradients in a narrow *pedestal* region near the last closed flux surface (LCFS). Because tokamak energy confinement depends strongly on the boundary condition imposed by the edge plasma pressure, one desires a predictive capability for the pedestal on a future tokamak. On Alcator C-Mod, significant contributions to ETB studies were made possible with edge Thomson scattering (ETS), which measures profiles of electron temperature ($20 \lesssim T_e[\mathrm{eV}] \lesssim 800$) and density ($0.3 \lesssim n_e[10^{20}\mathrm{m}^{-3}] \lesssim 5$) with 1.3-mm spatial resolution near the LCFS. Profiles of T_e, n_e, and $p_e = n_e T_e$ are fitted with a parameterized function, revealing typical pedestal widths Δ of 2–6mm, with $\Delta_{T_e} \gtrsim \Delta_{n_e}$, on average.

Pedestals are examined to determine existence criteria for the enhanced D_α (EDA) H-mode. A feature that distinguishes this regime is a quasi-coherent mode (QCM) near the LCFS. The presence or absence of the QCM is related to edge conditions, in particular density, temperature and safety factor q. Results are consistent with higher values of both q and collisionality $\nu^\star$ giving the EDA regime. Further evidence suggests that increased $|\nabla p_e|$ may favor the QCM; thus EDA may have relevance to low-$\nu^\star$ reactor regimes, should sufficient edge pressure gradient exist.

Scaling studies of pedestal parameters and plasma confinement in EDA H-modes varied operational parameters such as current I_P and L-mode target density $\bar{n}_{e,L}$. At fixed plasma shape, widths show little systematic variation with plasma parameters. Scalings are however determined for pedestal heights and gradients. The p_e pedestal height and gradient both scale as I_P^2, similar to scalings found on other tokamaks, though with differing pedestal-limiting physics. It is seen that the density pedestal value $n_{e,\mathrm{PED}}$ scales linearly with I_P, and more weakly with $\bar{n}_{e,L}$, indicating that neutral fueling plays a relatively limited role in setting H-mode density. Plasma stored energy scales in a linear fashion with the p_e pedestal, such that empirical confinement scalings are affected by edge pedestal scalings.

Empirical determination of neutral density and ionization source was made across

the pedestal region, enabling inferrence of neutral gradient scale length L_0 and effective diffusivity D_{eff}. The D_{eff} well is comparable in width to the pedestal, and L_0 tends to be less than Δ_{n_e}. Computation of L_0 in discharges with varying $\bar{n}_{e,L}$ yields a similar result, suggesting that Δ_{n_e} is generally set by the ETB extent and not neutral penetration length. Puffing gas into an existing H-mode edge yields no significant change in the values of $n_{e,\text{PED}}$, ∇n_e, which is qualitatively consistent with simulations using a coupled fluid-kinetic neutral model. Experiment and modeling indicate the importance of thermal equilibration of neutrals with ions, particularly in high density (collisional) plasmas.

Thesis Supervisor: Dmitri Mossessian
Title: former Research Scientist, Plasma Science and Fusion Center

Thesis Reader: Ian H. Hutchinson
Title: Professor of Nuclear Science and Engineering, Department Head

Acknowledgments

I first wish to thank Dr. Dmitri Mossessian for being a superb thesis supervisor. He worked closely with me to make this project successful, giving me instruction when I needed it and criticism when I deserved it. I could not have proceeded very far without his tireless involvement, and his dedication to doing science carefully and correctly is a continued inspiration to me. I am no less grateful to Prof. Ian Hutchinson, the reader of this thesis and constant purveyor of helpful scientific insight. As head of Alcator C-Mod, he secured financial support for me* and gave me an opportunity to succeed on the Alcator project. In addition, he was personally supportive throughout my Ph.D. program, particularly when I was enduring some difficult times in my life.

Additional Alcator team members and outside parties provided considerable support to this thesis as well. Data from sources other than Thomson scattering (TS) are courtesy of Amanda Hubbard, Brian LaBombard, Earl Marmar, Jim Terry, Yijun Lin, Alex Mazurenko and Nils Basse. I am grateful to Rich Groebner and Ali Mahdavi of General Atomics for discussing neutral fueling with me and also to Daren Stotler of PPPL for his assistance with neutral code benchmarking.

The TS diagnostic operated routinely only with the technical support of a number of individuals besides Dmitri and me. Much hardware support came from Dave Bellofatto, Joe Bosco, Willy Burke and Yuri Rokhman. TS system upgrades relied heavily upon the design work of Mike DeMaria and the labor of folks like Kenny Jensen, Bill Parkin and Edgar Rollins. Bob Childs provided vacuum expertise, and I can't thank Tom Toland enough for his weekend efforts to help calibrate the TS diagnostic. In the early stages of my research, Spencer Pitcher was quite helpful, as was Dave Johnson of PPPL. Dave provided vital assistance needed to configure and calibrate the edge TS system. Finally, gratitude goes to fellow student Kirill Zhurovich, who took over much of the laboratory work in 2002, and to Ted Biewer, whose presence on the Thomson crew gave me additional time to write this thesis.

The C-Mod physics operators—including Bob Granetz, Jim Irby, Prof. Ron Par-

*Supported in part by the U.S. Department of Energy Contract No. DE-FC02-99ER54512.

ker, Bill Rowan and Steve Wolfe (with Hutchinson, Marmar and Mossessian)—were vital to running these experiments, as were the RF scientists and engineers: Sergey Andreyev, Réjean Boivin, Paul Bonoli, John Goetz, Lin, Rick Murray, Steve Wukitch and the late Charley Schwartz. Computing support was provided by Henry Bergler, Tom Fredian, Felix Kreisel, Mark London, Don Nelson, Stuart Sherman and Josh Stillerman. Thanks also to Dave Arsenault, Bill Beck, Bill Byford, Charles Cauley, Bill Cochran, Gary Dekow, Ed Fitzgerald, Matt Fulton, Andy Pfeiffer, Sam Pierson, Jim Rosati, Ron Rosati, Frank Shefton, Maria Silveira and Rui Vieira.

Gratitude is due the kind and capable administrative alumnae of Alcator HQ—Valerie Censabella, Megan Tabak and Corrinne Fogg—and assorted scientists who have been extremely giving of their time and intellect: Peter Catto, Catherine Fiore, Prof. Jeffrey Freidberg, Martin Greenwald, Bruce Lipschultz, Prof. Kim Molvig, Miklos Porkolab, Steve Scott, Joe Snipes, Maxim Umansky and Stewart Zweben. I particularly want to recognize John Rice, Sc.D., hereafter known as the Sage of Alcator.

I have benefited from the company of many fellow graduate students, including Brock Böse, Chris Boswell, Taekyun Chung, Joe DeCiantis, Marco Ferrara, Sanjay Gangadhara, Tim Graves, Ishtak Karim, Natalia Krashennenikova, Davis Lee, John Liptac, Alan Lynn, Ken Marr, Rob Nachtrieb, Eric Nelson-Melby, Thomas Pedersen, Mike Pope, Matt Sampsell, Dave Schmittdiel, Brook Schwarz, Khash Shadman, Noah Smick and Vincent Tang. And then there's Howard Yuh, with whom I've shared an office and a lot of good times. I want to thank Howard for plentiful conversation and boisterous laughter, and for a wealth of flawless knowledge and technical advice on a million unrelated matters.

Finally there are my friends and loved ones outside of the workplace. Unconditional love and support from my parents, Jerry and Jane Hughes, have allowed me to achieve many great things throughout my life. Though my mother did not live to see the completion of my doctorate, I know she would be proud. My close friends stay dear to me, and Meredith Warner, Marc Weldon and Kevin Frye are among the dearest; thanks for being there. The lovely Eva Urban is the final piece to my puzzle. The joy she brings me makes me love life, and I am forever grateful.

Contents

1 Introduction **17**

1.1 Plasma fusion 18

1.1.1 Plasmas for thermonuclear fusion 18

1.1.2 Magnetic confinement 19

1.1.3 Tokamaks 21

1.2 Confinement and transport 24

1.3 Edge transport barriers 26

1.4 Alcator C-Mod 28

1.4.1 Plasma parameters and geometry 28

1.4.2 Operational regimes 32

1.4.3 Thomson scattering and other edge diagnostics 36

1.5 Thesis goals and outline 41

2 Edge Transport Barriers: Theory and Experiment **43**

2.1 H-mode and pedestal characterization 43

2.2 Pedestal scalings: Predictions from theory 46

2.2.1 Width from ion orbit loss 46

2.2.2 Width from neutral penetration 47

2.2.3 Other models for width and gradient 49

2.3 Experimental results from other tokamaks 51

2.3.1 JT-60U 52

2.3.2 DIII-D 53

2.3.3 JET 57

2.3.4 ASDEX Upgrade . . . 58
2.3.5 Summary of tokamaks . . . 59
2.4 Prior results on Alcator C-Mod . . . 59

3 Edge Thomson Scattering on C-Mod 63
3.1 Incoherent Thomson scattering . . . 64
3.2 Diagnostic setup and principles of operation . . . 70
3.2.1 Beam and collection optics . . . 71
3.2.2 Multi-channel polychromator . . . 74
3.2.3 Data acquisition and control hardware . . . 80
3.3 Calibrations . . . 81
3.3.1 General response to scattering . . . 83
3.3.2 Spectral functions . . . 84
3.3.3 Integral detector response . . . 85
3.3.4 Relative gains in DC and pulsed mode . . . 85
3.3.5 Absolute calibration . . . 86
3.4 Data analysis . . . 89
3.4.1 Inferred electron temperature and density . . . 89
3.4.2 Misalignment correction . . . 91
3.4.3 Edge profile mapping and fitting . . . 92
3.5 Comparisons with other diagnostics . . . 93
3.6 Notable contributions to C-Mod research . . . 98

4 Pedestal Structure and Properties 101
4.1 Extended profile characteristics . . . 101
4.2 Pedestal width . . . 104
4.3 Pedestal characteristics in H-mode regimes . . . 108
4.3.1 QCM phenomenology . . . 108
4.3.2 Guidance from theory and modeling . . . 110
4.3.3 Experimental pedestal “phase space” . . . 111

5 Experimental scalings of the pedestal **119**

5.1 Data selection . . . 119

5.2 The pedestal and confinement . . . 121

5.3 Operational variations in pedestal parameters . . . 124

5.3.1 Widths . . . 124

5.3.2 Heights and gradients . . . 126

5.4 Parametric scalings from multiple regression analysis . . . 129

5.4.1 Density pedestal . . . 131

5.4.2 Temperature pedestal . . . 135

5.4.3 Pressure pedestal . . . 136

5.5 Confinement . . . 139

5.6 Plasma triangularity variation . . . 141

6 Particle Transport Analysis **151**

6.1 Emprical analysis of transport . . . 151

6.1.1 Density pedestal variation with current . . . 152

6.1.2 Neutral characterization . . . 155

6.1.3 Radial plasma transport . . . 163

6.2 Kinetic neutrals and KN1D . . . 165

6.2.1 Benefits of a kinetic neutral analysis . . . 165

6.2.2 KN1D description . . . 166

6.2.3 Comparison with experiment . . . 168

6.3 Gas fueling experiments . . . 171

6.3.1 L-mode fueling . . . 173

6.3.2 Puffing into H-mode . . . 177

6.4 1-D modeling and computation . . . 183

6.4.1 The “warm neutral” model . . . 185

6.4.2 Kinetic input to fluid modeling . . . 188

6.5 Conclusions on particle transport . . . 194

7 Final Conclusions and Future Work **197**

7.1 Major contributions to ETB studies 197

7.1.1 Millimeter resolution profile diagnosis 198

7.1.2 Pedestal characteristics in H-mode regimes 198

7.1.3 Empirical scalings of the EDA H-mode pedestal 199

7.1.4 Neutral fueling in a high density pedestal 201

7.2 Directions for future work 202

A Benchmarking KN1D **205**

Bibliography **211**

List of Figures

1-1 General tokamak geometry 22

1-2 Schematic cross-section of Alcator C-Mod 29

1-3 Sample EFIT reconstruction and definitions of shaping parameters . . 31

1-4 Time-behavior of ELM-free H-mode 33

1-5 Time-behavior of EDA H-mode 35

1-6 Poloidal locations of Alcator C-Mod edge diagnostics 38

2-1 The five fit parameters of the modified tanh fit. 45

2-2 Density pedestal width *vs.* $n_{e,\mathrm{PED}}$ in DIII-D discharges 56

3-1 Photon scattering from a single charged particle 64

3-2 Incident and scattering wavevectors, with $\mathbf{k}_s \perp \mathbf{E}_i$ ($\alpha = \pi/2$) 67

3-3 Relativistic blue shift in $S(T_e, \theta, \lambda)$ 69

3-4 Relativistic spectral shift of $S(T_e, \theta, \lambda)$ as a function of T_e 70

3-5 Alcator C-Mod cross-section and layout of TS collection optics. . . . 72

3-6 TS fiber mount subassembly 74

3-7 Face of edge TS fiber holder 75

3-8 Layout of 4×25-channel polychromator 76

3-9 Edge TS response functions and spectral distributions 78

3-10 Responses of ETS detectors as a function of T_e 79

3-11 Raman scattering signal *vs.* pressure 88

3-12 Experimental signals and model responses to T_e 90

3-13 Edge profiles of T_e and n_e before and after *L-H* transition 94

3-14 Comparison of TS and ECE T_e profiles in L- and H-mode. 95

3-15 Comparison of edge TS and scanning Langmuir probe profiles 97
3-16 Comparison of visible continuum and edge TS diagnostics 98

4-1 Simultaneous edge profiles of n_e and T_e from multiple diagnostics . . 102
4-2 Simultaneous pedestal profiles of n_e, T_e p_e from ETS 105
4-3 Density of data in Δ_T-Δ_n space 106
4-4 Distribution of widths and relative positions of pedestals 107
4-5 EDA/ELM-free pedestal operational space: (T_e,n_e,q) 113
4-6 EDA/ELM-free pedestal operational space: (∇p_e,$\nu^\star_{95}$) 115
4-7 EDA/ELM-free pedestal operational space: ($\alpha_{\rm PED}$,$\nu^\star_{95}$) 116
4-8 Operational Δ_T-Δ_n space of EDA and ELM-free H-modes 117

5-1 Time windows for scaling analysis with sample traces of plasma data 120
5-2 Characteristic core T_e gradient *vs.* pedestal T_e in EDA H-modes . . . 122
5-3 Relation of W_P to $p_{e,\rm PED}$ in EDA H-modes 123
5-4 Pedestal widths *vs.* poloidal ion gyroradius in EDA H-mode 125
5-5 Density pedestal width *vs.* n_e atop pedestal in EDA H-modes 126
5-6 Profiles of edge T_e with varying $P_{\rm RF}$ 127
5-7 Dependence of pedestal temperature and gradient on $P_{\rm SOL}$ 128
5-8 Density pedestal width *vs.* $1/q_{95}$ in EDA H-modes 132
5-9 Pedestal n_e at top and base of pedestal *vs.* I_P, $\bar{n}_{e,L}$ and $1/B_T$ 133
5-10 Experimental pedestal n_e against empirical scaling prediction 134
5-11 Experimental pedestal T_e against empirical scaling prediction 136
5-12 Experimental pedestal p_e against empirical scaling prediction 137
5-13 Pedestal electron pressure gradient in EDA *vs.* $P_{\rm SOL}$, I_P 138
5-14 Variation of n_e pedestal width on triangularity 142
5-15 Upper and lower triangularity in shaping variation experiments 143
5-16 H-mode profiles of n_e, T_e and p_e over a range of triangularity. 145
5-17 Widths of n_e, T_e and p_e pedestals as a function of triangularity 146
5-18 Pedestal values as a function of average triangularity 147
5-19 Gradients as a function of average triangularity 148

5-20 Normalized density pedestal and pressure gradient *vs.* triangularity . 149

6-1 Time traces from discharges run at varying values of I_P 153
6-2 Pedestal profiles in families of discharges at three distinct currents. . 154
6-3 Pedestal trends in families of discharges at three distinct currents. . . 156
6-4 Smooth monotonic n_e, T_e profiles obtained from ETS and probe . . . 157
6-5 Measurement of radial D_α emissivity from 2-D camera image 158
6-6 Determination of neutral density and ionization profiles 160
6-7 Gradient scale lengths of n_e and n_D in the pedestal 161
6-8 Comparison of $\langle L_0 \rangle$ with Δ_n 162
6-9 Effective diffusivity D_{eff} in the pedestal at varying I_P 164
6-10 Simple picture of KN1D geometry 167
6-11 Examples of input and output profiles from a KN1D run 169
6-12 Matching output of KN1D with experimental D_α emissivity 172
6-13 Sample edge profiles at varying target density. 175
6-14 Behavior of $n_{e,\text{PED}}$ and Δ_n with variation of $\bar{n}_{e,L}$ 176
6-15 Characteristic scale lengths in the pedestal as $n_{e,\text{PED}}$ is varied 177
6-16 H-mode discharge with application of D_2 puff from inner wall 179
6-17 Video images of the inner column before and during H-mode D_2 puff 180
6-18 Edge profiles in H-mode before and during gas puffing 182
6-19 ETS profiles in H-mode before and during gas puffing 184
6-20 KN1D runs using model pedestal profiles with varying $n_{i,\text{PED}}$ 189
6-21 Matching n_i pedestal with the coupled kinetic-fluid neutral model . . 190
6-22 How to model the effect of neutral fueling changes on the pedestal . . 191
6-23 Results of perturbations to neutral source 192

A-1 n_{H} and T_{H} in a simple 1-D benchmark of KN1D against DEGAS 2 . . 208

List of Tables

2.1 Typical parameters of actual tokamaks 51
2.2 Summary of H-mode pedestal behavior on major tokamaks 60
3.1 CAMAC modules used in the edge TS diagnostic 81
5.1 Results of multiple regression analysis for pedestal parameters 130

Chapter 1

Introduction

The Plasma Science and Fusion Center, a part of the Massachusetts Institute of Technology, is a national facility for research into plasmas and their applications in nuclear fusion. The flagship program of the center has been since 1993 the Alcator C-Mod tokamak, [1] a magnetic plasma confinement device on which have been made considerable contributions to worldwide plasma fusion research. A small but significant contribution with regard to tokamak edge transport barriers is the subject of this dissertation.

Much can be said, and has been said, [2] about the energy needs of human civilization, both now and tomorrow. This thesis will not attempt to motivate the development of new sources of electricity production, but rather launch upon the assumption that a nuclear fusion reactor is a worthwhile endeavor, ultimately capable of supplying future energy needs. Numerous volumes have been written on plasma fusion and concepts of tokamak science, and the material reviewed below will be a small subset of that valuable information. The current chapter is meant only to present sufficient background needed to motivate the later chapters. Several excellent references are recommended to the reader in search of more information. [3][4][5][6]

1.1 Plasma fusion

1.1.1 Plasmas for thermonuclear fusion

Nuclear fusion for purposes of energy production will rely on reactions of light isotopes which give a net release of energy. Reactions involving hydrogen and helium isotopes are among the most promising candidates, and include

$$\begin{aligned} \mathrm{D} + \mathrm{D} &\longrightarrow \mathrm{T} + \mathrm{p} + 4.03\ \mathrm{MeV} \\ \mathrm{D} + \mathrm{D} &\longrightarrow {}^3\mathrm{He} + \mathrm{n} + 3.27\ \mathrm{MeV} \\ \mathrm{D} + \mathrm{T} &\longrightarrow {}^4\mathrm{He} + \mathrm{n} + 17.6\ \mathrm{MeV} \\ \mathrm{D} + {}^3\mathrm{He} &\longrightarrow {}^4\mathrm{He} + \mathrm{p} + 18.3\ \mathrm{MeV} \end{aligned}$$

Here D and T represent single nuclei of deuterium (^{2}H) and tritium (^{3}H). The D-T reaction is considered the most promising for use in a reactor device, due both to the high value of energy released and to its highly favorable cross section. Confining and heating plasmas composed of these reactants allows for a significant nuclear fusion rate

$$R_f = n_{\mathrm{D}} n_{\mathrm{T}} \langle \sigma v \rangle \tag{1.1}$$

where $\langle \sigma v \rangle$ is the cross section for D-T fusion averaged over the Maxwellian velocity distributions

$$f(v) = n \left(\frac{m}{2\pi T} \right)^{3/2} \exp\left(-\frac{m v^2}{2T} \right) \tag{1.2}$$

of each nuclear species with mass m, density n, and temperature T.

The reaction rate R_f is a sensitive function of the ion temperature, peaking near 70 keV in the case of D-T. The majority of fusing nuclei are in the hot tail of the ion energy distribution, and one relies on a broad thermal distribution to obtain significant fusion reaction rates. This gives rise to the term *thermonuclear fusion*. Nuclear fuel at fusion-relevant temperatures exists as a fully ionized plasma.

Plasma characteristics

In a plasma, ions and electrons freely interact with one another and are present with sufficient density to produce a quasi-neutral medium. Quasi-neutrality means that displacement of charge in a plasma results in a strong Coulomb restoring force that insures an approximately equal ion and electron charge density. For multiple ionic species i, each with charge Z_i, the relation is given by

$$n_e \approx \sum_i n_i Z_i \tag{1.3}$$

or, for a pure deuterium plasma,

$$n_e \approx n_{\mathrm{D}} \tag{1.4}$$

On sufficiently small spatial scales, these approximations can be violated. An important scale length is the distance above which the electric field associated with an ion is shielded by the surrounding ensemble of electrons. This is the Debye length:

$$\lambda_D = \left(\frac{\epsilon_0 T}{ne^2}\right)^{1/2} \tag{1.5}$$

The physical interpretation of λ_D is the distance over which the energy due to charge separation is balanced by the plasma internal thermal energy. It is the fundamental length scale of a given plasma. The restoring force due to charge separation also introduces a natural frequency to the plasma. The plasma frequency

$$\omega_p = \left(\frac{ne^2}{\epsilon_0 m_e}\right)^{1/2} \tag{1.6}$$

is the frequency at which a displaced group of electrons will oscillate in space.

1.1.2 Magnetic confinement

The large ion temperatures required for fusion imply that minimal plasma contact should be had with material surfaces, and so a fusion reactor requires confinement that does not rely on chamber walls to retain plasma pressure. By imposing strong

magnetic fields, one can increase the level of plasma particle confinement and reduce the contact of hot plasma particles with walls. Free charged particles of mass m and charge e in a magnetic field $\mathbf{B}$ feel a force

$$\mathbf{F} = m\frac{d\mathbf{v}}{dt} = e\mathbf{v} \times \mathbf{B} \tag{1.7}$$

which is perpendicular to both the field direction and the particle velocity $\mathbf{v}$. This causes the particle to execute gyrations about the magnetic field at its cyclotron frequency

$$\omega_c = \frac{eB}{m} \tag{1.8}$$

and with a radius

$$\rho = \frac{v_\perp}{\omega_c} = \frac{mv_\perp}{eB} \tag{1.9}$$

termed the Larmor radius or gyroradius. Here the subscript on $v_\perp$ distinguishes it from the velocity parallel to the field line $v_\parallel$. If a species of particles has a thermal distribution, then one can take $v_\perp^2 = v_t^2 = T/m$, and now

$$\rho = \frac{\sqrt{mT}}{eB} \tag{1.10}$$

is a characteristic gyroradius associated with the thermal velocity v_t.

This gyration about field lines restricts particle motion perpendicular to field lines, while allowing free streaming in the parallel direction. Good perpendicular, or cross-field, confinement accompanied by very poor confinement along field lines suggests that a torus would be the optimal geometry for a magnetically confined plasma. Having a volume of strong magnetic field with field lines bent around to close upon themselves reduces the extent of end losses that result in a strictly linear plasma device.

1.1.3 Tokamaks

A highly successful toroidal device is the tokamak,* a device in which confined plasma fills a torus with a major radius R_0 and minor radius a. Figure 1-1 diagrams one quarter of tokamak plasma, where a circular plasma cross-section is chosen, for the sake of simplicity. Radial (r), poloidal (θ) and toroidal (Φ) coordinates are used to describe the tokamak, as shown, with $R = R_0 + r\cos\theta$. A strong toroidal field B_T and plasma current I_P are oriented along Φ (and are sometimes referred to as B_Φ, I_Φ); a poloidal field B_P (or B_θ) oriented along θ is created by I_P. In general, the poloidal field strength is considerably smaller than the toroidal field strength, but is necessary in order to give a stable equilibrium. Currently, tokamaks require that I_P be driven by transformer action, using a central solenoid standing in the center of the torus (OH stack). Toroidal field is generated by TF magnets spaced regularly around the toroidal vacuum vessel. Finally, a number of toroidally symmetric equilibrium field (EF) coils are arranged about the device, in order to provide a vertical field that counters the outward expansion of a plasma of finite pressure. EF coils are also used to shape the poloidal cross section of the plasma, allowing for vertical elongation and special shaping.

Equilibrium

Tokamaks often operate with non-circular cross sections, and thus it is it useful to introduce the poloidal flux function ψ. Because they are axisymmetric in Φ, tokamak plasmas consist of an infinite number of radially nested surfaces of constant ψ. Field lines follow helical paths around the torus, due to the sum of toroidal and poloidal field, and the trajectory of a given field line will lie in a contour of constant flux. The cross-section of these ψ-contours can be non-circular. Due to force balance considerations, there is no plasma pressure gradient along field lines, and thus pressure is constant on a given flux surface. Because transport along field lines is very large, parallel thermal conductivity is high, and temperature can usually be considered a

*From the Russian *toroidalnaya kamera* and *magnitnaya katushka*, meaning "toroidal chamber" and "magnetic coil"[6, §1.10]

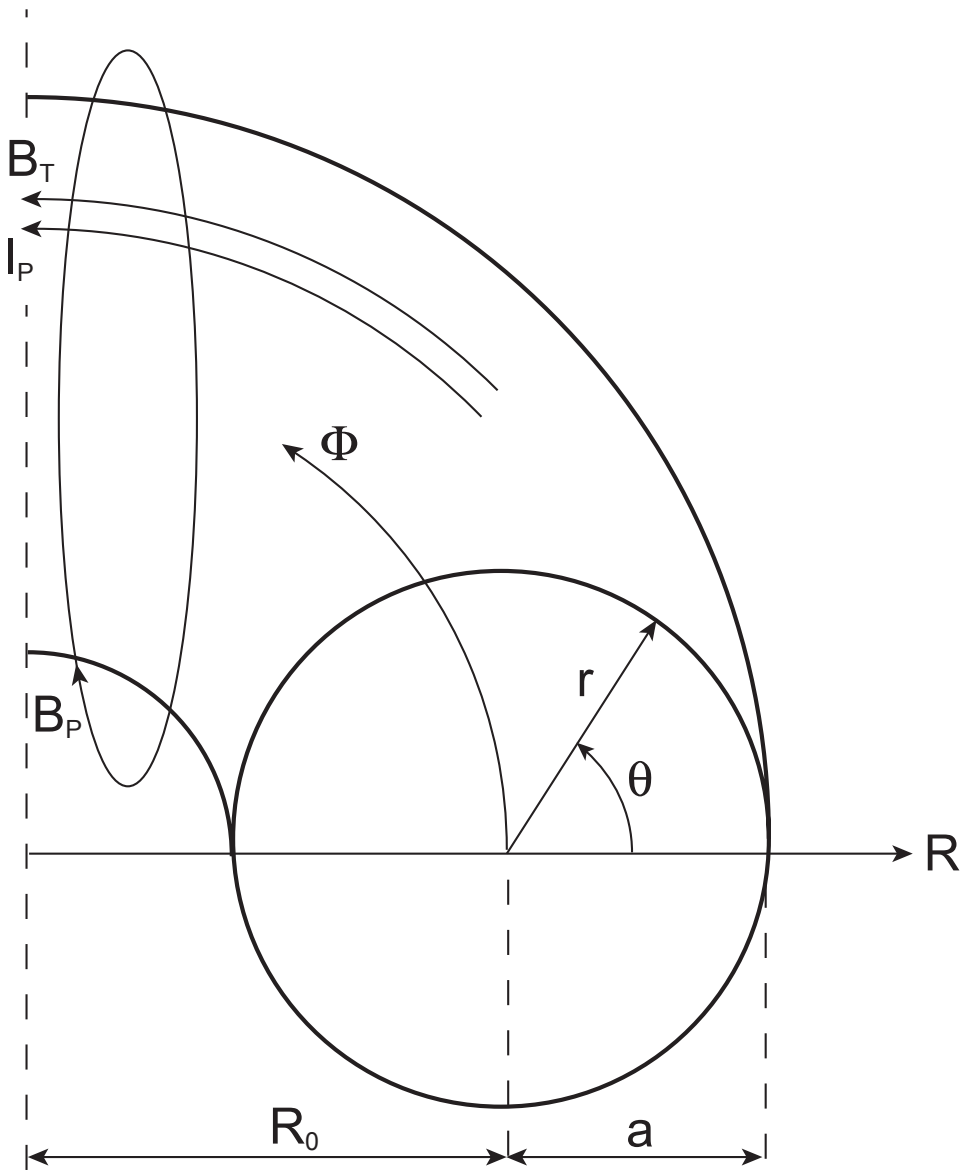

Figure 1-1: A circular tokamak plasma fills a torus of major radius R_0 and minor radius a, on a (r, θ, Φ) coordinate system, with $R = R_0 + r\cos\theta$. A strong toroidal field B_T and toroidal plasma current I_P are oriented along Φ, and a poloidal field B_P oriented along θ is created by I_P.

flux function as well. Therefore, the task of diagnosing tokamak profiles is aided by the assumptions $p = p(\psi)$, $T = T(\psi)$, and $n = n(\psi)$.

Associated with the pitch of the magnetic field lines is the safety factor q, which designates the number of circuits the field line must make in the toroidal direction before returning to the same poloidal position on the flux surface. Safety factor is also a flux function, $q = q(\psi)$, and may be approximated as

$$q = \frac{rB_T}{R_0 B_P} \tag{1.11}$$

for a circular cross-section plasma with a large aspect ratio R_0/a. In a more realistic magnetic geometry q is a more sophisticated integral around the flux contour, but scales in a way consistent with (1.11), being proportional to toroidal field and inversely dependent on plasma current. Generally, q is of order 1 near the plasma center and increases near $r = a$. The q-profile plays a significant role in plasma stability.

Drifts and particle orbits

In a collisionless plasma of infinite extent, with a uniform magnetic field, the guiding center of each particle orbit would be tied perfectly to a field line. However, in any real system, guiding center drifts occur due to spatial variation of $\mathbf{B}$ and the presence of electric field $\mathbf{E}$. Important guiding center drifts in a tokamak include the $\mathbf{E} \times \mathbf{B}$ drift, the ∇B drift and the curvature drift.

The first important drift occurs when a macroscopic electric field is oriented perpendicular to the ambient $\mathbf{B}$. This condition introduces a drift to the magnetized particles which is independent of particle charge, mass and energy. Thus all plasma incurs a bulk drift velocity, which can be shown [6, §2.6] to be equal to

$$\mathbf{v}_d = \frac{\mathbf{E} \times \mathbf{B}}{B^2} \tag{1.12}$$

This drift is important because when local changes in radial electric field generate sheared poloidal plasma flows, radial transport can be significantly reduced.

In tokamaks, there is found a significant gradient of **B** perpendicular to field lines, as well as field line curvature, both of which alter the gyroradii of particles. The guiding center of each particle experiences a displacement from its nominal flux surface, due to combined grad-B and curvature drift effects. Thus, these drifts have a significant impact on particle orbits. If collisions are ignored, then particles tied to field lines may be classified as either *trapped* or *circulating*, depending on their orbits as they move around the torus. Circulating particles have higher parallel velocity, and travel freely in the toroidal direction, while trapped particles experience a mirror force as they move into regions of smaller major radius and thus higher field. In the case of trapped particles, orbits in the shape of bananas result from the aforementioned drifts. The half-width of the banana orbit can be shown [6, §3.12] to scale as the ion Larmor radius, evaluated using the value of the poloidal field. This quantity is called the poloidal ion gyroradius $\rho_{i,\mathrm{pol}}$, and is considered in some models of edge transport barriers, to be discussed in Sec. 2.2.1.

1.2 Confinement and transport

Tokamak plasmas commonly are characterized by an energy confinement time τ_E, in essence an inverse loss rate for energy contained in the core plasma. If W_P is the plasma stored kinetic energy, and P_{in}, P_{loss} are the input and loss power, then

$$\frac{dW_P}{dt} = P_{\mathrm{in}} - P_{\mathrm{loss}} = P_{\mathrm{in}} - \frac{W_P}{\tau_E} \tag{1.13}$$

and, in steady state,

$$\tau_E = \frac{W_P}{P_{\mathrm{in}}} \tag{1.14}$$

Input power sources include the ohmic power, given by the product of plasma current and the resistive portion of the loop voltage ($P_{\mathrm{ohm}} = I_P V_\Omega$), auxiliary heating ($P_{\mathrm{aux}}$) from RF or neutral beam sources, and any alpha-particle heating (P_α) that may occur in a D-T fusion plasma. Power loss is connected to transport of particles and energy through the closed flux surfaces, into the region of open field lines, and ultimately

onto the walls of the vessel.

For a steady state plasma burning D-T fuel, it is possible to produce a simple figure of merit for reaching ignition. Taking $P_H = P_{\text{ohm}} + P_{\text{aux}}$ and $d/dt = 0$, one gets

$$P_H = \frac{W_P}{\tau_E} - P_\alpha = \left(\frac{3nT}{\tau_E} - \frac{1}{4}n^2\langle\sigma v\rangle E_\alpha\right) V \tag{1.15}$$

where V is the plasma volume, E_α is the energy yield per D-T fusion, and the reaction rate in (1.1) is calculated assuming a 50-50 mixture of D-T. Also, flat temperature and density profiles are assumed over the plasma volume. In the temperature range relevant to fusion (10–20 keV), $\langle\sigma v\rangle$ is approximately proportional to T^2, meaning that the ignition condition $P_H \leq 0$ simplifies to $nT\tau_E \geq C$, with C a constant. Thus the confined plasma pressure $p = 3nT$ and the energy confinement time τ_E are parameters that a tokamak designer should want to increase.

There is unfortunately an upper bound in the attainable plasma pressure, manifesting itself as a beta-limit, [6, §6.16] where plasma beta is the ratio of thermal energy to magnetic energy:

$$\beta = p\left(\frac{B^2}{2\mu_0}\right)^{-1} \tag{1.16}$$

The sources of β limits seem to be magnetohydrodynamic (MHD) instabilities, the form of which are subject to details of current and pressure profiles. The general trend from experiment shows that $\beta_{\max} \propto I_P/aB_T$, such that maximum attainable pressure ought to scale as $p_{\max} \propto I_P B_T/a$.

Energy confinement time τ_E is a single number that encapsulates a great amount of transport physics. Mechanisms of energy transport include convection, conduction and radiation, all of which should be taken into account in a complete model of transport and confinement. An extensive theory of *neoclassical transport* has been developed to account for diffusion processes in toroidal systems due to Coulomb collisions. However, the strong radial particle and thermal transport present in tokamak plasmas is not well characterized by these analytical means, as measured confinement times are considerably smaller than the predictions of neoclassical tokamak transport theory. [6, §4.12] Transport in real tokamaks is deemed *anomalous*, and is believed to

be dominated by a number of plasma instabilities of varying size scales. The relation between the resulting plasma turbulence and plasma transport is a topic of ongoing research.

Though detailed understanding of the processes governing transport is not had, it is possible to relate empirically global plasma confinement to simple machine parameters through power law scalings. The ITER89-P scaling is the result of such an exercise, taking advantage of a multi-machine database in an effort to generate a predictive formula for extrapolation to a future device. The empirical confinement time was given by

$$\tau_{E,\text{ITER89-P}} = 0.048 \frac{{I_P}^{0.85} {R_0}^{1.2} a^{0.3} \kappa^{0.5} n^{0.1} {B_T}^{0.2} A^{0.5}}{{P_{\text{aux}}}^{0.5}} \tag{1.17}$$

with I_P in MA, R_0, a in m, n in 10^{20} m^{-3} and P_{aux} in MW. κ is the vertical elongation and A is the isotopic mass in AMU. The scaling applies to *L-mode*, or low confinement mode, plasmas. These are obtained by applying auxiliary heating to an ohmically heated plasma. As demonstrated by the denominator of (1.17), increasing heating power to raise plasma temperature actually decreases τ_E. This diminished confinement at higher levels of heating power would be a discouraging result, had an enhanced mode of confinement, possessing an edge transport barrier, not been discovered.

1.3 Edge transport barriers

In tokamaks, global transport and confinement depend strongly on temperature and density at the plasma edge, which serve as boundary conditions for core plasma profiles. [7] [8] [9] [10] [11] This dependence makes edge transport a topic of great interest in current and future fusion devices. Of particular interest is the edge transport barrier (ETB) associated with the high confinement regime, or *H-mode*. This mode of operation was first observed on the ASDEX tokamak in 1982 [12], and the discovery increased expectations for energy confinement in tokamaks. ETB formation results in

a radially localized region of steep profile gradients. The result is a so-called *pedestal*, in both temperature and density, the parameters of which influence the core profiles and associated transport.

The enhancement of confinement obtained upon transitioning to H-mode from low confinement mode, or L-mode, is usually given in terms of the increase in τ_E. Energy confinement time, normalized to its L-mode value defines the H-factor: $H = \tau_E/\tau_{E,L}$. Here $\tau_{E,L}$ is taken from an L-mode scaling law, such as that in (1.17). The best H-modes generally exhibit $H \approx 2$. Direct calculation of power law scalings for the τ_E in H-mode result in exponents similar to those in (1.17), suggesting that the enhancement is not due to complex changes in the core plasma transport. Rather, local reduction in transport at the edge tends to boost overall confinement in a simple manner. Because of this confinement enhancement, H-mode is the recommended operational regime for a planned next-step device, the International Thermonuclear Experimental Reactor (ITER). [13]

ETBs exhibit short gradient scale lengths and exist in a region bridging closed and open field lines, which complicates the modeling of plasma transport in the pedestal. Poloidally asymmetric neutral fueling at the edge adds a particle source for which one should carefully account. Such difficulties are not encountered in the core plasma, well inside the edge pedestal. Thus core and edge modelling are usually treated separately, and efforts to model tokamak transport have largely focused on the core plasma, using numerical simulation to determine plasma profiles, and taking as input assumed pedestal values. For example, in simulations of turbulence driven by the ion thermal gradient (ITG) [7], a strong correlation is found between core confinement and edge T_i. The mechanism for this appears to be the tendency for ITG fluctuations to drive the core temperature gradient scale length L_T to a critical value.

Experimentally, a robust connection between edge conditions and core confinement often is observed. Correlations between plasma stored energy and edge pressure gradient were deduced on ASDEX Upgrade. [8][9] Work on the DIII-D tokamak shows a strong dependence of central temperature on edge beta [10], while evidence of a critical gradient scale length is seen in T_e profile measurements on Alcator C-

Mod. [11] These last two results imply that central temperature, on which fusion reaction rates are strongly dependent, is in turn quite sensitive to edge temperature. Thus, to predict confinement in any future device, one must first gain a quantitative prediction for ETB characteristics.

A number of models have been developed to explain the existence and characteristics of the H-mode pedestal, and some of this work will be discussed in Sec. 2.2. In particular these models must address the question of what sets the pedestal width and height, the values of which determine the boundary condition imposed on core transport. For a given pedestal width, the maximum pedestal height may be set by a limitation on pedestal gradient, and so the physics of edge gradient relaxation shows its relevance.

1.4 Alcator C-Mod

As previously mentioned, this thesis describes findings from a single tokamak called Alcator C-Mod [1] and examines these findings in the context of other machines. C-Mod is of a compact design, having $R_0 = 0.68$ m and $a = 0.22$ m. Due to its relatively small size, C-Mod may not appear relevant to a reactor-scale device at first glance. However, the tokamak is capable of running at high magnetic fields and densities likely similar to the operating parameters of a future igniting tokamak.

1.4.1 Plasma parameters and geometry

C-Mod typically runs with toroidal field at $R = R_0$ of 5.4 T, though this value can be made as high as 8 T. The tokamak typically operates with plasma currents of 0.6–1.4 MA, with central densities in the range of 1–5$\times 10^{20}$ m^{-3}. Central temperature is typically 2–4 keV. Auxiliary heating is supplied using ion cyclotron range of frequency (ICRF) heating. Transmitters are most often run at 80MHz, which, by solution of (1.8), corresponds to an ion cyclotron resonance where $B_T = 5.3$ T.

Figure 1-2 shows a cross-section of the device with a typical plasma outlined. C-Mod is a *divertor* tokamak, meaning that plasmas are preferentially shaped with EF

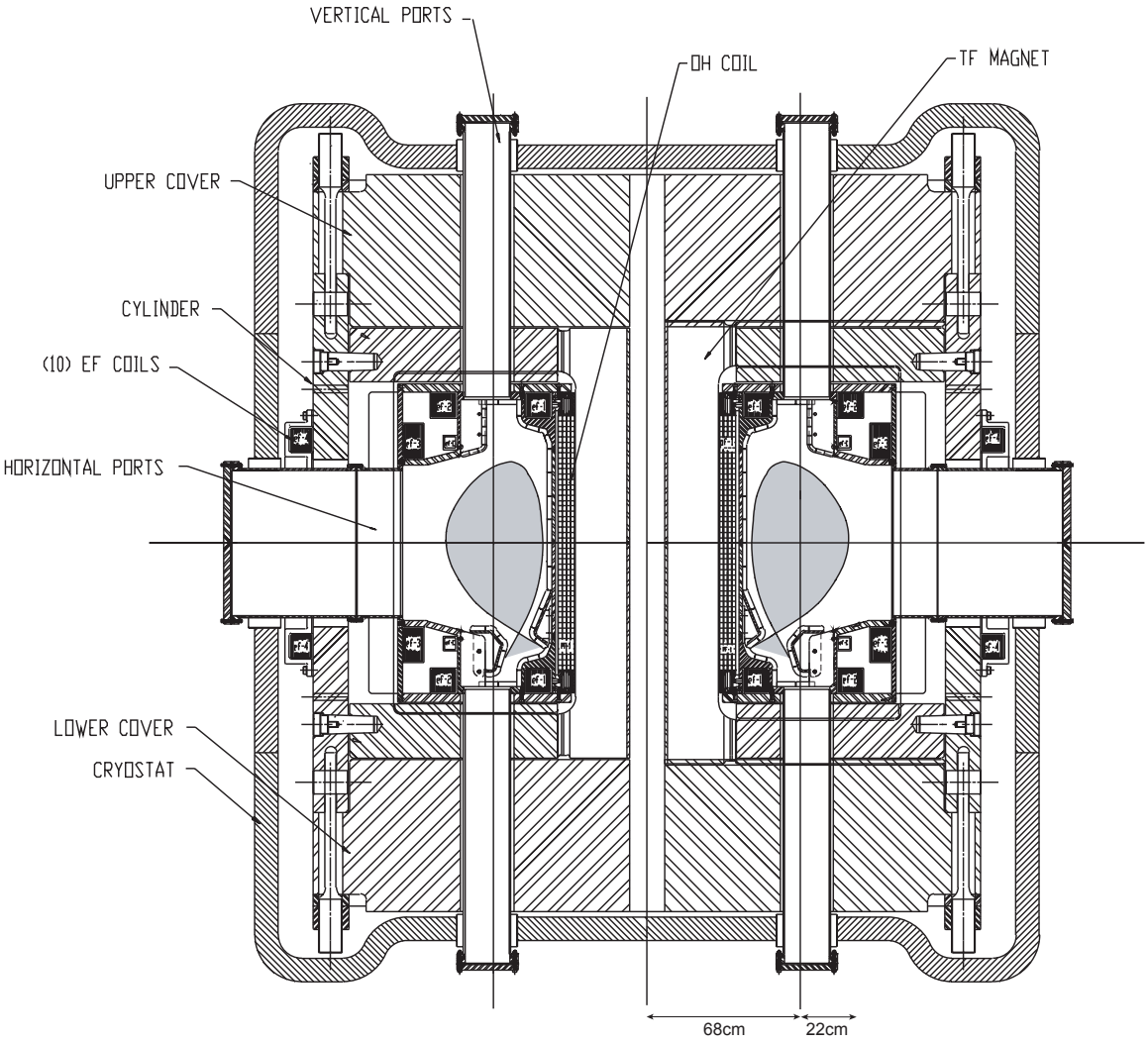

Figure 1-2: Schematic cross-section of Alcator C-Mod, showing the relative size and location of the plasma, vessel, field coils and supporting components. A typically shaped diverted plasma is pictured.

coils such that the last closed flux surface (LCFS) forms an X-point, or null, and the plasma facing components (PFCs) in the main chamber are contacted only with open field lines. (In diverted geometry the LCFS is also known as the *separatrix*.) The machine has a lower divertor, and typically runs lower single null (LSN) diverted discharges, though upper single null (USN) and even double null (DN) can be produced. The premise behind running with an X-point is that the high parallel transport will cause plasma to stream rapidly along open field lines into the divertor, which can be designed to handle high heat and particle loads. C-Mod can also be run *limited*, in which case the LCFS is tangent to a material surface, such as the inner wall or an outboard limiter. In all geometries, the LCFS forms the boundary between core plasma and scrape-off layer (SOL) plasma, where core plasma is confined on closed field lines, and the SOL plasma is on field lines that intersect material surfaces. The plasma "wetted" surfaces are mostly molybdenum (Mo) tiles, though for the period of time in which the current research was performed, some quantity of boron nitride (BN) tiles were used around ICRF antennae.

The EFIT code [14] is used to reconstruct a magnetic equilibrium from a set of magnetics measurements about the C-Mod vessel. The resultant equilibrium is an error-minimized fit to the Grad-Shafranov equation for axisymmetric systems. [6, §3.3][15, §6.2] EFIT output contains a set of flux contours defined on the $R-z$ grid for a sequence of time points throughout a given discharge. Nominally the EFIT time period is chosen to be 20 ms. A sample equilibrium is plotted in Fig. 1-3a, showing closed flux surfaces as solid curves and open flux surfaces as dotted curves. The LCFS is plotted with extra thickness, as is the limiter surface contour, which gives the outer boundary of axisymmetry.

Standard C-Mod plasma shape, like that of most diverted tokamaks, is not circular, but elongated and D-shaped. Figure 1-3b illustrates the definition of some important shape parameters. The parameter $\kappa = b/a$ measures the vertical elongation, where a is, as before, the minor radius along the R-axis, and b is the minor radius along z. The lower and upper triangularity (δ_L, δ_U) represent the fractional shift of the magnetic axis relative to the upper and lower extremes of the confined

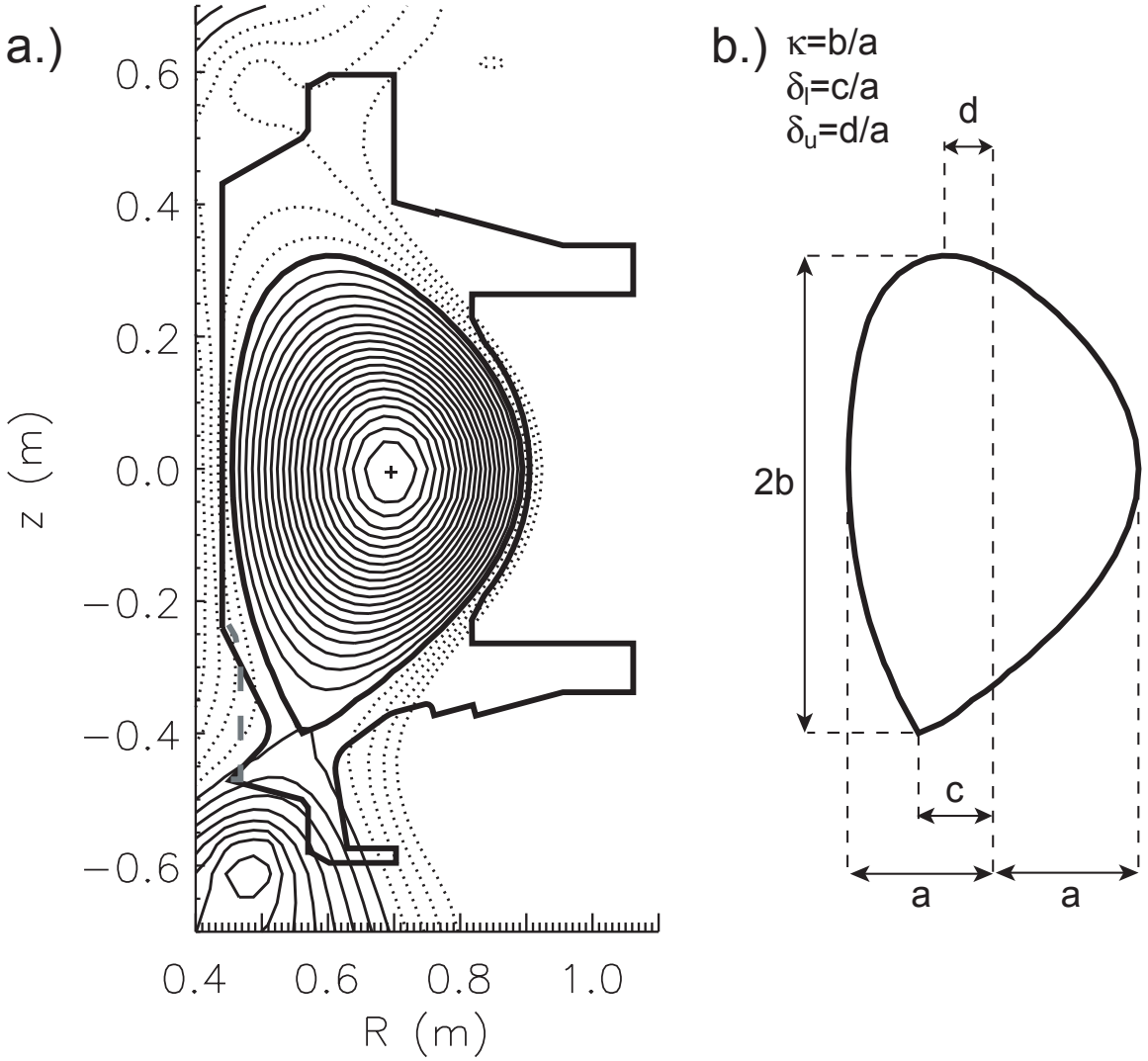

Figure 1-3: a.) Sample EFIT equilibrium reconstruction showing open (dotted) and closed (solid) contours of ψ in the $R-z$ plane. The cross is the magnetic axis. The thick angular boundary represents the limiter contour as it was prior to the year 2002, while the dashed gray curve illustrates the inner divertor shape from 2002 to the present. b.) Geometrical definitions of plasma elongation (κ) and lower and upper triangularity (δ_L, δ_U)

plasma. Higher values of $\delta = (\delta_L + \delta_U)/2$ correspond to a more triangular cross section. Shape is important to plasma stability and confinement. The effect of elongation on confinement time is evident in the scaling law of (1.17), for example. Greater triangularity assists some tokamaks in attaining higher edge pressures, as will be discussed in Sec. 2.3. A lower divertor modification, illustrated in Fig. 1-3a, increased the range of lower triangularity attainable in C-Mod starting in 2002.

1.4.2 Operational regimes

On C-Mod two major categories of H-mode are observed routinely. The regimes, ELM-free and EDA, occur in discharges of standard shape, and the differences in plasma parameters in either regime can be quite subtle in some cases. Yet transport and confinement characteristics differ significantly between the two modes of operation.

ELM-free

The ELM-free regime exhibits the higher confinement of the two regimes. It shows low levels of edge particle transport and no edge-localized modes (ELMs) [16] to relax or destroy the edge pedestal. ELM-free H-modes are characterized by increasing core density and impurity concentration, leading to termination of the H-mode by radiative collapse. This behavior can be seen clearly in Fig. 1-4, which shows the uncontrolled density and radiation rise in multiple ELM-free H-modes, triggered in this case by modest amounts of auxiliary ICRF power. When the radiated power P_{RAD} approaches the value of total input power, the H-mode can no longer be sustained.

As a result of increased particle confinement, particle recycling drops, and reduced levels of the Balmer alpha line from deuterium (D_α) are measured at the edge. The abrupt drop in D_α is a common signature of the L-H transition, as demonstrated in Fig. 1-4c. Yet another signature of H-mode onset is the reduced level of broadband turbulence at the edge. This can be shown by plotting the auto-power spectrum of signal from an edge reflectometer, [17] as in 1-4d.

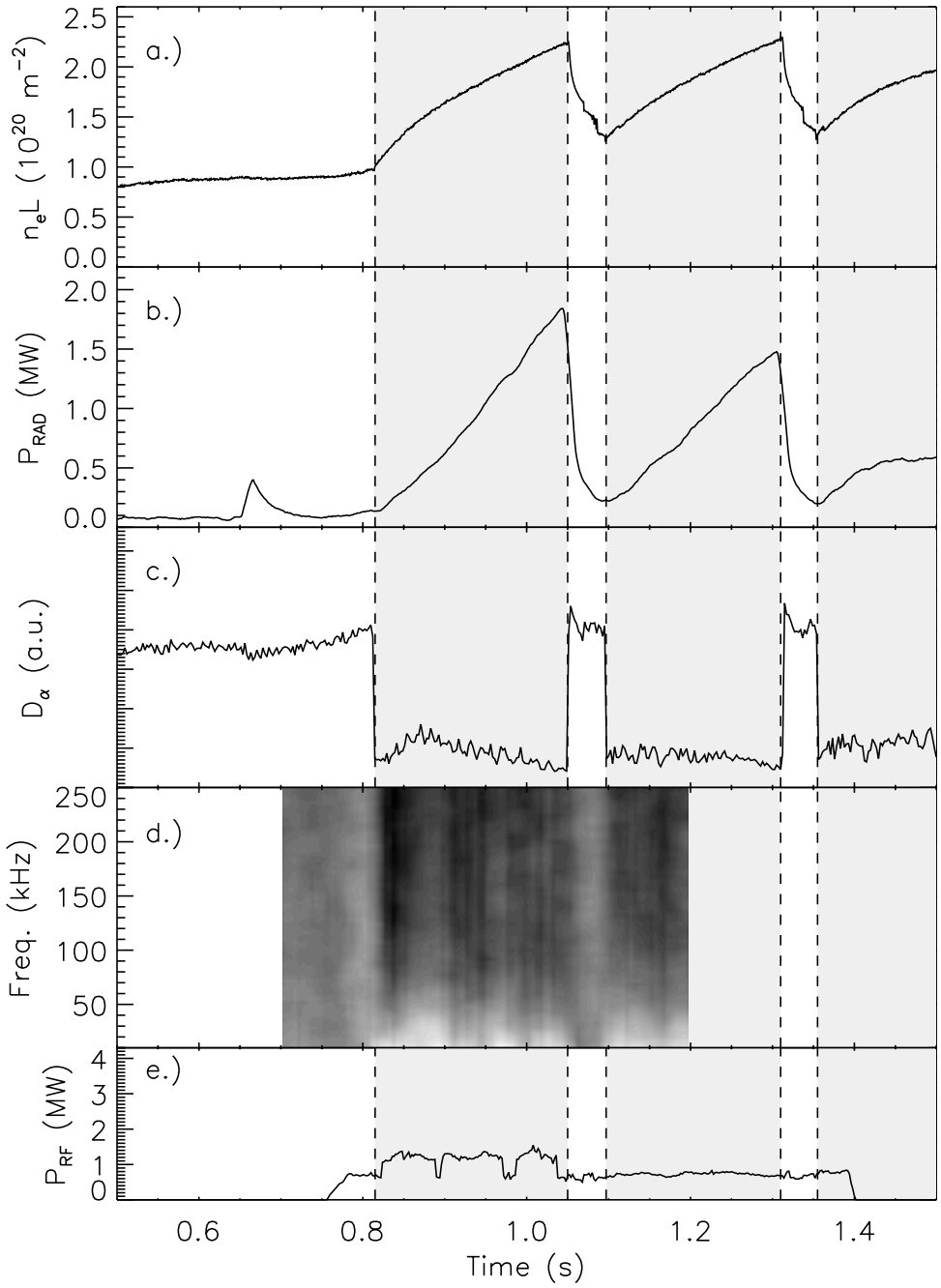

Figure 1-4: Characteristic time-behavior of ELM-free H-modes on C-Mod. Periods of H-mode are denoted by light gray shading. a.) Line-integrated density from interferometry shows a positive dn_e/dt throughout each H-mode, while b.) core radiated power continuously rises. c.) Measurements of D_α at the edge drop considerably from L-mode levels, indicating lower levels of particle recycling. d.) A spectrogram of edge reflectometer measurements shows decreased broadband fluctuations during the H-mode. e.) ICRF power is used to trigger H-modes.

Enhanced D-alpha

More common is the enhanced D_α (EDA) H-mode, [18] [19] [20] [21] [22] so named because measured D_α intensity can be much larger than that in ELM-free operation. Energy confinement in EDA H-mode is near that of ELM-free, but particle confinement is reduced, allowing a steady H-mode to be maintained with constant density and stored energy, and with no accumulation of impurities. Temporal behavior of a typical EDA H-mode is shown in Fig. 1-5. After the L-H transition, a period of approximately 20 ms follows in which the H-mode bears all the characteristic signatures of ELM-free H-mode, including abrupt density rise (1-5a), increasing radiated power (1-5b), depressed D_α (1-5c) and suppressed broadband fluctuations (1-5d). However, within about 100–200 ms, the density and radiated power reach roughly steady values, and the D_α brightness becomes much higher, even higher than that in L-mode in some instances. The indication is that, in contrast to the ELM-free regime, EDA operation demonstrates high particle recycling at the edge. All these signatures point to enhanced particle transport.

Strong experimental evidence has been presented [19] [22] [23] that suggests the enhanced particle transport of EDA is driven by a strong fluctuation localized to the pedestal region. This quasi-coherent mode (QCM) [24] is seen in edge reflectometer data in Fig. 1-5d. The mode generally becomes visible 10–50 ms after L-H transition, then settles upon a steady frequency (in the lab frame) of $f \approx 100$ kHz. The spectral width of the mode is typically $\Delta f/f \approx 0.05$–0.2. Within 100–200 ms, EDA H-modes typically reach steady state and can be maintained for times $t \gg \tau_E$ with the application of steady ICRF heating (1-5e).

The QCM is widely believed to provide a mechanism for reducing buildup of core density and impurity accumulation, leading to steady state H-mode operation. This contrasts with the confinement relaxation mechanisms on most other tokamaks. Often in these devices, the presence of large ELMs is seen to reduce confinement in bursts by expelling edge plasma into the SOL. [25] [26] [27] [28] Though ELMs allow for sustainable H-modes, the high intermittent heat fluxes present a challenge to divertor

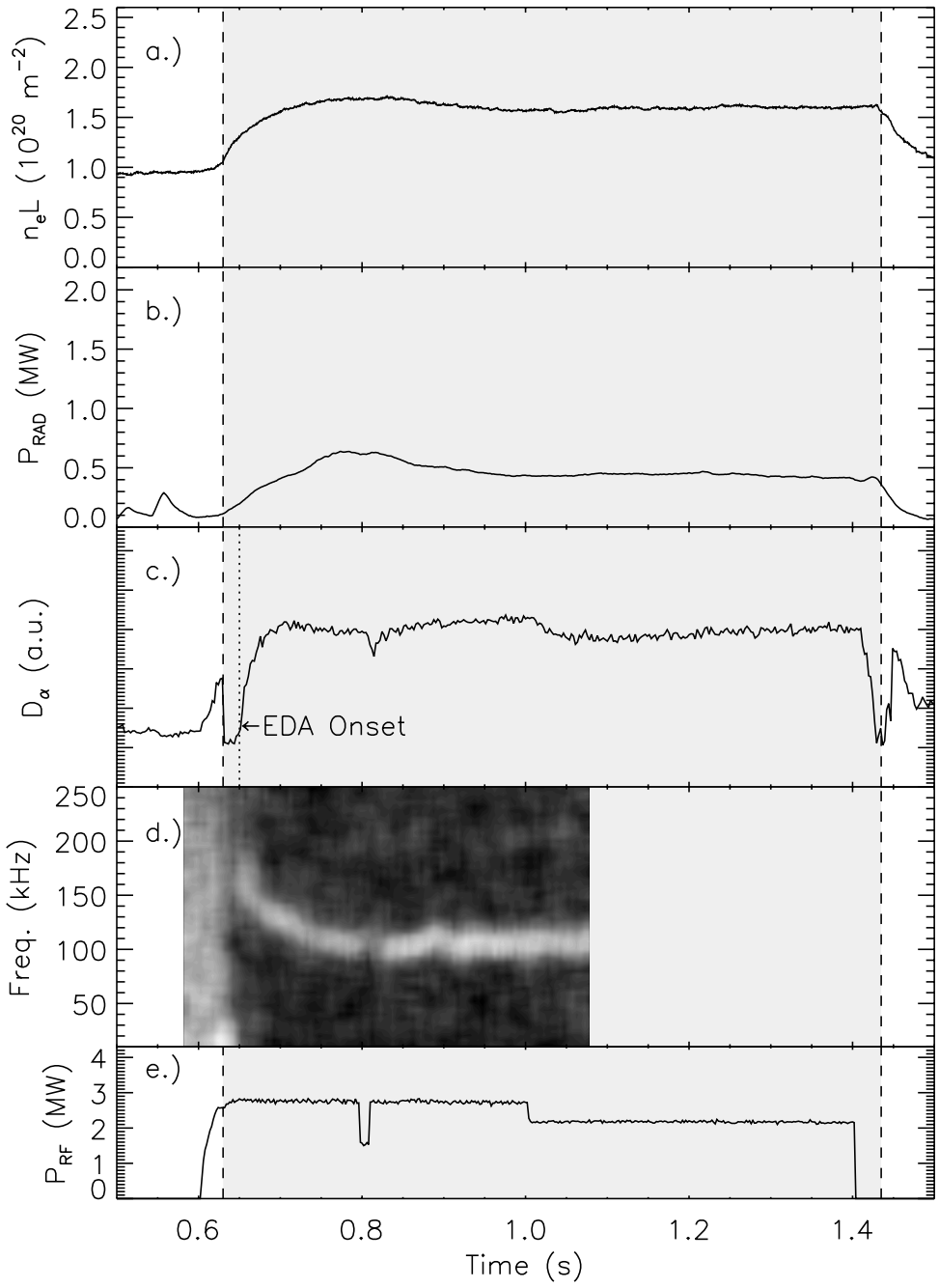

Figure 1-5: The onset of the EDA regime following an L-H transition gives steady-state H-mode operation. The period of H-mode is denoted by light gray shading. a.) Line-integrated density from interferometry shows a rollover in the particle inventory, while b.) the radiated power trace becomes steady in time. c.) Measurements of D_α at the edge rise significantly at the onset of EDA, indicating high particle recycling. d.) A spectrogram of edge reflectometer measurements reveals the existence of a quasi-coherent density fluctuation. e.) EDA H-mode can be sustained as long as sufficient ICRF power is delivered.

design in any tokamak of reactor scale. Because EDA is steady and absent of large ELMs, it has drawn interest as a possible reactor regime and has been examined extensively. Of particular interest are the conditions favoring EDA and how these conditions give rise to the QCM. Because this mode exists in the pedestal region, one would like to examine the characteristics of the ETB in both EDA and ELM-free H-modes, in order to understand the QCM existence criteria. This would give the best hope of reproducing it on other devices. This question will be addressed in Sec. 4.3.

1.4.3 Thomson scattering and other edge diagnostics

In order to study ETB structure, it is important to obtain data from all available edge diagnostics. Chief among these is an edge Thomson scattering (ETS) system [29] with high spatial resolution. This diagnostic was deployed on C-Mod in 1999 for the purposes of resolving electron density (n_e) and temperature (T_e) profiles in the ETB. It has operated routinely since that time and has proven to be very useful to experimental research on C-Mod. The working description of the diagnostic, and extensive results obtained from it, are the subject of later chapters. Its operation can be summarized briefly as follows.

The ETS system measures T_e and n_e at the upper edge of the plasma at $R = 69$ cm. The profiles have a nominal radial resolution of 1.3 mm after mapping along flux surfaces to the midplane. Typical profiles from edge TS extend from approximately 2 cm inside the LCFS to approximately 1 cm outside the LCFS and in the near SOL. The dynamic range of the edge TS diagnostic is approximately 20–800 eV, 3×10^{19}–5×10^{20} m^{-3}, which encompasses conditions throughout the pedestal region in most operational regimes. As will be shown, a dramatic steepening of T_e and n_e gradients is indeed observed over the ETB region upon transition from L to H-mode.

One can match ETS n_e with core profiles obtained from core Thomson scattering. [30] The core TS measurements are made using the same laser source as those of ETS, at six locations that are similarly mapped to midplane coordinates using EFIT equilibria. The midplane radii of the core measurements range from the magnetic axis to the plasma edge. The core TS system is optimized for higher T_e, n_e

than the edge system, and has a spatial resolution on the order of 1 cm. There is consistent agreement between the diagnostics, within the experimental uncertainties of each. The ETS results have also seen favorable comparison to several other edge diagnostics, [29] as will be shown.

In addition to ETS, the C-Mod edge plasma is diagnosed with a visible continuum array, [31] electron cyclotron emission (ECE) diagnostics [32] and scanning Langmuir probes. [33] These diagnostics measure profiles of T_e and n_e, or closely related quantities, at various poloidal locations, as shown in Fig. 1-6. Also shown are the tangential view locations of some neutral emissivity diagnostics, to be described below. These measure profiles of line radiation from atomic deuterium in edge region.

Measurements from different poloidal locations are mapped along surfaces of constant flux to the midplane using the equilibrium reconstruction from EFIT. This code reconstructs the C-Mod separatrix with a radial uncertainty of approximately 3 mm. Because the ETB region is only a few millimeters in radial extent, relative offsets often must be applied to profiles, once they are mapped to the midplane, in order to compare them properly. For the comparison to be meaningful, T_e and n_e must each be constant along a flux surface, a condition sometimes not met close to the X-point, particularly in high recycling regimes. [33] The measurements discussed herein are sufficiently removed from the X-point for the assumption of constant T_e, n_e along field lines to be reasonable.

Electron cyclotron emission

Edge T_e profiles can also be obtained using ECE, [34, §5.2] as measured by a nine-channel grating polychromator (GPC). [32] This diagnostic gives midplane T_e at nine radial locations, corresponding to nine distinct magnetic field values. The frequencies of the measured emission correspond to the second harmonic of cyclotron emission: $2\pi f = 2\omega_{ce}$, corresponding to frequencies of around 300 GHz for typical C-Mod B-fields. The temporal resolution of the diagnostic is good for measuring fast (< 1 ms) changes in local T_e, but its radial resolution is not sufficent to resolve very short scale lengths in the T_e profile. The spacing between radial measurements is approximatelly

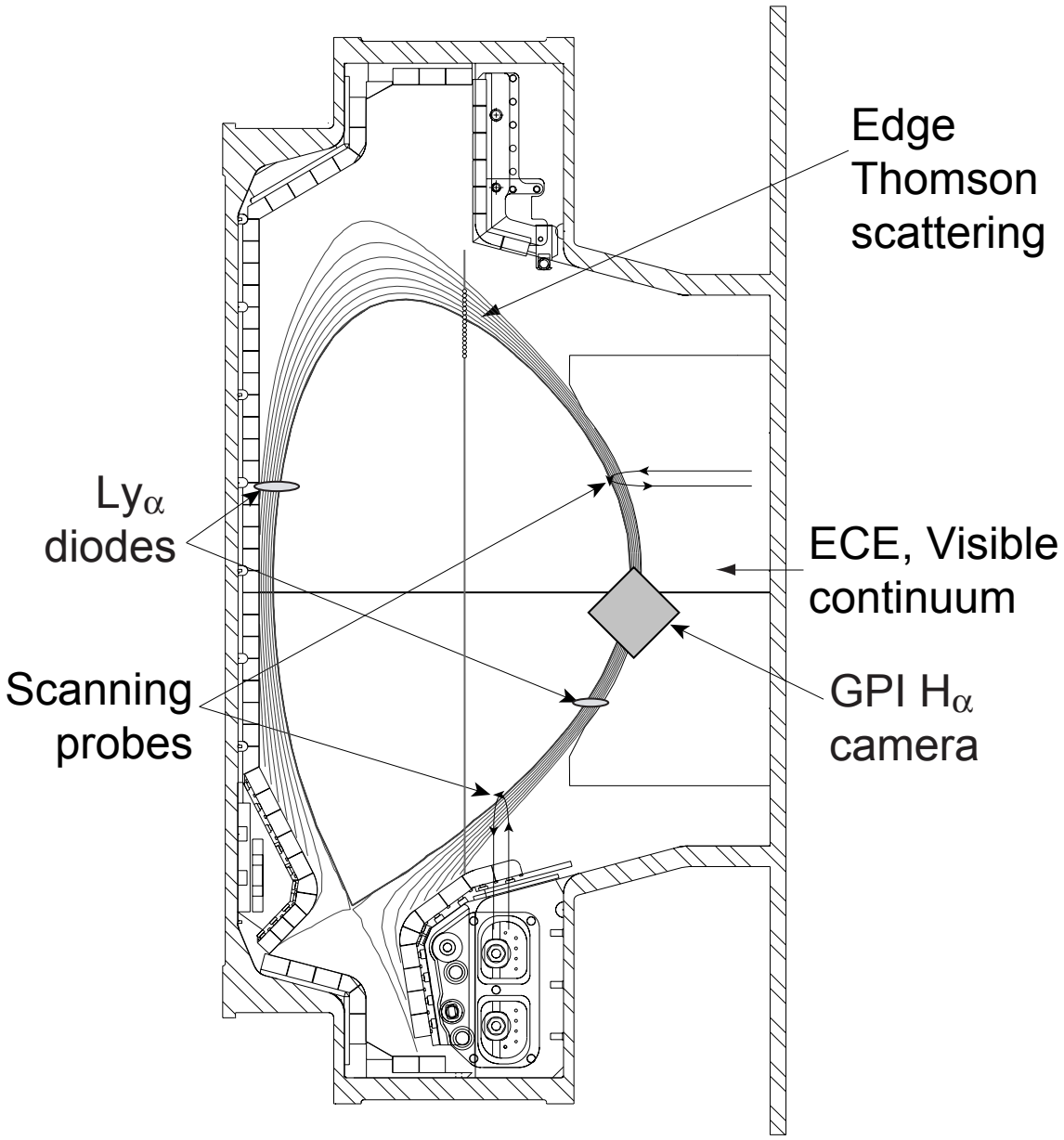

Figure 1-6: Schematic cross-section of Alcator C-Mod, showing the LCFS and SOL flux surfaces from a typical discharge and the poloidal locations of various edge diagnostic measurements.

2 cm, and the resolution of each channel is instrument-limited to 9 mm.

Visible continuum

Data are also available from a high-resolution visible continuum (VC) array [31], which measures line-integrated plasma emissivity at 536 nm along tangential chords at the midplane. The light is narrowly filtered to include no strong atomic spectral lines, such that the measured light results from bremsstrahlung and recombination radiation only. An Abel-inversion [34, §4.4] produces radial emissivity profiles with 1 mm resolution. In the core plasma the emissivity is dominated by free-free bremsstrahlung [35], and the photon intensity is given by

$$\mathrm{E} = \frac{9.5 \times 10^{-26} \bar{g}_{ff}(T_e)}{\lambda_0} \exp\left(\frac{-hc}{\lambda_0 T_e}\right) n_e^2 T_e^{-1/2} Z_{\mathrm{eff}} \tag{1.18}$$

where the Gaunt factor is

$$\bar{g}_{ff}(T_e) = -1.207 \log\left(\frac{12399}{\lambda_0 T_e}\right) + 0.556 \tag{1.19}$$

and the units of E, n_e, T_e and λ_0 are $\mathrm{cm^{-3}s^{-1}\AA^{-1}}$, $10^{20}\mathrm{m^{-3}}$, eV and Å. The quantity Z_{eff} is the effective ion charge of the plasma, taking into account the contributions of the majority and impurity ion species:

$$Z_{\mathrm{eff}} = \frac{\sum_i n_i Z_i^2}{\sum_i n_i Z_i} \tag{1.20}$$

The emissivity profile has a fairly weak dependence on T_e, which can be got from either ECE or ETS. The visible continuum can then be converted into a profile of $n_e\sqrt{Z_{\mathrm{eff}}}$, as in Refs. 31 and 36. In the colder regions of the edge, a more sophisticated expression is used in place of (1.18) in order to include contributions from recombination. [37] Typically, the profiles are truncated at the LCFS, since the SOL emissivity contains a poorly characterized contribution from molecular deuterium.

Scanning Langmuir probes

Measurements of n_e and T_e in the SOL are made with two scanning probes, which are inserted into the SOL and withdrawn during a period of 50–100 ms, obtaining radial profiles with sub-millimeter resolution. [38] A horizontally reciprocating probe is positioned several centimeters above the midplane, and a vertically scanning probe enters the SOL from the divertor. The probes are at different toroidal locations, separated by $\Delta\Phi = 180°$.

In most H-mode plasmas, ICRF heating results in higher edge temperatures, which prevents insertion of the scanning probes into the pedestal region. However, the n_e and T_e profiles of the near SOL provide a useful extension of the edge TS data. The probes obtain good profiles at densities below the sensitivity level of TS.

Neutral emissivity

Information about neutral density at the edge is obtained by measuring line radiation from the neutral species. Instruments on C-Mod have successfully measured radial profiles of emission from two atomic transition lines in D^0: the Lyman alpha (Ly_α: $n = 2 \rightarrow 1$, $\lambda = 1215$Å) and the Balmer alpha line (D_α: $n = 3 \rightarrow 2$, $\lambda = 6561$Å). [39] Typically, instruments measure chord-integrated brightness, and an Abel inversion is performed to obtain radial profiles of local emissivity. When taken together with profiles of n_e and T_e from ETS and perhaps probes, the local ionization rate and neutral density can be inferred as a function of radius, using well-known branching ratios. [40]

The Ly_α line is measured by two photodiode arrays, [41] viewing along chords tangential to field lines in the plasma edge. One array views the outer edge at a location 12.5 cm below the midplane, while the second array is trained on the high-field side SOL, 10 cm above the midplane. Each array is filtered to admit Ly_α, which dominates its spectral region under normal plasma conditions. The inboard-viewing array looks through the outboard SOL and should pick up additional Ly_α, though the chord-integrated radiation on the low-field side is expected to be smaller than

from the tangential chords on the high-field side. A potentially worse problem for evaluating the inboard Ly_α measurements is the large optical depth τ calculated for views through the high-field side SOL. A calculation with an atomic radiation transfer code [42] showed $\tau > 0.1$ for neutral densities greater than about 10^{18} m^{-3}. Thus, when neutral densities are very high near the inner wall, reabsorption of Ly_α is expected to be significant, making the brightness measurement and emissivity profile reconstruction highly questionable. Furthermore, the arrays have traditionally suffered from high levels of electronic noise and sensitivity to hard X-rays, [43] which have prompted the use of additional instruments, such as the gas puff imaging (GPI) camera, which is described below.

Single wide-angle measurements of D_α emission are obtained routinely, as in Figs. 1-4c and 1-5c. The line is not as desirable as Ly_α for making detailed profile measurements, since it is generally weaker and is more subject to reflections in the vessel. However, satisfactory 2-D images of D_α have been obtained [44] using a telescope with a tangential view at the outboard midplane and having a viewing dump in the far field. A fast-gated intensified camera collects the emission, filtered for D_α, with a spatial resolution of about 2 mm. Though the purpose of the camera is to obtain fast exposures and yield visual information about the 2-D structure of edge turbulence from a transient gas puff, collecting images of the ambient D_α is useful for determining the ionization rate and population of neutrals in the edge. A slice taken through the image at the midplane location gives a radial brightness profile, analogous to what is obtained directly from the Ly_α photodiode array. The detailed use of these data will be explored in Sec. 6.1.

1.5 Thesis goals and outline

The experimental objective of this thesis project is to utilize the edge diagnostics of Alcator C-Mod, in particular the edge Thomson scattering system, to characterize with high radial resolution the radial plasma profiles in the presence of ETBs. Given the ability to make routine measurements of this type, it is possible to study trans-

port and stability of ETBs. This thesis describes the implementation of Thomson scattering for this purpose, discusses the phenomenology of ETB profiles, and examines the relevance of edge quantities to operational regime. Experimental scalings of the pedestals with operational parameters are examined, as is the radial transport of neutral deuterium in the ETB.

The current chapter is intended to lay out the background knowledge, with pointers to relevant references, necessary to understanding the discussion in the following chapters.

- Chapter 2 discusses in more detail the existing understanding of ETBs in terms of predictions for pedestal scaling from theoretical modeling. Experimental results from other tokamaks, and prior results from C-Mod, are also discussed.

- Chapter 3 introduces Thomson scattering theory and describes the ETS hardware deployed on Alcator C-Mod. A series of required calibrations to the diagnostic is outlined, as well as the data analysis routines that produce the electron density and temperature profiles used in the subsequent analyses.

- Chapter 4 presents experimental phenomenology of ETB profiles, specifically describing typical pedestal widths. The regions in pedestal parameter space occupied by EDA and ELM-free operation are mapped.

- Chapter 5 examines the relation of confinement to the ETB, and details the empirical n_e, T_e and p_e characteristics as a function of plasma operational parameters such as current, field and input power. The effects of equilibrium shape on the pedestal are also considered.

- Chapter 6 more carefully considers the role of plasma and neutral transport in the development of the density pedestal. Empirical profiles of effective diffusivity are determined, and the limited effects of H-mode neutral fueling are examined experimentally. Comparisons are made to a kinetic model for the neutral fueling process.

- Chapter 7 summarizes the results and points to some directions for future work.

Chapter 2

Edge Transport Barriers: Theory and Experiment

Though the H-mode was discovered more than two decades ago, the physics behind L-H transitions and ETB sustainment is still an area of considerable research. Of specific importance to this topic is the scaling of pedestal characteristics with tokamak parameters. Numerous theoretical models have been proposed to explain H-mode results, while experimental work has produced large amounts of data. However, quantitative matching between theory and experiment is difficult, and the experimental results from different tokamaks often seem in contradiction. In order to predict the width and height of the H-mode pedestal on an unbuilt machine such as ITER, a better quantitative understanding of the ETB physics should be had. This chapter will descibe the basic features of the H-mode and the associated pedestal, then discuss existing theoretical efforts in pedestal modeling, and finally review the experimental scaling results obtained on various machines. Included is a description of C-Mod pedestal results obtained prior to the current work.

2.1 H-mode and pedestal characterization

Since its discovery on ASDEX, [12] the H-mode has been observed repeatedly on diverted tokamaks with auxiliary heating, somewhat less often in ohmically heated

plasmas, and very rarely in limited discharges. H-modes have certain universal characteristics. [45] First, a sudden change in plasma confinement occurs, resulting in global density and temperature rise. Stored energy increases, as would be expected from an increase in τ_E in (1.13). Second, edge pressure rises significantly immediately inside the LCFS, implying large increases in ∇p at the boundary. When the measurements are available, one typically sees strong gradients in both temperature and density, a reduction in broadband turbulent fluctuations, and a drop in the level of particle recycling. In many instances radial variation of E_r has also been inferred. The set of experimental results is consistent with a model for turbulence suppresion via shear in the plasma $\mathbf{E} \times \mathbf{B}$ velocity. [46] Shear in the poloidal plasma velocity decorrelates edge turbulence, in effect breaking up turbulent eddies, while linearly stabilizing a large number of damaging plasma modes.

Measurements of ETB profiles are made with a number of methods, including reflectometry for density and charge exchange recombination spectroscopy (CXRS) for ion temperature and velocity. Some of the most useful results have been obtained with Thomson scattering, which can measure simultaneously n_e and T_e at distinct spatial locations in the pedestal region. For profiles that exhibit a narrow region of strongly enhanced gradient, such as n_e and T_e, a set of several parameters is chosen for describing and comparing these pedestals. One can describe an H-mode radial profile in terms of its baseline (b), height (h), width (Δ), and location (R_0).

Though much ETB modeling does not provide specific predictions for profile shapes, some models [47][48][49] do suggest a pedestal profile with a tanh-like functional form. The DIII-D group proposed using such a function to routinely fit pedestal data and to yield the above pedestal parameters. [50][51] The function is defined on midplane radius R:

$$f(R) = b + \frac{h}{2}\left[\tanh\left(\frac{R_0 - R}{d}\right) + 1\right] + m(R_0 - R - d)H(R_0 - R - d) \qquad (2.1)$$

The fit of this modified tanh to real electron density on C-Mod is demonstrated in Fig. 2-1, with the fitting parameters called out. Here $d = \Delta/2$ is the pedestal half-

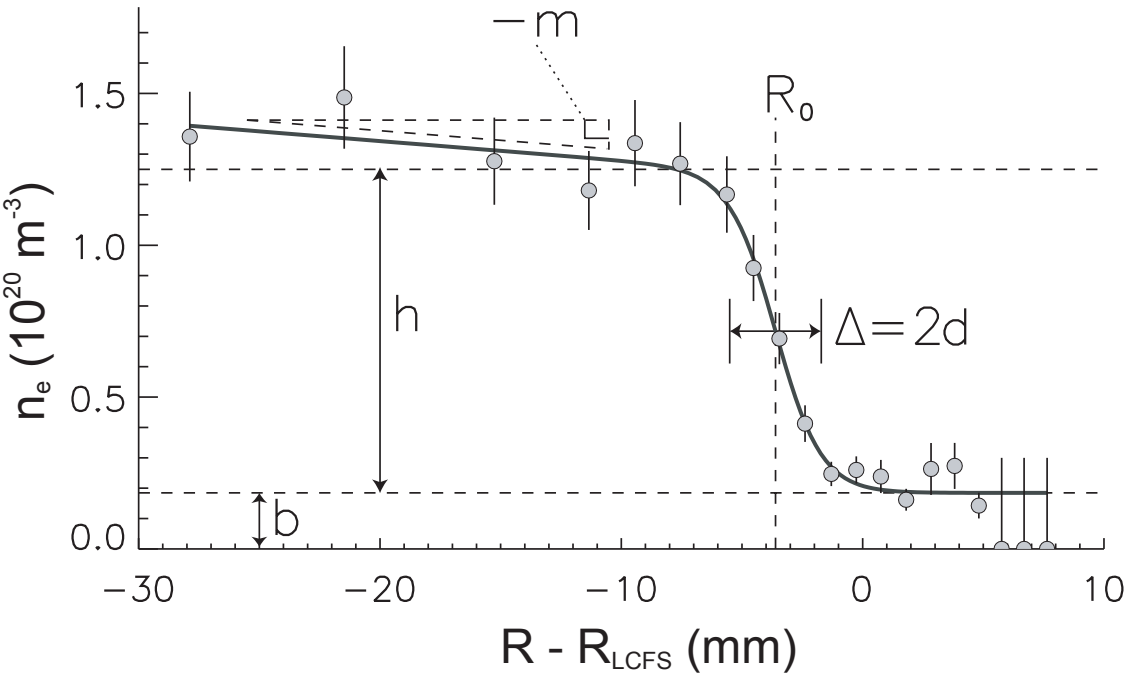

Figure 2-1: Typical n_e pedestal with modified tanh fit, with the five fit parameters highlighted.

width. The Heaviside function, $H(R_0 - R - d)$, allows one to account for the finite radial slope, $-m$, that exists inside the pedestal region. At the base of the pedestal ($R = R_0 + d$), $f \approx b$; the value of f atop the pedestal ($R = R_0 - d$), is approximately $b + h$. (2.1) has its maximum radial derivative at $R = R_0$: $|\nabla f|_0 = h/\Delta$. This notation will subsequently be used to denote the largest gradient of a given pedestal. Also, the subscript PED on a given variable will signify the value of that variable near the top of its pedestal (*e.g.*, $T_{e,\mathrm{PED}} = b_T + h_T$).

The modified tanh-fit is used in pedestal characterization on some tokamaks, and not on others. Often, the fit is an inappropriate choice because data lack sufficient spatial resolution. Some other techniques for determination of pedestal parameters will be mentioned in Sec. 2.3.

2.2 Pedestal scalings: Predictions from theory

Modeling serves as a guide to the experimentalist when it provides testable predictions. Hubbard [52] compiled a list of leading pedestal theories, selecting them based on the predictions they gave for scalings of pedestal parameters. These models and others will be described briefly below, followed by a summary of major experimental results on various tokamaks. In subsequent chapters, C-Mod experimental results will be examined in the context of some of this theoretical work.

2.2.1 Width from ion orbit loss

Initial efforts to model L-H transitions and ETB sustainment examined the localized change in radial electric field that results in sheared poloidal velocity and edge turbulence suppression. A potential source of E_r is ion orbit loss, which occurs when the guiding centers of particles drift sufficiently far off their native flux surfaces, that their orbits intersect material surfaces. Orbit loss effectively leaks current from the plasma edge to the vessel, resulting in electric field. If orbit loss is assumed to cause a variation in E_r, [53] then the region of stong turbulence suppression ought to be governed by the banana width, which scales as the poloidal ion gyroradius $\rho_{i,\mathrm{pol}}$. One might also expect the ETB width to scale similarly. This would be testable in an experiment by varying edge temperature and plasma current systematically, since $\rho_{i,\mathrm{pol}} \propto T_i^{1/2}/B_p \propto T_i^{1/2}/I_P$.

The simple ion orbit loss model has been modified and extended in subsequent work, though not necessarily in ways conducive to experimental testing. Taking into account the effects of the radial electric field on the banana width, Shaing [54] gives the scaling

$$\Delta = \rho_{i,\mathrm{pol}}\epsilon^{1/2}\left|1 - \frac{1}{B_p\omega_{ci,p}}\frac{dE_r}{dr}\right|^{-1/2} \tag{2.2}$$

where $\omega_{ci,p}$ is the ion cyclotron frequency evaluated using the poloidal field. For $|dE_r/dr| \gg B_p\omega_{ci,p}$, the B_p-dependence of Δ actually vanishes. Itoh and Itoh build on this result, and further complicate matters, by including viscosity shear effects. [55]

Increasing viscosity enlarges the width of the barrier.

2.2.2 Width from neutral penetration

Another theoretical approach that gives testable predictions for pedestal width scaling is one that models neutral fueling at the edge with minimal description of plasma transport. The original formulation was for impurities, and is known as the Engelhardt model. [56] In later work it was applied to the bulk fuel species as well. [57] The model is defined in slab geometry and assumes purely diffusive plasma transport, with a diffusion coefficient $D_\perp$ constant in space. Neutral ionization is assumed to occur at a singular radial location inside the LCFS. The resulting plasma pedestal has a width given by the neutral penetration length in the plasma:

$$\lambda_{\text{ion}} = \frac{v_n}{n\langle\sigma v\rangle_{\text{ion}}} \tag{2.3}$$

Here v_n is the characterstic neutral velocity, n is the plasma density, and $\langle\sigma v\rangle_{\text{ion}}$ is the velocity-averaged ionization cross section. In the simplest approximation, v_n is assumed constant and given approximately by the neutral thermal velocity at the LCFS. Then, with $\langle\sigma v\rangle_{\text{ion}}$ roughly constant over the region of interest, λ_{ion}, and thus Δ_{PED}, scales inversely with plasma density.

This simple model has been expanded with varying degrees of sophistication by Mahdavi *et al.*, with the introduction of poloidally asymmetric fueling sources [58] and generalizing to different diffusion coefficients for the core and SOL plasma: D_C, D_S. [59] In the slab geometry defined on x, with $x > 0$ corresponding to the SOL and $x < 0$ the confined plasma, the solution to the continuity equations, with plasma and neutral flux balanced exactly, gives

$$n_e(x) = n_{e,\text{PED}} \tanh(C - x/\Delta) \tag{2.4}$$

where

$$\Delta = \frac{2v_n}{E\langle\sigma v\rangle_{\text{ion}} n_{e,\text{PED}}} \tag{2.5}$$

Here E is a factor that accounts for flux surface expansion between the measurement location and the neutral fueling source, which is assumed to be localized at one poloidal location. When the flux surfaces are more spread out at the fueling location (higher E), the neutral penetration length in flux coordinates is smaller, leading to a decreased Δ. The parameter C is an integration constant that depends on SOL boundary conditions, namely the density e-folding length in the SOL λ_{SOL} and D_S:

$$C = \frac{1}{2}\sinh^{-1}\left(\frac{2\lambda_{\mathrm{SOL}}}{\Delta}\frac{D_C}{D_S}\right) \tag{2.6}$$

For small values of C, (2.4) functionally resembles (2.1), which is found to fit experimental data well. Thus, despite its simplicity, the model gives physical predictions that are easily tested: $\Delta_n \propto 1/n_{e,\mathrm{PED}}$ and $|\nabla n_e|_{\max} \propto n_{e,\mathrm{PED}}^2$. Also noteworthy is that this model is equally applicable in both L- and H-mode.

This extended Engelhardt, or Mahdavi, model is limited to a range of T_e from 20 to 300 eV, over which the ionization cross section stays fairly constant. Its chief limitations include the lack of charge exchange reactions and the inability of the neutrals entering from the SOL to increase in temperature or velocity. Mahdavi incorporated a modification to v_n via charge exchange in [49], and found the basic width scaling prediction unchanged. Around the same time, Stangeby [60] examined the model under the assumption of a diffusivity well associated with the H-mode transport barrier, as well as a spatially distributed ionization source. He determined that these were potentially important inclusions, the characteristics of which could significantly affect pedestal scaling, and that the boundary condition λ_{SOL} plays a strong role as well. In the course of attempting a first-principles model of the n_e pedestal, accounting for ion momentum and particle balance and neutral atom transport, Stacey [61] shows results consistent with the predictions of the Mahdavi model, but highlights the importance of radial ion velocity and cautions against using a purely diffusive model for interpreting data. Consideration of the Mahdavi model in the context of C-Mod density pedestals will be discussed further in Chs. 5 and 6.

Hinton and Staebler generated a pedestal width scaling prediction in H-mode

similar to that above using a more sophisticated model for plasma transport in the edge. [62] In their model, increased $|\nabla p|$ and $|\nabla n|$ drive the E_r shear, upon which particle and diffusion coefficients depend. The H-mode appears above a threshold value of the product of particle flux and energy flux ΓQ. The width of the barrier layer is shown to be set largely by the particle source. Defining the density gradient scale length at the LCFS as $L_{n,\mathrm{SEP}} = n_{e,\mathrm{SEP}}/|\nabla n_e|_{\mathrm{SEP}}$, and taking the mean free path to ionization at the LCFS as in (2.3), for sufficiently large values of $\lambda_{\mathrm{ion,SEP}}/L_{n,\mathrm{SEP}}$, the barrier width is shown to scale as $\Delta \propto \sqrt{\lambda_{\mathrm{ion,SEP}} L_{n,\mathrm{SEP}}}$. Otherwise, $\Delta \propto \lambda_{\mathrm{ion,SEP}}$. In either case, the width increases with heat flux as $\ln Q$.

2.2.3 Other models for width and gradient

When the pedestal has been analyzed in the context of ideal magnetohydrodynamics (MHD) theory, [15] stability to ballooning modes has usually been considered as the main limitation to the development of a large pressure gradient. An important parameter is the MHD alpha parameter [63]:

$$\alpha_{\mathrm{MHD}} = -\nabla p \frac{2\mu_0 R q^2}{B_t^2} \tag{2.7}$$

This parameter is essentially a dimensionless pressure gradient developed from the theory of ideal MHD for the assessment of stability to such modes. The critical value of the alpha parameter is $\alpha_c \sim 1$, and depends on the level of magnetic shear $s = r(dq/dr)/q$ at the edge. By assuming a pedestal at the critical gradient for MHD stability, one can predict p_{PED}, given Δ_p, according to

$$p_{\mathrm{PED}} = \Delta_p \times |\nabla p| = \Delta_p \frac{B_t^2 \alpha_c(s)}{2\mu_0 R q^2} \tag{2.8}$$

A prediction for transport barrier width can be determined from the solution of the drift mode equation, which includes the physics of the ITG mode and electron drift wave, in a large aspect ratio circular tokamak geometry. [64] Here the Reynolds stress associated with edge drift-ballooning modes (EDBMs) generates flow shear

at the edge. Assuming this shear is sufficient to stabilize turbulence and suppress transport, the radial extent of EDBMs should determine pedestal width. The theory yields an approximate scaling of $\Delta \propto a^{1/3}\rho_{i,\mathrm{pol}}^{2/3}$. This width scaling should be difficult to distinguish from the orbit loss scaling of 2.2.1. This work also discusses a more sophisticated treatment of ballooning modes, showing a radial structure of the modes differing from that of the standard treatment, but having the same stability properties. Coupling ballooning modes with surface peeling modes in a model for the type I ELM cycle [65] yielded the same result. An approximate scaling for the pressure pedestal at fixed plasma shape results from (2.8): $p_{\mathrm{PED}} \propto \rho_{i,\mathrm{pol}}^{2/3} I_P^2$

An alternative approach to ballooning mode analysis utilized 3-D numerical simulations of the Braginskii transport equations [66] in a flux tube geometry, supplemented by 2-D fluid stability analysis. [67] It was found that short gradient scale lengths should stabilize conventional MHD ballooning modes, and that the drop in pressure across the pedestal, rather than the gradient, determines the stability limit for the edge. The critical radial scale length was shown to scale with the total, rather than the poloidal, gyroradius: $\delta_R \approx \rho_i^{2/3} R^{1/3}$. For $\Delta > 2\delta_R$ the pressure pedestal is given by (2.8). For $\Delta < 2\delta_R$, the maximum pressure pedestal is given by

$$p_{\mathrm{PED,max}} = \frac{2B_t^2 \alpha_c}{3\mu_0 q^2} \frac{\delta_R}{R} \tag{2.9}$$

At fixed shape, both cases give scalings of approximately $p_{\mathrm{PED}} \propto \rho_i^{2/3} I_P^2$, with the ∇p much higher in the case of smaller pedestal width. The actual pedestal width is not predicted by this modeling.

Width scaling with total ion gyroradius has been predicted by other theoretical considerations. The effect of magnetic shear on turbulence suppression was considered by Sugihara *et al.*, giving $\Delta \propto \rho_i s^2$. [68] Gyrokinetic simulations demonstrated the most linearly unstable modes at the edge, if stabilized by $\mathbf{E} \times \mathbf{B}$ shear, would set a corresponding scale length for the ETB proportional to ρ_i, but modified by an unspecified function of plasma parameters. [69] In either case the ρ_i dependence could be easily masked in experiment by the variation of other parameters. For example,

Tokamak	JT-60U	JET	DIII-D	ASDEX Upgrade	C-Mod
major radius R_0 (m)	3.4	2.96	1.67	1.65	0.68
minor radius a (m)	0.9	1.2	0.67	0.5	0.22
maximum B_T (T)	4.8	3.8	2.2	3.9	8.0
typical I_P (MA)	3–4	3–5	1–3	~ 1	0.6–1.2
H-mode central n (10^{20} m^{-3})	0.2–0.5	0.2–0.5	0.4–0.8	0.5–1.0	2–5
H-mode central T (keV)	10–20	10–20	5–10	2–3	2–5

Table 2.1: Typical parameters of tokamaks mentioned in this thesis

as I_P increases, s tends to decrease, causing the Sugihara scaling to manifest itself as $\Delta \propto \rho_{i,\mathrm{pol}}$.

2.3 Experimental results from other tokamaks

As discussed in Sec. 1.3, global confinement on tokamaks in general, and C-Mod in particular, is correlated strongly with edge conditions. Because confinement and edge conditions are tightly coupled, extrapolation of pedestal parameters to reactor-scale devices is of great interest to the community. The factors determining pedestal widths and heights in tokamaks are not yet well understood, despite experimental efforts on major experiments, including JT-60U [70], DIII-D [71], ASDEX Upgrade [72], JET [73], and C-Mod. The community's experimental work was reviewed in some detail in [52]. This section will highlight much of what was mentioned therein, and add mention of more recent results as well. Basic characteristics of machine operation are parametrized for each machine in Table 2.1. Diverted tokamaks with significant H-mode pedestal research programs are included in this table, and in the subsequent discussion.

2.3.1 JT-60U

The Japanese tokamak JT-60U has made substantial contributions to the advancement of H-mode confinement and pedestal studies. A thorough review of this work appears in [74]. Pedestal widths in these studies are not determined by fitting to the modifed tanh function of (2.1); rather, the pedestal width Δ is calculated as the radial distance between the top of the pedestal, given by the break in slope of the profile, and the LCFS. These derived Δ are found roughly proportional to what would have been determined from the tanh-fit. [75]

Temperature pedestal width

Evidence for a $\rho_{i,\mathrm{pol}}$ dependence on pedestal width emerged early in the operation of JT-60U, given the reported $1/B_p$ dependence of T_e width from Thomson scattering. [76] In ELM-free H-modes, systematic scaling studies were attempted with considerable variation in I_P and pedestal T_i, in order to examine the dependences on each variable. [77] T_i profiles from CXRS were examined and pedestal widths fitted in terms of independent variables: $\Delta_{T_i} \propto \epsilon^{0.56} T_i^{0.77} B_p^{-1.07}$ This relation compares well with the relation in (2.2) with its final term approximately unity. In fact, if the functional form of the ion-orbit-loss prediction is chosen, the JT-60U ELM-free data are well fit by the expression

$$\Delta_{T_i} = 3.3\sqrt{\epsilon}\rho_{i,\mathrm{pol}} \tag{2.10}$$

Variations in plasma elongation and triangularity did not change the results.

A similar form was found for the pedestal width in the Type I ELMy regime, [25] with T_i measurements from CXRS averaging over several ELM periods. Over the course of ELMy periods, the pedestals tend to grow in height and width on time scales of seconds, much longer than the energy confinement time ($\tau_e \approx 0.2$s). During profile evolution, the $\rho_{i,\mathrm{pol}}$ scaling remains, though the widths are 2–3 times larger than in ELM-free, and an additional dependence on safety factor is observed:

$$\Delta_{T_i} = 5\rho_{i,\mathrm{pol}} q_{95}^{-0.3} \tag{2.11}$$

Pressure gradient

By examining pedestal conditions at the onset of Type I ELMs, it was shown [78] that pressure gradients were consistent with the ELMs being triggered by high-n ballooning modes. Part of the evidence is that the calculated value of α_{MHD} is nearly constant at ELM onset. Thus, a critical pressure gradient can also be said to exist, potentially limiting the growth of the pedestal. Here the average magnitude of the pressure gradient is calculated according to $\nabla p = p_{\text{PED}}/\Delta$. The onset value of α_{MHD} was seen to increase with elongation for $\kappa > 1.5$ and to increase with triangularity for $\delta > 0.15$. Interestingly, in the long periods of ELMy discharge mentioned above, the derived pedestal ∇p rises, simultaneous with the Δ increase.

2.3.2 DIII-D

The first pedestal studies on DIII-D used CXRS measurements at the edge to evaluate E_r in the H-mode pedestal, where a significant shear was determined. [79] The width of the E_r well is similar in scale to $\rho_{i,\text{pol}}$ (≈ 1 cm), though exhaustive scans of current and field showed no width scaling with operational parameters. [80] Further advancement in scaling studies occurred with the addition of high resolution TS in the pedestal region, and the routine fitting of the modified tanh in (2.1) to the measured profiles. The high availability of T_e and n_e profiles led to scaling studies of the pedestal [81] and its relation to confinement, [10] based mostly on the behavior of the electron pedestals. The H-mode regime examined is almost universally Type I ELMy.

No clear correlation with machine operational parameters is observed in the values of $T_{e,\text{PED}}$ or $p_{e,\text{PED}}$, suggesting they depend exclusively on local parameters. The approach taken is to concentrate on the behavior of ∇p_e and Δ_{p_e}. Then the physics limiting the pedestal growth can be extrapolated by means of the assumption that $p_{e,\text{PED}} = \Delta_{p_e} |\nabla p_e|$.

Pressure gradient

As in JT-60U, the value of α_{MHD} appears to reach a saturated value at ELM onset, suggesting that the trigger for the ELM is tied to high-n ballooning modes. [10] However, the measured values of α_{MHD} significantly exceed the critical value for onset expected from theory. These modes, it has been shown, [82] can be stabilized by the bootstrap current induced by sufficiently large pressure gradient. Further work on the stability to coupled peeling-ballooning modes [83] suggested more elaborate physics are involved in the ELM cycle. The amount by which α_{MHD} exceeds the critical value increases in more strongly shaped (*i.e.*, more triangular or more square) plasmas. [84]

Electron pressure width

Scalings which seemed to fit experimental measurements of p_e pedestal width were found using an extensive database. [81] One such relationship was $\Delta_{p_e} \propto |\nabla n_e|^{-0.5}$, which seems to hold quite well when data are averaged over many ELM periods ($\tau_{\mathrm{ELM}} \approx$ 10–20 ms), but does not fit systematically within the period between ELM crashes, when the pedestal profiles evolve continuously. This scaling result resembles the prediction of the Hinton-Staebler formulation in Sec. 2.2.2, in which $\Delta \propto \sqrt{L_n}$.

A second, dimensionless, scaling was determined as $\Delta_{p_e}/R \propto (\rho_{i,\mathrm{pol}}/R)^{0.67}$, where the gyroradius is calculated in the pedestal assuming $T_i = T_e$. In contrast to the previous scaling, this relationship holds on the short time scales between ELMs but does not match trends on longer time scales. The form of this scaling can be compared to theories of ion orbit loss in Sec. 2.2.1, as well as to the empirical scaling found on JT-60U, from which an exponent of one would be expected. The exponent of approximately 2/3 more closely resembles the prediction of the MHD-motivated theory of Sec. 2.2.3

A correlation was found for the p_e width that reproduced Δ trends on both long and short time scales. Here the width increased with poloidal beta in the pedestal: $\Delta_{p_e}/R \propto \beta_{\mathrm{pol}}^{0.4}$. The proportionality of width with overall pressure is unsurprising, at least for time scales $\tau \gg \tau_{\mathrm{ELM}}$, if the pedestal is ∇p-limited. That the scaling is good

between ELMs perhaps suggests an additional role for pressure in determining the width.

In an attempt to connect the separate scaling results obtained on DIII-D and JT-60U, the temperature pedestal width data on JT-60U were adjusted numerically to match the expected values of Δ that would have been obtained by a completely tanh-fit data set. It was determined [75] that both the ELM-free JT-60U scaling, $\Delta \propto \epsilon^{0.5}\rho_{i,\mathrm{pol}}$, and the DIII-D inter-ELM scaling, $\Delta \propto R\beta_{p,\mathrm{PED}}^{0.4}$, fit the data from either machine reasonably well. A more sophisticated scaling was also developed that provided a somewhat better fit to the data using the dimensionless poloidal ion gyroradius $\rho_\star = \rho_{i,\mathrm{pol}}/a$ and dimensionless Greenwald density $n_{G\star} = n_e a^{1.75}/I_P$:

$$\Delta \propto a\rho_\star^{0.4} n_{G\star}^{0.3} \kappa^{-1.5} \tag{2.12}$$

Electron density width and gradient

Dedicated experiments [81] were performed on DIII-D to directly test the predictions of the Mahdavi theory discussed in Sec. 2.2.2. Given an unchanging poloidal distribution of neutral fueling, the distance between the pedestal top and the LCFS is expected to scale as $\Delta \propto 1/n_{e,\mathrm{PED}}$. The pedestal width $\Delta_{n_e} = 2d_{n_e}$ obtained from fitting (2.1) to the entire edge profile is generally different, but it scales in the same manner.

Ohmic, L-mode and H-mode discharges were obtained and subjected to either gas puffing or cryopumping in order to raise or lower the density. Over a significant range of pedestal density, H-mode data were averaged over a number of ELM periods. A decrease in Δ_{n_e} was observed with increasing $n_{e,\mathrm{PED}}$, as shown in Fig. 2-2. The model was successfully fitted to the measurements using reasonable assumptions for D_C, D_S, T_i and E. For lower density plasmas, including most ohmic and L-mode discharges, the model was only successful when the assumption of $T_n \approx T_{i,\mathrm{LCFS}}$ was relaxed, and the incoming neutrals were assumed to have a Frank-Condon dissociation energy of about 3 eV. The same data were shown to follow a $|\nabla n_e|_{\max} \propto n_{e,\mathrm{PED}}^2$ dependence, as predicted from theory.

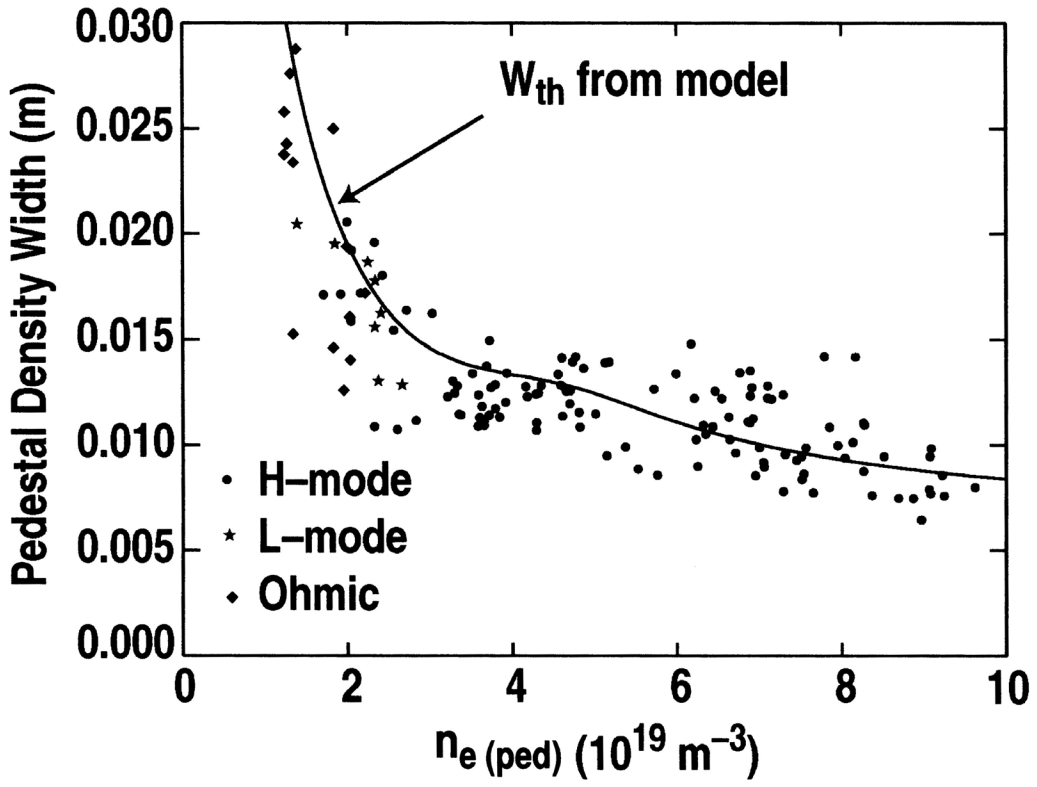

Figure 2-2: Density pedestal width falls with increasing $n_{e,\mathrm{PED}}$ in DIII-D discharges. The fitting curve is derived using the neutral penetration model outlined in the text. (From [85])

L- and H-mode plasmas obtained with similar values of $n_{e,\mathrm{PED}}$ were seen to have similar values of Δ_{n_e}, a finding that is consistent with density pedestal width depending on neutral penetration and not on plasma physics in the transport barrier. The higher transport in L-mode, it was claimed, was reflected in a smaller profile gradient and higher $n_{e,\mathrm{LCFS}}$.

The T_e pedestal width tracks similarly to that of n_e, but experimental statistics show that the ratio $\Delta_{T_e}/\Delta_{n_e}$ can be significantly larger than 1 as the temperature pedestal extends farther into the core plasma than does the density pedestal. [85] Because $\Delta_{T_e} \gtrsim \Delta_{n_e}$, it was suggested that the actual transport barrier is wider than the density pedestal as determined by neutral penetration. Modeling indicates that if this were indeed the case, the qualitative trends of the Mahdavi model would be reproduced, in accord with experiment.

Experiments intended to evaluate the impact of neutral fueling on the density pedestal were also attempted on C-Mod. Significant differences in behavior were noted, and will be discussed further in Sec. 6.3.

2.3.3 JET

Initial pedestal characterization on JET focused on ELM-free discharges. [86], and combined measurements from several diagnostics. The break-in-slope of the ECE profile was used to determine $T_{e,\mathrm{PED}}$ and Δ_{T_e}. A Li beam and a reciprocating probe were employed to determine the n_e profiles. Ion temperature and density were measured with CXRS. A Δ_{T_e} of 3–4 cm was observed, and exhibited no clear dependence on either I_P or $T_{e,\mathrm{PED}}$. The ELM-free T_i width was of similar scale, but did scale linearly with $T_{e,\mathrm{PED}}$, displaying a roughly constant gradient. No scaling with I_P was observed in the T_i width. In a typical ELM-free discharge, $\Delta_{n_e} \approx \frac{1}{2}\Delta_{T_e}$. Type I ELM formation was observed when the inferred p_e gradient grew to half the expected critical gradient, assuming ideal MHD ballooning.

Because there was insufficient spatial resolution to resolve the pedestal region, in subsequent research, Δ_{p_e} was inferred by measuring $p_{e,\mathrm{PED}}$ and assuming the limit on pressure gradient in the Type I ELMy regime was due to ideal ballooning. [27][87] Pressure pedestal width did vary, and was consistent with a $\rho_{i,\mathrm{POL}}$ scaling using the gyroradius of the thermal ions in the pedestal. [88][89] The pedestal pressure rose with increasing triangularity while at fixed I_P, a result attributed to the increasing edge shear S at stronger shaping, which gives a larger limiting gradient. Combining the results of scans of plasma current, input power, density and shape led to the semi-empirical scaling for the maximum pressure pedestal

$$p_{\mathrm{PED,max}} \propto I_P^2 S^2 \rho_{i,\mathrm{pol}} \propto I_P S^2 \sqrt{m_i T_{\mathrm{PED}}} \tag{2.13}$$

2.3.4 ASDEX Upgrade

Edge profiles on ASDEX upgrade are diagnosed using a variety of instruments, [90] including Thomson scattering for T_e and n_e, a Li beam diagnostic and a far infrared laser interferometer to cross-check the density, and electron cyclotron emission to cross-check T_e. CXRS and low energy neutral particle analysis are available to diagnose T_i, albeit with low spatial resolution. The tanh-fit of (2.1) is used to characterize measured pedestals.

H-modes on ASDEX Upgrade typically exhibit ELMs of type I, II or III, depending on plasma geometry and edge conditions. [90] The prevalent regimes in single null geometry are type I and III, with the former occurring at the highest values of edge pressure gradient, and the latter occurring over a wide range of $|\nabla_{p_e}|$, but only below a threshold $T_{e,\mathrm{PED}}$ of 300–350 eV. [9] Highly transient ELM-free H-modes are observed at high edge temperature and low edge density. When double null geometry is approached, type II ELMs are observed.

Scaling studies were performed using type I ELMing discharges at various values of plasma triangularity. At low to medium values of triangularity ($\delta \lesssim 0.4$), $\Delta_{p_e} \approx \Delta_{T_e} \approx 2$ cm, with somewhat wider density pedestals. There was no evidence at these δ of a systematic trend in pedestal widths with $\rho_{i,\mathrm{pol}}$, [91] in contrast to the results on JT-60U, DIII-D and JET. However, for higher triangularity, such a trend was observed, indicating perhaps the ion-loss mechanism of 2.2.1 is at work, but depends on the shaping of the plasma. [90] The pressure gradient in these ELMy discharges was roughly consistent with a ballooning-limited pedestal, with an approximate empirical scaling $|\nabla p_e| \propto I_P^2$. Invariance of the pedestal width results in a similar scaling for $p_{e,\mathrm{PED}}$. By varying shape, it was further found that α_{MHD} could be increased a factor of 2–3 by increasing lower triangularity from 0.25 to 0.4. [91]

Much work has been done on ASDEX Upgrade relating the edge transport barrier to overall core confinement. It was found that, due to self-similarity of core profiles, plasma stored energy is approximately proportional to the pressure pedestal in the case of a pedestal limited by type I ELMs. [9] (A much broader selection of discharges

showed a $|\nabla p_e| \propto W^2$ dependence. [8]) The relation is independent of plasma shaping.

2.3.5 Summary of tokamaks

Reviewing the published results on pedestal structure and scalings reveals a considerable variation among the tokamaks of the world, illustrating that the physics determining the transport barrier is not understood. No single theoretical model can universally explain the experimental observations among the various machines. Sometimes, as in the case of changing triangularity on ASDEX Upgrade, operation in different regimes can produce results either consistent or inconsistent with a given model. The richness of variation in results and interpretation makes extrapolation to a next-step device a challenge.

Attempts have been made to test pedestal data from multiple machines against theoretical predictions. Onjun [92] examined numerous data points from the International Pedestal Database, [93] combining Type I ELMy discharges from JT-60U, ASDEX Upgrade, JET and DIII-D. He compared experimental $T_{\rm PED}$ with predictions from theoretical models, evaluated using the conditions present in each discharge. Each model had a distinct prediction for Δ_p and it was assumed that ballooning stability limits determine the pressure gradient. This formulation, along with experimental values of $n_{\rm PED}$, determine $T_{\rm PED}$. Chief among findings was that most models predicted the observed pedestals to about the same accuracy, with root mean squared errors between about 30 and 40%. No model stood out as being in exceptional agreement with experiment.

Table 2.2 gives a concise list of some of the more important findings from the above machines. In particular, the scalings (or lack of scaling, in some cases) give a starting point for comparison experiments on Alcator C-Mod.

2.4 Prior results on Alcator C-Mod

At the inception of this thesis project, a picture of the C-Mod ETB pedestal was slowly emerging. Since, on other tokamaks, Δ/a tends to be a few percent, it might

Tokamak	Regime	Empirical Pedestal scalings
JT-60U	ELM-free	$\Delta_{T_i} \propto \sqrt{\epsilon}\rho_{i,\mathrm{pol}}$
	Type I ELMy	$\Delta_{T_i} \propto \rho_{i,\mathrm{pol}} q_{95}^{-0.3}$
		$\alpha_{\mathrm{ELM}} = \text{const. at fixed shape}$ $\alpha_{\mathrm{ELM}} \uparrow \text{ as } \delta,\ \kappa \uparrow$
DIII-D	Type I ELMy	$\Delta_{p_e} \propto \lvert\nabla n_e\rvert^{-0.5}\ (\text{for } \tau \gg \tau_{\mathrm{ELM}})$ $\Delta_{n_e} \propto 1/n_{e,\mathrm{PED}}\ (\text{for } \tau \gg \tau_{\mathrm{ELM}})$ $\Delta_{p_e}/R \propto (\rho_{i,\mathrm{pol}}/R)^{0.67}\ (\text{for } \tau \lesssim \tau_{\mathrm{ELM}})$ $\Delta_{p_e}/R \propto \beta_{\mathrm{pol}}^{0.4}$
		$\nabla n_e \propto n_{e,\mathrm{PED}}^2\ (\text{for } \tau \gg \tau_{\mathrm{ELM}})$ $\alpha_{\mathrm{ELM}} = \text{const. at fixed shape}$ $\alpha_{\mathrm{ELM}} \uparrow \text{ as } \delta,\ \kappa \uparrow$
JET	ELM-free	$\Delta_{T_e} \approx \text{constant}$ $\Delta_{T_i} \propto T_{i,\mathrm{PED}}$ $\Delta_{n_e} < \Delta_{T_e}$
	Type I ELMy	$\Delta_{p_e} \propto \rho_{i,\mathrm{PED}}$
		$p_{e,\mathrm{PED}} \propto I_P^2 \rho_{i,\mathrm{pol}}$ $p_{e,\mathrm{PED}} \uparrow \text{ as } \delta \uparrow$
ASDEX Upgrade	Type I ELMy	$\Delta_{p_e} \propto \rho_{i,\mathrm{pol}}$ for large δ *only*
		$\lvert\nabla p_e\rvert, p_{e,\mathrm{PED}} \propto I_P^2$ $\alpha_{\mathrm{ELM}} \uparrow \text{ as } \delta \uparrow$ $W \propto \lvert\nabla p_e\rvert$

Table 2.2: Summary of H-mode pedestal behavior on major tokamaks in given regimes of operation. Empirical reults for both pedestal widths and gradients are given.

be expected that the ETB region on C-Mod would be less than a centimeter in radial extent. Indeed, the H-mode pedestals on C-Mod appeared to have gradient scale lengths of this order or smaller, and proved a challenge to diagnose from the beginning.

The core Thomson scattering (CTS) diagnostic on C-Mod [30] was capable of measuring T_e and n_e near the edge, but only with 1–2 cm radial resolution. Data from CTS could roughly estimate $T_{e,\mathrm{PED}}$ and $n_{e,\mathrm{PED}}$, but give no information on pedestal structure. ECE scans of the H-mode temperature profile using B_T sweeps placed an upper bound of 8 mm on Δ_{T_e}, with measurements limited by the spatial resolution of the GPC. [94] Reflectometer profiles of edge n_e demonstrated that the density pedestal width was no larger than about 1 cm. [95].

Narrow pedestals were suggested by higher resolution diagnostics. Probe plunges into H-mode near the LCFS showed n_e and T_e gradient scale lengths of millimeters. [94] [96] New measurements became available in the form of soft X-ray arrays [97] and the visible continuum array. [31] Pedestal widths in the range of 2–6 mm were soon routinely observed from both diagnostics.

What was missing from this diagnostic set was a complete, well-resolved measurement of plasma temperature and density from just inside the ETB and into the SOL region. The edge Thomson scattering system was installed in 1999 to remedy this deficiency. The details of this diagnostic and a description of its results are given in the following chapter.

Chapter 3

Edge Thomson Scattering on C-Mod

Thomson scattering (TS) of laser light from plasma electrons [34, Ch.7][98] has become a common diagnostic in modern fusion experiments, [30] [99] [100] [101] [102] [103] [104] [105] [106] [107] [108] [109] as documented in an interesting review by DeSilva. [110] The spectral shape and intensity of the scattered light unambiguously conveys the temperature and the density of the electrons in the plasma during a laser pulse of several nanoseconds, producing an effective "snapshot" of these quantities at a number of spatial locations. Thomson scattering produces no significant perturbation to the plasma system, thus making these measurements highly desirable, even in the face of difficult technical challenges.

When this thesis research began, an edge Thomson scattering (ETS) system was highly desirable for use on Alcator C-Mod, due to intense interest in the character of plasma profiles in the ETB during H-mode. Questions surrounding plasma transport and MHD stability could not be satisfactorily answered without accurate measurement of plasma density and temperature in this region. As mentioned in Sec. 2.4, the sub-centimeter gradient scale lengths existing in the ETB region necessitated an instrument with resolution on the order of millimeters. It was thought that ETS could fill these needs, and that a successful diagnostic could be built for relatively little expense using existing components from a prior project. [111]

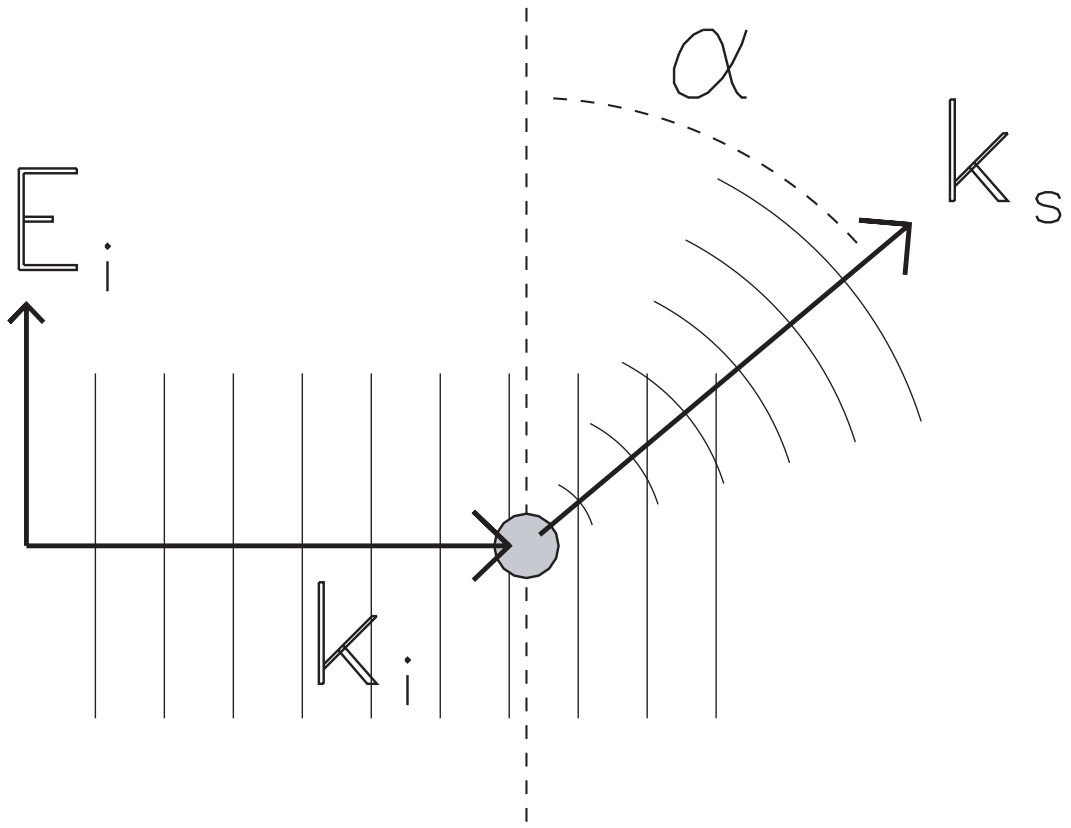

Figure 3-1: Photon scattering from a single charged particle

The ETS diagnostic was deployed beginning in the 1999 experimental campaign on C-Mod. [29] It succeeded almost immediately in measuring edge n_e and T_e profiles, and has routinely supplied the C-Mod group with data to the present day. The following sections will describe the standard theory behind the diagnostic, the hardware used to take the data and the method of data analysis and calibration.

3.1 Incoherent Thomson scattering

In plasma experiments, Thomson scattering from an ensemble of free electrons is measured from a given scattering volume. To calculate the form of the scattered radiation, one must start with scattering of an electromagnetic (EM) wave from a single charged particle. This can be thought of as a two-step process, sketched in Fig. 3-1. First, the particle is accelerated by the electric field $\mathbf{E}_i$ of the incoming wave

with wavevector $\mathbf{k}_i$. Second, the accelerating particle emits radiation in the form of a scattered wave, having a scattering wavevector $\mathbf{k}_s$. We consider only radiation with energy much less than the rest mass of the particle, so that negligible momentum is imparted to the particle. (This distinguishes Thomson scattering from Compton scattering, in which a sufficiently energetic photon imparts significant momentum to the particle.) This condition, $h\nu \ll m_e c^2$, is well satisfied by soft X-rays and longer wavelength radiation.

In the nonrelativistic limit [112, §14.2], the radiated power per solid angle from a particle of charge q with acceleration $\dot{\mathbf{v}}$ is given by the "dipole approximation":

$$\frac{dP}{d\Omega} = \frac{q^2}{16\pi^2\epsilon_0 c^3}|\dot{\mathbf{v}}|^2 \sin^2\alpha \tag{3.1}$$

where α is the angle between the acceleration vector and the scattering vector (note Fig. 3-1). If the particle has mass m and is accelerated solely by the electric field of an incoming wave $\mathbf{E}_i$, then we can substitute

$$\dot{\mathbf{v}} = \frac{q}{m}\mathbf{E}_i \tag{3.2}$$

into (3.1) to obtain an expression for the radiated power proportional to m^{-2}. Due to this strong inverse mass dependence, power scattered from plasma ions is insignificant, and we need only consider scattering from electrons. Inserting the electron mass m_e and charge e into the above equations, and recalling the classical electron radius:

$$r_e \equiv \frac{e^2}{4\pi\epsilon_0 m_e c^2} \tag{3.3}$$

we have

$$\frac{dP}{d\Omega} = r_e^2 c\epsilon_0 E_i^2 \sin^2\alpha \tag{3.4}$$

Since we assumed acceleration by an EM wave, (3.4) is further simplified by writing the incident power density of the wave according to the magnitude of the Poynting

flux:

$$s_i = \left| \frac{\mathbf{E}_i \times \mathbf{B}_i}{\mu_0} \right| = \frac{1}{c\mu_0} E_i^2 = c\epsilon_0 E_i^2 \tag{3.5}$$

Now the scattered power per solid angle is related to incident power density as

$$\frac{dP}{d\Omega} = s_i r_e^2 \sin^2 \alpha \tag{3.6}$$

implying a differential Thomson scattering cross-section of

$$\left(\frac{d\sigma}{d\Omega} \right)^T = r_e^2 \sin^2 \alpha \tag{3.7}$$

Integrating over all α yields the total Thomson cross-section:

$$\sigma^T = \frac{8\pi}{3} r_e^2 \tag{3.8}$$

The smallness of σ^T (6.65×10^{-29} m^2 or about $\frac{2}{3}$ barn) indicates that a large source of photons is necessary in order to obtain a significant amount of scattered light. The fraction of photons scattered from a beam traversing a length of plasma $L = 3$ mm with density $n = 5 \times 10^{19}$ m^{-3} would be given by

$$Ln\sigma^T = (3 \times 10^{-3} \text{ m})(5 \times 10^{19} \text{ m}^{-3})(6.65 \times 10^{-29} \text{ m}^2) \approx 10^{-11} \tag{3.9}$$

The optics of a TS system can of course only collect a limited amount of the scattered light, and therefore must be arranged for optimal collection. For example, an α of 90° is usually chosen to maximize (3.7), thus giving the special geometry sketched in Fig. 3-2. This is essentially the geometry of the C-Mod TS diagnostic, the details of which are presented in Sec. 3.2

In fact, the calculation in (3.9) is only strictly valid if the scattering powers from each electron can be summed to give the power scattered in the far field. This is the case if the phases of all scattering components are uncorrelated. It can be shown [34, §7.2] [98, Chs.6–7] that this condition is satisfied when $k\lambda_D \gg 1$, where $k = |\mathbf{k}_s - \mathbf{k}_i|$. If this condition is not satisfied, then the observed radiation scattered from an electron

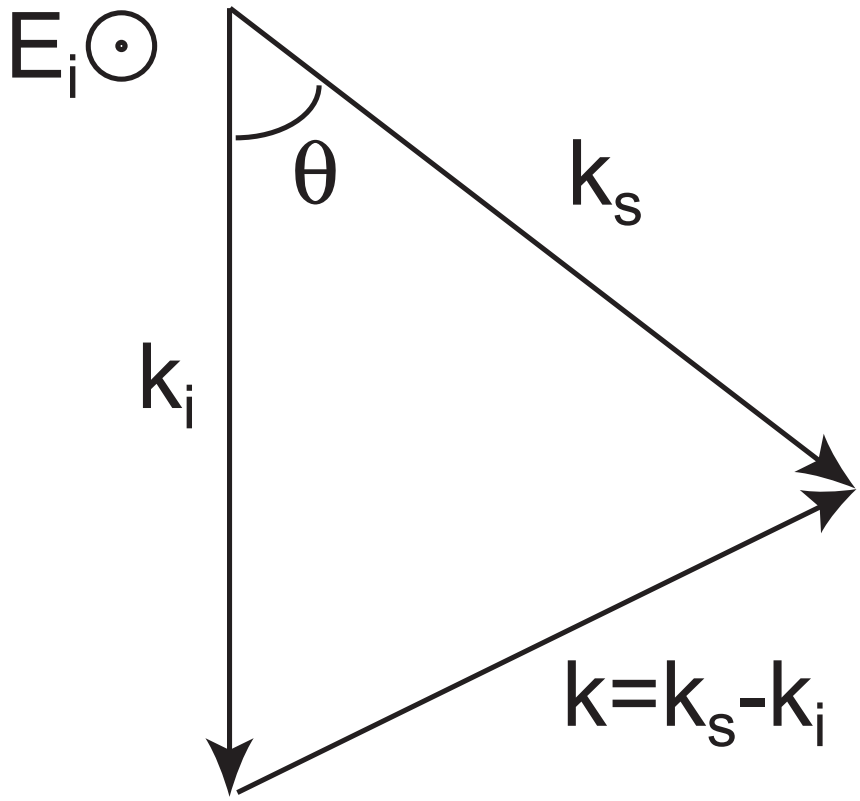

Figure 3-2: Incident and scattering wavevectors, with $\mathbf{k}_s \perp \mathbf{E}_i$ ($\alpha = \pi/2$)

and its Debye shielding cloud will have negligible phase difference, and they will add coherently. Put another way, the scattering from a sample electron will be nearly balanced by the absence of electron scattering within its shielding cloud, and reduced radiation will be measured from the shielded electron. On the other hand, scattering from electrons in an ion shielding cloud will not be balanced by ion scattering, since the heavier ion scatters less power. Thus, measured coherent TS is predominately from the ion shielding clouds and gives information about ion velocity distributions. [34, §7.3]

Satisfying the above incoherence condition ensures a large phase difference between scattering from electrons and their shielding clouds. Then the randomness of the electron distribution will allow the scattering radiation to add incoherently. Since $k_s \approx k_i$, one can write $k \approx 2k_i \sin(\theta/2)$, where θ is the angle between the incident and

scattering vectors. Then the condition for inchorent scattering simplifies to

$$\frac{\lambda_i}{\lambda_D} \ll 4\pi \sin\frac{\theta}{2} \tag{3.10}$$

leading one to choose incident wavelength λ_i and scattering angle θ accordingly. This generally means using a sufficiently large angle and picking $\lambda_i < \lambda_D$. Restricting the incident wavelength in this way generally ensures that it will be smaller than all relevant plasma length scales.

As noted above, the spectrum of incoherent Thomson scattering conveys information about the electron distribution function. Light scattered from a still electron has a frequency identical to the incident frequency: $\omega_s = \omega_i$. However an electron of finite velocity $\mathbf{v}$ will see a Doppler-shifted incident wave, and likewise radiate a Doppler-shifted scattered wave, such that we may write generally

$$\omega_s = \omega_i + \mathbf{k}\cdot\mathbf{v} = \omega_i + (\mathbf{k}_s - \mathbf{k}_i)\cdot\mathbf{v} = \omega_i \left(\frac{1 - \hat{\mathbf{k}}_i\cdot\mathbf{v}/c}{1 - \hat{\mathbf{k}}_s\cdot\mathbf{v}/c}\right) \tag{3.11}$$

Assuming a Maxwellian velocity distribution for the electrons, a full expression for the ratio of scattered power to incident power P_s/P_i is obtained [98, Ch.3]:

$$\frac{P_s}{P_i} = r_e^2 n_e L |\hat{\mathbf{k}}_s \times (\hat{\mathbf{k}}_s \times \hat{\mathbf{E}}_i)|^2 S(T_e, \theta, \lambda) \tag{3.12}$$

where L is the length of the scattering volume and S is a form factor determining the shape of the spectral distribution in terms of electron temperature T_e, scattering angle θ and scattered wavelength λ. The double cross-product is exactly one for the $\alpha = \pi/2$ geometry, and the non-relativistic calculation gives a form factor of

$$S_{\text{non-rel}}(T_e, \theta, \lambda) = \frac{1}{\lambda_0}\frac{1}{2\pi^{\frac{1}{2}}\sin(\theta/2)}\frac{c}{v_t}\exp\left[\frac{-c^2(\lambda-\lambda_0)^2}{4v_t^2\lambda_0^2\sin^2(\theta/2)}\right] \tag{3.13}$$

where $v_t = (2T_e/m_e)^{\frac{1}{2}}$ is the thermal speed of electrons and λ_0 is the incident wavelength of the TS source. This expression is a Maxwellian centered at $\lambda = \lambda_0$ and with a width determined by both T_e and θ.

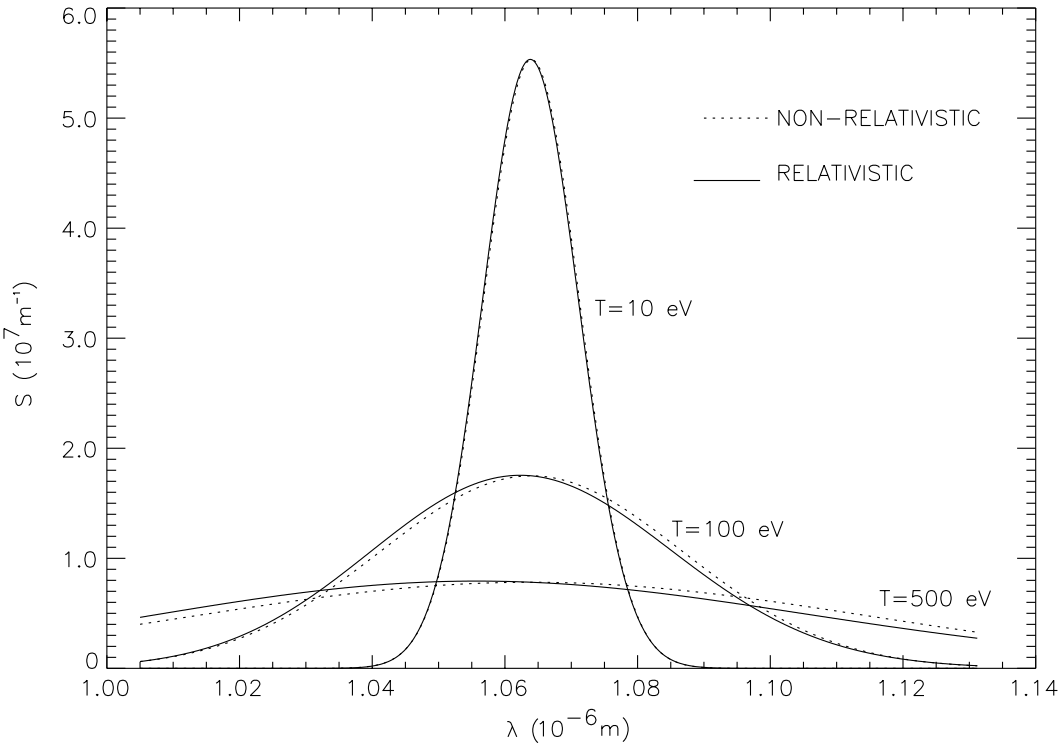

Figure 3-3: Relativistic blue shift in $S(T_e, \theta, \lambda)$

Sheffield's fully relativistic analysis [98, Ch. 9] develops a correction to (3.13):

$$S_{\text{rel}}(T_e, \theta, \lambda) = S_{\text{non-rel}}(T_e, \theta, \lambda) \left[1 - \frac{3.5(\lambda - \lambda_0)}{\lambda_0} + \frac{c^2(\lambda - \lambda_0)^3}{4 v_t^2 \lambda_0^3 \sin^2(\theta/2)} \right] \tag{3.14}$$

This corrected form is shown, plotted along with the uncorrected form, in Fig. 3-3. The relativistic form is blue-shifted by an amount that is roughly linear with T_e, as illustrated in Fig. 3-4. The shift was calculated at various temperatures by finding the difference in position of the maxima of (3.13) and (3.14). The analytic expression is taken from Sheffield:

$$\Delta\lambda_m = -\frac{7\lambda_0 v_t^2 \sin^2(\theta/2)}{c^2} \tag{3.15}$$

As Fig. 3-4 shows, at T_e of 200 eV, the spectral shift is already -30 Å. As will be seen below, the narrowest spectral band used by the ETS diagnostic has a width comparable to this shift, and so the relativistic effect on the Thomson spectrum should be included.

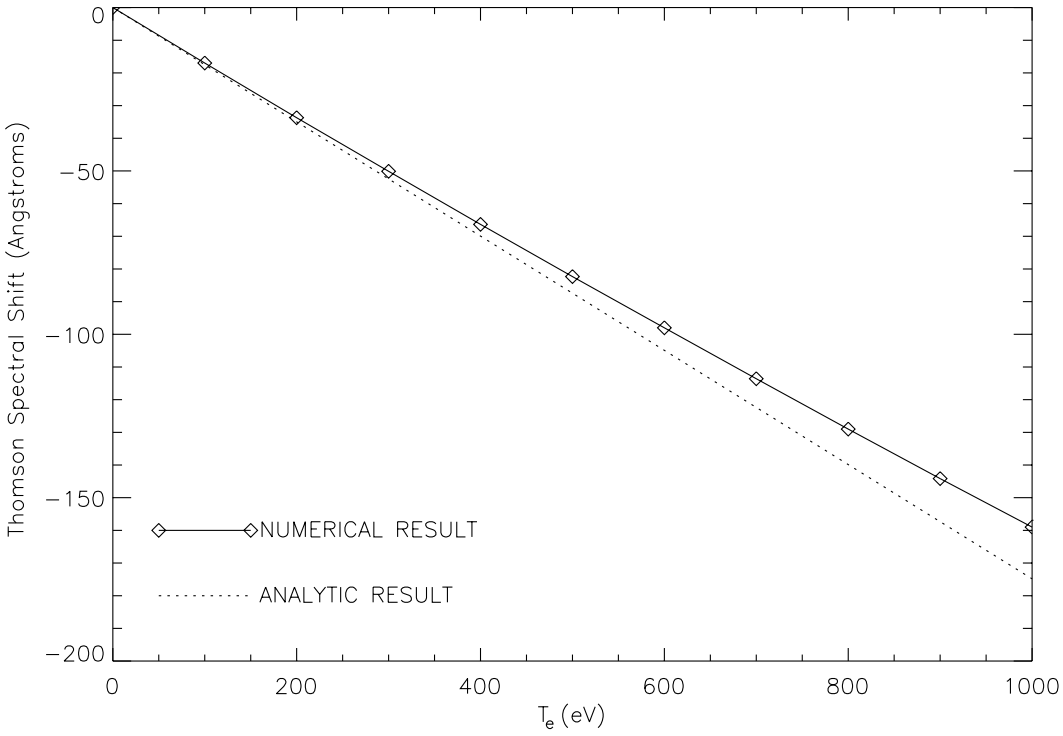

Figure 3-4: Relativistic spectral shift of $S(T_e, \theta, \lambda)$ as a function of T_e

3.2 Diagnostic setup and principles of operation

Because the TS spectrum is well characterized as a function of T_e and n_e, sampling this spectrum from several scattering volumes around the plasma edge is an excellent method of obtaining profiles of these quantities. An ideal measurement would yield the complete spectrum of scattered power, given by (3.12) and (3.14), at a number of spatial locations, minimizing the scattering volume length L for the highest possible spatial resolution, and maximizing the incident power P_i in order to boost measured signal. The width of the TS spectrum would give the local T_e, and the area under the curve would provide n_e. Complete spectral measurements are not practical to implement; however, because the spectral shape of TS is well known, it is possible to reconstruct the width and amplitude of the wavelength distribution using only a few bandpasses, each taking an integral measurement over a distinct range of wavelength space. As will be shown below, the ETS diagnostic on C-Mod accomplishes this using four spectral bandpasses at a number of spatial locations. The ETS system is built

to satisfy all the necessary conditions for incoherent scattering, and is configured to accurately diagnose the TS spectrum across the range of typical plasma edge paramters. The relevant hardware is described below.

3.2.1 Beam and collection optics

The ETS diagnostic measures light scattered from an incident neodymium-doped yttrium aluminum garnet (Nd:YAG) laser at a wavelength $\lambda = 1064$ nm. Two Continuum PowerLight 9030 Nd:YAG lasers [113] with 1.5 J pulse energy, 10 ns pulse duration and 30 Hz repetition rate are available, and can be operated simultaneously, their beam paths steered nearly collinear through the tokamak. Coaligned with the Nd:YAG beams are separate He-Ne lasers, operating CW and serving as "tracers" for the pulsed beams. The beams are steered through a vertical port and maintained at a major radius of 0.69 m. Figure 3-5 lays out a cross-sectional view of the C-Mod ETS system. The angle of scattering θ is about 80°, and $\lambda_i/\lambda_D \lesssim 0.1$ meaning that (3.10) is well-satisfied.

A 3 m focal length doublet atop the tokamak focuses the beam such that its width is less than 2 mm over the beam path through the plasma. Scattered Nd:YAG light is focused onto collection fiber optics by a Cooke triplet, which is a configuration for optical imaging that consists of a negative lens between two positive lenses and is designed to eliminate astigmatism and minimize chromatic aberration. [114, §10.5] The triplet, as designed for C-Mod, collects light at $f/7$ and provides a demagnification of 1:2 [115]. The most tightly focused portion of the beam is imaged onto collection fibers of 1 mm active diameter, which are positioned so that they image scattering volumes at the upper edge of the plasma, as detailed in Fig. 3-5. Ray tracing calculations indicate an imaged spot size of 1 mm for scattering locations 30 cm above the optical axis, determining an absolute limit on spatial resolution, which in turn suggests a minimum useful dimension for the collection fibers. Each fiber consists of a 1000 μm diameter silica core and plastic clad and jacketing layers, which yield an outer diameter of 1200 μm. The fibers have a total acceptance angle of approximately 13° and transmit collected light to an imaging filter polychromator, to be described

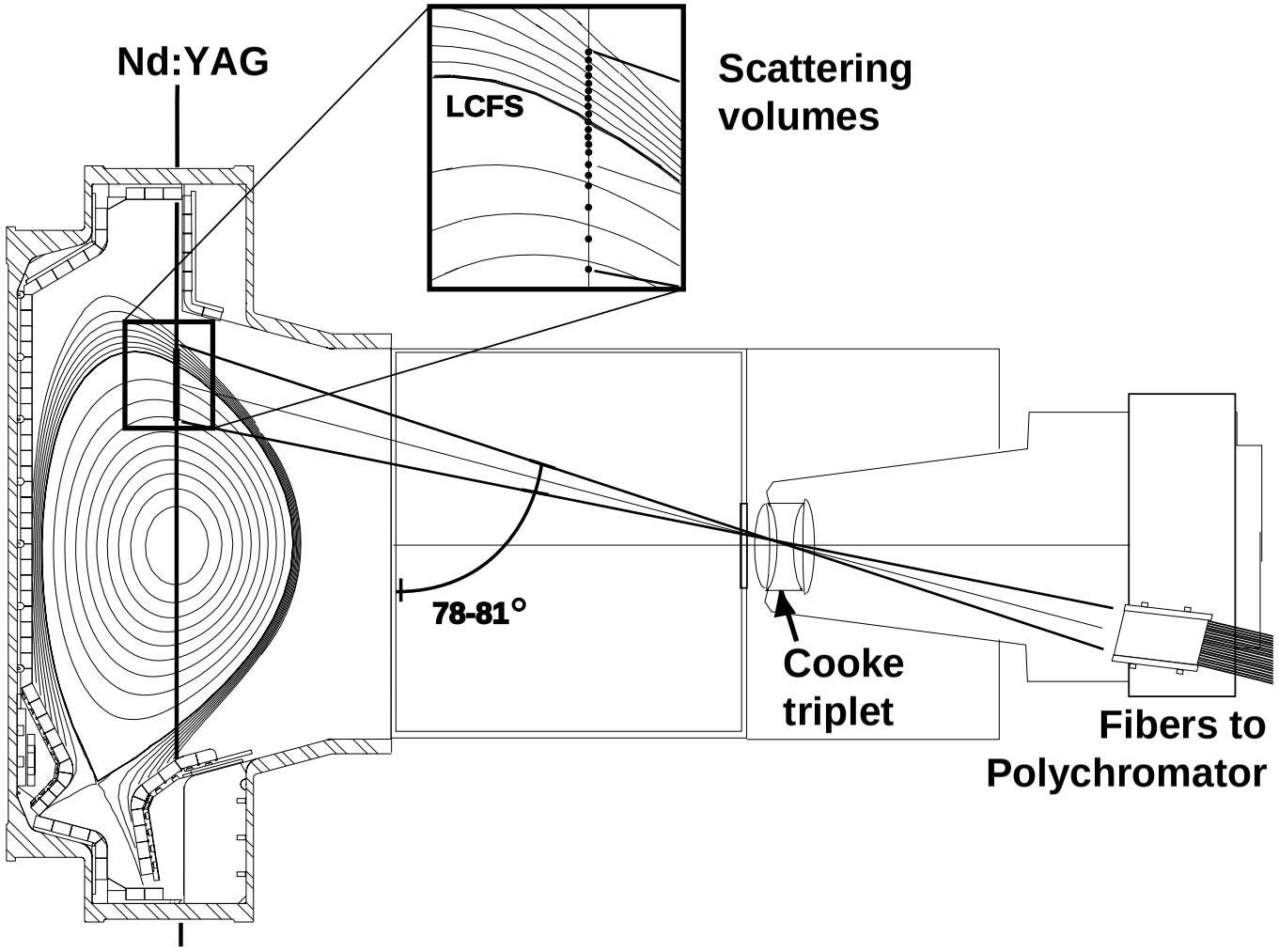

Figure 3-5: Alcator C-Mod cross-section and layout of TS collection optics.

in Sec. 3.2.2.

Proper alignment of the beams with respect to the TS collection fibers is critical to the operation of the diagnostic, and an operator must be able to make corrections for drifts in the optical alignment that might occur throughout a C-Mod run day. Remote beam steering is enabled by programmable logic controller (PLC) modules, which deliver analog voltages to various actuating devices. Two adjustable mirror stages roughly 15 m up the beam path from the tokamak are used to control the radial and toroidal position of the beams. So that remote beam steering is possible, the stage axes are equipped with actuators driven either by DC motors or by piezoelectric devices. Another piezoelectric actuator may also be used remotely to adjust the tilt of the mirror directly above the vertical port and, subsequently, the angle of the beam in a vertical plane tangent to the magnetic axis of the tokamak. An upgrade of the TS diagnostic performed in 2002 [116] introduced a pair of stepper motors and a tilt plate to the collection fiber assembly, shown in Fig. 3-6, allowing the TS operator the freedom to align the fibers to the beam image.

The active edge TS fibers are arranged in a linear array and mounted to the lowermost portion of the fiber mount plate. Shown in Fig. 3-7 is a diagram of the fiber holder forward face, as it was assembled in June 2002. The width of the imaged beam is comparable to the diameter of the fibers, and with optimal alignment, most of the observed signal falls in the central channel. However, even slight deviations from optimal alignment result in lost photons and underestimated densities. Two alignment fibers are arranged on either side of the fiber with the innermost plasma view, and the signals from these three fibers are used to evaluate the degree of misalignment. Corrections to the density derived from the active channels are obtained based on the degree and direction of misalignment found in the alignment fiber trio, according to a method to be discussed in Sec. 3.4.2. In the course of an experimental run day, the TS operator monitors the signals in the three alignment channels, and finely tunes the alignment of the beam between plasma discharges using the remote controls described above. Gross beam misalignment, which requires much coarser beam steering, is often diagnosed by mere visual inspection. Charge-coupled device (CCD) televi-

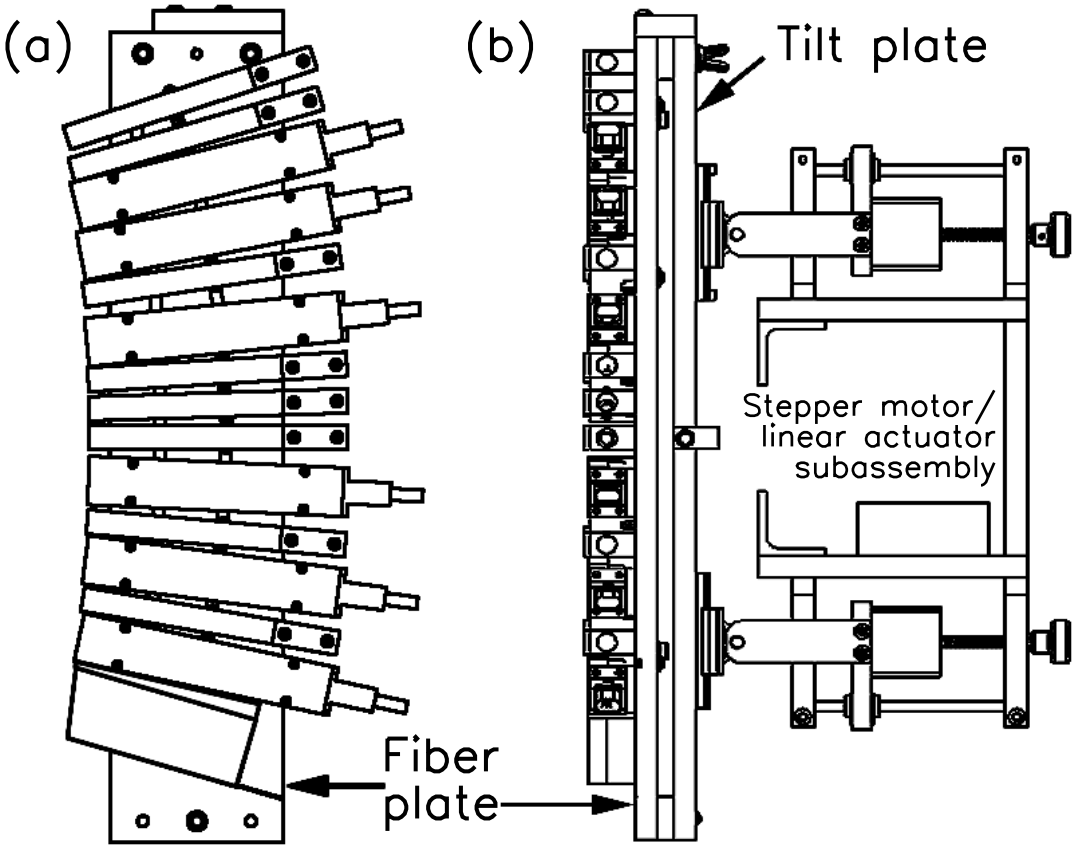

Figure 3-6: TS fiber mount subassembly from a.) side and b.) rear, showing linear actuators for horizontal position and tilt adjustment.

sion cameras view both beam leakage through a mirror atop the tokamak vertical port and beam reflection from the beam dump beneath the port. Targets at both of these locations allow frequent monitoring of the gross beam alignment quality. The pulsed Nd:YAG beams appear on camera as they fire, and when they are dormant, the He-Ne lasers act as guides to alignment.

3.2.2 Multi-channel polychromator

The collection fibers deliver TS photons to a filter polychromator [111] with 25 spatial channels in four spectral bands. The purpose of the polychromator is to separate the incoming TS spectrum into distinct spectral bands and measure the intensity in each band. The spectral bands have widths ranging from approximately 5 to 50 nm, and

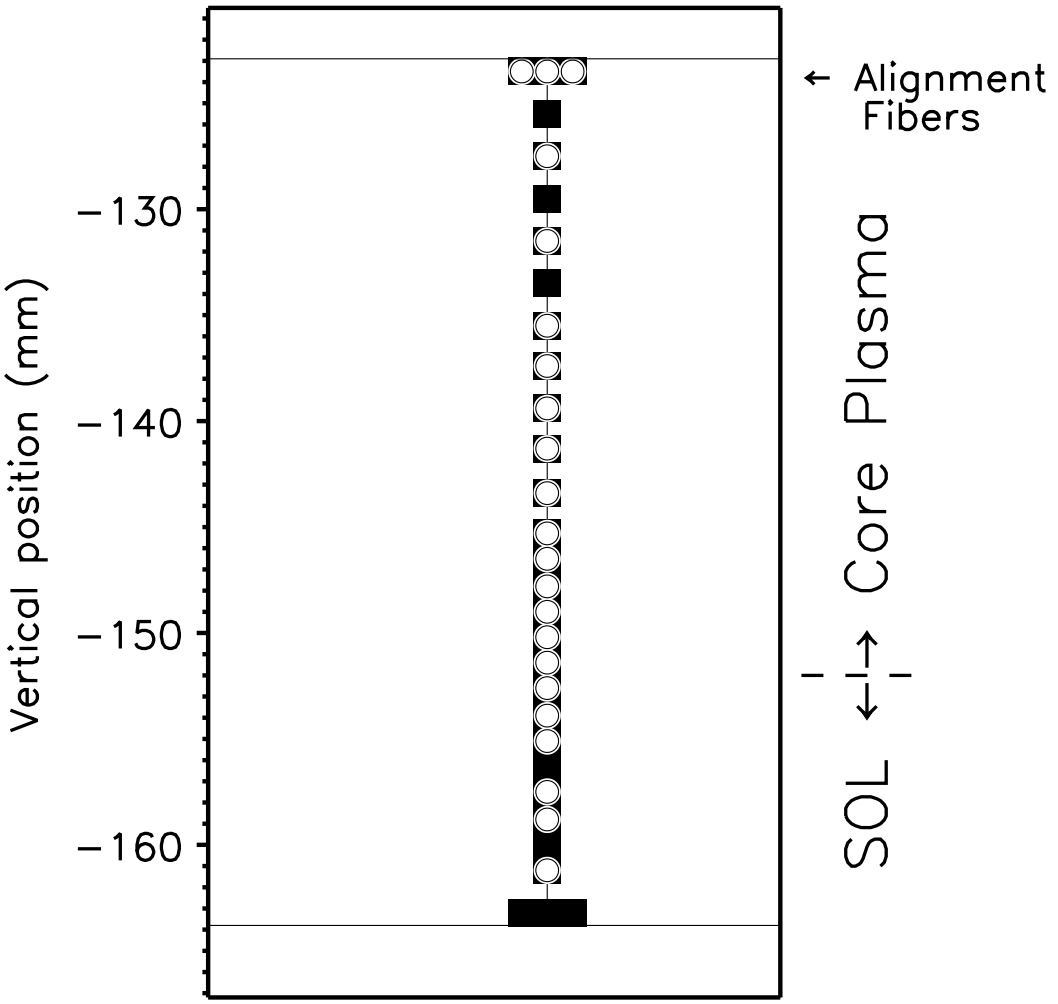

Figure 3-7: Face of edge TS fiber holder. Empty black areas represent spaces currently unfilled by active fibers.

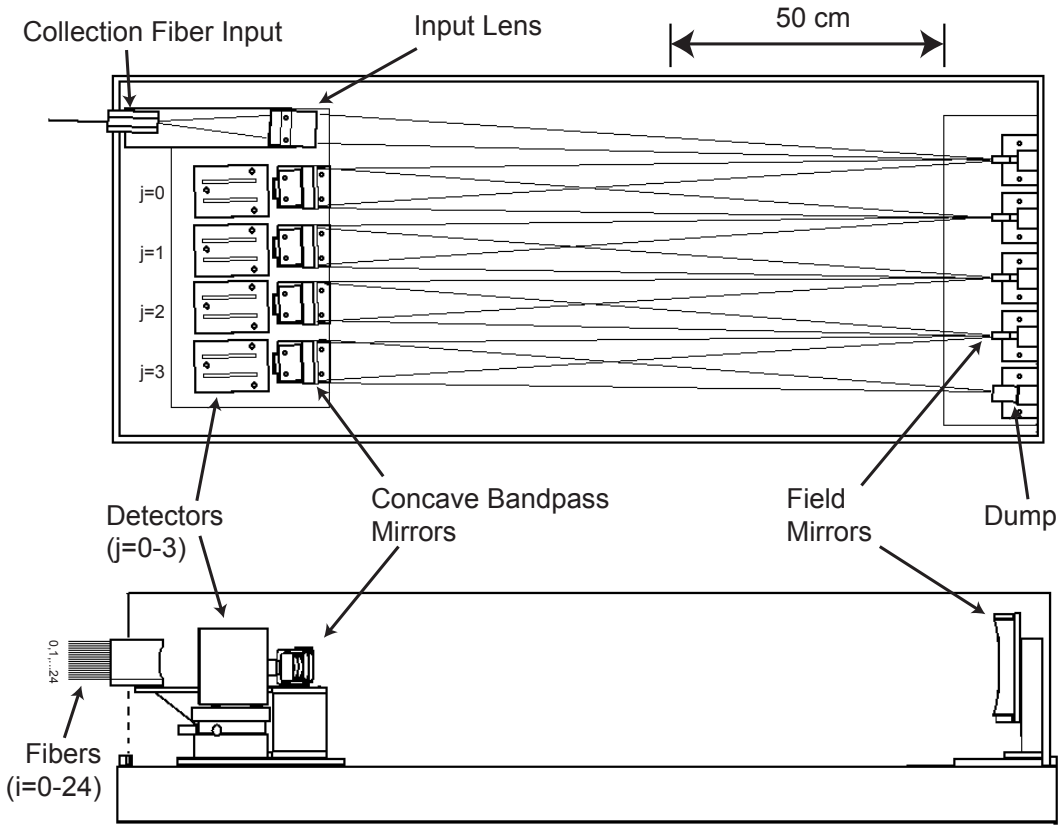

Figure 3-8: Layout of 4×25-channel polychromator; plan and side views. (Adapted from [111].)

effectively integrate over the distribution of TS light to produce four signals at each spatial point. As T_e increases at a given value of n_e, the spectrum of the scattered light, which is roughly centered about the laser line, spreads. As will be demonstrated below, the T_e increase results in higher signal in the spectral bands far from the laser line, and reduced signal in the bands that are close. The relative amounts of signal in each spectral channel can thus be used to compute T_e, and the total signal collected gives n_e.

The physical layout of the polychromator is presented in Fig. 3-8. The polychromator input lens focuses light from the collection fibers onto the first of a series of four concave mirrors, which act as field elements. Each of these field element mirrors reflects light onto a concave bandpass mirror, which is placed before a detector

housing. Each bandpass mirror at the detector end has a multilayer dielectric filter coating that transmits light in a particular spectral range. The light that is reflected from each of these bandpass filters is focused onto the next field mirror in the series, or, in the case of the fourth filter, onto a dump. The filters are designed to have very high rejection of the laser line, and the field mirrors are coated with a narrow pass dielectric filter that transmits the laser line. The result is a high degree of stray light attenuation. A blocking filter is placed on the polychromator input lens in order to reject background light outside the range of the four bandpasses.

Light transmitted through each bandpass filter is focused onto a 25-element avalanche photodiode (APD) array. Each array element is 300×250 μm, and there is 50 μm of dead space between elements. The focus and alignment of the image spots on the APDs is optimized by backlighting the collection fibers and adjusting the APD positions until the cross-talk between adjacent APDs is minimized. Because the focus and alignment are sensitive to small changes in position, thermal expansions and contractions within the position control mechanism must be minimized. In addition, APD response is highly sensitive to temperature. Thus, the polychromator is enclosed in thermal insulation, while automatically regulated heaters maintain a constant internal temperature of 32°C.

Each of the 100 APD elements in the polychromator is indexed by the fiber it images and the spectral filter behind which it sits. The spatial index is i, and the spectral index is j, where $i \in [0, 1, \ldots 24]$ and $j \in [0, 1, 2, 3]$. Figure 3-8 demonstrates the indexing order of each. Each channel has a unique responsivity to incoming photons as a function of wavelength. Examples of the four measured response functions for a specific spatial channel are shown in Fig. 3-9. Also shown are $S(T_e, \lambda)$ at $\theta_i = \pi/2$, for two values of T_e. These functions are the analytical expressions for the TS spectral distributions, normalized to electron density, sampled by the polychromator. The signal measured in the i, jth channel will be proportional to both n_e and the integral of the product of spectral response and responsivity. Assuming accurate knowledge of $S(T_e, \lambda)$, the relative amounts of signal in each spectral channel can be used to determine T_e, and the absolute level of signal measured gives n_e.

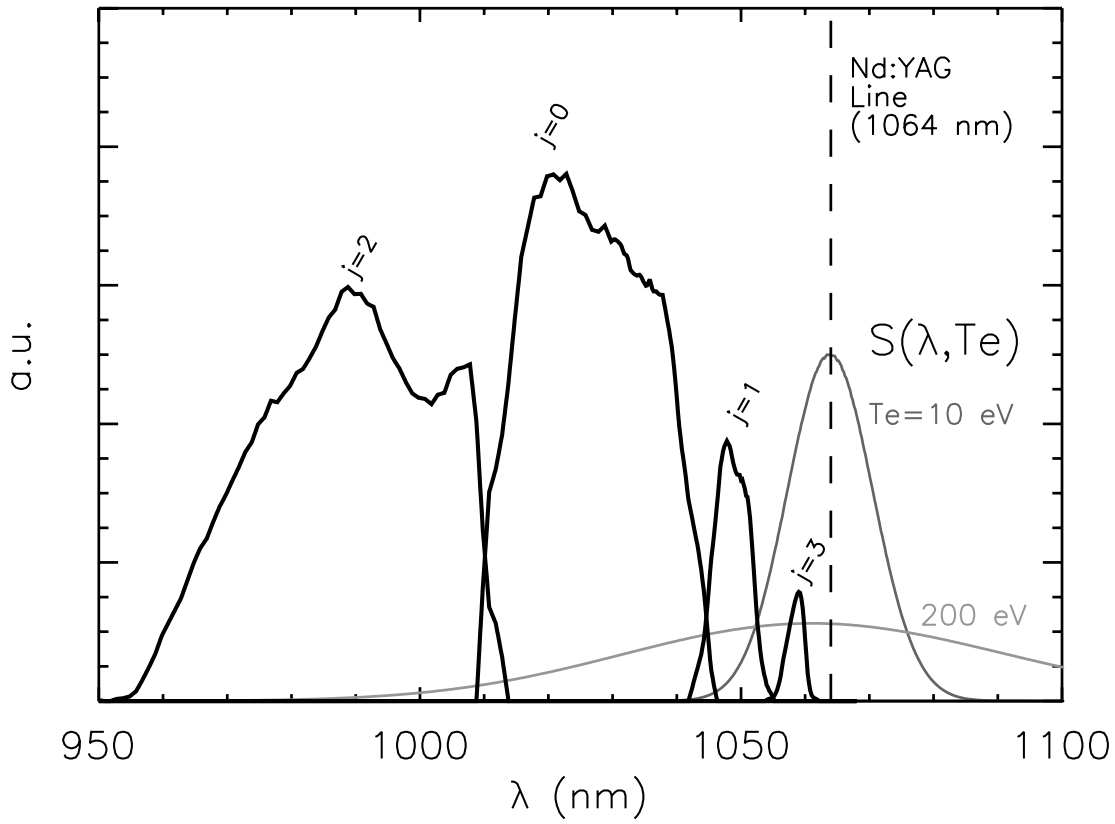

Figure 3-9: Edge TS polychromator response functions and spectral distributions $S(T_e, \lambda)$ of Thomson light at 10 and 200 eV ($\theta = \pi/2$). Spectral indices j correspond to the numbering layed out in Fig. 3-8.

Because higher T_e results in greater spread of the spectral function, the position and width of a spectral channel in wavelength-space determines the T_e range over which it is relevant. As $S(\lambda, T_e)$ spreads, and its tail passes through the j-th spectral channel, that channel begins to measure significant signal. Consultation of Fig. 3-9 suggests that the $j = 1$ channel (second from the laser line) starts becoming useful only for $T_e \gtrsim 10$ eV, while the $j = 2$ channel (fourth from the laser line) sees significant signal only for $T_e \gtrsim 200$ eV. On the other hand, at the higher T_e, the signals in the $j = 1, 3$ channels nearest the laser line are declining as temperature rises, meaning they have become less useful to reconstructing the measurement.

These effects are seen explicitly in Fig. 3-10. These are the modeled responses

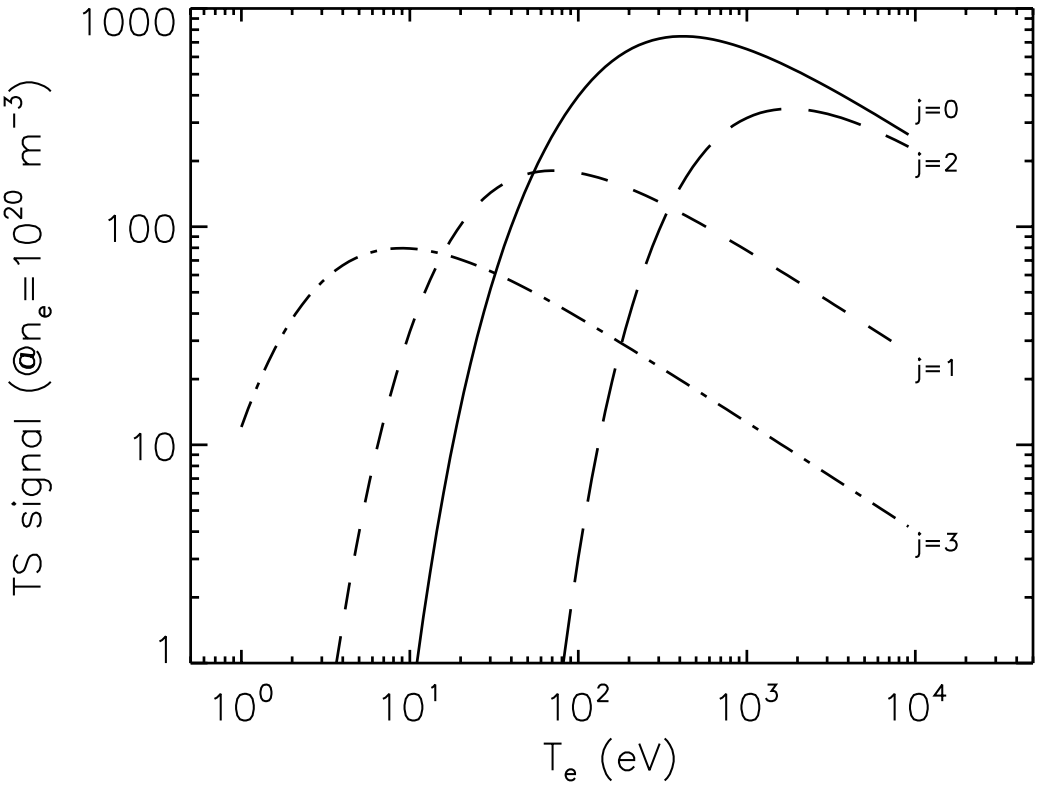

Figure 3-10: Responses of ETS detectors as a function of T_e in plasma with $n_e = 1 \times 10^{20}$ m^{-3}

of polychromator spectral channels in a given spatial channel, after application of several calibration factors. The complete derivation of these curves will be explained in Sec. 3.3; simply put, they are proportional to the integrals of the curves of TS and polychromator response shown in Fig. 3-9. The y-axis shows measured counts in the ETS digitizer per 10^{20} m^{-3} of electron density, assuming approximately 1 J laser energy. Direct measurements of APD response to simulated laser signals indicates that, in order to achieve a signal-to-noise (S/N) of 3 or more, a minimum of about 30 digitizer counts is needed. Signals below this threshold generally are not considered useful. From the curves in Fig. 3-10, it is seen that, below 2 eV, there is no measurable signal in any spectral channel at a density of 1×10^{20} m^{-3}. At such low temperatures, the TS spectral function $S(\lambda)$ is simply too narrow to be measured by

the available spectral channels. In the range of 2–10 eV, measurable signal exists in $j = 3$ only, and then only at densities $n_e \gtrsim 1 \times 10^{20}$ m^{-3}. In practice, temperatures below 50 eV typically coincide with n_e in the range of 0.2–0.5$\times 10^{20}$ m^{-3}, which means that significant signals are obtained in more than one spectral channel ($j = 3, 1$) only when T_e rises above about 15–20 eV. This sets the approximate lower bound of the ETS T_e range. Further inspection of Fig. 3-10 shows that $j = 0$ becomes important for $T_e \gtrsim 40$ eV, and that $j = 2$ does indeed become useful above about 200 eV.

Above about 800 eV, the APD responses are relatively flat ($j = 2$), slowly declining with T_e ($j = 0, 1$), or not above the noise threshold ($j = 3$), which makes T_e reconstruction highly uncertain in this region, given experimental noise. This behavior gives the practical upper bound of measurable T_e. (During initial operation, prior to October 1999, the $j = 2$ spectral bandpass was not available, which limited accurate T_e measurement to about 200 eV.) The lower bound in measurable n_e is set by the amplitude of these response curves and the acceptable S/N. Its value depends on the local T_e, and is roughly 2–5$\times 10^{19}$ m^{-3}.

3.2.3 Data acquisition and control hardware

The APD signals have both pulse contributions from TS and slowly varying contributions from plasma background light. The plasma background signal is isolated and subtracted from the total signal by means of a delay line technique [117] in the detector circuitry, which has a design similar to that of Hsieh [118]. Because both the slow background (BG) and fast pulse (SIG) signals contribute to the noise in the TS measurements, both signals are needed for analysis of each channel. Having both SIG and BG for each of four spectral channels in 25 spatial channels gives 200 total signals to be sampled, multiplexed and digitized, with timing triggers obtained from a fraction of the Nd:YAG beam leaking through a steering mirror atop the tokamak.

The hardware used for control of the diagnostic is largely based on the Computer Automated Measurement And Control (CAMAC) standard and driven by MDS-Plus data acquisition software [119]. CAMAC modules are used to program and monitor high voltage (HV) to the APD arrays, to generate flash lamp and Q-switch triggers for

Manufacturer	Model	Function
Aeon	H321	DAC for controlling HV supply to APDs
Joerger	ADC-P	ADC for monitoring HV supply
Jorway	J221	Timing module for flash lamp and Q-switch pulses
LeCroy	8212A	12-bit digitizer for recording multiplexed APD signals
LeCroy	FERA	Fast charge digitizer for Nd:YAG energy measurement
BiRa	2048	Serial time interval counter to record laser pulse timing

Table 3.1: CAMAC modules used in the edge TS diagnostic

the Nd:YAG lasers, to record precisely the timing of the laser pulses in the tokamak, and to digitize the multiplexed edge TS signals and laser energy. Table 3.1 lists these modules, for the interested reader.

A LeCroy 8212A digitizes the multiplexed SIG and BG signals with 12-bit resolution translating input voltages of 0–10V into counts of 0–4095. The upper limit of this digitizer defines the upper bound on n_e in which accurate measurements are obtained, since at sufficiently high densities, some spectral channels may become saturated. Figure 3-10 shows that the $j = 0$ spectral channel is subject to saturation when T_e is from 200 to 800 eV and n_e is higher than 5×10^{20} m^{-3}. This density is usually quoted as the effective upper bound for ETS.

In addition to the CAMAC hardware, PCs are employed in the remote operation of the diagnostic, both driving the PLC-driven devices for beam steering with PARAGON control software and controlling the Nd:YAG lasers via a LabVIEW-based control panel.

3.3 Calibrations

When TS data are collected, signals are obtained from each APD at a number of discrete time points corresponding to laser pulses. For each spatial channel at each pulse, the data from the four spectral channels are fitted with model functions using

T_e, n_e as adjustable fit parameters. The model signal in each channel is meant to approximate the real Thomson signal, and is calculated from the integral of responsivity with the TS spectral function. In order to obtain accurate model signals, an extensive set of calibrations is performed on the ETS diagnostic:

1. The normalized spectral response of each channel is determined. This determines the response of the i, jth channel purely as a function of temperature.

2. The relative integral response of the spectral channels to a steady and uniform light source is found. This gives the relative gains of the spectral channels in a given spatial channel.

3. The ratios of detector response to fast and slow pulsed light sources is measured for all channels. These numbers allow a correction for variations in the relative gains for fast and slow signals ranging across the 100 detectors. This and the previous steps are sufficient for computation of T_e from TS.

4. The throughput of the optical system is measured for each spatial channel. This absolute calibration allows for the accurate determination of n_e from TS.

Once these calibrations are complete, the model TS signals $M_{i,j}(T_e)$ are computed according to

$$M_{i,j} = A_{i,j} \int_0^\infty f_{i,j}(\lambda) S_{\mathrm{rel}}(T_e, \theta_i, \lambda)\, d\lambda \tag{3.16}$$

where $f_{i,j}(\lambda)$ are the normalized spectral response functions determined in the first calibration listed above, and where $A_{i,j}$ are absolute sensitivity coefficients derived from calibrations 2–4. If collected TS signal $Y_{i,j}$ is assumed noiseless, it can be written

$$Y_{i,j}^{\mathrm{T}}(n_e, T_e) = n_e E_{\mathrm{laser}} M_{i,j}(T_e) \tag{3.17}$$

where E_{laser} is the Nd:YAG energy. It is easily seen that the measured $Y_{i,j}/E_{\mathrm{laser}}$ (which will, of course, have experimental noise) can be fitted with the model curves $M_{i,j}$ using n_e and T_e as fit parameters, as will be discussed in Sec. 3.4.

In the following discussion, $Y_{i,j}$ will refer to signal measured in the i,jth SIG channel, and $B_{i,j}$ will refer to signal measured in the i,jth BG channel. As mentioned in Sec. 3.2.3, the SIG channels are sensitive to fast ($\sim$ 10 ns) pulses only, while the BG channels respond to more slowly varying light.

3.3.1 General response to scattering

It is instructive to examine the generalized expression for raw signal measured in the APD channels: $Y_{i,j}$. For a given laser pulse of energy E_{laser} into a plasma or gas of density n, the noiseless response of the edge TS hardware to scattered light is given by

$$Y_{i,j} = nE_{\text{laser}} L_i \Phi_i \eta_{i,j} \left(\frac{G_S}{G_B}\right)_{i,j} \left(\frac{d\sigma}{d\Omega}\right) \int_0^\infty f_{i,j}(\lambda) g_i(\lambda)\, d\lambda \tag{3.18}$$

with the terms defined as follows:

- L_i: the length of the ith scattering volume
- Φ_i: a factor comprising the wavelength-independent transmission of the collection optics and the collection solid angle, Ω_i
- $\eta_{i,j}$: polychromator detection efficiency, the response of the i,jth channel to a steady light source entering the fibers
- $(\frac{G_S}{G_B})_{i,j}$: the ratio of APD gain in response to laser pulses, G_S, to APD gain in response to slowly varying background light, G_B
- $(\frac{d\sigma}{d\Omega})$: the differential cross-section of the given type of scattering
- $f_{i,j}(\lambda)$: the normalized polychromator instrument function
- $g_i(\lambda)$: the spectral distribution of scattered light

For Thomson scattered light, $g_i(\lambda)$ is given by an appropriate theoretical expression for $S_{\text{rel}}(T_e, \theta_i, \lambda)$, such as the relativistic evaluation given in (3.14). For scattered light perpendicular to the incident light polarization the Thomson cross

section, $(\frac{d\sigma}{d\Omega})^T$, is just the square of the classical electron radius, r_e^2. Thus (3.18) for TS can be written

$$Y_{i,j}^{\mathrm{T}} = n_e E_{\mathrm{laser}} r_e^2 L_i \Phi_i \eta_{i,j} \left(\frac{G_S}{G_B}\right)_{i,j} \int_0^\infty f_{i,j}(\lambda) S_{\mathrm{rel}}(T_e, \theta_i, \lambda)\, d\lambda \tag{3.19}$$

Comparing with (3.17) and (3.16), one obtains the definition of the absolute sensitivity coefficient as

$$A_{i,j} = r_e^2 L_i \Phi_i \eta_{i,j} \left(\frac{G_S}{G_B}\right)_{i,j} \tag{3.20}$$

3.3.2 Spectral functions

The spectral functions $f_{i,j}(\lambda)$ represent the wavelength-dependent response of the polychromator detectors to DC light entering the edge TS fibers. In order to measure the spectral functions $f_{i,j}(\lambda)$, the input fibers of the polychromator are filled at $F/3.5$ with the output of a scannable Czerny-Turner monochromator having a known spectral function. Wavelength scans are performed for all polychromator channels over a range of 600–1200 nm, yielding absolute responses $B_{i,j}(\lambda)$. These are normalized according to

$$f_{i,j} = \frac{B_{i,j}}{\int_0^\infty B_{i,j} d\lambda} \tag{3.21}$$

Since all the APDs for a given spectral channel lie behind a common dielectric filter, one might assume the $f_{i,j}$ could be written f_j and tabulated for individual spectral channels only. However, it is necessary to tabulate the instrument functions separately for each spatial channel as well, due to a subtle dependence of the filter transmission functions on the location at which the light passes through the filter. This effect is most clearly seen in the central wavelength of the narrowest spectral band, nominally centered at 1059 nm. In spatial channels farthest from the center of the APD array, the central wavelength of this band is red-shifted by as much as 3 nm, which is comparable to the spectral width of the bandpass.

3.3.3 Integral detector response

Subsequent to the collection of the normalized spectral response, the integral DC response of the individual channels is measured by illuminating the collection fibers with a uniform source of known spectral brightness. For this "white plate" calibration, the fibers are filled at $F/3.5$ using a Labsphere integrating sphere with spatially uniform intensity J and spectral intensity $\mu(\lambda)$, which varies little over the domain of the $f_{i,j}$. The polychromator BG response to this source is

$$B_{i,j}^{\mathrm{W}} = \eta_{i,j} \int_0^\infty f_j(\lambda) J \mu(\lambda)\, d\lambda \tag{3.22}$$

Since the integrating sphere is absolutely calibrated at its maximum intensity, J as well as $\mu(\lambda)$ are known, and one could in principle determine the coefficients $\eta_{i,j}$ directly from white plate measurements. Unfortunately, when the edge fibers are illuminated with the source set at maximum intensity, most of the BG channels in the edge TS digitizer become saturated. The iris on the source must be contracted in order to lower the intensity and record unsaturated signals. The measurement then results in a white plate coefficient proportional to $\eta_{i,j}$ by an unknown factor J:

$$W_{i,j} \equiv \frac{B_{i,j}^{\mathrm{W}}}{\int_0^\infty f_j(\lambda)\mu(\lambda)\, d\lambda} = J\eta_{i,j} \tag{3.23}$$

The product of the white plate coefficients $W_{i,j}$ and the $f_{i,j}(\lambda)$ determine the relative response of each polychromator channnel to a DC light source. Additional information is required to obtain the response to fast signal.

3.3.4 Relative gains in DC and pulsed mode

The gains in each APD circuit differ between DC and pulsed mode, and the APD response must be measured upon illumination with both pulsed and DC light. The fast/slow gain ratios $(\frac{G_S}{G_B})_{i,j}$ in (3.18) are determined experimentally with a laser diode source set up to illuminate the APD arrays directly. The laser diode can deliver 8 ns pulses in fast mode in order to simulate laser pulse illumination. Signal in fast mode

is recorded in the SIG polychromator channels. The diode can also operate in slow mode, giving 4 μs pulses, which are broad enough for signal to appear only in BG channels. By measuring the laser diode power in either mode and the SIG and BG signals, the fast/slow gain ratios are easily derived. The variation in $(\frac{G_S}{G_B})_{i,j}$ from channel to channel is as high as 20% and is therefore an important consideration in fitting measured Thomson signal.

During this procedure, the levels of noise in the SIG channels for both fast and slow diode modulation are recorded. These data determine the contributions to signal-to-noise in these channels as a function of the overall signal in either SIG and BG channels. This is useful in estimating the variance of TS signals from plasma, when noise is induced both by background plasma light and the laser pulsed light itself. This will be described further in Sec. 3.4

3.3.5 Absolute calibration

Once the spectral response, integral response and fast/slow gain ratios are determined, the edge TS calibration is suffcient to infer accurate T_e from measured TS photons. In order to complete the calculation of the absolute sensitivity coefficients and obtain n_e from TS, the contribution to $A_{i,j}$ from spatial factors L_i and Φ_i in (3.20) must be determined. These factors are specific to laser scattering from inside the tokamak, as they depend on scattering geometry and the configuration of the collection optics. What is needed to determine these calibration factors is a laser scattering mechanism of well-known cross-section and spectral density.

Scattering from room temperature gas is an obvious candidate, with two main mechanisms available. Rayleigh scattering occurs in all gas species and has a well-characterized cross-section. The scattered light is unshifted in wavelength, making for a trivial spectral function. This type of scattering is not useful for the ETS system, given the excellent rejection of the laser line by the polychromator. Therefore, gas scattering calibrations rely on Raman scattering, which does exhibit a known wavelength shift. Cross-sections for scattering in both H_2 and D_2 are known to reasonable accuracy. [120]

Raman scattered light is observed from diatomic gases, and is shifted in frequency relative to the incident light as a result of rotational energy transitions. The shifted Raman line k, usually denoted by transition indices $m \rightarrow n$, can be useful for TS calibration if it falls within at least one of the diagnostic spectral bands, and if parasitic light from unshifted Rayleigh scattering is rejected effectively. Because the positions of the Raman lines and the differential Raman cross sections, $(\frac{d\sigma}{d\Omega})_k^R$, are known, the absolute sensitivity can be calculated and applied to TS measurements.

The line width of Raman scattered light is on the order of a few Angstroms [121], and so the spectral function for the kth Raman line is well approximated by $g_i(\lambda) = \delta(\lambda - \lambda_k^R)$. Plugging this function into (3.18) and summing over k gives the response to Raman scattering in a gas of density n_0:

$$Y_{i,j}^R = n_0 E_{\text{laser}} L_i \Phi_i \eta_{i,j} \left(\frac{G_S}{G_B}\right)_{i,j} \sum_k \left(\frac{d\sigma}{d\Omega}\right)_k^R f_{i,j}(\lambda_k^R) \tag{3.24}$$

One can express n_0 in terms of measurable gas pressure P_g and temperature T_g, arriving at

$$n_0(\text{m}^{-3}) = 2.687 \times 10^{25} \cdot \frac{P_g(\text{Torr})}{760} \frac{273.15}{T_g(\text{K})} = 9.657 \times 10^{24} \cdot \frac{P_g(\text{Torr})}{T_g(\text{K})} \tag{3.25}$$

Let $C = 9.657 \times 10^{24}$, define the new quantity $q_{i,j} = Y_{i,j}^R / P_g E_{\text{laser}}$, and divide (3.24) by both the gas pressure and the laser energy:

$$q_{i,j} = L_i \Phi_i \eta_{i,j} \left(\frac{G_S}{G_B}\right)_{i,j} \left[\sum_k \left(\frac{d\sigma}{d\Omega}\right)_k^R f_{i,j}(\lambda_k^R)\right] \frac{C}{T(\text{K})} \tag{3.26}$$

The left hand side of this equation is precisely what is measured during a sequence of Raman scattering calibrations, and is proportional to the absolute sensitivity of each channel. In order to measure this quantity, the tokamak is filled with scattering gas, in this case hydrogen or deuterium, and the pressure is varied over a range of 0–500 torr. At each discrete pressure, scattered light is measured over the course of several thousand laser pulses. Average laser signal in a given channel is normalized to the laser energy, then examined as a function of gas pressure. Figure 3-11 shows

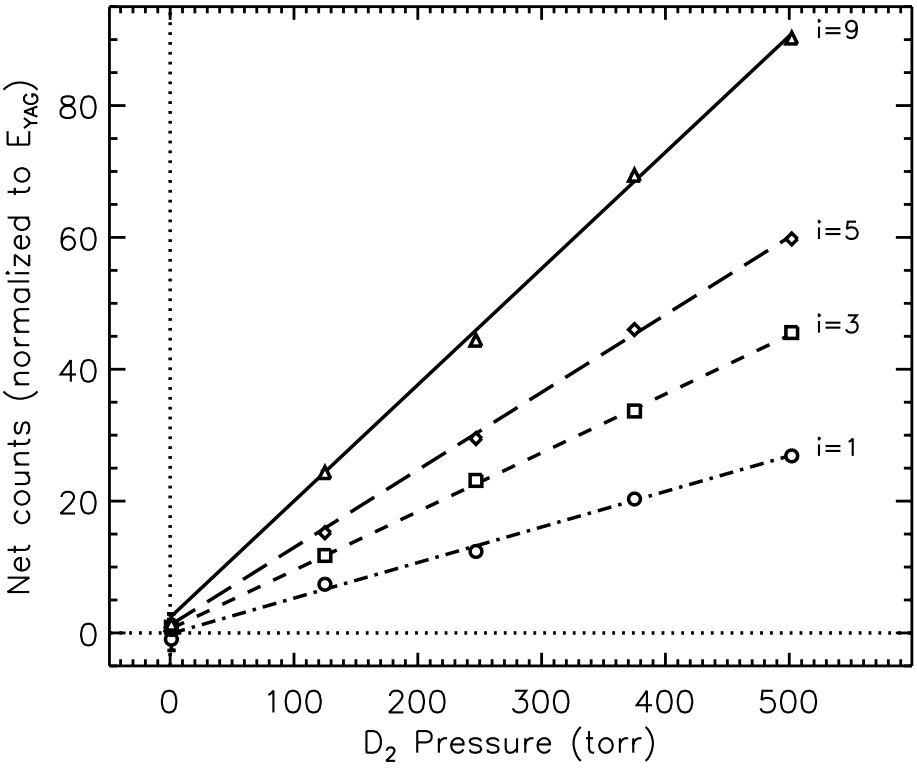

Figure 3-11: Raman scattering signal in $j = 0$ *vs.* D_2 pressure. Computed error estimates in net counts are too small to see for most data above 100 torr.

data from calibration in D_2 for spectral channel $j = 0$. The slopes of the fitted lines are the $q_{i,0}$.

If every spectral channel yielded signal from Raman lines, the absolute sensitivity coefficients for every channel could be instantly obtained from the $q_{i,j}$. The relation could be got by combining (3.20) and (3.26) to arrive at

$$A_{i,j} = q_{i,j} \frac{r_e^2}{\sum_k \left(\frac{d\sigma}{d\Omega}\right)_k^R f_{i,j}(\lambda_k^R)} \frac{T_g(\mathrm{K})}{C} \tag{3.27}$$

However, this does not occur in practice. Raman lines for D_2 are observed only in the $j = 0, 1$ spectral channels, while the $j = 0, 2$ channels observe H_2 lines. Therefore another coefficient, independent of spectral channel, is needed to relate the Raman results from one spectral channel to all the others.

One can use (3.23) to replace the polychromator detection efficiency $\eta_{i,j}$ in (3.26) with the normalized white plate coefficient $W_{i,j}/J$. Then the unknown quantities are moved to the left hand side, leaving only measured quantities on the right. This defines the Raman calibration coefficient, R_i:

$$R_i \equiv \frac{L_i \Phi_i}{J} = \frac{q_{i,j}}{W_{i,j}\left(\frac{G_S}{G_B}\right)_{i,j} \sum_k \left(\frac{d\sigma}{d\Omega}\right)_k^R f_{i,j}(\lambda_k^R)} \frac{T_g(\mathrm{K})}{C} \tag{3.28}$$

One requires Raman signal in only one spectral channel to calculate R_i, and from there, the absolute sensitivity is determined for all i, j, according to

$$A_{i,j} = r_e^2 R_i W_{i,j} \left(\frac{G_S}{G_B}\right)_{i,j} \tag{3.29}$$

This is equivalent to (3.20), and can be inserted along with $f_{i,j}$ into (3.16) in order to generate polychromator lookup tables $M_{i,j}$ for temperature and density fitting.

3.4 Data analysis

During a plasma discharge, the TS laser fires repeatedly, and at every laser time point, the ETS system digitizes a set of 100 laser signal measurements $Y_{i,j}$ and 100 plasma background measurements $B_{i,j}$. Algorithms run after each plasma discharge, the purposes of which are to infer T_e, n_e for each pulse, correcting for laser misalignment; to map the measurements to machine midplane coordinates; and to fit the resultant radial profiles with an appropriate fitting function. The codes are queued automatically by the C-Mod job dispatch server after data storage has completed.

3.4.1 Inferred electron temperature and density

Initial estimates of temperature and density are obtained by the method of ratios described by Greenfield [122], and are then used as the initial guess for a non-linear least squares fitting routine. The final algorithm uses the gradient-expansion method of Marquardt [123], which returns fitting parameters T_e, n_e that minimize the goodness-

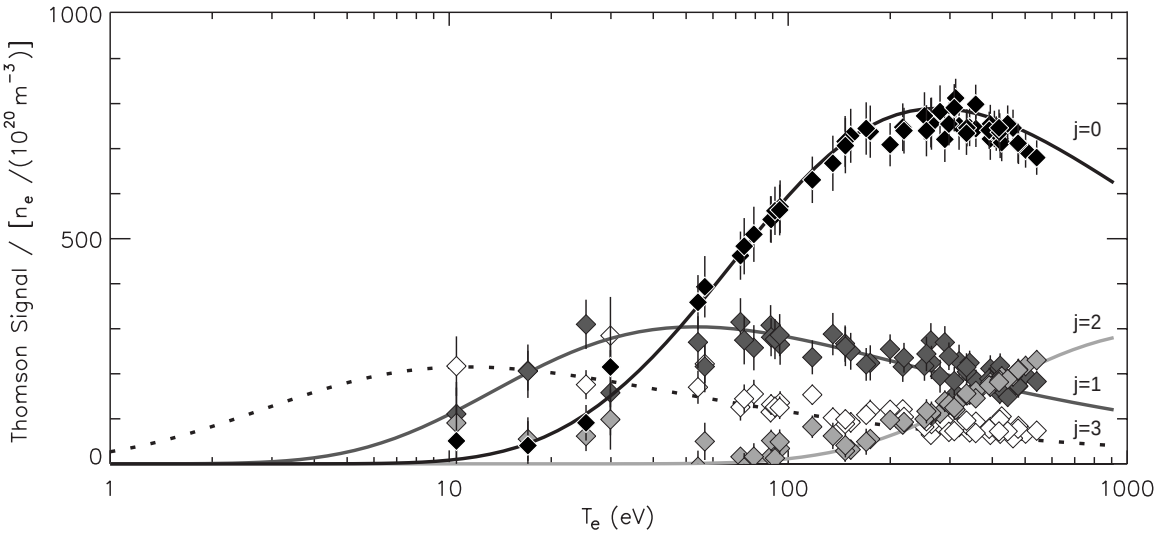

Figure 3-12: Experimental signals (diamonds) in each of four spectral channels, *vs.* fitted T_e, for a given discharge. Curves represent the model response to which the experimental signals are fit. Both model and measured signals are normalized to laser energy and n_e.

of-fit parameter χ_i^2:

$$\chi_i^2 = \sum_j \frac{[s_{i,j} - n_e M_{i,j}(T_e)]^2}{\sigma_{s_{i,j}}^2} \tag{3.30}$$

where $s_{i,j} = Y_{i,j}^T / E_{\text{laser}}$ are the YAG-normalized TS signals and $\sigma_{s_{i,j}}^2$ are the estimated variance of the measured signals. Sample results from the fitting algorithm are seen in Fig. 3-12, which shows density-normalized experimental signals $s_{i,j}/n_e$ from a specific spatial channel plotted against their fitted T_e, accompanied by the model responses $M_{i,j}$.

The experimental variance is calculated based on the magnitude of signals in both the SIG and BG channels, $Y_{i,j}$ and $B_{i,j}$, as well as the laser energy variance σ_E^2 and the SIG "dark" noise level in the absence of incident light $\sigma_{D_{i,j}}^2$:

$$\sigma_{s_{i,j}}^2 = \frac{1}{E_{\text{laser}}^2} \left(\sigma_{Y_{i,j}}^2 + \sigma_E^2 s_{i,j}^2 \right) \tag{3.31}$$

with

$$\sigma_{Y_{i,j}}^2 = \alpha_{i,j} Y_{i,j} + \beta_{i,j} B_{i,j} + \sigma_{D_{i,j}}^2 \tag{3.32}$$

Here the coefficients $\alpha_{i,j}$ and $\beta_{i,j}$ are experimentally measured values obtained during the aforementioned laser diode calibration, during which all APDs are stimulated directly with both fast (SIG) and slow (BG) pulses of light, separately inducing noise in the SIG channels. Calculated uncertainties in T_e from the least squares fit are typically in the 10–20% range for individual time points, an amount roughly consistent with the observed scatter. Densities are less prone to noise-induced uncertainty, though the Raman calibration coefficients introduce an additional systematic uncertainty that must be considered.

3.4.2 Misalignment correction

An additional consideration for determining the density is the goodness of alignment of the laser with respect to the collection fibers. Sec. 3.2 described how a set of three alignment fibers are used to monitor the alignment of the scattered Nd:YAG beam image with the linear array of collection fibers. The degree of misalignment, as well as the resulting loss of photons in the collection fibers, can be quantified and used to correct the fitted density. Alignment correction functions $\phi_i(X)$ are defined for each spatial channel on the measured lateral beam displacement X. If the signals in the left, center and right alignment channels are Y_L, Y_C and Y_R, then the displacement is defined as

$$X \equiv \frac{Y_R - Y_L}{Y_L + Y_C + Y_R} \tag{3.33}$$

It is clear that $-1 \leq X \leq 1$, and $X = 0$ corresponds to optimal alignment, with equal amounts of signal in either alignment side channel. Most data taken during a Raman calibration have $X \approx 0$ by design, but a select set of data is taken as X is varied manually over its entire range (either by moving the beam or by moving the fiber positions horizontally). For each spatial channel

$$\phi_i(X) = Y_i(X)/Y_i(0) \tag{3.34}$$

is a function peaking at a value of one when $X = 0$, and vanishing as $|X| \to 1$. One can see that dividing the ith density measurement by ϕ_i accounts for photons lost due to misalignment. Since this is a scattering geometry effect, the correction factor can be applied with equal validity to the Thomson scattering density results. So that ϕ can be calculated on the fly during post-shot analysis, analytic functions are fitted to the Raman scattering misalignment measurements. A form that has been found useful is the polynomial expression

$$\ln \phi_i = \sum_{k=0}^{m} C_k X^k \tag{3.35}$$

where the C_k are the coefficients of the fit, and $m = 9$. After n_e, T_e are inferred from the Marquardt fit of the TS data, the density is divided by ϕ_i and recorded.

3.4.3 Edge profile mapping and fitting

The parametric fitting of n_e, T_e to the measured signals, as described above, is performed for every spatial channel and for every laser pulse, giving a time series of edge Thomson profiles along the Nd:YAG path. The scattering locations (R, z) are mapped to the tokamak midplane along surfaces of constant magnetic flux using results from the EFIT magnetics reconstruction code [14]. Assuming that T_e and n_e remain constant along flux surfaces, this mapping gives midplane radial profiles of these quantities. The minimum collection fiber spacing (1.2 mm), the Cooke triplet demagnification (2:1) and the typical flux expansion between midplane and the upper edge of the plasma (~ 2) combine to give a radial resolution of slightly greater than 1 mm. The Nd:YAG repetition rate of 30 Hz gives a temporal resolution of 33.3 ms for single laser operation, though dual laser operation with staggered triggers has been used to reduce this number to 16.7 ms.

Edge profiles of n_e, T_e are processed in order to determine parameters of interest. As discussed in the previous chapters, during H-mode operation profiles tend to develop sharp gradients over a narrow radial region near the LCFS, giving rise to a pedestal. Typical profiles of T_e and n_e measured at time points before and after the

H-mode transition are shown in Fig. 3-13, illustrating the steepening in parameter gradients that characterizes high confinement. Also shown in Fig. 3-13 are the fits of the standard parameterized tanh function (2.1) to the H-mode data. This routine fitting yields the parameters b (baseline), h (height), R_0 (position), Δ (full width) and m (interior slope). The distribution and scalings of these parameters will be discussed in detail in Chs. 4 and 5.

3.5 Comparisons with other diagnostics

Where possible, it is desired to perform direct comparisons of ETS results with measurements from some of the other diagnostics discussed in Sec. 1.4.3. The available diagnostics for this kind of benchmark are the CTS system (channels with large r/a), ECE, the VC array and SOL scanning probes. As previously mentioned, n_e and T_e between CTS and ETS agree well. It is found that, within experimental uncertainties, consistent comparisons with the other diagnostics are also obtained.

A fairly straightforward comparison can be made to the T_e measurement from the GPC measuring ECE. Edge profiles are obtained by sweeping the toroidal field by 2–3% over a period of 100–200 ms, producing a radial scan of the edge T_e profile. [94] In steady-state plasmas the TS temperatures during the sweep are time averaged and compared with the ECE profile. Due to uncertainties in both the location of these measurements and the EFIT mapping of TS points to the midplane, the profiles must undergo a relative radial shift before a successful match is obtained. The extent of the shift is nominally less than 5 millimeters, which is reasonable given the uncertainties in equilibrium reconstruction and position calibration. Over certain periods, however, the required shift has been as high as 1 cm. An error of only 1% in the calibration of the B_T measurement would justify a centimeter radial shift. This error is somewhat larger than the quoted uncertainty of at most 0.5%, [124] but was fairly reproducible throughout the 2000 C-Mod run campaign, when the sweeps shown in this thesis were performed. Thus, swept ECE profiles shown herein have required translation by approximately 1 cm. The shift has been removed in Fig. 3-14, which compares

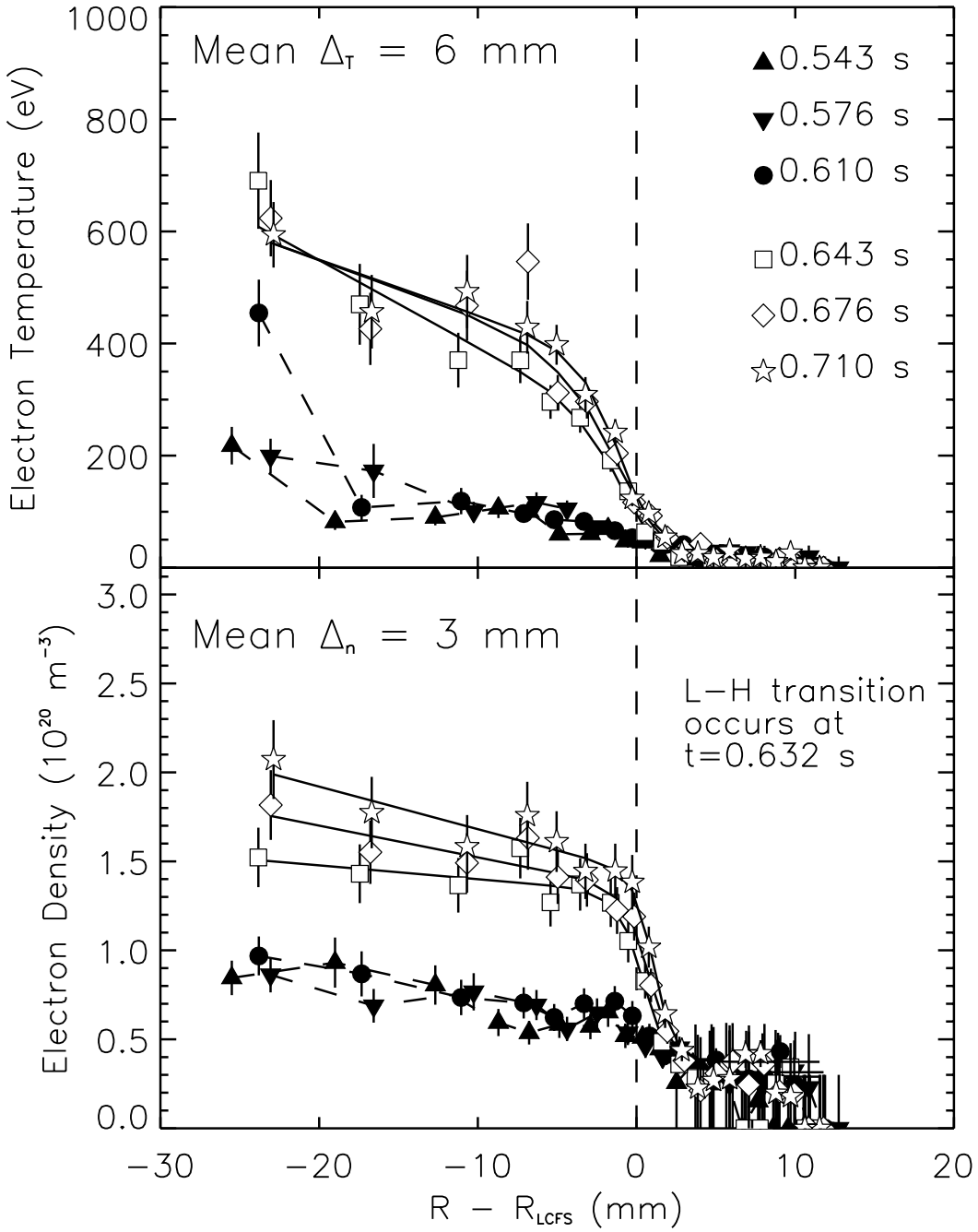

Figure 3-13: Edge profiles of T_e and n_e before and after *L-H* transition. Solid curves are are the modified tanh fitting function of (2.1)

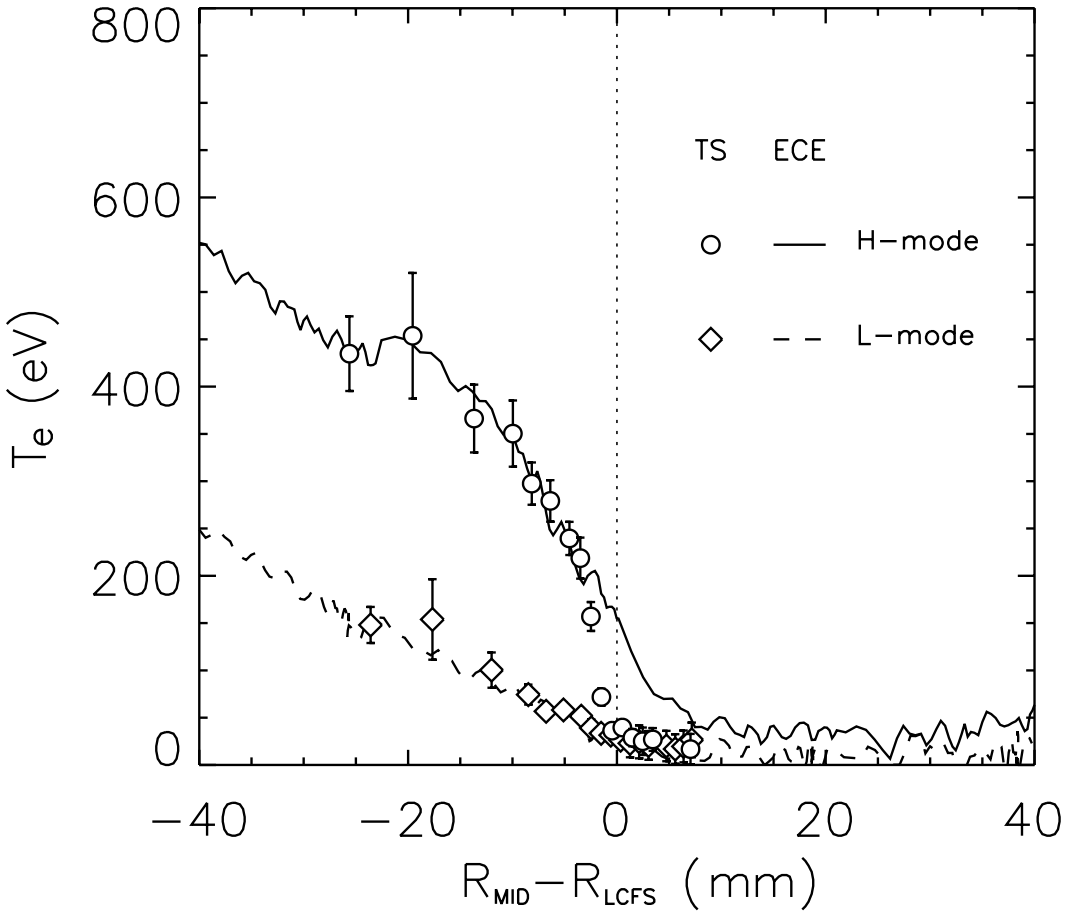

Figure 3-14: Comparison of TS and ECE T_e profiles in L- and H-mode.

profiles obtained in L-mode and H-mode plasmas. Each ECE profile was recorded during a 150-ms sweep of B_T. The plotted TS profiles are averages over the duration of the sweep.

Agreement between ECE and TS is generally very good in L-mode, and also in H-mode when the T_e gradient is not too large. In Fig. 3-14, the H-mode profile from ETS shows a pedestal less than 5 mm in width. This makes for a gradient scale length of T_e that is considerably smaller than the 9-mm resolution of ECE. Because of this resolution limit, Δ_{T_e} from ECE is generally larger than that from ETS. In the region of smaller $|\nabla T_e|$ inboard of the edge pedestal, T_e agreement is generally excellent. As explained in Sec. 3.2.2, the ETS becomes inaccurate for $T_e \gtrsim 800$ eV, and agreement with ECE is lost at such high temperatures.

Reasonable agreement is also had between ETS and scanning probes. Figure 3-15 shows n_e and T_e profiles from a probe insertion into the pedestal of an ohmically heated H-mode, in which the penetration of the probe is sufficient to resolve most of the n_e pedestal profile. All but the innermost millimeter of the probe profiles agree favorably with the TS profiles, and no radial shifts of the data were required to obtain this agreement. Possible causes for the divergence of the profiles at high density and temperature include both overheating of the probe and actual perturbation of local conditions near the probe. As mentioned before, high temperatures in H-mode edges usually prevent deep insertion of the scanning probes. Probes are frequently used to complement the ETS measurements by extending into the SOL. Figure 3-15 shows that as the n_e and T_e profiles fall below the lower bounds of the edge TS dynamic range, denoted by the error bars on the zero measurements, probe data provides useful profile information.

A comparison can also be made with measurements from the VC array. [31] As discussed in Sec. 1.4.3, this instrument provides radial emissivity profiles with millimeter resolution. To compare these profiles with TS results, the emissivity at $\lambda_0 = 536$ nm is calculated from the Thomson T_e and n_e profiles. The estimated value of Z_{eff} at the plasma center is used, and is typically between 1 and 2. These profiles are compared in H-mode plasmas as in Fig. 3-16, again after relative shifts are introduced. The measured emissivity profile contains a significant component outside the LCFS that is due to neither bremsstrahlung nor atomic recombination, and is thought to show a contribution from molecular deuterium. In addition, a bump occurring consistently at the top of the emissivity pedestal is thought to be an artifact of the inversion process. Ignoring this feature, reasonable agreement exists between the measured and calculated emissivity profiles. Often agreement is worse, sometimes due to instrumental artifacts in the VC profiles, and sometimes simply because the Z_{eff} radial profile is not truly flat, as this method assumes. Overall comparisons of the pedestal values are however consistent with the expected uncertainties of 10–15% in the absolute calibrations of both instruments, as well as the uncertainty in Z_{eff}.

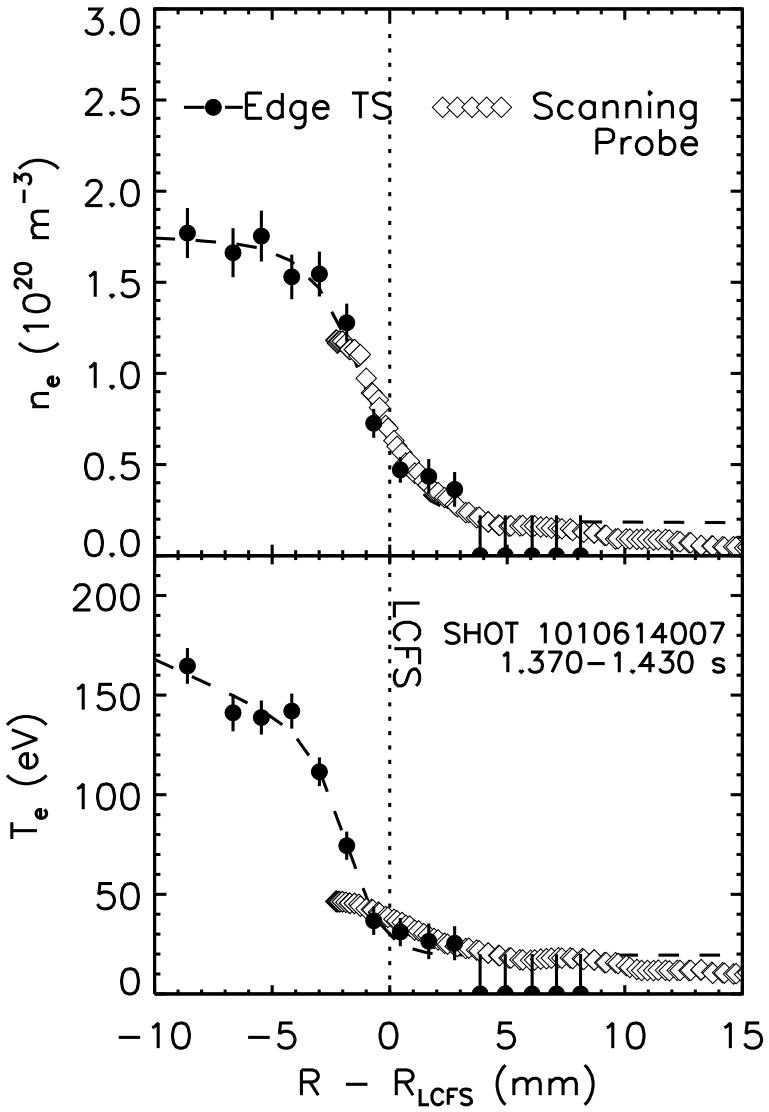

Figure 3-15: Comparison of edge TS profiles (circles) of n_e, T_e with a 60 ms scanning probe plunge (diamonds) through the last closed flux surface (LCFS) of an ohmic H-mode discharge (toroidal field $B_T = 3.4$ T, plasma current $I_P = 0.73$ MA). TS data are average values from profiles measured during the probe scan; dashed curves represent tanh fits to the TS profiles.

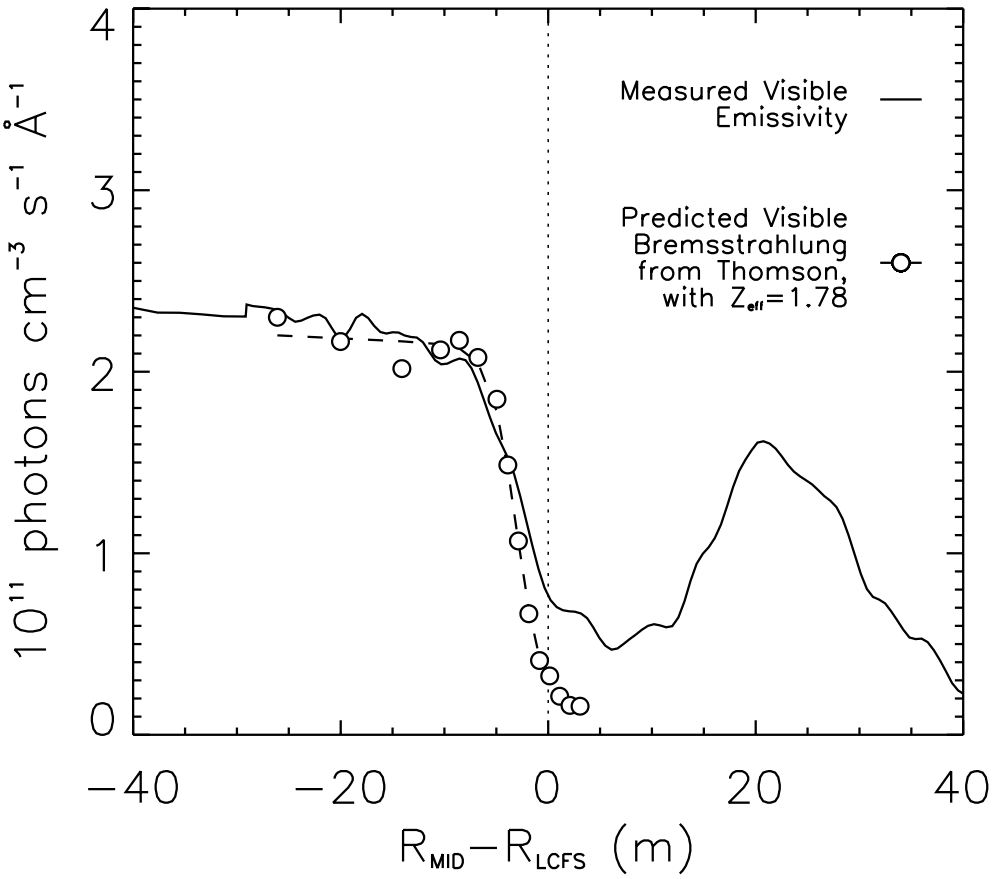

Figure 3-16: Comparison of visible emissivity measurements (solid curve) and bremsstrahlung emissivity profiles (circles) calculated from edge TS T_e and n_e.

3.6 Notable contributions to C-Mod research

Data obtained with the ETS diagnostic have been extremely valuable to advancing understanding of plasma transport at the tokamak edge. High-resolution profiles from ETS resolved for the first time H-mode pedestal profiles on Alcator C-Mod, and allowed a number of empirical observations to be made. Pedestal structure was examined and empirical scalings of pedestal heights and gradients with plasma operational parameters (e.g. plasma current, toroidal field, input power) were determined. [125] Also, the character of edge fluctuations and access to the EDA regime has been correlated with edge parameters such as pedestal pressure gradient and temperature, collisionality and edge safety factor. [22] [125] Experimental response of the n_e pedestal

to neutral fueling variations was also examined using ETS, and the profile data from the diagnostic have served as inputs to modeling that examines the influence of fueling on H-mode edge. [126] These results are discussed at length in the remaining chapters.

Edge TS data have contributed heavily to other segments of edge plasma research as well. These topics are not covered in this thesis, though the interested reader may consult Refs. 127–131. The existence of small ELMs, which are sometimes seen in otherwise EDA plasmas, have been correlated with high edge temperature and pressure gradient, as measured by ETS. To understand this result, the experimental profiles were used as inputs to 2-D magnetohydrodynamic stability calculations, which suggested small ELMs could be explained by instability to coupled peeling-ballooning modes. [127] Also, similarity studies between C-Mod and other tokamaks showed that matched pedestal shapes could be obtained on tokamaks of different size by developing discharges with identical dimensionless parameters at the edge. [128] Additionally, ETS profiles have been examined to determine relationships between heat flux and temperature gradient in L- and H-mode, [129] as well as threshold conditions for obtaining an L-H transition, [130] giving means of testing theoretical predictions. Finally, in concert with scanning Langmuir probe data, ETS also gives information about the evolution of edge profiles as plasmas approach the Greenwald density limit. [131]

Chapter 4

Pedestal Structure and Properties

This chapter presents observations of the pedestal region on the Alcator C-Mod tokamak, focusing on pedestal structure. The radial profile characteristics measured in the C-Mod edge with ETS and other diagnostics are discussed in the following section. Sec. 4.2 discusses the radial extent of the n_e, T_e and p_e pedestal region as measured by ETS exclusively. Section 4.3 then compares pedestals measured in ELM-free and EDA discharges, and progress is made toward understanding the edge conditions that favor either regime. The discharges examined herein all are in deuterium, having a lower single null diverted geometry with ion ∇B drifts directed toward the X-point. All discharges have auxiliary power supplied by ICRF heating at 80 MHz, which is resonant with minority hydrogen ions at a field of 5.3 T.

4.1 Extended profile characteristics

The radial profiles of n_e and T_e have an extended structure that can be examined using a combination of ETS and some of the diagnostics discussed in Sec. 1.4.3. As an example, Fig. 4-1 shows a complete profile obtained by simultaneous use of ETS, ECE, the VC array and scanning probes. Here a steady H-mode discharge was maintained, and B_T was swept from 5.4 to 5.6 T and back over a period of 200 ms, giving a radial ECE sweep of approximately 2 cm. The n_e profile from VC is averaged over this time window, as are six ETS time points. Within this time period the scanning probes

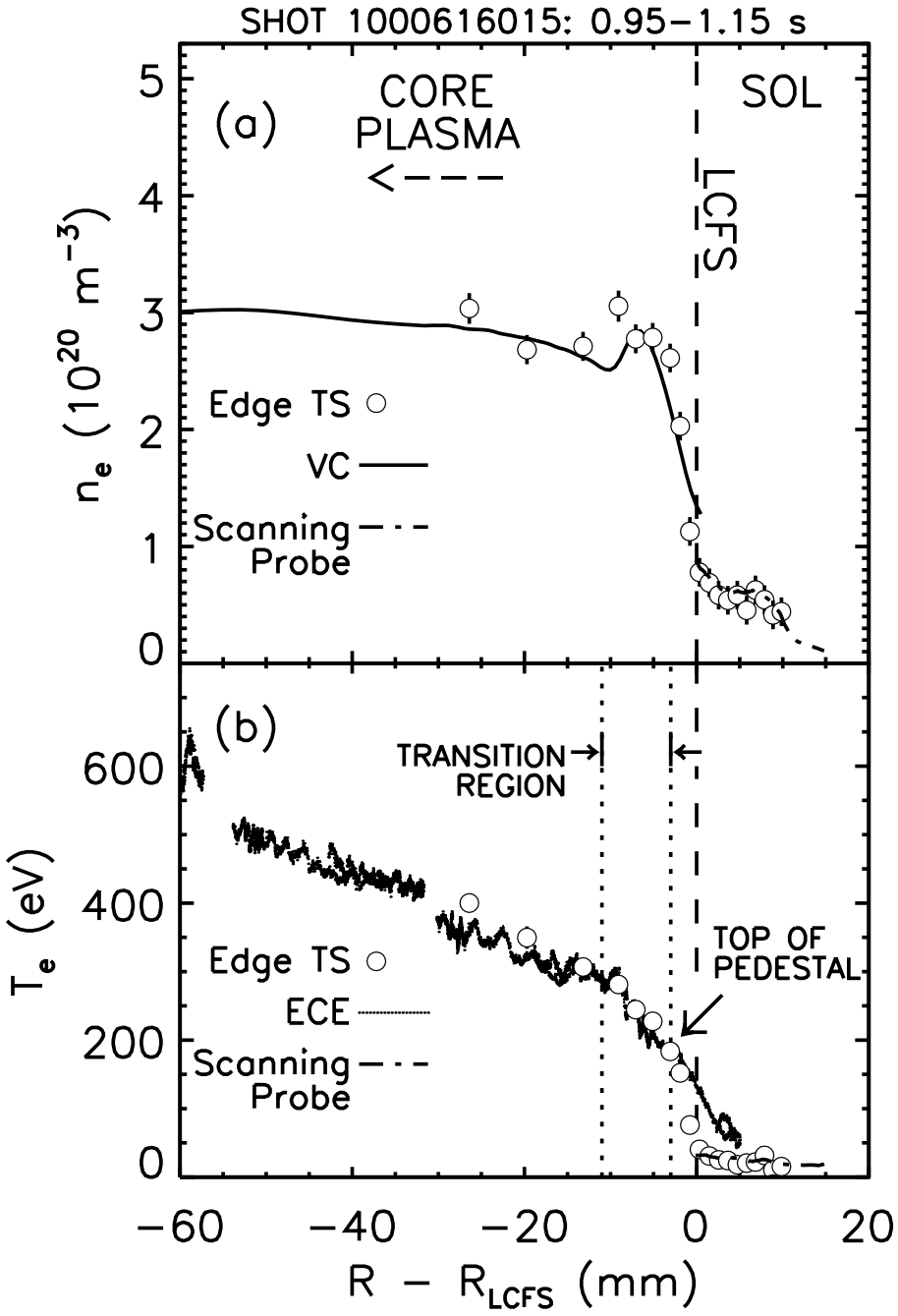

Figure 4-1: Combined profiles of (a) n_e and (b) T_e near the C-Mod edge from multiple diagnostics during a toroidal field sweep between 5.4 and 5.6 T. Scanning probes are used in the SOL, while core profiles are obtained with VC and ECE measurements. ETS resolves the region about the LCFS. VC and ETS data are time-averaged over 200 ms. The T_e profile shows a transition region approximately 1 cm in width between the pedestal and core, exhibiting $|\nabla T_e|$ intermediate between pedestal and core gradients.

were driven through the SOL into the vicinity of the LCFS. As previously discussed, it is necessary to apply relative radial shifts to the profiles in order for matching to occur.

The profiles in Fig. 4-1 illustrate the typically good agreement, after correction for errors in radial coordinates, among the C-Mod diagnostics observing the plasma edge, within the experimental uncertainties of each. Profiles from TS (circles) agree with probe data (dot-dashed curves) in the SOL. The profiles of n_e and T_e flatten at the foot of the pedestal and exhibit radial scale lengths $L_n = n_e/|\nabla n_e|$, $L_T = T_e/|\nabla T_e|$ of a few centimeters in the SOL. The large drop in the probe n_e profile approximately 10 mm outside the LCFS happens because the probe is in the shadow of outboard poloidal limiters; here field lines have shorter connection length, meaning that the distance along a field line to a material surface is less, and that the characteristic dwell time in the SOL is smaller. Behind the limiter boundary, as plasma is transported radially outward by diffusive and convective processes, particles travel a smaller average cross-field distance before striking a surface and recycling in the form of neutral gas. The shorter density gradient scale length results.

Moving inward radially toward the LCFS, the probe passes from the far SOL into the near SOL, where a strong reduction in gradient scale lengths begins. The narrow region near the LCFS exhibits scale lengths of millimeters. Probes, the VC measurement and ETS all show the steepening of gradients associated with ETBs. As was the case previously, the discrepancy between the ECE and TS profiles in the pedestal region is explained by the larger spatial resolution of the ECE diagnostic. Several millimeters inside the LCFS, gradients relax, and ECE and ETS produce mutually consistent profiles of core plasma T_e. There is also good overall agreement between TS and VC. Though the profiles in Fig. 4-1(a) seem to show small variations in n_e atop the pedestal, these are actually related to measurement uncertainties. In the case of TS, there are uncertainties of 5–10% in absolute calibration coefficients, which vary channel to channel, and are not included in the plotted error bars. The local maximum present in the VC inversion is not a real pedestal structure, since it appears even during the L-mode portion of this discharge. It may be the result of an

unwanted reflection within the machine.

Both profiles exhibit core gradients roughly constant in R, with gradient scale lengths such that $L_T < L_n$. An interesting feature in the T_e profile, observed in a number of steady H-mode discharges, is a region of T_e gradient intermediate between that in the pedestal ($|\nabla T_e| \sim$ 50–100 keV/m, typically) and that in the core plasma ($|\nabla T_e| \sim$ 5–10 keV/m). This region is located immediately inside the T_e pedestal and is approximately 1 cm in radial extent. The change in T_e gradient in this region has been observed with both ECE and ETS, though the adjacent pedestal seen with ETS is too localized to be measured with ECE. Fitting (2.1) to ECE profiles generally results in pedestals that are wider (> 1 cm) and hotter than those from ETS. Thus there is no contradiction between the current work and results shown prior to ETS T_e measurements, in which ECE swept profiles suggested $\Delta_{T_e} \gtrsim 1$ cm. [96] [132] [133] One can infer that similar instrumental differences could also impact the comparison of pedestal data of different machines, and that the simple tanh-like equation may insufficiently model H-mode edge temperature and pressure profiles on C-Mod.

The two breaks in slope found in the T_e profile indicate that perhaps there are two distinct edge regions with generally different edge transport characteristics. Unfortunately the radial extent of the transition region between pedestal and core is not routinely diagnosed, and not well characterized at this time. The outer ETB profiles, however, are regularly measured with ETS. The remainder of this chapter and the next will focus on T_e and n_e profiles measured by ETS only, mapped to the midplane, and fit with the tanh-like function. Absolute radial position of the pedestals is not considered, and therefore radial uncertainties in the EFIT placement of the separatrix should have no effect on the chief results.

4.2 Pedestal width

Figure 4-2 shows typical profiles of T_e, n_e and $p_e = n_e T_e$ measured at a single time point in a C-Mod H-mode. The solid curves in the figure show the results of an error-weighted fitting of the tanh-like function of (2.1) to the measured profiles. The

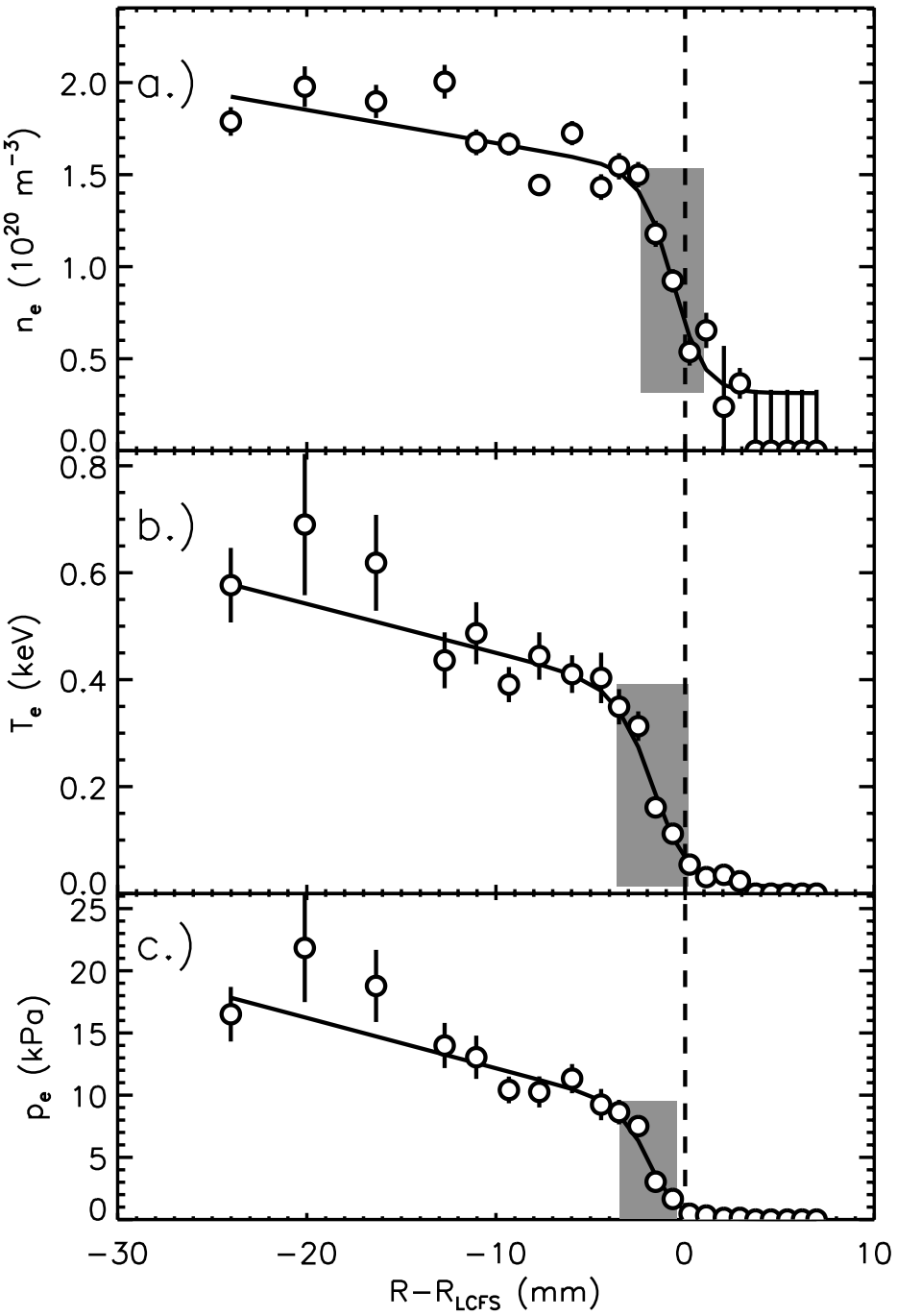

Figure 4-2: Simultaneous H-mode profiles of a.) electron density n_e, b.) temperature T_e and c.) pressure p_e from ETS. The solid curves represent the results of fitting the H-mode profile data with the modified tanh function of (2.1). The gray boxes represent the extent of the pedestal region given by the four main fit parameters; the bottom and top borders of each box are given by b and $b+h$, while the left and right sides are $R_0 - d$ and $R_0 + d$. The vertical dashed line indicates the position of the LCFS, as given by EFIT.

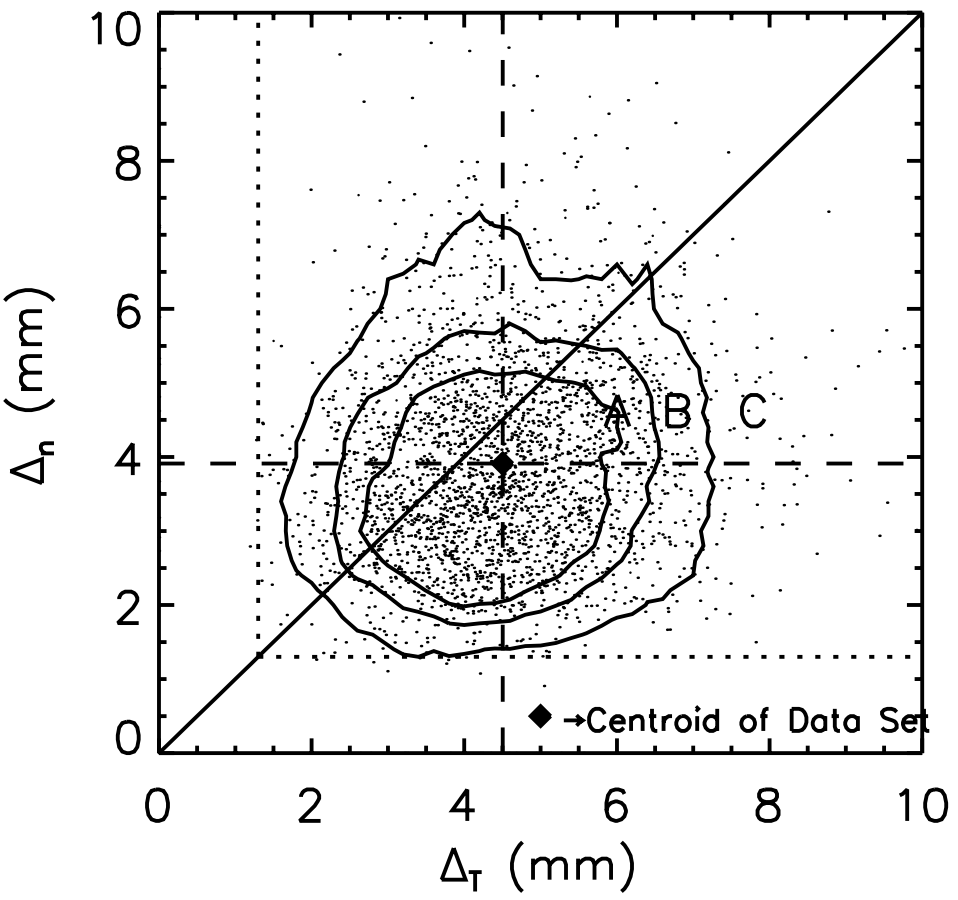

Figure 4-3: Scatterplot illustrating typical range of T_e, n_e pedestal widths, with all types of H-mode included. Contours A, B and C enclose 50, 75 and 95% of the 2,809 data points. Dotted lines signify the nominal lower bound of ETS resolution.

radial extent of these pedestals is typical. Most pedestal widths are in the range of 2–6 mm ($\Delta/a \approx$1–3%), with Δ_T slightly larger, on average, than Δ_n. This is seen by plotting a large number of individual pedestal measurments in Δ_T-Δ_n space, as in Fig. 4-3. Here the density of data is highest in the region where $\Delta_n < \Delta_T$. Fig. 4-4(a) compares the distributions of n_e and T_e pedestal widths for the same data. The difference in the first moments of these distributions is approximately 0.5 mm. A similar scale length characterizes the average difference in radial position of the T_e and n_e pedestals. The distribution of $R_{0,T} - R_{0,n}$, shown in Fig. 4-4(b), is centered about -0.7 mm.The feet of the T_e and n_e pedestals, where the respective profile values tend toward b_T and b_n, both exist near the LCFS, as determined by

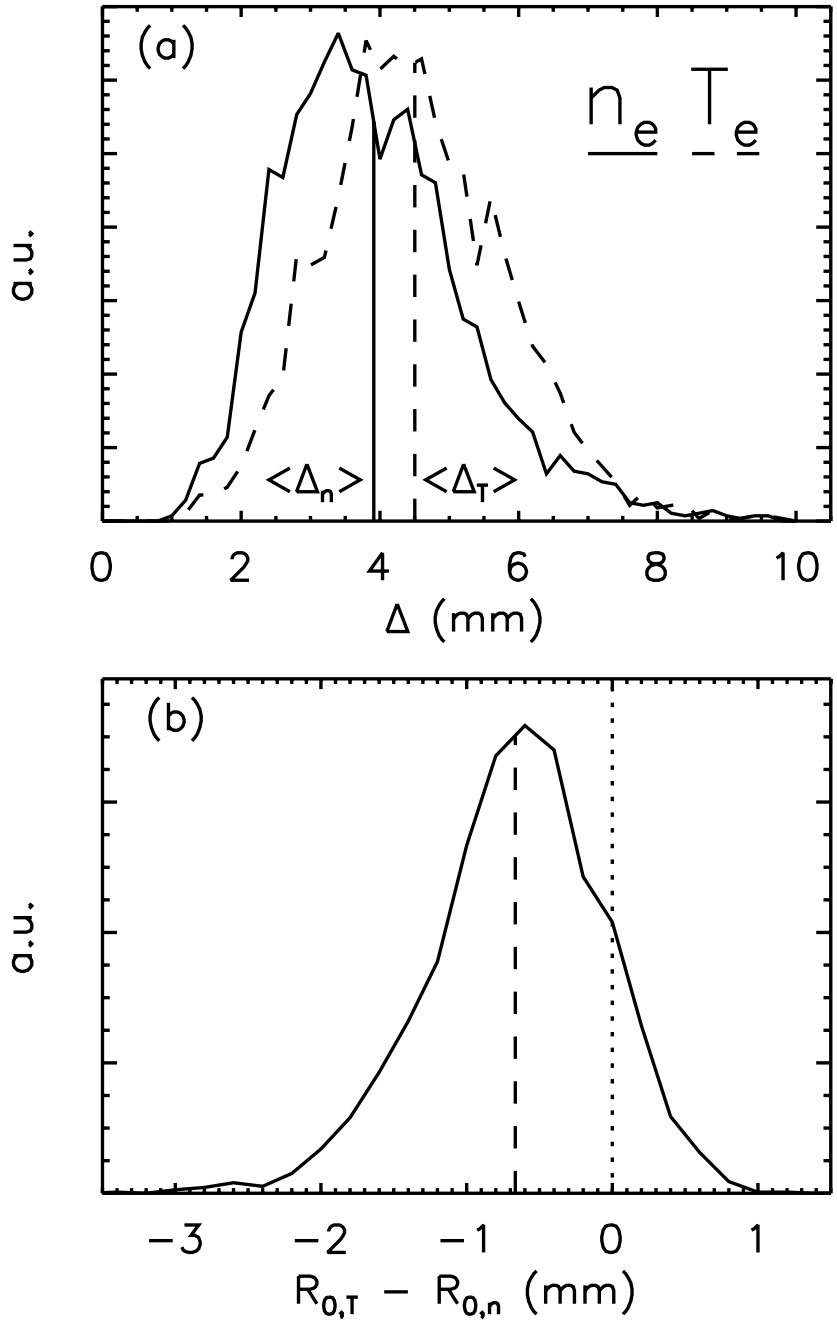

Figure 4-4: (a) Distributions of ETS H-mode data points according to T_e, n_e pedestal widths. All types of H-mode are included. (b) Distribution of the difference in T_e, n_e pedestal radial position ($R_{0,T} - R_{0,n}$), of the same data.

EFIT. The baseline values typically measure 15–30 eV and 3–5$\times 10^{19}$ m^{-3}. Because the T_e profile is monotonic, and because SOL power balance arguments [134] require T_e between 50 and 70 eV at the separatrix of almost all C-Mod plasmas, it is safe to conclude that the foot of the pedestal lies slightly outside the LCFS. Pedestal gradients and quantities at the top of the pedestal in general depend on a number of plasma parameters, and the scalings with these parameters are discussed in some detail in Sec. 5.4. It will be shown that pedestal widths do not respond readily to changes in global plasma paramters, such as toroidal field and current, and thus the spread in Δ_T-Δ_n space is dominated either by random profile fluctuations or hidden variables.

The data plotted in Figs. 4-3 and 4-4 were from discharges within a limited range of triangularity: $0.35 < \delta < 0.45$. It has been seen, however, that varying δ outside of this range has an effect on the pedestal width, and other ETB properties. This effect of shaping on pedestals will be addressed in Sec. 5.6.

4.3 Pedestal characteristics in H-mode regimes

Because the quality of particle transport differs considerably between EDA and ELM-free H-modes, and because the change is attributable to the edge fluctuation known as the QCM (Sec. 1.4.2), it makes sense to examine the variation in edge characteristics in these two regimes, and therefore to explore the operational space for EDA in terms of pedestal parameters. Presumably, existence criteria for the QCM might be determined and the physics governing the mode might be better illuminated.

4.3.1 QCM phenomenology

As mentioned in Sec. 1.4.2, the QCM is an edge fluctuation, which is presumed to give rise to the enhanced particle transport of the EDA regime. The most easily identified component of the fluctuation is that of density, as seen using edge reflectometry or a phase contrast imaging (PCI) diagnostic. [135] Typically the mode appears less than 50 ms after the L-H transition at frequencies of 200 kHz or higher, then decreases in

frequency while the EDA H-mode evolves to its steady state over 100 ms or less. The final QCM frequency is usually in the range of 50–150kHz, and the FWHM of the peak in frequency spectrum is given by $\Delta f/f \approx 0.05$–0.2. This behavior is illustrated by the reflectometry data in Fig. 1-5. Multi-channel reflectometry localizes the QCM to the pedestal region. [136] PCI, on the other hand, measures line-integrated fluctuations along several vertical chords; it provides no spatial localization, though it does give a poloidal wave number $k_\theta \approx 4$ cm^{-1} near $R = 0.68$ m.

In ohmic EDA H-modes, [20] penetrations with the fast scanning Langmuir probes show local fluctuations at about 100 kHz in both electron density and electric potential on the order of 50%, and correlating these fluctations predicts a large radial ion flux. [22] This result demonstrates the role of the QCM in enhancing particle and impurity transport across the pedestal in EDA H-modes. The fully electromagnetic nature of the oscillation was found by mounting a small pick-up coil to the scanning probe head and measuring similar fluctuations in B_P near the LCFS. From the radial decay length of these fluctuations, and from the phase difference between two poloidally spaced Langmuir probes on the scanning probe head, k_θ was determined to be approximately 1.2–1.6 cm^{-1} at the probe location, 10 cm above the midplane. [23]

The general operational conditions favoring EDA have been determined for some time. Experiments show [19] that EDA is favored by both high safety factor at the 95% flux surface ($q_{95} \gtrsim 3.7$) and higher values of triangularity. ($\delta \gtrsim 0.3$). More than magnetic geometry plays a role, however. Discharges at fixed shape and magnetic configuration show a threshold also in the target density $\bar{n}_{e,L}$, which is the line-averaged density prior to the L-H transition, below which H-modes are ELM-free and do not exhibit the QCM. [137] [138] In addition, the amplitude of the mode is seen to increase as $\bar{n}_{e,L}$ is raised above the threshold value (about 1.3×10^{20} m^{-3} in 5.3T, 0.8MA plasmas). [22] Because continuous variation of the QCM amplitude is obtained when transitioning between EDA and ELM-free regimes, the operational boundary between the two modes of operation is often described as "soft".

4.3.2 Guidance from theory and modeling

Much like ELMs, the QCM provides a means of enhanced transport across the LCFS and appears to be brought on by an instability triggered in a certain range of parameter space. Unlike the bursty behavior of ELMs, the QCM produces a continuous level of radial transport, and does not destroy the edge pedestal. Extensive modeling of edge stability in EDA discharges [138] demonstrated that, while the pressure pedestals are above the critical gradient for infinite-n ballooning modes given by ideal MHD, they are stable if a collisionally damped bootstrap current [139] is included. This stabilization is the result of parallel current modifying magnetic shear s in the high-gradient region. In addition, when discharges were examined for instability to intermediate-n coupled peeling-ballooning modes, [65] [140] [141] EDA plasmas in the absence of ELMs were found to be stable to these ideal (*i.e.*, non-resistive) MHD modes as well.

Early on in the study of EDA H-modes, links to drift ballooning modes [142] and resistive ballooning modes [143] were suggested. In work on the diamagnetic stabilization of ideal ballooning modes, [67] previously mentioned in Sec. 2.2.3, Rogers and Drake showed that electromagnetic edge turbulence simulations could produce a coherent feature with characteristics similar to the QCM, and which was made less stable at higher values of q. The criterion for this marginally stable regime is that

$$\Delta/2 < \delta_R \approx \rho_i^{2/3} R^{1/3} \tag{4.1}$$

which, for typical pedestal values, corresponds to a pedestal width of less than a centimeter. Thus, the requirements for the predicted mode are roughly satisfied in experiment.

Turbulence simulations obtained by solving similar equations, but accounting for the realistic diverted C-Mod magnetic equilibrium, also yields a mode consistent with the QCM in terms of both localized frequency and wave number, [24] though the predicted wave number is at the lower limit of what the simulation grid is able to resolve. [144] This "X-point" mode [145] is a modification to resistive ballooning

that accounts for magnetic geometry near the X-point of a diverted geometry. The simulation is reported to yield fluctuation-driven radial particle fluxes consistent with those inferred from probe measurements. [146] This body of work has led to the belief that resistive ballooning is largely responsible for destabilizing the QCM, and much of the analysis of pedestal trends in EDA and ELM-free regimes has been guided by this idea.

4.3.3 Experimental pedestal "phase space"

In order to relate pedestal profiles to H-mode type, ETS data are categorized according to either the presence or the absence of the QC mode, as observed using either reflectometry or phase contrast imaging diagnostics. It is convenient to sort the data by value of edge safety factor q, since this parameter plays a role in determining the strength of the QCM. Because pedestal safety factor is not well defined, values of q_{95} from EFIT equilibria (ranging from 3.2 to 6.5) are used to group the data. Because C-Mod typically runs at $B_T \approx 5.4$ T and often at one of three discrete values of current ($I_P = 0.8, 1.0, 1.2$ MA), the data naturally fall into three clusters corresponding to $q_{95} \approx 3.4, 4.0, 4.8$. Here $q_{95} = 3.7$ is chosen as a convenient boundary between low q operation (the first cluster of data) and high q operation (the second and third clusters). Also important to note is that the plasma shaping is being held roughly constant, with average triangularity chosen in the range of 0.35 to 0.45.

Safety factor, density and temperature

It is sensible to first examine the QCM existence criteria in terms of directly measured pedestal parameters. Measurements of n_e and T_e at "midpoint" pedestal values given by

$$\begin{aligned} n_{e,\mathrm{MID}} &= \frac{h_n + b_n}{2} \\ T_{e,\mathrm{MID}} &= \frac{h_T + b_T}{2} \end{aligned}$$

are plotted in Fig. 4-5 for both low and high values of edge q. The motivation for choosing these mid-pedestal values, as opposed to the values at the top of the pedestal, is the indication from reflectometry and probe measurements that the QCM is localized to the pedestal region. It is reasonable to expect that access to the mode may be determined by the local profile values in the steep gradient region that forms the pedestal, particularly if a gradient drive is important. If, however, the crucial parameters for destabilizing the QCM are the full pedestal values, then these midpoint values are suitable surrogates, given that $n_{e,\mathrm{MID}} \approx n_{e,\mathrm{PED}}/2$ and $T_{e,\mathrm{MID}} \approx T_{e,\mathrm{PED}}/2$.

For low q [Fig. 4-5(a)], H-modes are predominately ELM-free. However, the QCM can exist even at these q, provided mid-pedestal n_e is above 1.3–1.5$\times 10^{20}$ m^{-3}. There is no such density threshold for high q operation [Fig. 4-5(b)], where EDA predominates. For mid-pedestal $T_e \gtrsim 200$ eV, the QCM disappears, leading to ELM-free operation. It is unclear from Fig. 4-5(a) whether a similar T_e threshold exists at low q, high n_e (above dotted line).

Collisionality

When examining edge stability properties, a useful quantity to examine is the collisionality $\nu^\star$, defined as the ratio of the effective electron-ion collison frequency to the bounce frequency,

$$\nu^\star = \frac{\nu_{\mathrm{eff}}}{\nu_b} = \frac{qR\nu_{ei}}{\epsilon^{3/2} v_{\mathrm{th},e}} \tag{4.2}$$

where ϵ is inverse aspect ratio and $v_{\mathrm{th},e}$ is the electron thermal speed. Collisionality is closely related to plasma resistivity, and so higher values of $\nu^\star$ can lead to mitigation of current-driven MHD modes [138] and potentially increase the instability of resistive modes. As noted by Lin, [136] the growth rate for the collisional resistive ballooning mode [143] [147] is sensitive to the parameter $\nu^\star q^2$.

Taken altogether, the tendency for EDA operation at higher q_{95} and pedestal n_e and lower pedestal T_e suggests that edge $\nu^\star$ may play an important role in determining the existence the QCM. At fixed shape, $\nu^\star \propto q n_e \ln\Lambda / T_e^2$, where the Coulomb logarithm varies weakly with n_e, T_e ($\ln\Lambda \approx 15$). Clearly the functional form of $\nu^\star$

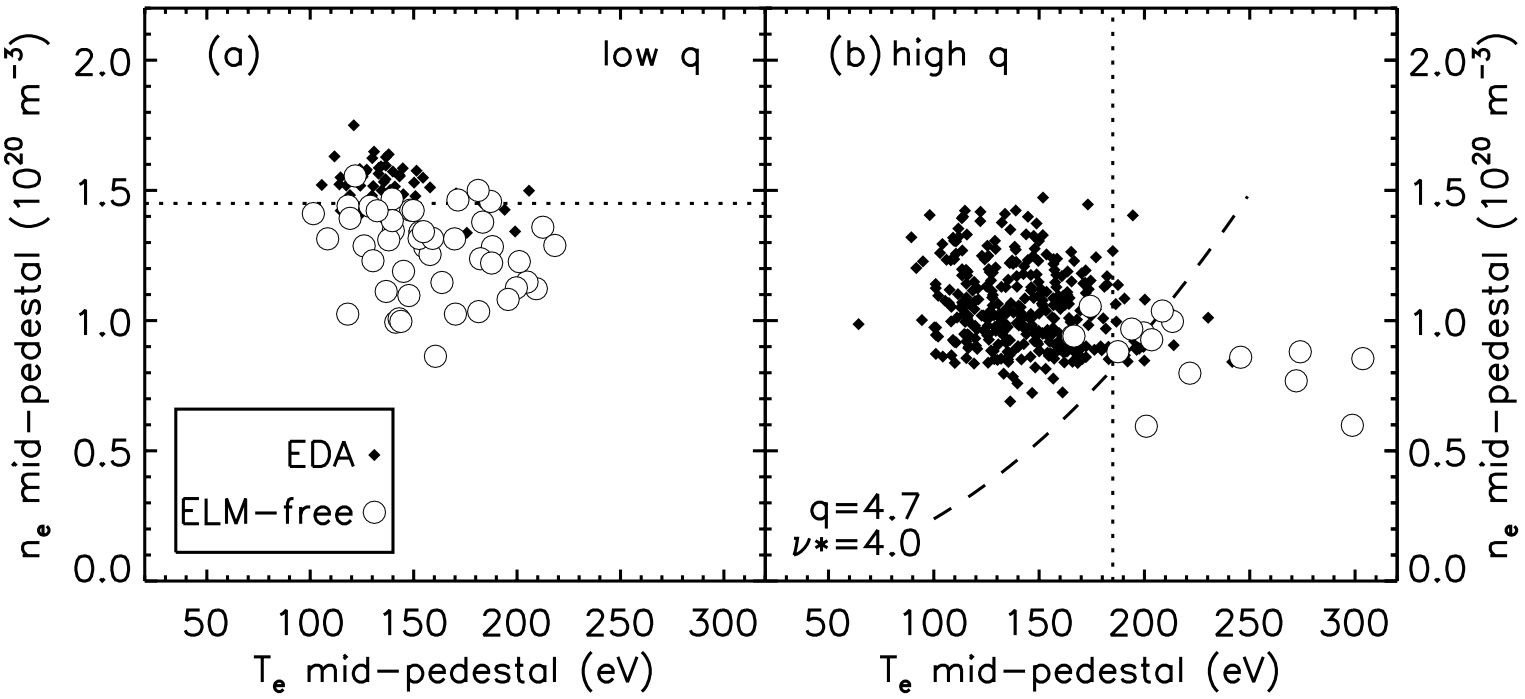

Figure 4-5: Operational space of EDA (diamonds) and ELM-free H-modes (circles). T_e, n_e are taken at the point of maximum pedestal gradient. Data are from (a) low q ($3.2 < q_{95} < 3.7$) and (b) high q ($3.7 < q_{95} < 6.5$) discharges with average triangularity $\delta_{\rm AV}$ between 0.35 and 0.45. Dotted lines represent apparent thresholds for EDA in parameter space. The dashed curve in (b) represents a contour of constant collisionality $\nu^\star$ at fixed q.

gives a higher value in the parameter space occupied by EDA operation. A contour of constant $\nu^\star$ at $q = 4.7$ is represented by the dashed curve in Fig. 4-5(b), roughly denoting a boundary between EDA and ELM-free operation. In the high-q regime, EDA operation occurs mainly at $\nu^\star \gtrsim 4$.

In contrast the EDA points at low q exist at considerably higher values of $\nu^\star$, and it is not possible to construct a parabolic curve of constant collisionality that satisfactorily separates the EDA and ELM-free points in Fig. 4-5(a). A collisionality threshold alone is therefore insufficient to explain the appearance and disappearance of the QCM, at least at low q. If the QCM is classifiable as a collisional resistive ballooning mode, and its growth rate depends strongly on $\nu^\star q^2$, then higher collisionality should be required to obtain the QCM when safety factor becomes low. This is roughly consistent with the results shown in Fig. 4-5.

Pressure gradient

Because the QCM appears ballooning-like, it is natural to ask whether the mode exhibits a pressure gradient threshold, demonstrating an onset at a critical $|\nabla p_e|$ in the same manner as ideal MHD instabilities that lead to ELMs. The data at low q can be plotted in terms of $\nu^\star$ and mid-pedestal electron pressure gradient $|\nabla p_e|_0$, as in Fig. 4-6. The indication from this figure is that at low q and low collisionality, EDA operation is possible at higher values of pressure gradient. As pressure gradient is lowered, it appears that greater collisionality is required for the QCM to exist. This picture differs when examined for the high-q discharges, however. There, the pressure gradients in EDA and ELM-free discharges are very similar, and too few ELM-free data exist to conclude what effect, if any, pressure gradient has on determining the presence of the QCM.

Nonetheless, a very clear boundary between EDA and ELM-free operation can be observed in terms of $\nu^\star$ and the normalized pressure gradient α defined in (2.7) Figure 4-7 represents all data from Fig. 4-5 in α-$\nu^\star$ space, where $\nu^\star$ and q are evaluated at the 95% flux surface, and the maximum pedestal p_e gradient is used to compute α_{PED}. Rendering the data in this way allows us to recast in one phase space the

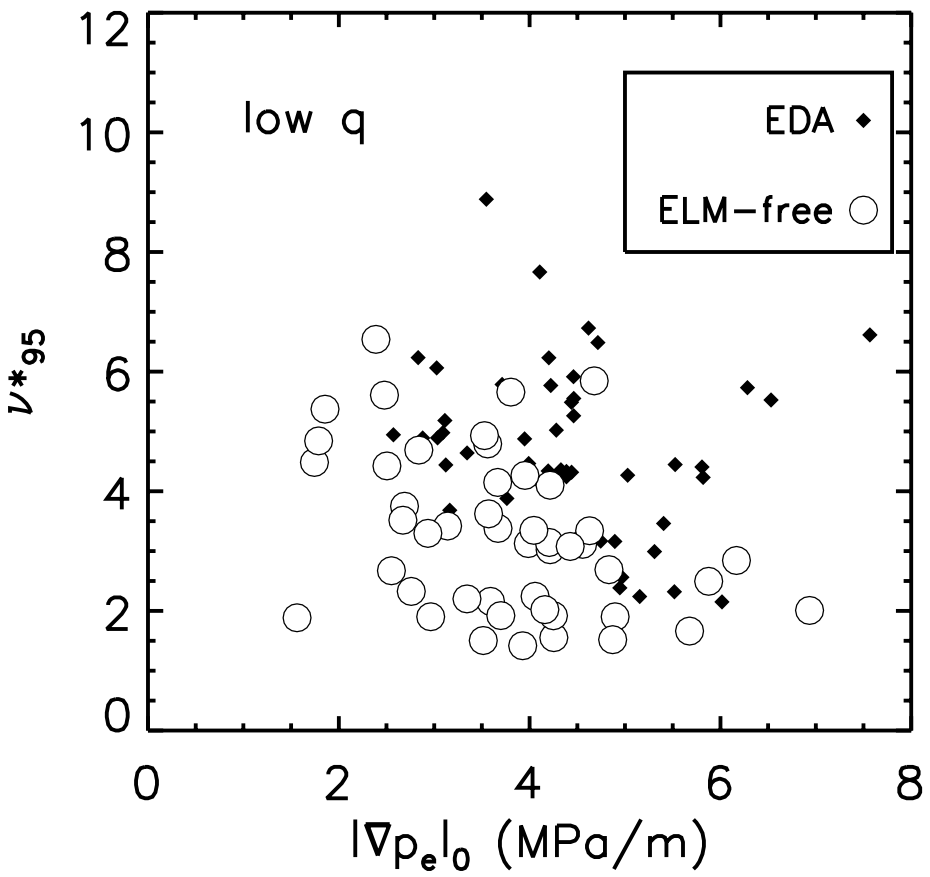

Figure 4-6: EDA (diamonds) and ELM-free H-modes (circles) at low q_{95}. Here collisionality at the 95% flux surface $\nu^{\star}_{95}$ is plotted against maximum electron pressure gradient $|\nabla p_e|_0$. Even at low collisionality, EDA can be obtained with sufficient pressure gradient.

separations between EDA and ELM-free operation evident in both Figs. 4-5(b) and 4-6. The α parameter scales as $q^2 dp/dr$, and so arranging the data in this way is similar to, but not exactly the same as, plotting $\nu^{\star}$ *vs.* q^2. In fact, considerable overlap of EDA and ELM-free data occurs for low q discharges if one fails to account for pressure gradient and simply plots $\nu^{\star}$ *vs.* q^2 or $\nu^{\star}$ *vs.* q. Also, there is virtually no operational boundary to be observed if q is ignored and only $\nu^{\star}$ *vs.* ∇p_e is examined.

Roughly speaking, the data show the QCM pedestals experimentally satisfy the condition $\alpha_{\rm PED}\nu^{\star}_{95} \gtrsim 8$–10. It is not an unreasonable condition, given the state of understanding of the mode. Assuming small variations in pressure gradient, this condition implies $q^2_{95}\nu^{\star}_{95} \gtrsim C$, with C constant. This would be expected if the mode

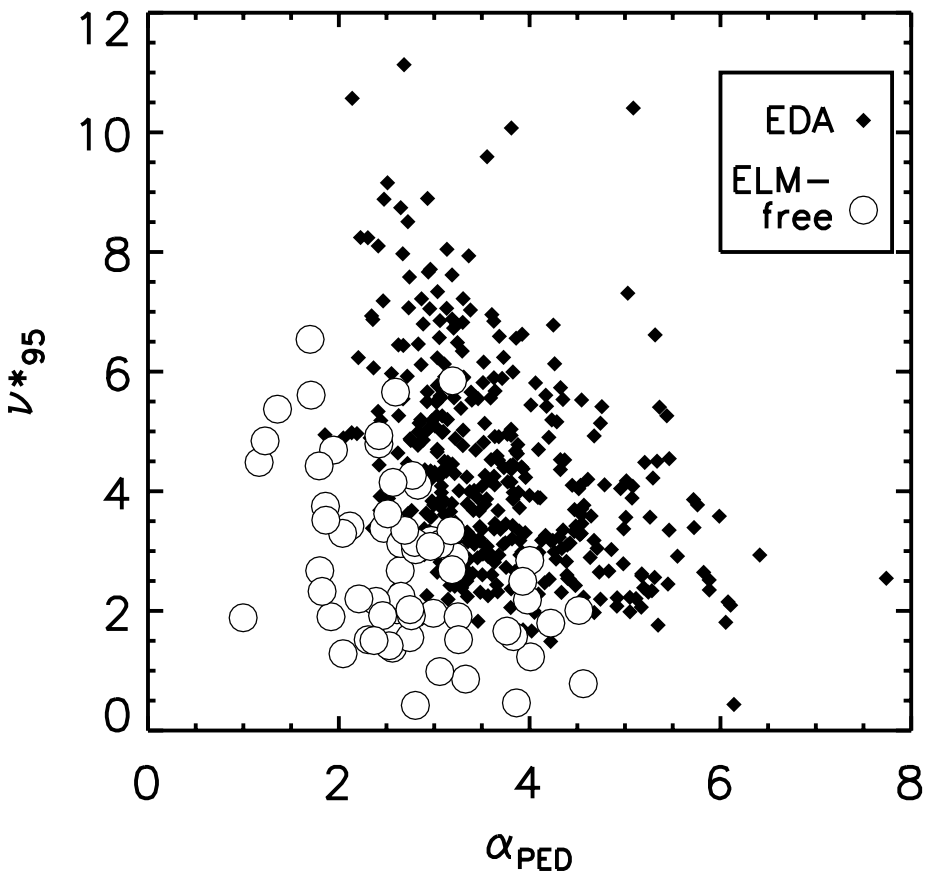

Figure 4-7: Operational space of EDA (diamonds) and ELM-free H-modes (circles). Here $\alpha_{\rm PED}$ is proportional to $(q_{95}^2 R)/B_T^2 \times |\nabla p_e|_0$. Larger values of each quantity favor EDA operation.

onset corresponded to the aforementioned resistive ballooning growth rate increasing above a critical value. In addition, the theory and simulation of drift ballooning modes [67] suggests the existence of a pressure-driven fluctuation, unstable above a particular value of α.

Pedestal widths

There is no clear contrast in pedestal widths between EDA and ELM-free H-modes at low values of q_{95}. However, for high q, Fig. 4-8 shows that widths of T_e, n_e pedestals are larger on average in ELM-free (4–7 mm) than in EDA (2–6 mm). Though the maximum T_e gradient is smaller on average in high q EDA operation than in high

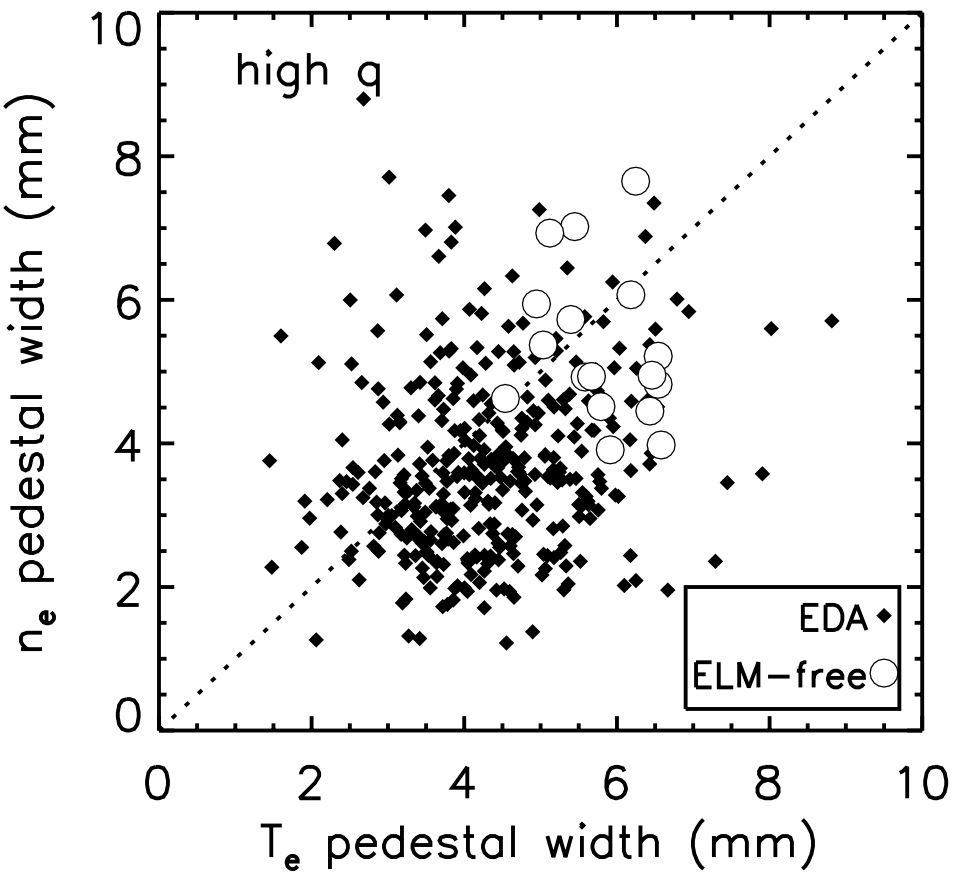

Figure 4-8: Operational Δ_T-Δ_n space of EDA (diamonds) and ELM-free H-modes (circles) in high q discharges with $0.35 < \delta < 0.45$.

q ELM-free operation (due to the requirement that pedestal T_e should not be too large), the n_e gradients are systematically larger than in ELM-free. A consequence of these competing trends is that the p_e gradient at high q shows little variation between EDA and ELM-free discharges, as mentioned above.

This increased $|\nabla n_e|$ occurs despite the enhanced particle transport of EDA, and is counter to the observation that the impurity pedestal, as determined from soft X-ray measurements, widens in EDA H-mode. [97] This result is interesting, as it suggests that a smaller pedestal width is a criterion for QCM growth. This is qualitatively consistent with the modeling of Rogers and Drake [67], which leads to the requirement in (4.1) for formation of the pressure-driven mode having qualities similar to the QCM. For typical C-Mod edge parameters, the maximum Δ for obtaining the theoretical

mode is in the range of 6–10 mm, which corresponds roughly to the ELM-free region in Fig. 4-8.

Chapter 5

Experimental scalings of the pedestal

The next step in pedestal characterization is studying the scaling of pedestal parameters with tokamak operational parameters, as well as the correlation with global confinement. In doing so, one hopes to learn more about the physics setting the widths and heights of the pedestal on C-Mod, thus allowing comparison to modeling and experimental results on other tokamaks. One can then ask, what results are most relevant to the unbuilt, larger, tokamak of the future.

5.1 Data selection

A large amount of scatter exists in the pedestal parameters derived from ETS profiles, which complicates the interpretation of pedestal scalings. There appear to be comparable contributions to the variance in the data from both statistical uncertainty and actual edge fluctuations. To reduce scatter, TS and other plasma measurements are time averaged over periods of finite and constant input ICRF power, P_{RF}, with stored energy, W_P, changing by less than 10%. A data base allows the compilation of these windows, several of which may occur during a plasma discharge, as shown in Fig. 5-1.

Restricting study to steady H-modes leads to the selection of EDA windows only

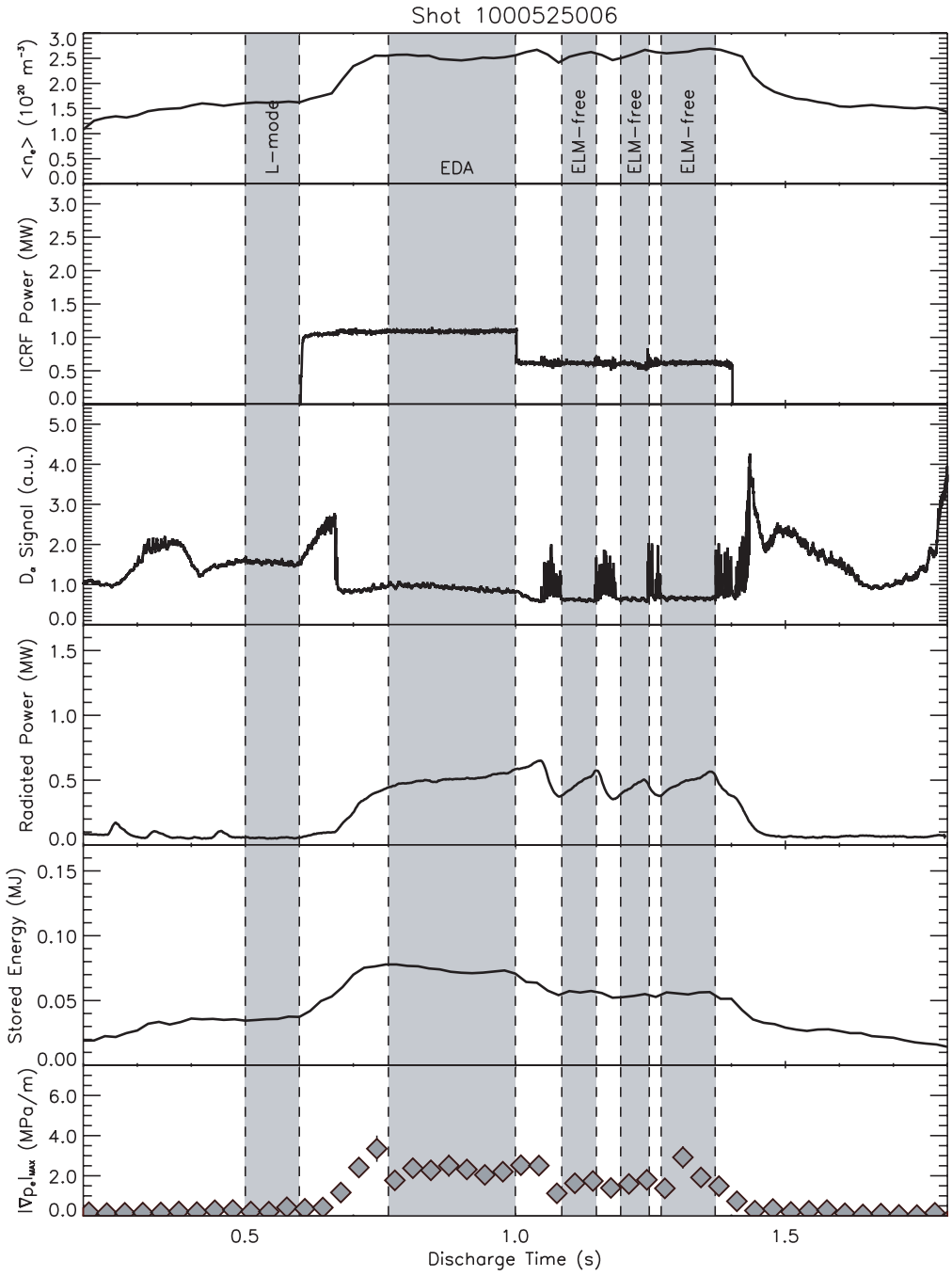

Figure 5-1: Choices of time windows in a scaling study discharge, with sample traces of plasma data: line-averaged density, ICRF power, edge D_α signal, core radiated power, plasma stored energy and maximum edge p_e gradient. A data base is populated with time-averaged quantities during each highlighted period. In this example, one L-mode, one EDA H-mode and three ELM-free H-modes are chosen.

for the pedestal scaling analysis. Discharges that exhibit small ELMs or impurity injections are also excluded from study, since the associated pedestals have significant transient variations. To broaden the range in dependent parameters, dedicated experiments were conducted in which steady discharges were run at various plasma currents ($0.6 < I_P[\mathrm{MA}] < 1.2$), magnetic fields ($4.5 < B_T[\mathrm{T}] < 6.0$), and target densities ($1.3 \times 10^{20} < \bar{n}_{e,L}[\mathrm{m}^{-3}] < 2.6 \times 10^{20}$). Here $\bar{n}_{e,L}$ is defined as the line averaged density immediately prior to transition from L to H-mode. H-modes were triggered and maintained with steady P_{RF}, which was varied in the range of 1–3 MW. RF absorption is on minority H ions, and heating efficiency η_{RF} is known to drop if the minority fraction in the plasma becomes too high. For this reason, when an accurate global power balance is needed for scaling studies, discharges with $n_{\mathrm{H}}/(n_{\mathrm{H}}+n_{\mathrm{D}}) > 0.08$ are excluded. Plasma shaping, as discussed in Sec. 4.2, can affect the pedestal. For these studies only a standard C-Mod equilibrium is considered, having $R = 68$ cm, $a = 22$ cm, elongation $\kappa \approx 1.7$, and average triangularity $\delta_{\mathrm{AV}} \approx 0.4$.

5.2 The pedestal and confinement

TS data support the notion that the edge pedestal acts as a boundary condition to set core transport and confinement. Figure 5-2 shows the characteristic core electron temperature gradient in EDA H-modes, given by $(T_{e,0} - T_{e,\mathrm{PED}})/a$, as a function of pedestal T_e. Here $T_{e,0}$ is measured by the central CTS channel, and $T_{e,\mathrm{PED}}$ is from ETS. The positive dependence of the core thermal gradient on edge T_e corroborates previous results obtained on C-Mod with the use of ECE [11] and suggests the core profile may be determined by a critical gradient scale length for ion temperature, as mentioned in Sec. 1.3. This connection depends on the assumption that T_i, which is not well diagnosed on C-Mod, is tightly coupled to the measured T_e. The validity of this assumption can be checked by calculating the ion-electron thermal equilibration time for typical C-Mod parameters. For a D plasma with $T_e \approx T_i$, this is given by

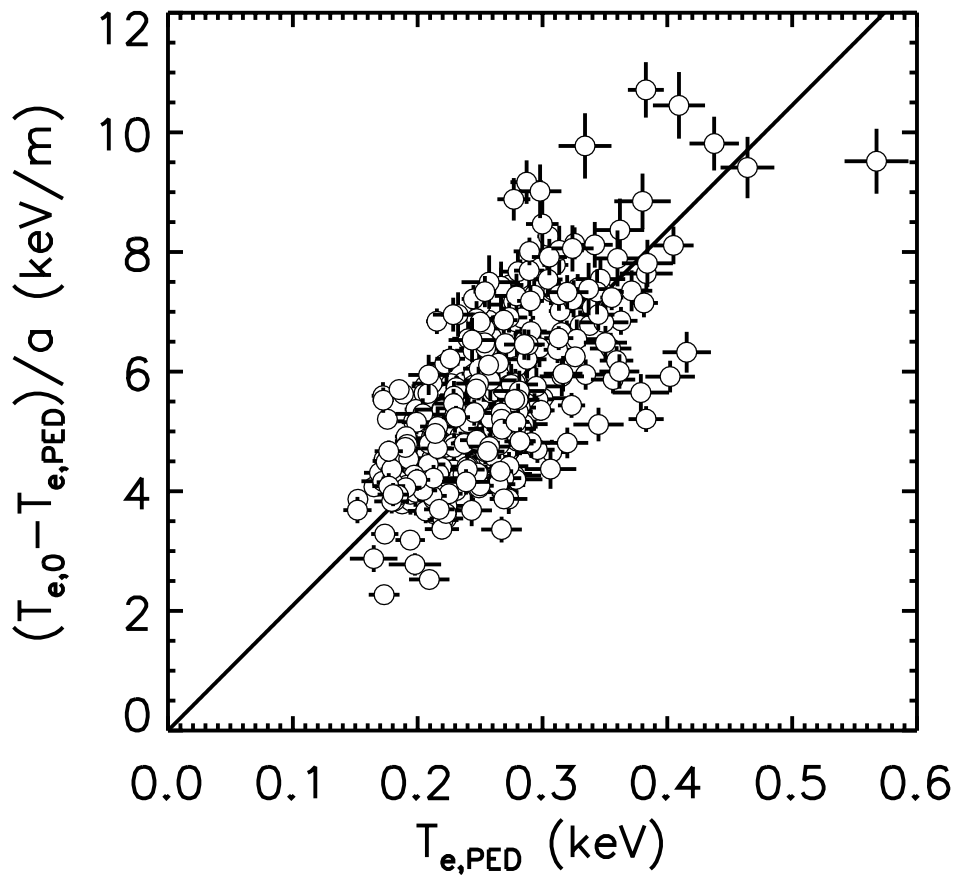

Figure 5-2: Characteristic core T_e gradient *vs.* pedestal T_e in EDA H-modes on C-Mod. Measurements are from the central CTS channel ($T_{e,0}$) and the ETS pedestal fit ($T_{e,\mathrm{PED}}$).

the energy exchange time [6, §14.6]

$$\tau_{ex} = \frac{0.20 \times T_e^{3/2}}{n_e \ln \Lambda} \text{ s} \tag{5.1}$$

where T_e is in units of keV, n_e is in 10^{20} m^{-3}, and the Coulomb logarithm $\ln \Lambda$ is of order 15–20. For a 1 keV, 10^{20} m^{-3} plasma, this equilibration time is about 10 ms, which is smaller than the energy confinement time, and other operational time scales. Small collision times are a general feature of the C-Mod device, largely due to its ability to run at high density, and this can have important consequences. For example, ions and neutrals at the plasma edge undergo rapid thermal equilibration, strongly affecting the neutral transport, as will be discussed in Sec. 6.4.

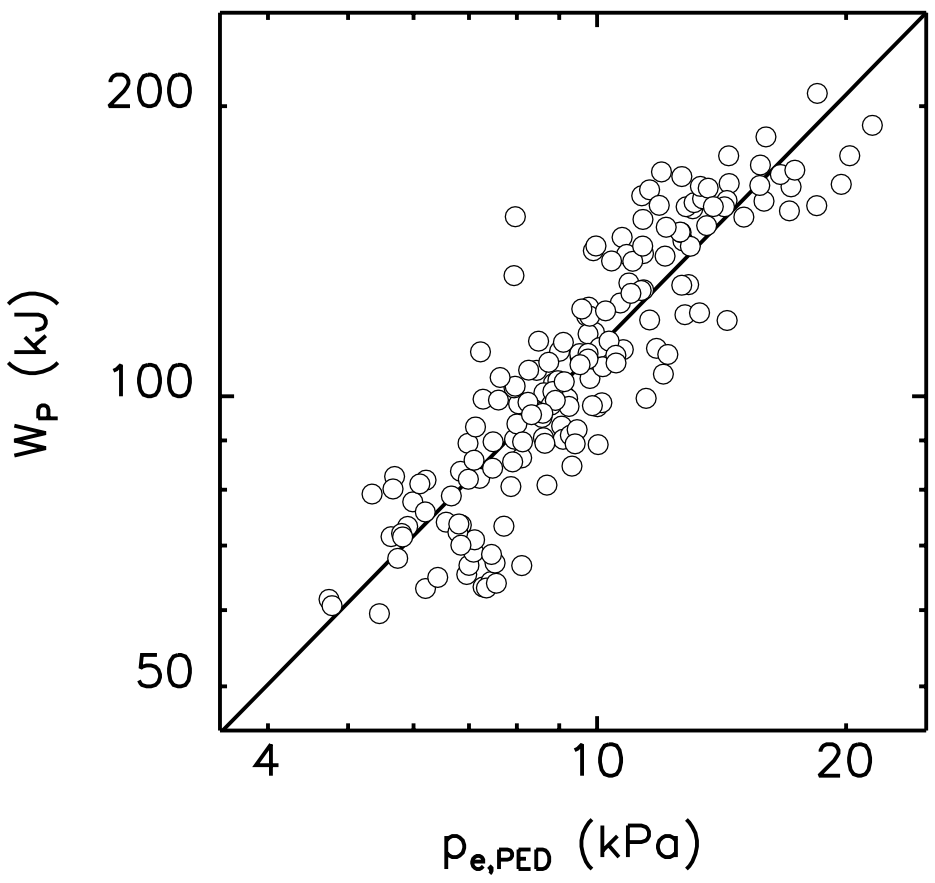

Figure 5-3: Relation of global plasma energy W_P to the electron pressure pedestal $p_{e,\mathrm{PED}}$ in EDA H-modes. The best power law fit to the data gives $W_P \propto (p_{e,\mathrm{PED}})^{0.88\pm0.03}$.

Another important observation is that total plasma stored energy has a nearly linear correlation with pedestal pressure, as shown in Fig. 5-3. The line through the plot represents a power law fit to the data:

$$W_P \propto (p_{e,\mathrm{PED}})^{0.88\pm0.03} \tag{5.2}$$

An implication of this result is that scaling laws for energy confinement time τ_E should be closely linked to scalings of the pressure pedestal with parameters that are externally controlled, such as plasma current, magnetic field, and input power. This will be addressed in Sec. 5.5.

5.3 Operational variations in pedestal parameters

Populating the pedestal database with both parameters from ETS and concurrent data from other diagnostics allows the analysis of trends in pedestal parameters with other plasma parameters. In this way, the knobs needed to optimize plasma pressure and stored energy can be discerned. Also, some of the leading scalings from theory can be evaluated for their validity on C-Mod, provided their terms can be either measured or inferred easily.

5.3.1 Widths

Of particular interest is the manner in which pedestal widths Δ scale with plasma parameters, since, for a given pedestal gradient, Δ determines the pedestal height. On C-Mod, at a fixed shape, there is no clear systematic variation in the electron temperature and pressure pedestal widths Δ_T and Δ_p. This contrasts with results described in Sec. 2.3 from DIII-D and JT-60U, in which width variation with I_P and edge T_e was demonstrated. Theoretical predictions that pedestal width should scale with poloidal ion gyroradius $\rho_{i,\mathrm{pol}}$ (Sec. 2.2.1) do not appear to hold on C-Mod, though the measured Δ are of the same order as $\rho_{i,\mathrm{pol}}$. The apparent lack of correlation is illustrated in Fig. 5-4 for the widths of the T_e, n_e and p_e pedestals. The invariance of T_e and p_e pedestal width is similar to results on ASDEX Upgrade at low triangularity, (Sec. 2.3.4) in which Δ_p is invariant as I_P is scanned and global confinement correlates equally well with either $p_{e,\mathrm{PED}}$ or pedestal ∇p_e.

In contrast to Δ_{T_e} and Δ_{p_e}, there are coarse variations in density pedestal width. Higher pedestal n_e favors larger Δ_n in C-Mod EDA discharges, as shown in Fig. 5-5, a result that contrasts with DIII-D results showing Δ_n scaling with $1/n_{e,\mathrm{PED}}$. (Compare Figs. 2-2 and 5-5.) The indication is that, unlike ∇T_e and ∇p_e, density pedestal gradient varies weakly on C-Mod. This suggests strongly that the width of the density pedestal is not set entirely by the neutral penetration length at the edge, as predicted by the simple neutral fueling model discussed in Sec. 2.2.2. As mentioned, altering the plasma shape can change the pedestal width considerably. Some departures from

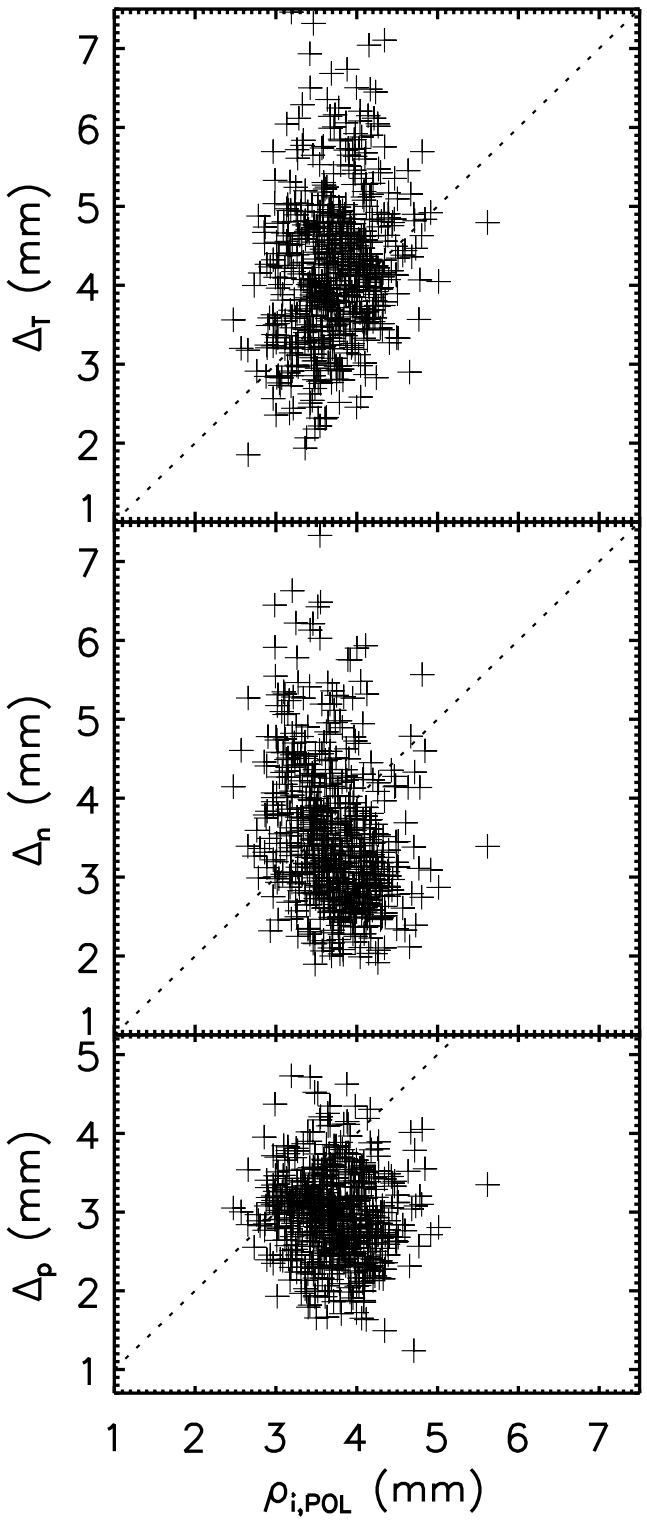

Figure 5-4: C-Mod pedestal widths Δ_T, Δ_n and Δ_p *vs.* poloidal ion gyroradius $\rho_{i,\mathrm{pol}}$, in a variety of EDA H-modes. No significant correlation is observed.

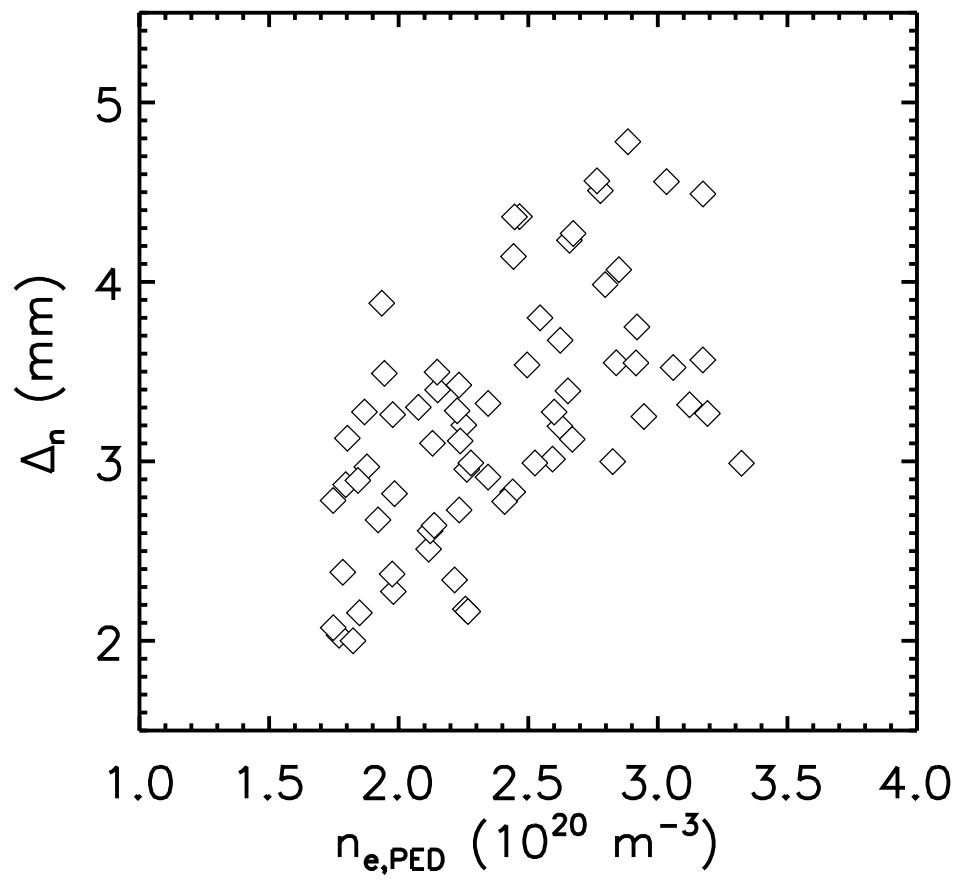

Figure 5-5: Density pedestal width *vs.* n_e atop pedestal in EDA H-modes at 5.4 T and fixed L-mode target density, $\bar{n}_{e,L} \sim 1.6 \times 10^{20}$ m^{-3}. Higher density favors larger Δ_n.

the trend observed in Fig. 5-5 can also be observed by extreme variation in other parameters. In the next chapter, for example, rather wide pedestals will be shown in low density discharges, in which I_P is below 0.6 MA.

5.3.2 Heights and gradients

In contrast to the widths, pedestal heights and gradients show clear scalings with control parameters. Electron temperature profiles from ETS and ECE, obtained in identical discharges with varied levels of ICRF power, are shown in Fig. 5-6. As $P_{\rm RF}$ is raised, the T_e pedestal rises, both in height and gradient, while the width remains constant. The n_e pedestals are unchanged in these three discharges. When other

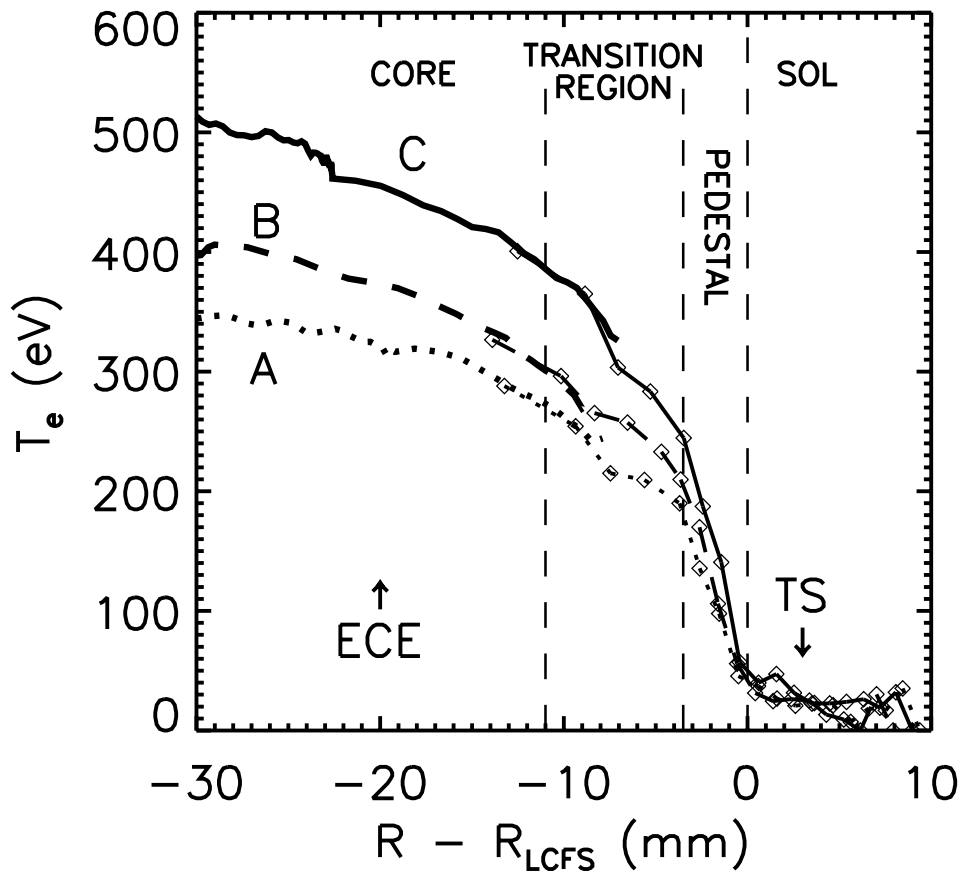

Figure 5-6: Profiles of T_e obtained from ECE (thick curves) and edge TS (diamonds) in 5.4 T, 0.8 MA discharges with varying levels of input ICRF power $P_{\rm RF}$: 1.6 MW (profile A), 2.1 MW (profile B) and 2.7 MW (profile C). Both pedestal electron temperature $T_{e,\rm PED}$ and maximum T_e gradient $|\nabla T_e|_0$ increase with $P_{\rm RF}$.

control parameters are held constant, both pedestal T_e and $|\nabla T_e|_0$ can be scaled in terms of the power passing into the scrape-off layer $P_{\rm SOL}$ given by the power balance relation,

$$P_{\rm SOL} = P_{\rm OH} + \eta_{\rm RF} P_{\rm RF} - P_{\rm RAD} - \frac{dW_P}{dt} \tag{5.3}$$

where both the rate of change in plasma stored energy dW_P/dt and the core radiated power measured from bolometry $P_{\rm RAD}$ are subtracted from the ohmic power $P_{\rm OH}$ and auxiliary heating power $\eta_{\rm RF} P_{\rm RF}$. For each discharge analyzed $P_{\rm SOL}$ is calculated, assuming an ICRF heating efficiency $\eta_{\rm RF} = 0.8$. Figure 5-7 plots the T_e pedestal and its gradient as a function of $P_{\rm SOL}$ for discharges made during pedestal scaling

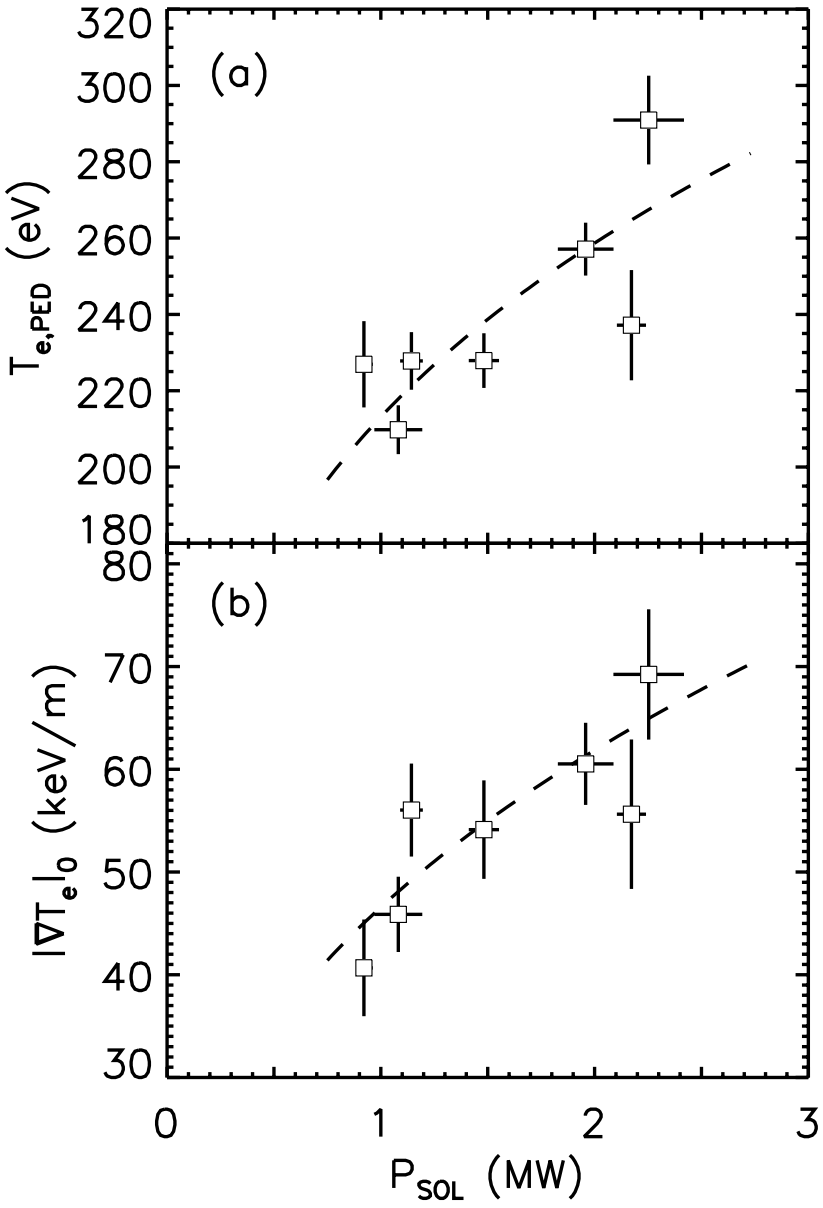

Figure 5-7: Dependence of (a) pedestal temperature and (b) gradient on power passing into the SOL ($P_{\rm SOL}$). Data are from 5.4 T, 0.8 MA discharges with fixed L-mode target density. Dashed curves represent power law fits to these data. In (a), $T_{e,\rm PED} \sim P_{\rm SOL}^{0.3\pm0.1}$, and in (b), $|\nabla T_e|_0 \sim P_{\rm SOL}^{0.4\pm0.1}$.

experiments, all having the same B_T and the same target density $\bar{n}_{e,L}$. It is evident that $T_{e,\mathrm{PED}}$ and $|\nabla T_e|_0$ scale with power in a similar fashion.

5.4 Parametric scalings from multiple regression analysis

The preceding section shows that pedestal trends can be observed as functions of control parameters. To quantify the scalings of pedestal parameters with these other parameters, multiple regression analysis was performed on the data set described above. For simplicity a power law form was chosen for the fitting function:

$$g = C_0(I_P)^{\alpha}(\bar{n}_{e,L})^{\beta}(B_T)^{\gamma}(P_{\mathrm{SOL}})^{\delta} \tag{5.4}$$

where g is a given pedestal parameter. The units of I_P, $\bar{n}_{e,L}$, B_T and P_{SOL} will be [MA], [10^{20} m^{-3}], [T] and [MW] in the scaling expressions derived from this method.

Current, field and power during the H-mode are obvious control parameters for studying the pedestal. Somewhat less obvious is the choice of L-mode target density over H-mode line averaged density $\bar{n}_{e,H}$. This is a suitable choice, since the examined discharges utilize no gas puffing or pumping during H-mode and therefore lack density control following an L-H transition. Essentially, the core n_e during H-mode is a "natural" density that is well correlated with the pedestal density: $n_{e,\mathrm{PED}} \approx 0.8 \times \bar{n}_{e,H}$. The experimental observation is that higher target densities yield higher values of $\bar{n}_{e,H} \propto n_{e,\mathrm{PED}}$. This is reasonable, since the magnitude of the ionization source that fuels the H-mode edge is determined largely by the densities of neutral and atomic hydrogen in the SOL, which in turn have a positive dependence on the rate of fueling needed to obtain the original L-mode density.

To determine the significance of each independent parameter in determining the power law scaling, an additional term F-test is performed, [148] allowing computation of the probability $P_{F,\mu}$ that a given exponent μ ($\mu \in \alpha, \beta, \gamma, \delta$) is representative of a physical correlation, rather than being a result of random scatter. Table 5.1 contains

Dependent Parameter	Number of points	R^2	exponent of I_P: α	$P_{F,\alpha}$	exponent of $\bar{n}_{e,L}$: β	$P_{F,\beta}$	exponent of B_T: γ	$P_{F,\gamma}$	exponent of P_{SOL}: δ	$P_{F,\delta}$
Δ_n	175	0.24	0.79±0.14	>0.99	0.14±0.14	0.67	-0.99±0.29	>0.99	-0.01±0.08	0.10
Δ_T	144	0.03	0.21±0.15	0.84	-0.17±0.15	0.72	-0.05±0.28	0.14	0.15±0.08	0.93
Δ_p	116	0.09	0.14±0.11	0.77	0.28±0.13	0.97	-0.36±0.22	0.89	0.01±0.06	0.06
$n_{e,\mathrm{PED}}$	175	0.72	0.94±0.07	>0.99	0.40±0.06	>0.99	-0.46±0.14	>0.99	-0.02±0.04	0.50
$T_{e,\mathrm{PED}}$	144	0.63	0.95±0.10	>0.99	-0.78±0.11	>0.99	0.80±0.19	>0.99	0.64±0.06	>0.99
$p_{e,\mathrm{PED}}$	116	0.76	1.97±0.12	>0.99	-0.567±0.13	>0.99	0.18±0.22	0.58	0.48±0.06	>0.99
$\lvert\nabla n_e\rvert_0$	175	0.26	0.89±0.13	>0.99	0.01±0.13	0.05	-0.01±0.29	<0.01	-0.07±0.07	0.66
$\lvert\nabla T_e\rvert_0$	144	0.54	1.18±0.13	>0.99	-0.83±0.13	>0.99	0.72±0.23	>0.99	0.53±0.07	>0.99
$\lvert\nabla p_e\rvert_0$	116	0.74	2.03±0.13	>0.99	-0.90±0.14	>0.99	0.44±0.24	0.93	0.46±0.07	>0.99

Table 5.1: Results of multiple regression analysis for pedestal parameters as functions of control parameters, assuming scalings of the form $f = (I_P)^\alpha(\bar{n}_{e,L})^\beta(B_T)^\gamma(P_{\mathrm{SOL}})^\delta$. Included for each exponent μ is the probability $P_{F,\mu}$ that μ is not due merely to random variation, computed using the F-test for additional fitting parameters. [148]

the results of the regression performed on the pedestal widths, heights, and gradients. Listed are the number of points used in each fit, the multiple correlation coefficient R^2, the value of each exponent with its statistical uncertainty, and each $P_{F,\mu}$. For a scaling to be considered significant, its $P_{F,\mu}$ must be larger than 0.95.

Results of tests for pedestal width scalings are shown in the first three rows of Table 5.1. The analysis demonstrates that the electron temperature and pressure pedestal widths are largely independent of control parameters. The only correlation of these two widths meeting our criterion for significance is that of Δ_p with $\bar{n}_{e,L}$, and the dependence is unconvincing in light of the very low value of the associated R^2. The n_e width demonstrates a more significant correlation with $(I_P)^{0.8}(B_T)^{-1.0}$, though the R^2 value is relatively low and indicative of considerable scatter in the data set. Despite the scatter, the form of this scaling suggests a correlation between Δ_n and the inverse of edge safety factor. Indeed, regression on 100 points with constant target density using q_{95} as the sole dependent parameter yields $\Delta_n \propto q_{95}^{(-0.90\pm0.15)}$, with $R^2 = 0.27$. This trend is illustrated in Fig. 5-8.

Though pedestal widths generally lack clear correlations with plasma parameters, this could be a consequence of both large scatter in the ETS data set and the somewhat restricted range of Δ at the standard C-Mod shape. There are considerable effects on pedestals due to shaping, to be discussed in Sec. 5.6. In contrast, scanning I_P, $\bar{n}_{e,L}$, B_T, and P_{SOL} demonstrates varying degrees of effect on the values atop each pedestal, as shown by rows 4–6 of Table 5.1. For example, though power is strongly correlated with pedestal T_e, there is virtually no correlation between P_{SOL} and $n_{e,\mathrm{PED}}$.

5.4.1 Density pedestal

The effects on n_e from scanning the other three control parameters is exhibited both in Table 5.1 and in Fig. 5-9. In each panel of the figure, two parameters are nominally fixed, while the third density control parameter is varied. Values of n_e at both the top and base of the pedestal are plotted. Because the n_e baseline is typically at the lower limit of the dynamic range of ETS, it cannot be determined satisfactorily whether the baseline can be correlated with the scanned parameters. The top of the pedestal,

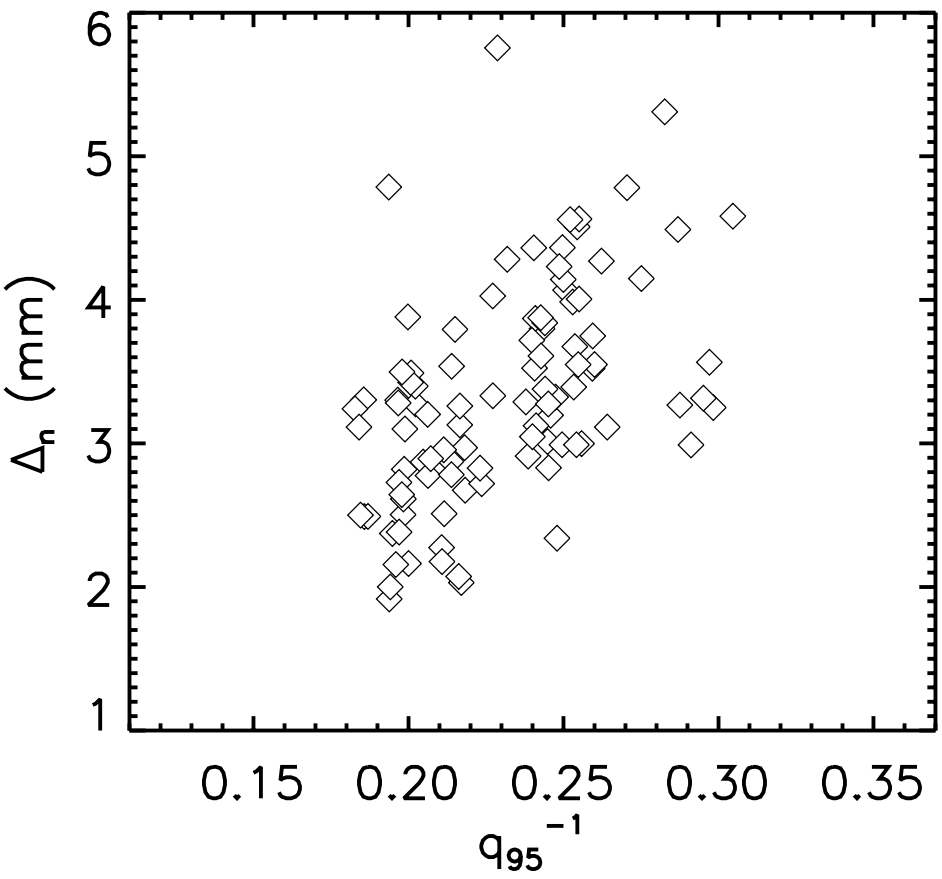

Figure 5-8: Density pedestal width *vs.* inverse edge safety factor $1/q_{95}$ in EDA H-modes with fixed L-mode target density, $\bar{n}_{e,L} \sim 1.6 \times 10^{20}$ m^{-3}. Higher q favors smaller Δ_n.

however, scales with I_P [5-9(a)], $\bar{n}_{e,L}$ [5-9(b)] and $1/B_T$ [5-9(c)].

Repeating the power law regression of Table 5.1, row 4 with the insignificant parameter $P_{\rm SOL}$ removed from consideration, a predictive scaling is found:

$$n_{e,\rm PED}[10^{20}\ \rm m^{-3}] = 4.6 \times I_P^{(0.95\pm0.06)} \bar{n}_{e,L}^{(0.39\pm0.06)} B_T^{(-0.46\pm0.14)} \tag{5.5}$$

having $R^2 = 0.72$. The goodness of this fit is illustrated in Fig. 5-10. Some scatter remains, but to lowest order the predictive scaling reproduces the experimental measurement of $n_{e,\rm PED}$. What is instantly notable about (5.5) is the nearly linear scaling with plasma current. The dependence on I_P is the strongest, and has the smallest fractional uncertainty. Operationally this means that the hardiest knob for

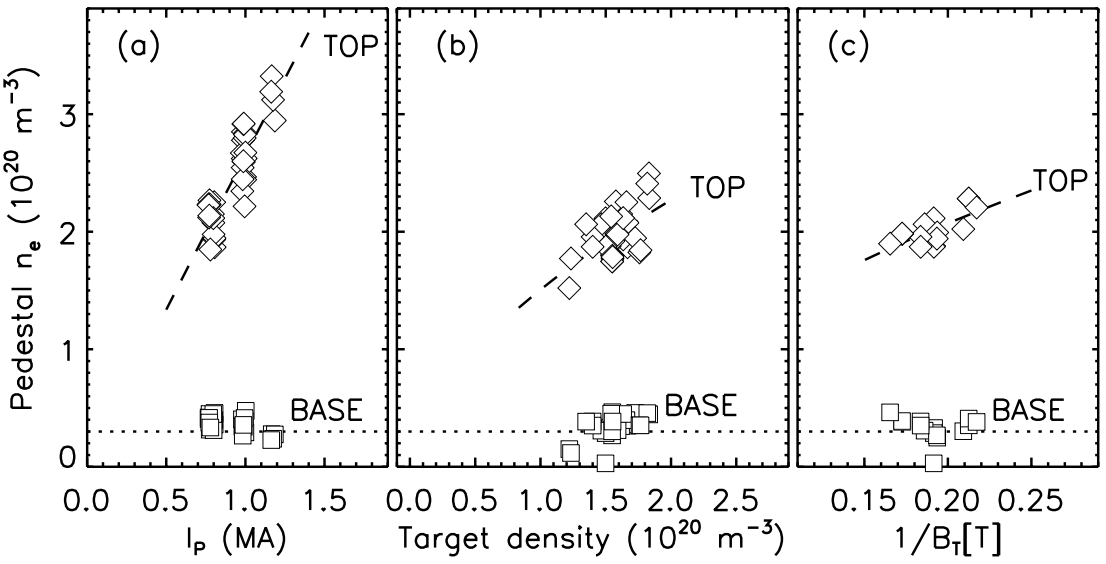

Figure 5-9: Pedestal n_e, at top (diamonds) and base (squares) of pedestal, *vs.*: (a) plasma current I_P, with fixed toroidal field, $B_T = 5.4$ T and fixed L-mode target density, $\bar{n}_{e,L} \approx 1.5 \times 10^{20}$ m^{-3}; (b) $\bar{n}_{e,L}$, with fixed $B_T = 5.4$ T, $I_P = 0.8$ MA; (c) $1/B_T$, with fixed $I_P = 0.8$ MA, $\bar{n}_{e,L} \approx 1.5 \times 10^{20}$ m^{-3}. Dotted line is the estimated lower limit of the ETS dynamic range.

changing the pedestal density is the programmed plasma current, and varying the other quantities produces a very weak variation in $n_{e,\mathrm{PED}}$.

The $n_{e,\mathrm{PED}} \propto I_P$ scaling is robust, but the physics of it is not well understood. The relation suggests a strong connection between particle confinement in the pedestal and a quantity related to current, such as edge poloidal field, or safety factor. The particle transport will be examined in more detail in Ch. 6. It is worth noting that the Δ_n scaling mentioned above is qualitatively similar to that of $n_{e,\mathrm{PED}}$ on current and field, though the exponents differ somewhat. If the combined plasma transport and neutral fueling processes in the pedestal force roughly constant n_e gradients to exist throughout the typical range of EDA plasmas, then it is natural that $n_{e,\mathrm{PED}} \propto \Delta_{n_e}$.

The weakly positive scaling with $\bar{n}_{e,L}$ can be understood in terms of the initial fueling source on which the H-mode is allowed to draw. As mentioned previously, the H-modes under study are not puffed or pumped, and therefore fuel only from deuterium recycling from walls and limiters. This balance is determined by the ini-

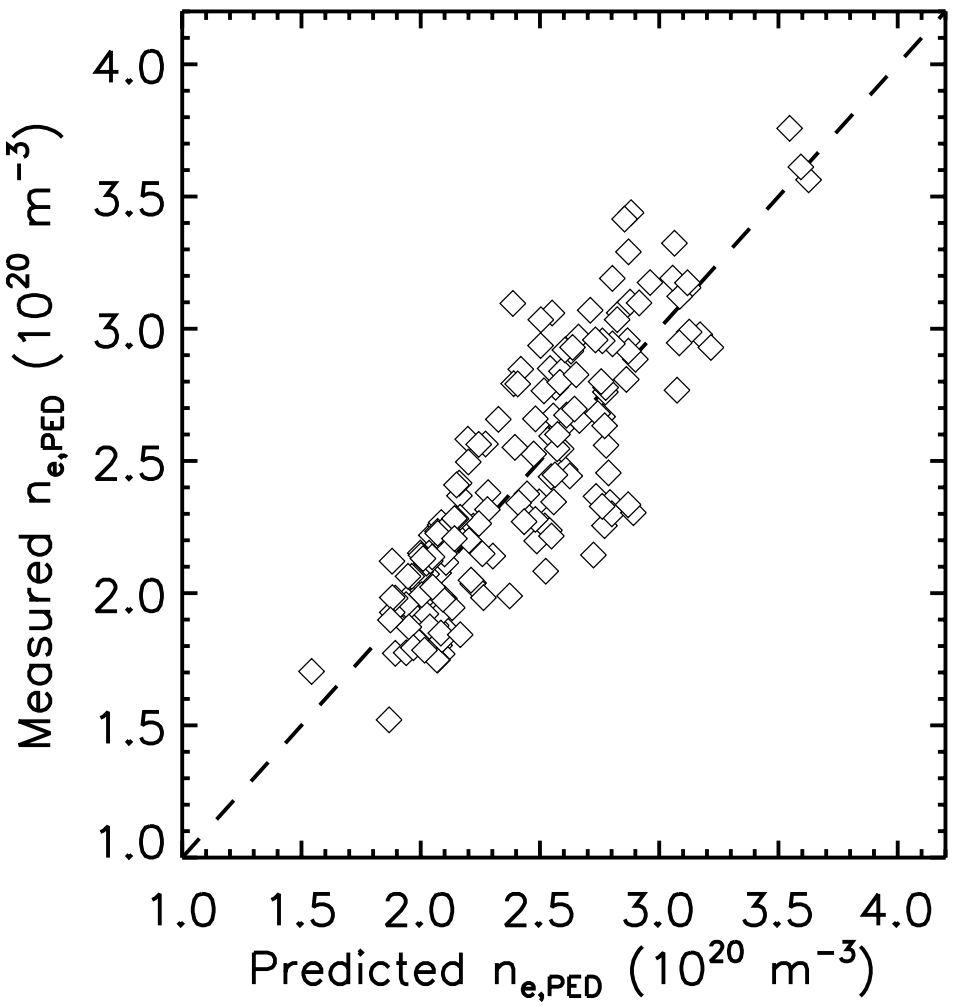

Figure 5-10: Experimental values of pedestal n_e plotted against values predicted by the empirical scaling of (5.5).

tial condition set by maintaining a given target density. The scaling in (5.5) is not necessarily complete, of course, since the physics governing the n_e pedestal is modeled in only the simplest manner by a simple power law representation using four control parameters. However, it gives some guiding insight into how to conduct further examinations of the density pedestal. These experiments will be discussed in the next chapter.

5.4.2 Temperature pedestal

In Sec. 5.3.2 it was shown that the T_e pedestal and gradient depend strongly on power through the plasma edge. In fact they exhibit significant variation with each of the control parameters, as shown by the coefficients in rows 5 and 8 of Table 5.1. Not surprising is that for a given $P_{\rm SOL}$, lower target density results in higher $T_{e,\rm PED}$. Also, there is an linear dependence of $T_{e,\rm PED}$ on I_P for a given $P_{\rm SOL}$. This additional I_P dependence implies that the effect of plasma current on the T_e pedestal is not explained solely by the contribution of ohmic power. The T_e pedestal also correlates with B_T, which may be a consequence of changing the ICRF resonance location ($R_{\rm RF} \propto 1/B_T$) and the resulting alteration to the power deposition profile. Over the range of B_T examined here, the resonance of 80 MHz RF is located at $(R_{\rm RF} - R_0)/a$ from -0.5 to 0.3. From Table 5.1, row 5, the predictive scaling on control parameters for the T_e pedestal is

$$T_{e,\rm PED}[\rm eV] = 83 \times I_P^{(0.95\pm0.10)} \bar{n}_{e,L}^{(-0.78\pm0.11)} B_T^{(0.80\pm0.19)} P_{\rm SOL}^{(0.64\pm0.06)} \tag{5.6}$$

with $R^2 = 0.63$. Figure 5-11 illustrates the correlation of measured to predicted values. When the dependent parameter $\bar{n}_{e,L}$ is replaced with $n_{e,\rm PED}$, the scaling obtained is similar, but with a somewhat poorer $R^2 = 0.54$:

$$T_{e,\rm PED}[\rm eV] = 154 \times I_P^{(1.13\pm0.18)} n_{e,\rm PED}^{(-0.50\pm0.13)} B_T^{(0.49\pm0.22)} P_{\rm SOL}^{(0.52\pm0.06)} \tag{5.7}$$

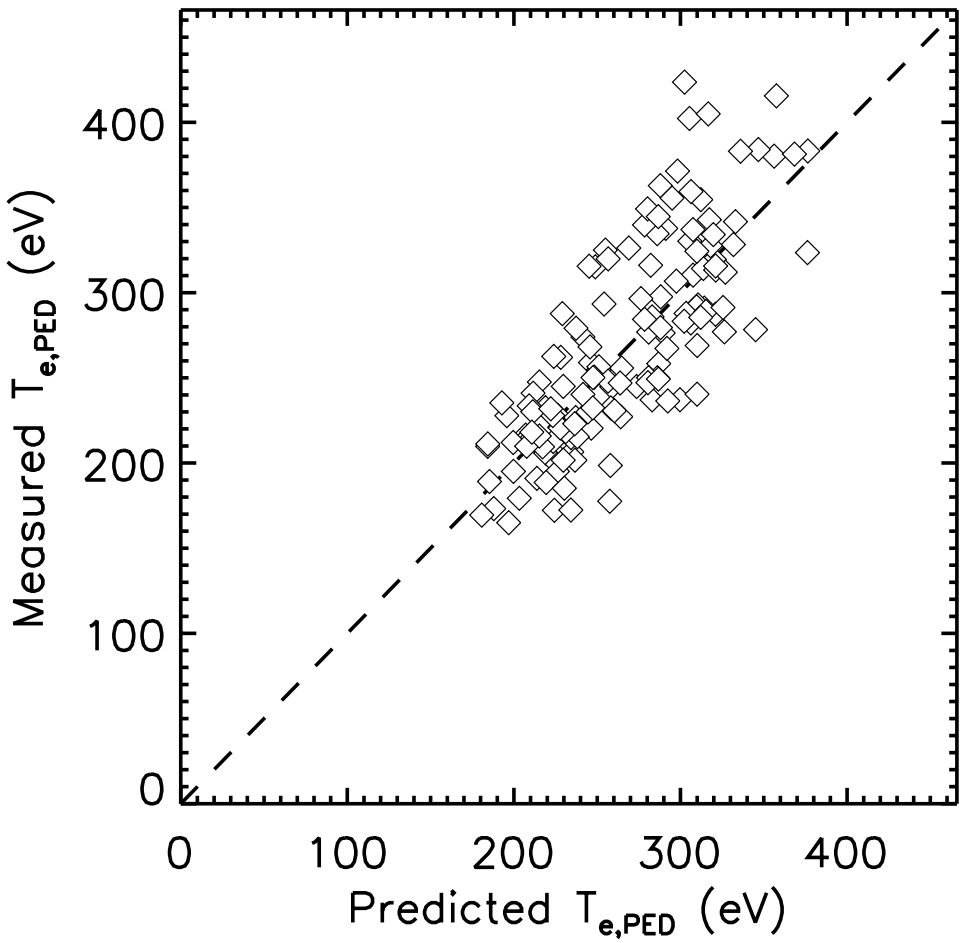

Figure 5-11: Experimental values of pedestal T_e plotted against values predicted by the empirical scaling of (5.6).

As a consequence of the invariant pedestal width, qualitative statements about the $T_{e,\mathrm{PED}}$ scalings apply equally well to $|\nabla T_e|_0$. The two parameters scale in almost exactly the same manner.

5.4.3 Pressure pedestal

Because $p_{e,\mathrm{PED}} \sim n_{e,\mathrm{PED}} \times T_{e,\mathrm{PED}}$, one would expect the p_e pedestal scalings to have characteristics in common with the n_e and T_e scalings. This is the case, as a clear correlation with current, power and target density is observed, while the toroidal field effects seem largely to cancel. Repeating the regression of Table 5.1, row 6 without

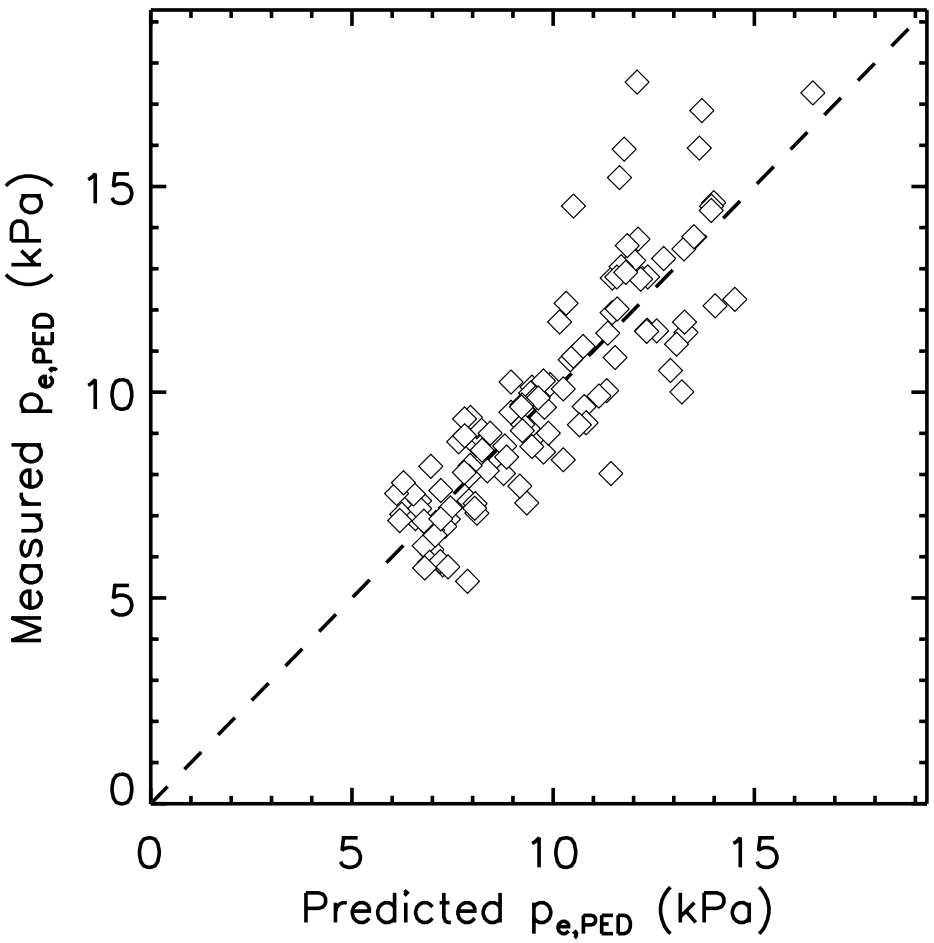

Figure 5-12: Experimental values of pedestal p_e plotted against values predicted by the empirical scaling of (5.8).

B_T gives

$$p_{e,\mathrm{PED}}[\mathrm{kPa}] = 9.4 \times I_P^{(1.98\pm0.11)} \bar{n}_{e,L}^{(-0.56\pm0.13)} P_{\mathrm{SOL}}^{(0.48\pm0.06)} \tag{5.8}$$

with $R^2 = 0.76$. This relatively good fit is shown in Fig. 5-12. Similar exponents result for the $|\nabla p_e|_0$ scaling. Pressure gradient data from a current scan at constant target density are plotted in Fig. 5-13 *vs.* P_{SOL}, and have been grouped according to I_P. The strong scaling with current demonstrated by the plot is unsurprising, given the linear dependence on current of both $n_{e,\mathrm{PED}}$ and $T_{e,\mathrm{PED}}$.

It is interesting to note that an I_P^2 dependence would be expected in a pedestal limited by ideal ballooning modes, as in type I ELM-ing discharges on JET ASDEX

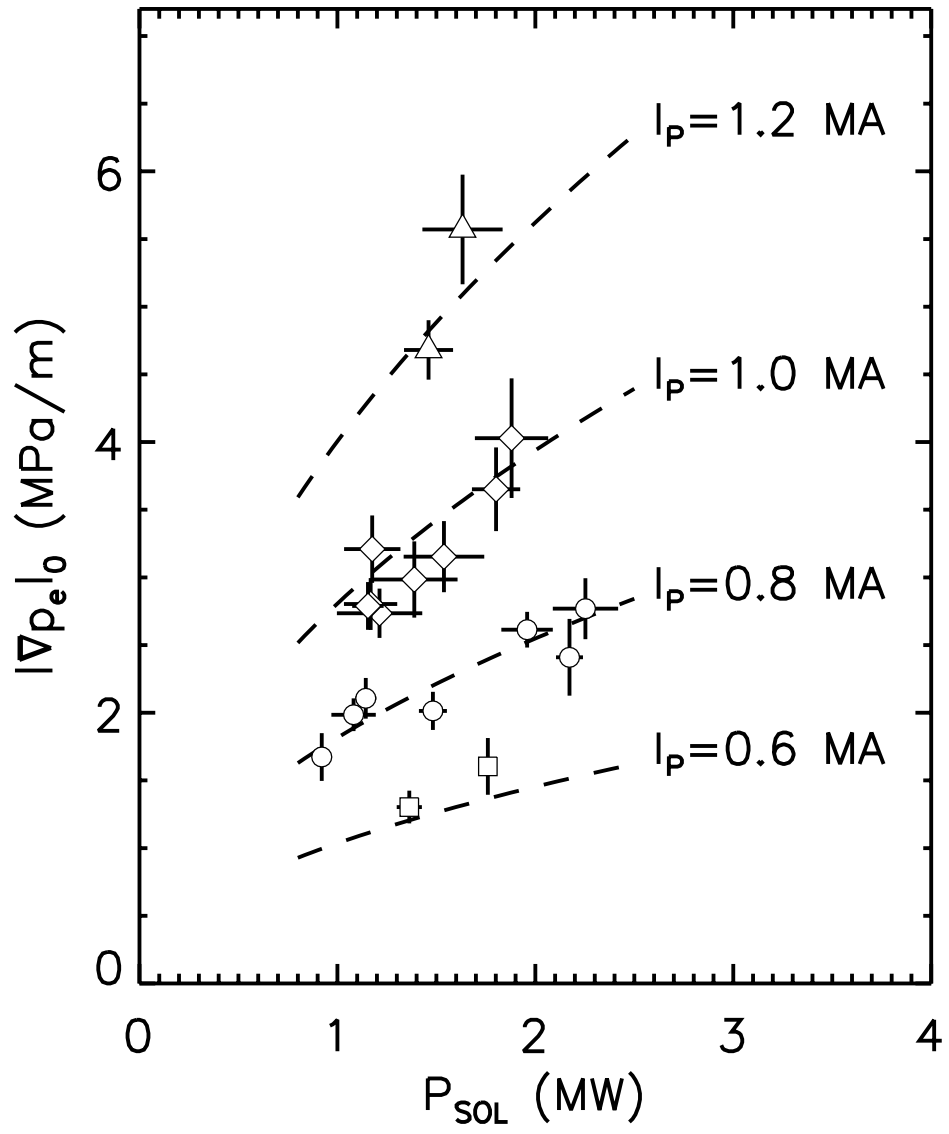

Figure 5-13: Pedestal electron pressure gradient in EDA pedestals *vs.* $P_{\rm SOL}$ at four distinct values of I_P: 0.6 (squares), 0.8 (circles), 1.0 (diamonds), and 1.2 MA (triangles). The scaling with power is similar to that of the T_e pedestal, while the scaling with current is quite strong. Dashed curves represent the empirical scaling law, $|\nabla p_e|_0 \propto I_P^{(2.0)} P_{\rm SOL}^{(0.5)}$, evaluated at the four noted values of I_P.

Upgrade. (See Sec. 2.3.) As discussed in Sec. 4.3.2, typical EDA pedestals are believed to have bootstrap current stabilization of ideal high-n ballooning modes as well as intermediate-n peeling-ballooning modes. However, the model of Rogers and Drake [67] discussed in previous chapters gives a pressure pedestal scaling as I_P^2, even with ballooning modes stabilized by short pedestal scale lengths. The expression in (5.8) and the curves in Fig. 5-13 demonstrate that the pedestal ∇p does not hit a hard limit dictated by I_P alone. The gradient can be increased at a given current by increasing the power flux at the LCFS. A possible speculation, inspired by the results of Sec. 4.3.3 is that in EDA H-mode, the pedestal tends to maintain a nearly constant value of $\nu^\star \alpha_{\rm MHD}$, rather than $\alpha_{\rm MHD}$ alone. This allows pressure gradient to rise along with temperature as more power is inserted into the plasma.

The scaling $p_{e,\rm PED} \sim P_{\rm SOL}^{1/2}$ is directly related to the similar scaling of the temperature pedestal. Equation 5.8 reveals too that the strong negative scaling of $T_{e,\rm PED}$ with target density (5.6) is not overcome by the weaker positive scaling of $n_{e,\rm PED}$ with $\bar{n}_{e,L}$. (5.5) Physically, this reflects the tokamak heat loss terms growing larger at higher density, and the plasma cannot support a very high T_e pedestal without additional power. Therefore, for a given current and input power, the pressure pedestal actually falls with increasing target density.

5.5 Confinement

Above it was stated that total plasma stored energy scales linearly with $p_{e,\rm PED}$, and in fact a power law similar to (5.8) is obtained for W_P:

$$W_P[\rm kJ] = 94 \times I_P^{(2.08\pm0.07)} \bar{n}_{e,L}^{(-0.43\pm0.08)} P_{\rm SOL}^{(0.75\pm0.04)} \tag{5.9}$$

with $R^2 = 0.92$. The confinement time τ_E can also be determined from the multivariable regression, giving

$$\tau_E[\rm ms] = 19 \times I_P^{(1.31\pm0.01)} \bar{n}_{e,L}^{(-0.37\pm0.09)} B_T^{(0.54\pm0.14)} P_{\rm SOL}^{(0.09\pm0.03)} \tag{5.10}$$

with $R^2 = 0.78$. The scatter in the power law fit to τ_E is large relative to the W_P fit, and there does not seem to be a simple relationship between the expressions in (5.9) and (5.10). This is because $\tau_E = W_P/P_{\rm LOSS}$ in steady state, where $P_{\rm LOSS} = P_{\rm SOL}+P_{\rm RAD}$. Because the functional dependence of $P_{\rm RAD}$ is not simply expressed in terms of the other parameters, and because the radiated power fraction can be considerable (up to 60% in the discharges considered, and strongly dependent on density), attempts to determine scalings of confinement time meet with less clear results than for scaling W_P alone.

Furthermore, it is not entirely straightforward to compare these results to commonly used cross-machine confinement scalings, due to differing choices of fitting parameters. Power laws determined from analysis of the International Tokamak Experimental Reactor (ITER) confinement database [149] have as a dependent parameter the line averaged H-mode density $\bar{n}_{e,H}$ rather than $\bar{n}_{e,L}$, and use total power loss $P_{\rm LOSS}$ instead of $P_{\rm SOL}$. Performing a fit with these parameters results in

$$\tau_E[\text{ms}] = 94 \times I_P^{(1.83\pm0.12)} \bar{n}_{e,H}^{(-0.28\pm0.13)} P_{\rm LOSS}^{(-0.33\pm0.06)} \tag{5.11}$$

with $R^2 = 0.79$. Comparing to the ITER H-mode scaling laws for ELMy and ELM-free plasmas, one sees a very different scaling on C-Mod. The I_P dependence is closer to 2 than to 1, and the the $P_{\rm LOSS}$ dependence is significantly less negative. Finally, the density dependence is negative, rather than positive. Of course, there is an almost perfect correlation between H-mode density and plasma current on C-Mod, which should make for algebraic cancellation in (5.11). Thus it makes sense to exclude density as a dependent variable altogether. In this case,

$$\tau_E[\text{ms}] = 70 \times I_P^{(1.66\pm0.10)} P_{\rm LOSS}^{(-0.38\pm0.06)} \tag{5.12}$$

with $R^2 = 0.79$ again. This is closer to the ITER H-mode scalings in [149], though still quite different. Based on this work, it appears the EDA H-mode has energy confinement properties somewhat different from that observed in ELM-free and ELMy regimes on other tokamaks.

5.6 Plasma triangularity variation

Whereas the preceding portion of this chapter was concerned with the standard C-Mod shape, there is an effect of triangularity on the pedestal, as noted in Sec. 4.2. Early measurements with ETS showed that when δ was increased dynamically during discharges, a clear increase was observed in the density pedestal width, as shown in Fig. 5-14. Two data series are included in this plot. The first series is taken in lower single null (LSN) geometry, and was gathered prior to the optimization of the ETS diagnostic for higher temperatures. Because of this limitation, no accurate data were obtained for the T_e pedestal response. The second series was obtained at a later date, with good spectral optimization, but in an upper single null (USN) geometry that is unfavorable to the noise characteristics of ETS signals. The T_e pedestal data are poorer in this case as well. Nonetheless, the fitted n_e widths are of acceptable accuracy, and trend roughly the same way in either case. The H-mode physics is expected to be similar in both cases, since the USN plasmas were run with B_T reversed from its normal direction, yielding an ion ∇B drift toward the X-point.

This observation prompted further experiments, which would employ the fully optimized ETS system, capable of diagnosing the T_e pedestal as well as n_e. Furthermore, a modification to the inner nose of the C-Mod divertor prior to the year 2002 campaign allowed for a greater freedom in placing the X-point in LSN plasmas, thus allowing a broad range in triangularity to be obtained. Finally, triangularity would be held approximately fixed during the duration of the H-mode, such that more data could be obtained by the edge TS, improving the statistics of the study. The variation obtained in both lower and upper triangularity is shown in Fig. 5-15, along with the same variation in the previous experiment, with dynamic shape scanning. The quantities δ_u and δ_l roughly tracked together over a broad range in average δ, and making it impossible to separately distinguish the effect of upper and lower triangularity. In these discharges, toroidal field was held fixed at 5.4 T, and plasma current ranged from 0.6 to 1 MA.

Direct comparison of pedestals in discharges with similar field, current and ICRF

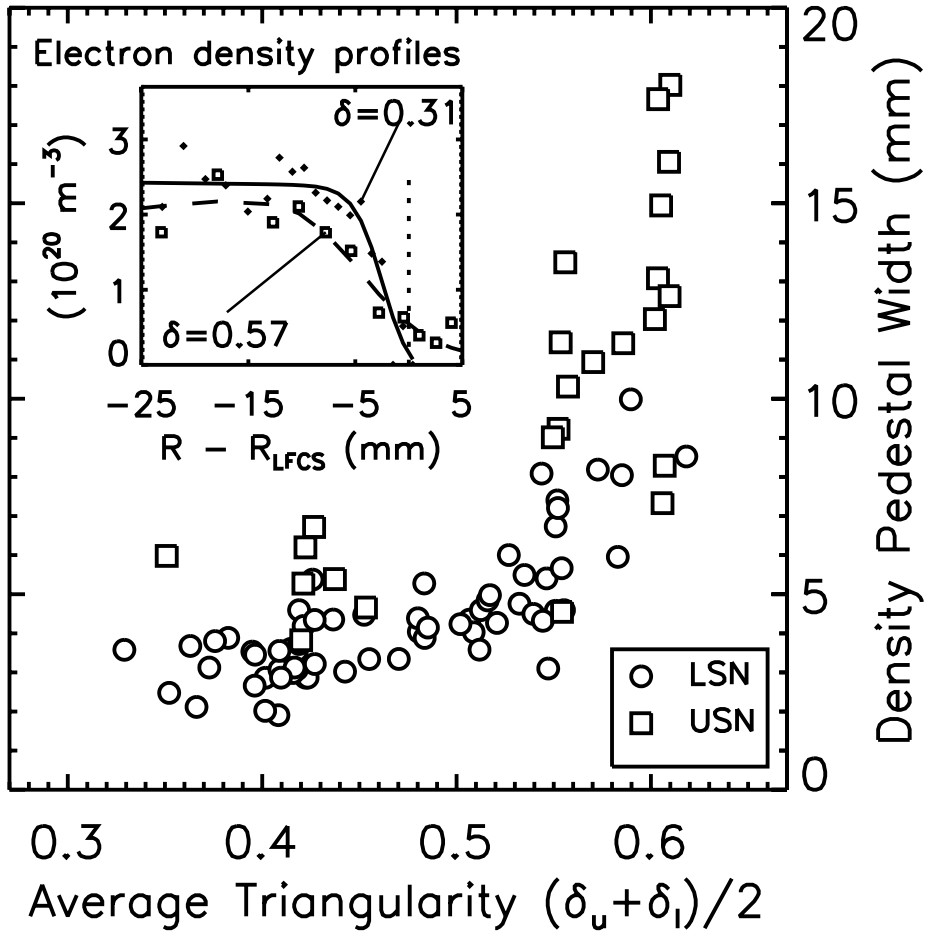

Figure 5-14: Variation of n_e pedestal width on the average of upper and lower triangularity (δ_u, δ_l) observed during shaping scans. Data from plasmas with lower single null geometry (circles) and upper single null geometry with reversed B_T (squares) are included. Points shown are in the range: $5.0 < B_T[\mathrm{T}] < 5.6$, $0.7 < I_P[\mathrm{MA}] < 1.3$, $3 < q_{95} < 5$, $1.55 < \kappa < 1.70$. Inset shows two sample pedestal profiles at low and high δ_{av}

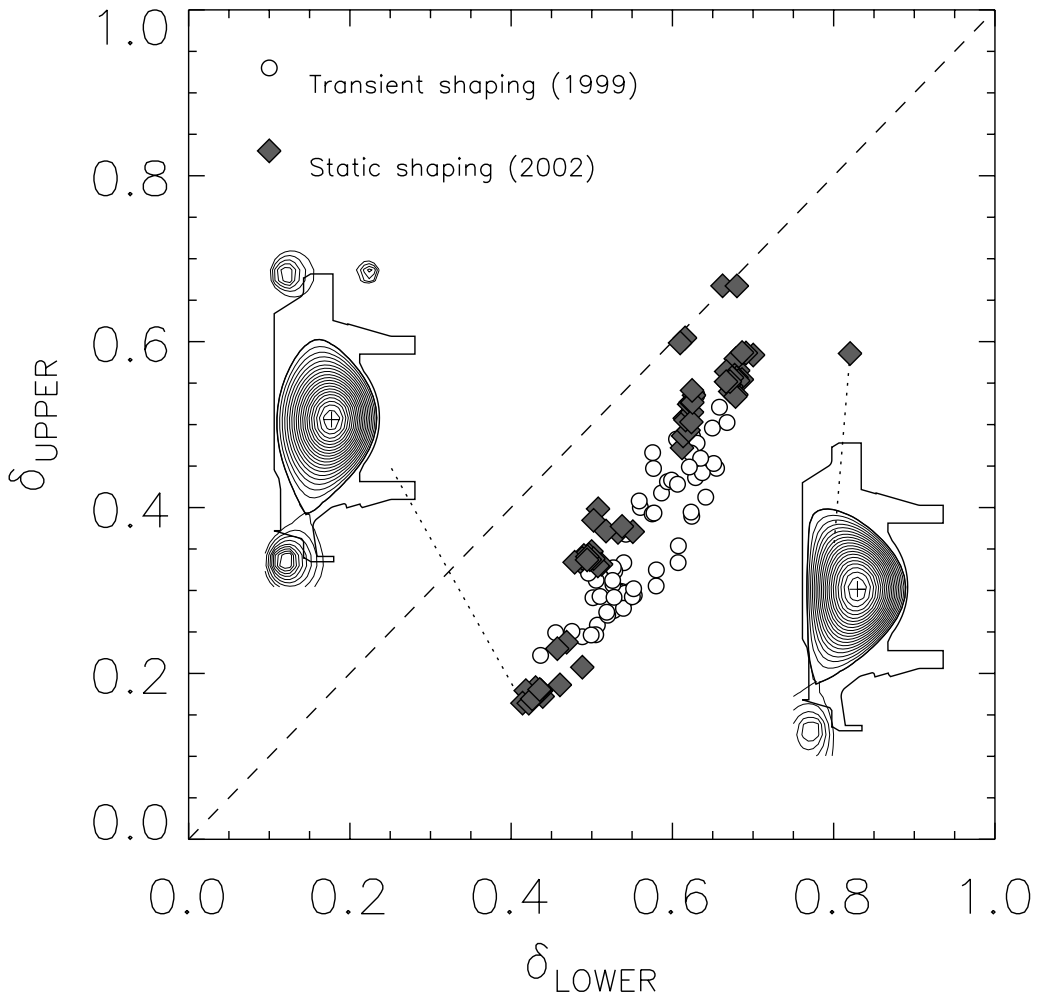

Figure 5-15: Upper and lower triangularity of points obtained in shaping variation experiments. White circles represent discharges from 1999, in which shape was scanned dynamically during discharges. Gray diamonds are discharges in which shape was held fixed. A similar range in δ_l and δ_u was obtained in either experiment. Sample flux contours from low δ (left) and a high δ (right) equilibria are shown. The dashed line corresponds to up-down symmetry.

input power is possible, as in Fig. 5-16. Here the n_e gradient is seen to relax with increasing δ, with pedestal height falling and width increasing. As edge density falls, the T_e pedestal rises, such that any variation in the pressure pedestal is small. By accumulating data from a number of H-modes, the trends in Δ_n, Δ_T and Δ_p are examined, as in Fig. 5-17. In these steady H-modes, the density width increase is less dramatic than in plasmas of transiently varying shape (Fig. 5-14). Somewhat surprisingly, there was increased scatter in the data from the pedestal fits, and averaging over multiple TS time points had to be performed. Though the strong increase in average Δ_{n_e} at $\delta > 0.55$ was not reproduced, it does appear that the maximum Δ_{n_e} obtained in the statically shaped discharges is consistent with the average Δ_{n_e} in the dynamic scans. These data show no significant trend in the T_e and p_e widths.

Because the EDA scalings for pedestal values of n_e, T_e and p_e depend so strongly on plasma current (Sec. 5.4), these data must be sorted more finely by I_P in order to determine trends of pedestal quantities with δ. Figure 5-18 shows $n_{e,\mathrm{PED}}$, $T_{e,\mathrm{PED}}$ and $p_{e,\mathrm{PED}}$ for I_P near 1MA, plotted against δ_{av}. As Fig. 5-16 suggested, density drops and temperature rises as triangularity increases. In this limited data set, $p_{e,\mathrm{PED}}$ has no systematic variation with triangularity. Finally, the gradients in the pedestals are plotted in Fig. 5-19. The only trend observed is that of $|\nabla n_e|$ decreasing at higher δ. This trend is of questionable significance, given the small number of points. It is useful to combine the data from the various ranges of I_P as to make a meaningful comparison.

Two trends emerge if normalizations to current are introduced to the larger data set. The first is a significant drop in the value of $n_{e,\mathrm{PED}}/I_P$, shown in Fig. 5-20a. Dividing by I_P aims to remove the natural scaling determined for EDA H-modes in Sec. 5.4. Likewise, the I_P^2 scaling in pressure gradient can be divided out, resulting in an overall downward trend in the maximum obtained $|\nabla p_e|$ as δ is increased. This result, shown in Fig. 5-20b, is rather interesting. It contrasts with results on other machines which show the attainable normalized pressure gradient (characterized by the MHD parameter α) *increasing* with stronger shaping. [78][84][91] Unlike on the other tokamaks, the pedestal ∇p on C-Mod is not limited by Type I ELM activity. Such

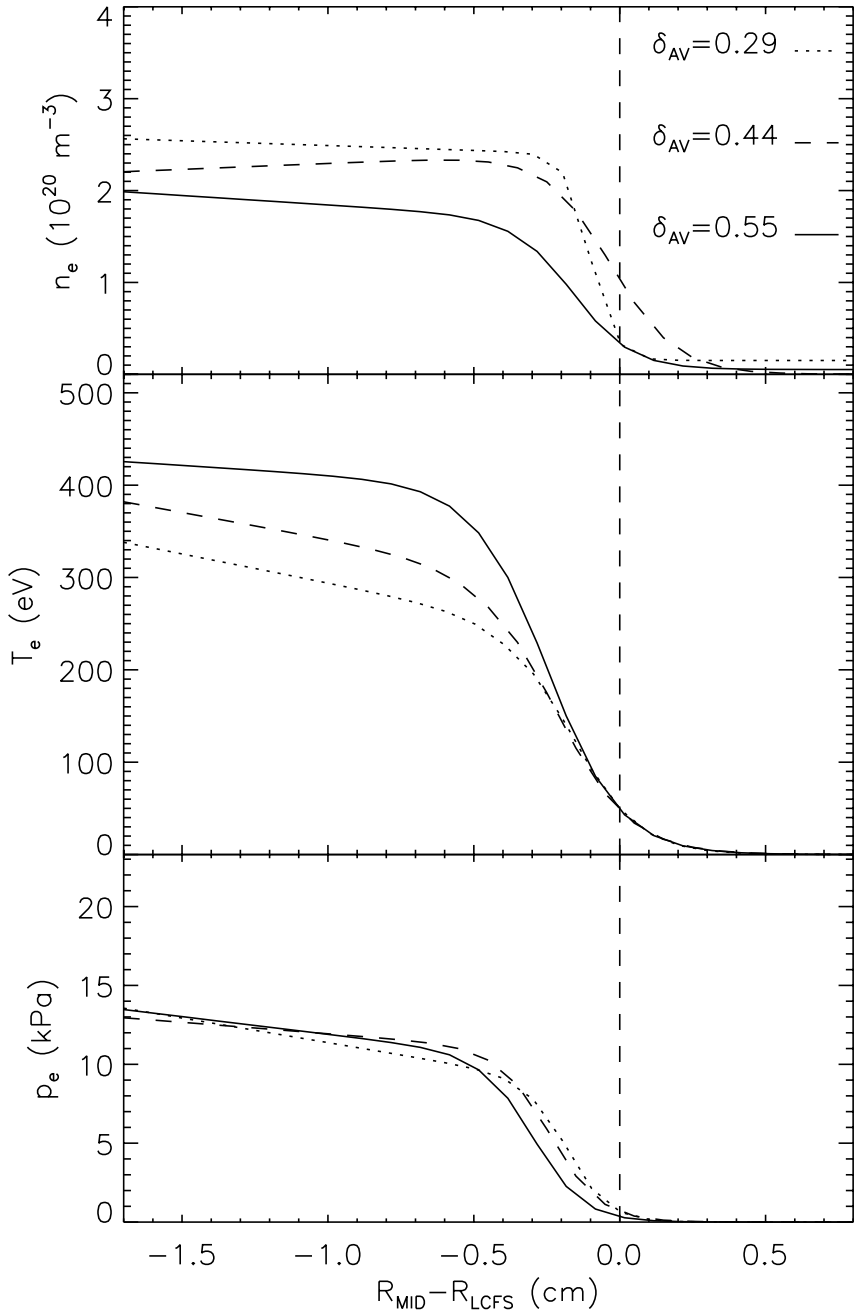

Figure 5-16: H-mode profiles of n_e, T_e and p_e over a range of triangularity. The density pedestal tends to relax as δ increases. Higher T_e pedestals and few changes in the p_e pedestal are observed. Plasmas are at 5.4 T, 0.9–1.0 MA, with P_{ICRF}=2.2 MW. Profiles are time-averaged over 2–4 TS pulses during H-mode and shifted radially to force $T_{e,\mathrm{LCFS}}$=50 eV.

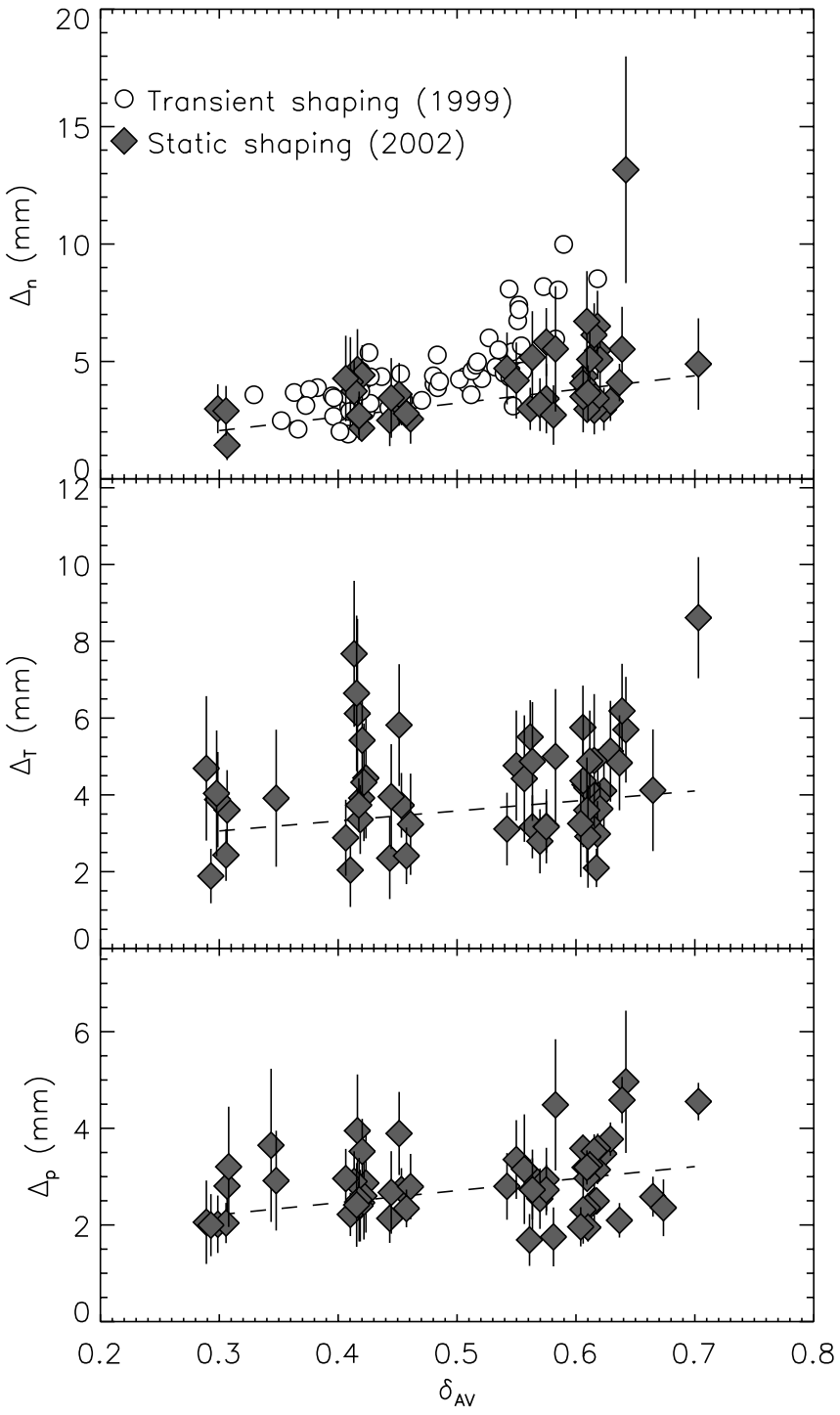

Figure 5-17: Widths of n_e, T_e and p_e pedestals as a function of average triangularity in steady H-modes. Gray diamonds represent discharges with static shaping, having I_P in a range of 0.6–1.0 MA. White circles are data points from an experiment with dynamically changing shaping, for comparison of Δ_{n_e}. Dashed lines are the results of error-weighted linear least squares fits to the data.

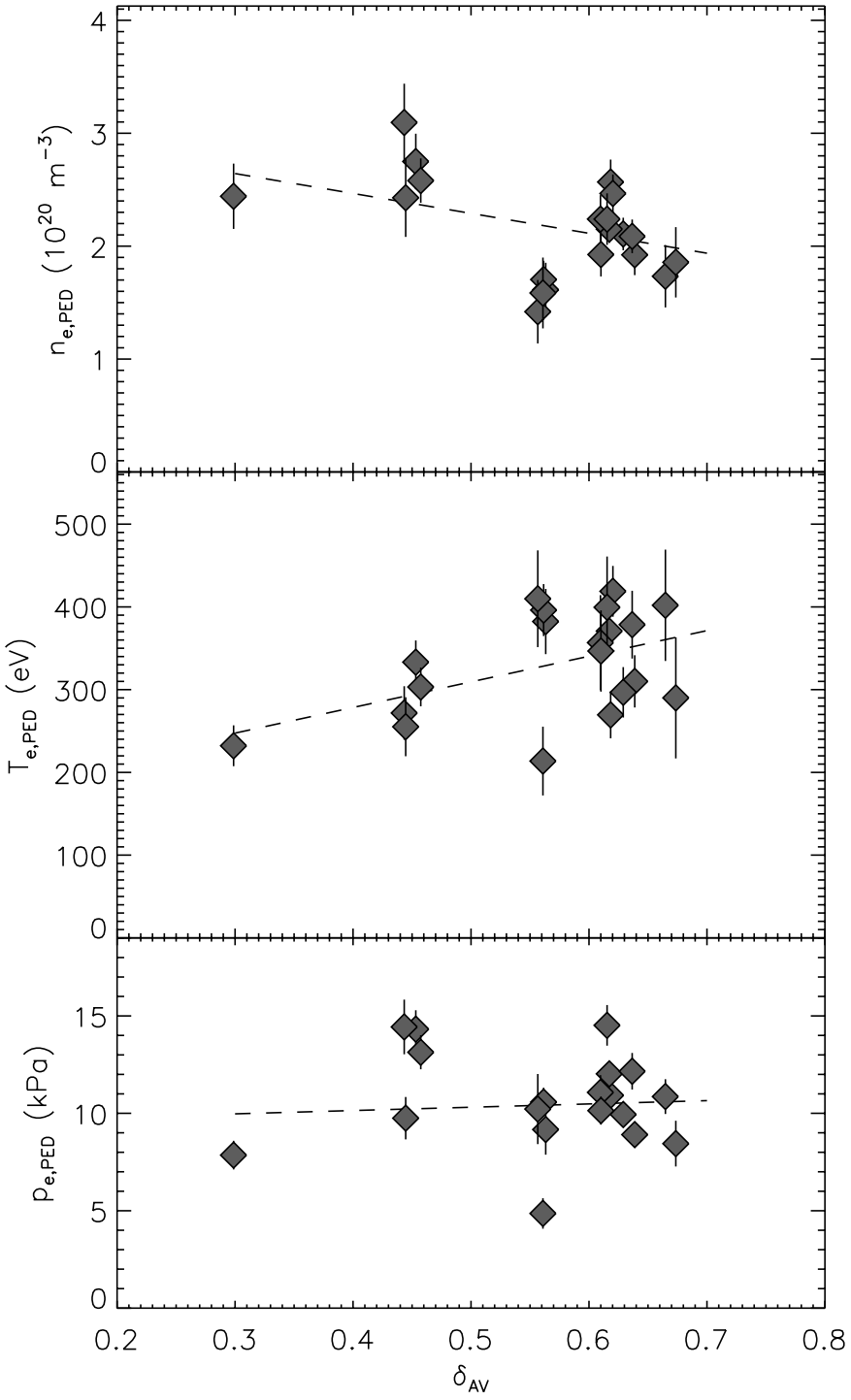

Figure 5-18: Pedestal values of n_e, T_e and p_e as a function of average triangularity in steady H-modes. I_P ranges from 0.9 to 1.0 MA.

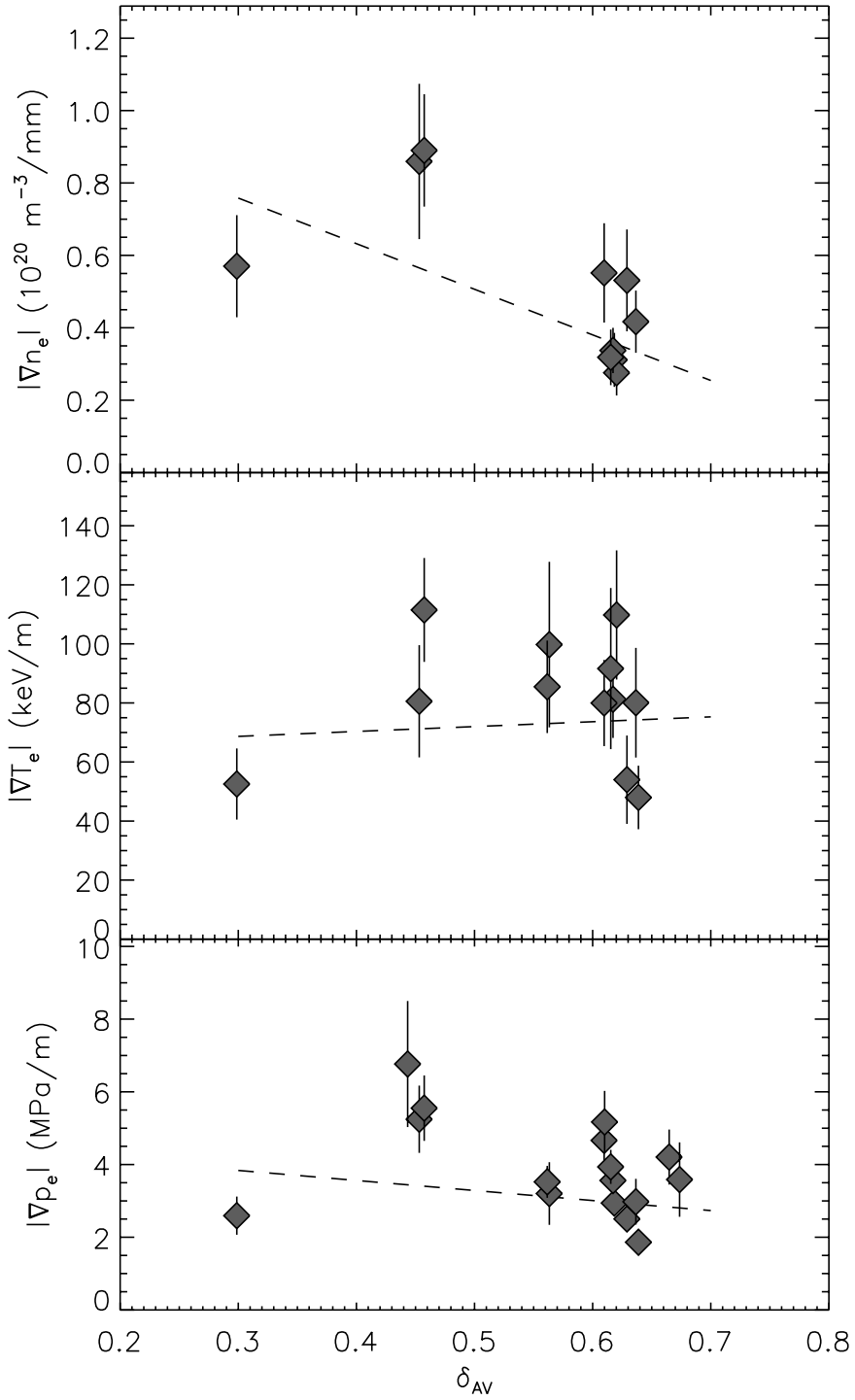

Figure 5-19: Gradients of n_e, T_e and p_e as a function of average triangularity in steady H-modes. I_P ranges from 0.9 to 1.0 MA.

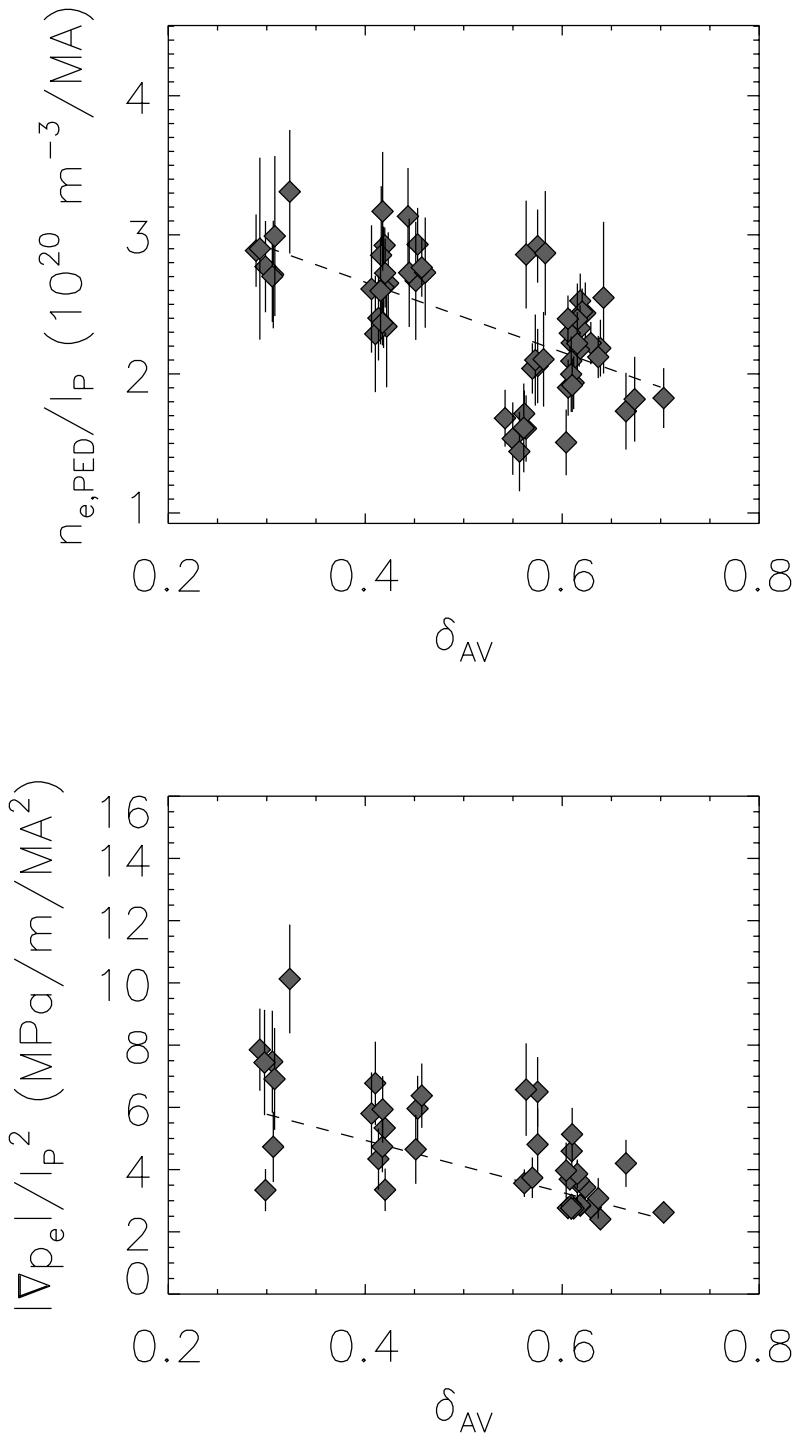

Figure 5-20: a.) Density pedestal normalized to current and b.) pressure gradient normalized to I_P^2 as a function of average triangularity. I_P ranges from 0.6 to 1.0 MA.

ELMs become less frequent at higher δ due to increased stability to high-n ballooning modes. The difference in ∇p behavior highlights the point that the EDA pedestal is set by mechanisms other than high-n ballooning. The changes in the pedestal with plasma shaping could result from a mixture of physics, including changes in QCM stability and variations in the neutral fueling.

Chapter 6

Particle Transport Analysis

To better understand the physical mechanisms giving rise to the pedestal scalings demonstrated in Ch. 5, it is desirable to examine transport in the edge barrier carefully. Several experimental and computational tools are available and provide the opportunity for quantitative analysis of transport. The purely experimental approach calls for diagnosing, in addition to the edge plasma quantities, the radial profiles of neutral density and ionization rate in the SOL and pedestal. From these quantities, the levels of effective plasma diffusivity can be determined and perhaps scaled with plasma parameters. This technique is supplemented with kinetic calculation of the spatially dependent neutral atom distribution function. As will be shown below, accounting for the effects of thermalizing neutrals in the pedestal may help to explain observed differences in n_e pedestal scalings on C-Mod and larger machines.

6.1 Emprical analysis of transport

The combined high resolution profiles from various edge diagnostics afford the opportunity for improved understanding of the particle transport in EDA H-modes. Given that the quasicoherent mode (QCM) drives particle transport through the pedestal, and that the amplitude of this mode is sensitive to global and local plasma parameters (see Secs. 1.4.2 and 4.3.3), it is natural to ask whether this variation in plasma transport is not the dominant factor in setting density pedestal parameters.

An experiment that explored the variation in QCM characteristics created an opportunity for examining radial transport in detail. As shown in Figure 6-1, plasma current was varied over a significant range to affect a large change in edge q. H-modes were triggered in all cases with 2.0–2.5 MW of ICRF power. Discharges at 0.8 MA ($q_{95} \approx 5.5$) demonstrate the ordinary EDA behavior, exhibiting a strong QCM and reaching a steady-state global density. At 1.0 MA ($q_{95} \approx 4.2$), the QCM is weaker, and density and impurity accumulation becomes an obstacle to achieving steady state H-mode. The experiment intended to push the upper range of q as well, and discharges with $I_p \approx 0.5$ MA, $q_{95} \approx 9$ were obtained. These very low current discharges displayed a QCM that was rather broad in frequency space and with a low overall amplitude. Density in H-mode reached steady state, but the overall density increase above that in L-mode was marginal.

6.1.1 Density pedestal variation with current

Pedestal profiles from ETS were obtained in these three families of discharges, and the tanh-fits to these profiles, are shown in Fig. 6-2, where the distance above the midplane z is chosen as the spatial coordinate. Plotting the pedestals in real space, prior to mapping along flux surfaces to the midplane, is done to emphasize the reproducibility of the n_e profiles at a given current, before EFIT errors introduce randomly distributed radial shifts of the pedestals. Systematic errors in the EFIT mapping are also avoided; the dashed vertical lines indicate the average separatrix position as determined by EFIT for each plasma current. Based on where the EFIT-determined LCFS crosses ETS T_e profiles, the error increases with decreasing plasma current (smaller poloidal field).

The familiar trend of $n_{e,\mathrm{PED}}$ decreasing with lower I_P is reproduced clearly in these data. Though the target density was varied significantly at each value of I_P, there is little variation of $n_{e,\mathrm{PED}}$ within each constant-current cluster. The profiles also show a clear relaxation of n_e gradient as I_P is lowered. T_e profiles show little variation between the 0.8 and 1.0 MA cases, though $T_{e,\mathrm{PED}}$ is significantly lower at $I_P = 0.5$ MA. The large degree of variation in the temperature profiles may be

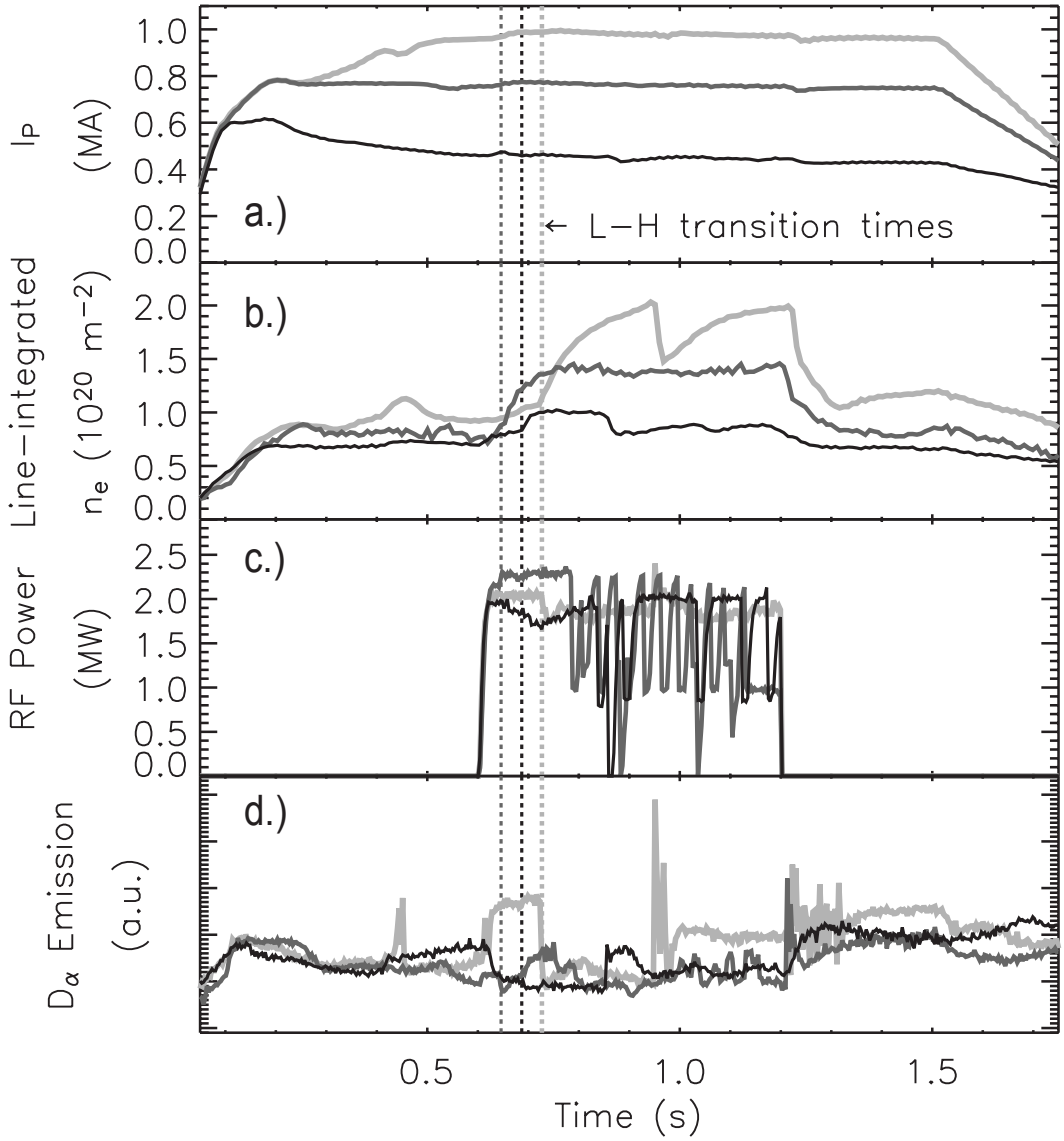

Figure 6-1: Time traces from discharges run at I_P of 0.46, 0.77 and 0.98 MA (a.). Changing edge q strongly effects particle transport, as shown by the density traces (b.), where the 0.98 MA discharge shows a greater particle build-up than the more EDA-like discharges at lower current. ICRF power (c.) for triggering and sustaining the H-mode is similar in all three cases.

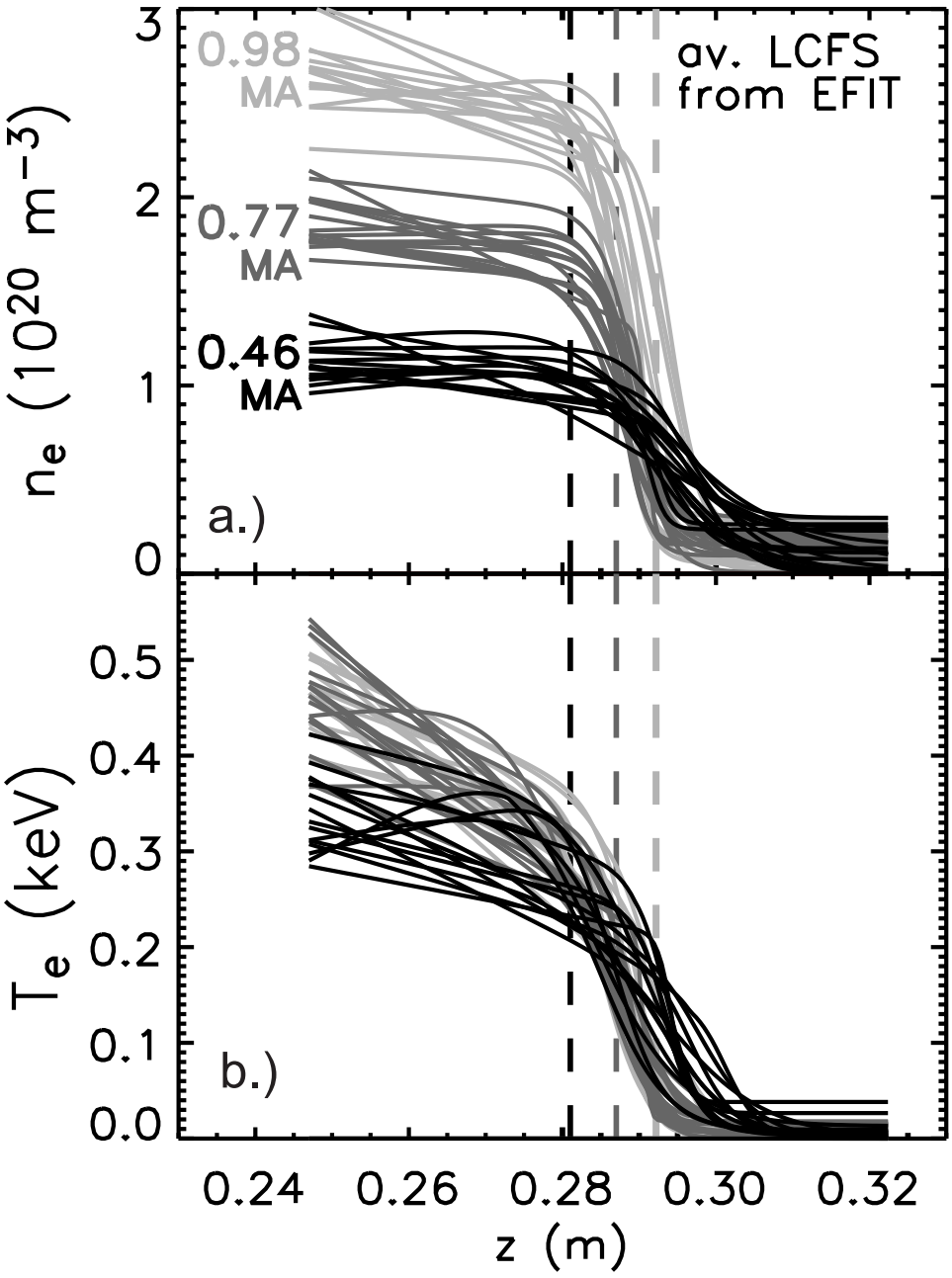

Figure 6-2: Pedestal profiles in families of discharges at three distinct currents. Shown are the tanh fit to a.) n_e and b.) T_e profiles in z-space, where z is the height above the machine midplane. Significant variation is obtained in both $n_{e,\mathrm{PED}}$ and n_e gradient as I_P is changed. Vertical dashed lines represent the position of the separatrix, as determined by the EFIT magnetic reconstruction, the error of which increases as I_P is lowered.

attributed to unsteady levels of auxiliary heating. Examining the trends in the density pedestal further, the profiles are mapped to the midplane and averaged over time windows including 2–3 TS laser pulses. The tanh-fits to these profiles determine width and maximum gradient. These quantities are grouped by I_P and plotted against $n_{e,\mathrm{PED}}$ in Fig. 6-3. The results of the scaling study in Ch. 5 suggested that in EDA H-modes, $\Delta_{n_e} \propto n_{e,\mathrm{PED}}$ or $\Delta_{n_e} \propto 1/q$. If this trend extended down to low currents, one would expect the narrowest pedestals at the lowest values of I_P. Figure 6-3a demonstrates that this scaling breaks down, and that in this low-confinement H-mode, Δ_{n_e} can take on values from 4 to 10 mm at the midplane. Exceptionally small gradients are also exhibited (6-3b), no more than double the typical values of $|\nabla n_e|$ in L-mode.

For many of these data points, additional data were available from a scanning probe. By fitting the ETS profiles with the modified tanh function, and connecting the fits to smoothed probe data, monotonic profiles of n_e and T_e with millimeter spatial resolution are compiled, as illustrated in Fig. 6-4. Radial shifts of a few millimeters or less are applied to each profile for mutual consistency, and also to give a temperature at the LCFS that is consistent with power balance considerations.

6.1.2 Neutral characterization

In order to uncover the radial density of the neutral fueling source, D_α emissivity is determined from the GPI camera, as described in Sec. 1.4.3. Shown in Fig. 6-5 is an image from the camera, averaged over several frames at 60 frames per second. A slice taken through the image at the midplane location gives a radial brightness profile. The lower right hand plot shows the inverted emissivity profile, which can then be used together with n_e, T_e to compute neutral density and ionization profiles. Because these measurements are roughly at the machine midplane, and the inversion of the data take advantage of toroidal axisymmetry, the EFIT mapping is not needed to reconstruct the emissivity profile. When using this in concert with the mapped n_e and T_e, error in the EFIT placement of the LCFS at the outer midplane could become an issue. The estimated upper bound on this error is 3 mm, but is otherwise not well characterized. Thus analysis must proceed assuming EFIT correctly determines

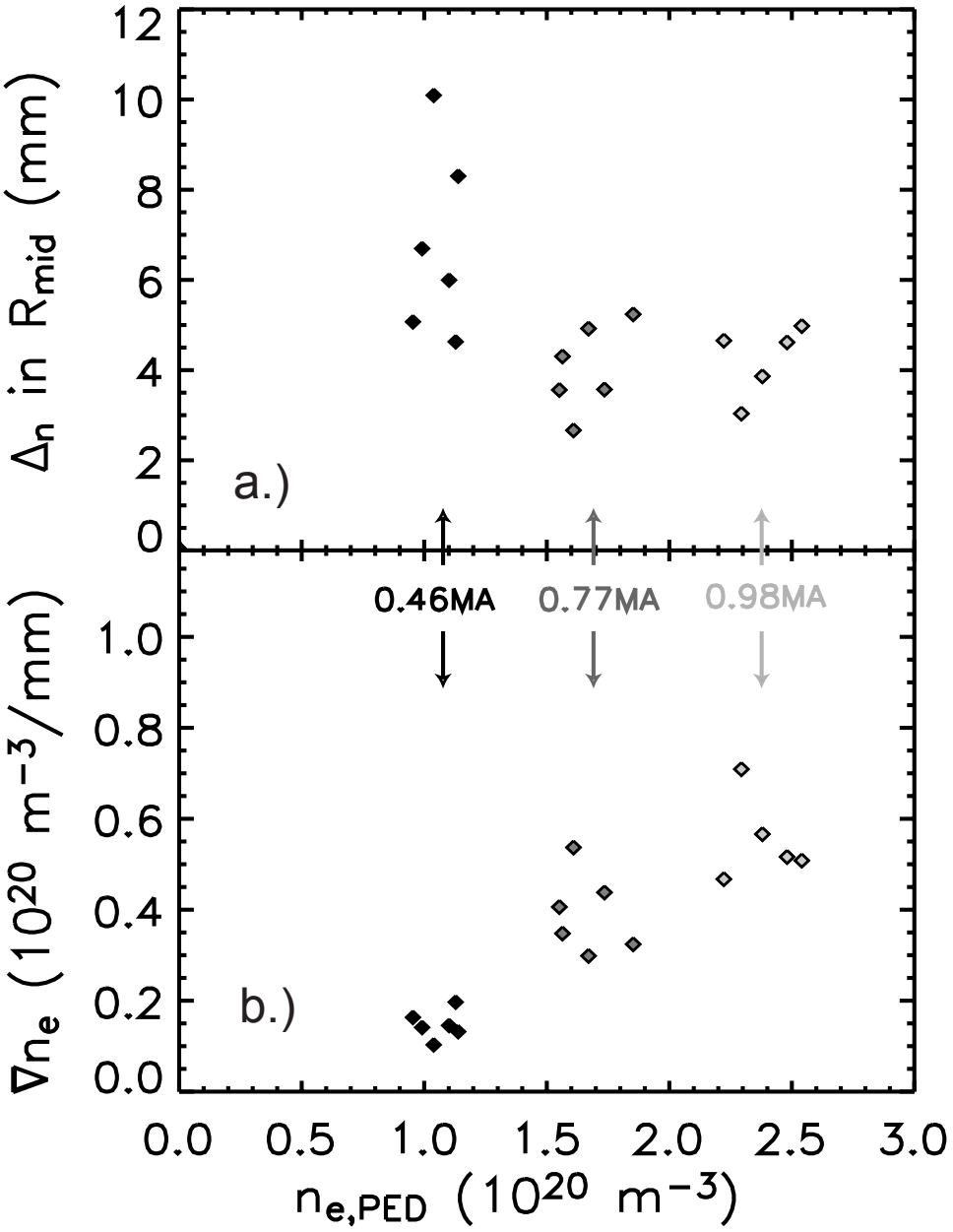

Figure 6-3: Pedestal trends in families of discharges at three distinct currents. a.) Density pedestal widths are in the usual range for the 0.77 and 0.98 MA discharges, but become much wider at $I_P = 0.46$ MA. b.) $|\nabla n_e|$ drops dramatically when going to the lowest current as well.

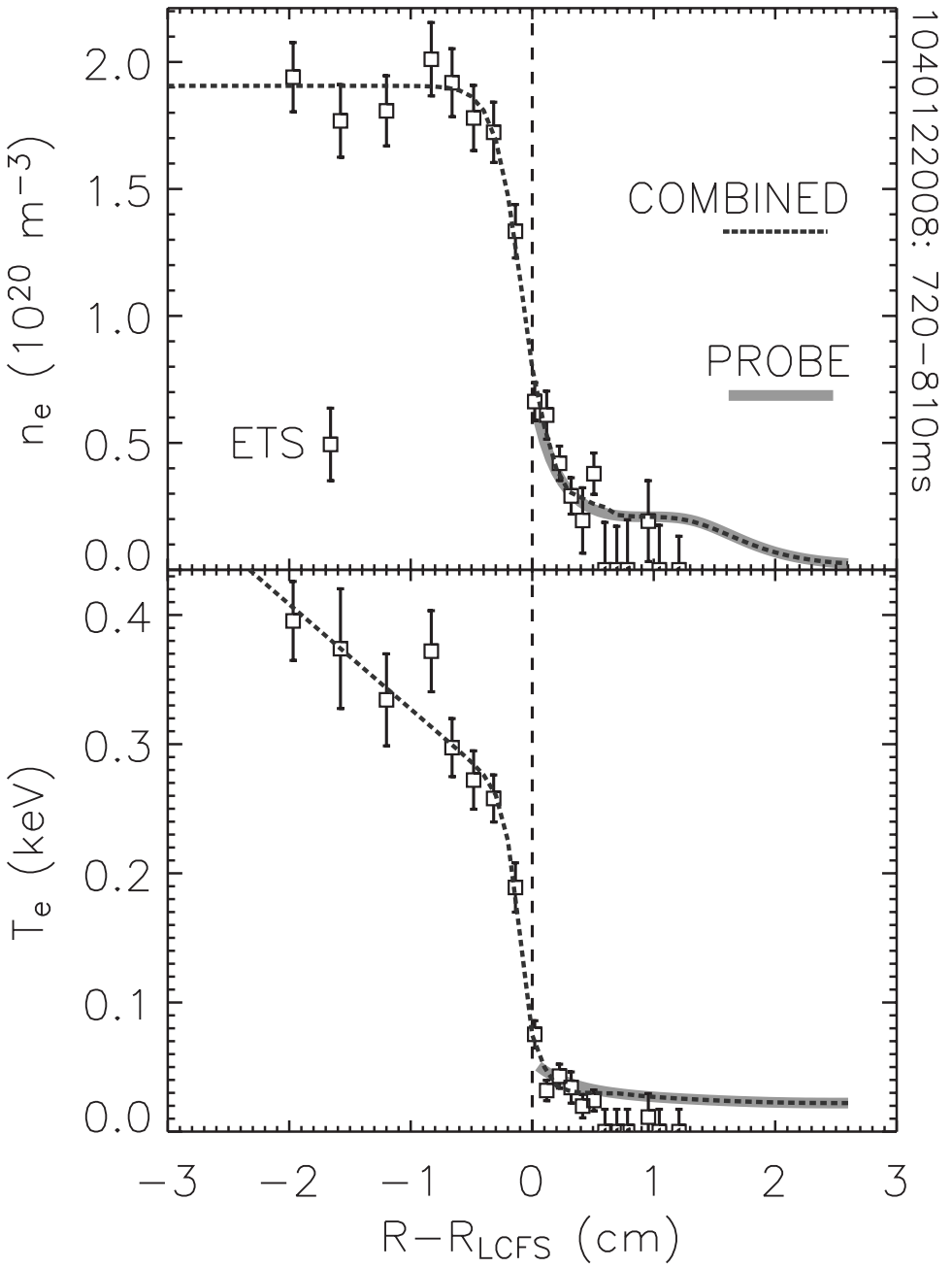

Figure 6-4: Smooth monotonic n_e, T_e profiles obtained from simultaneous ETS and scanning probe measurements in an H-mode edge. ETS profiles are averaged over multiple laser pulses ocurring near the time of the probe plunge. The tanh-fit to the ETS profiles is smoothly joined to the processed probe data.

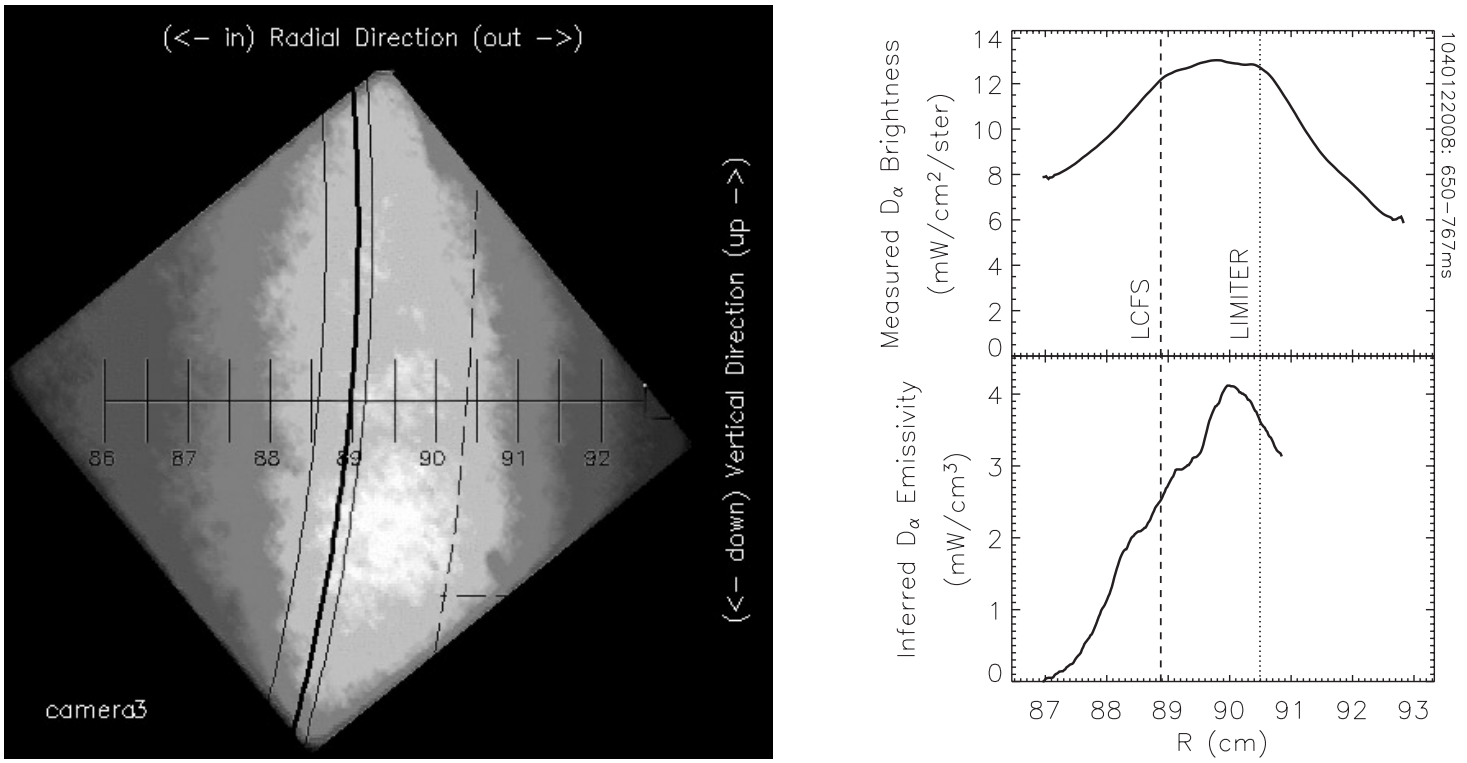

Figure 6-5: Measurement of radial D_α emissivity from 2-D camera image. Several exposures over the time period of interest are averaged at left. A slice through the image at the midplane gives the chord-integrated brightness (top right). Finally, an Abel inversion renders the local emissivity as a function of radius (bottom right).

$R_{\rm LCFS}$. The mapped ETS profiles are shifted such that $T_{e,\rm LCFS} = 50$ eV, consistent with SOL power balance requirements.

Figure 6-6a–c shows the density, temperature and emissivity determined by the above method, for the run in which plasma current was varied to alter the characterisitics of the QCM. The neutral density n_D (6-6d) and ionization rate $S_{\rm ion}$ (6-6d) are calculated using the results of Johnson and Hinnov. [40] One can see that in the 0.98 MA case, ionization in the SOL is relatively small, and a peak in $S_{\rm ion}$ occurs in the density pedestal, as expected from simple modeling of neutral fueling. As current is lowered the relative distribution of ionization begins to shift from inside the LCFS to outside. The peak in $S_{\rm ion}$ disappears at smaller I_P, and at 0.46 MA, the SOL region is highly ionizing and a large source of D_α. The results are consistent with enhanced particle transport into the SOL at higher q, which results in a higher SOL n_e .

Of course, significant ionization occurs in the core plasma, and at $I_P = 0.46$ MA, the consequent small pedestal density gives a longer average penetration length for neutrals, and considerably deeper penetration for the n_D profile (6-6d). Plotting the gradient scale lengths L_0 and L_n of the neutral and plasma density profiles in Fig. 6-7, one sees that their local minima are similar and exhibit the same trend with plasma current. That is, the scale lengths of each increase significantly upon lowering I_P to below 0.5 MA. These local scale lengths tend to be less than estimates of neutral mean free paths based on ionization and charge exchange cross-sections. Fig. 6-8 shows estimates of $\lambda_{\rm ion} = v_D/n_e\langle\sigma v\rangle_{\rm ion}$ and $\lambda_{\rm CX} = v_D/n_e\langle\sigma v\rangle_{\rm CX}$ with the n_e and $\langle\sigma v\rangle$ evaluated for average values of n_e and T_e in the pedestal, and v_D determined by the thermal velocity of SOL neutrals with a temperature of 20 eV. These values are approximately the same as the maximum pedestal width obtained from the tanh-fit. However, the local L_0 are smaller, and are consistent with a composite scale length, such as the $\lambda_{\rm eff}$ shown. This result indicates that simple estimates of neutral penetration length in the pedestal may be insufficient to determine the true neutral gradient scale length.

Note also in Fig. 6-7 how the neutral density gradient scale length increases slightly when going from the pedestal region toward the core plasma. Because $\langle\sigma v\rangle_{\rm ion}$ and

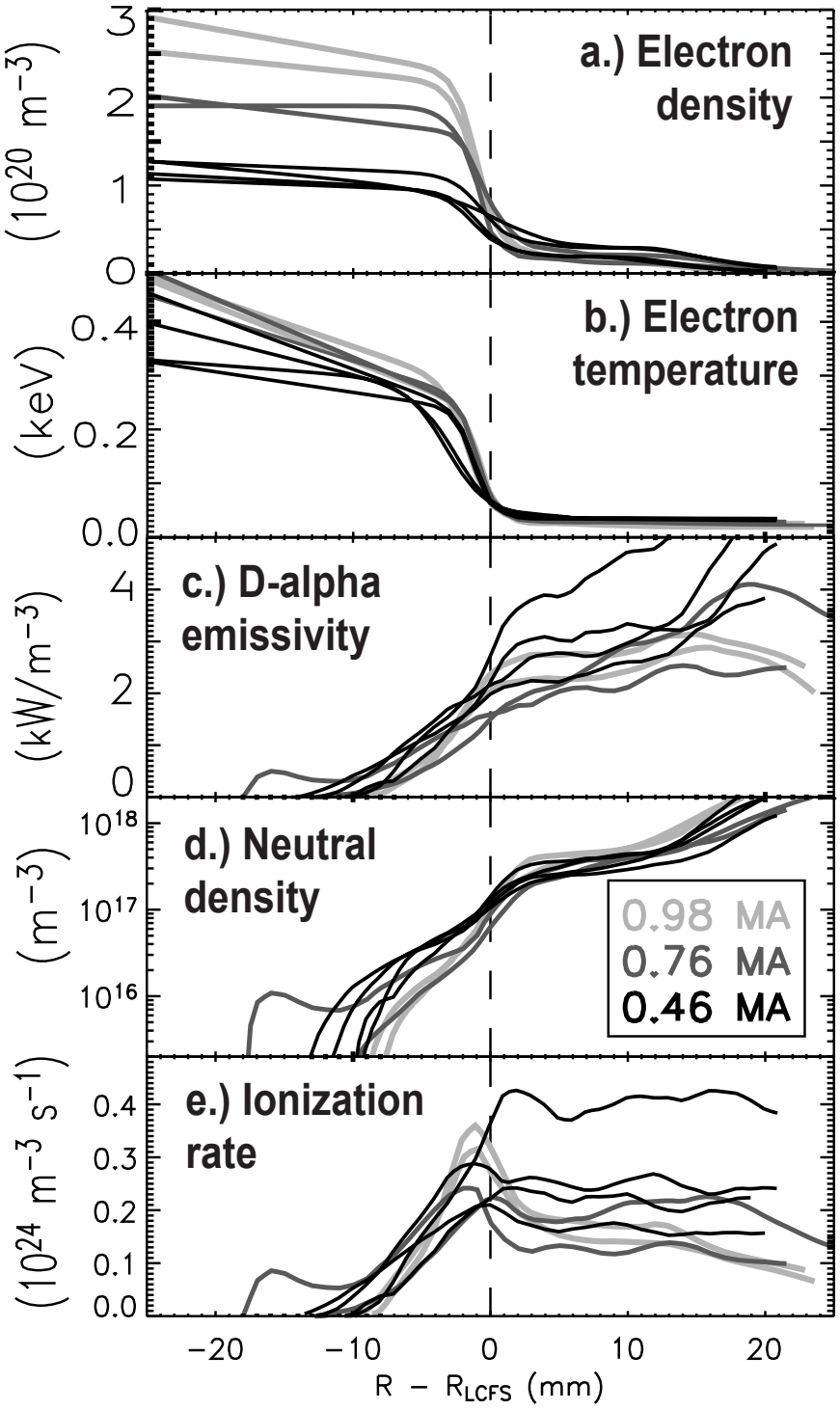

Figure 6-6: Using spatially resolved profiles of a.) n_e and b.) T_e from ETS and c.) D_α emissivity from the GPI camera, profiles of d.) neutral density and e.) ionization rate are determined for three families of discharges at different currents.

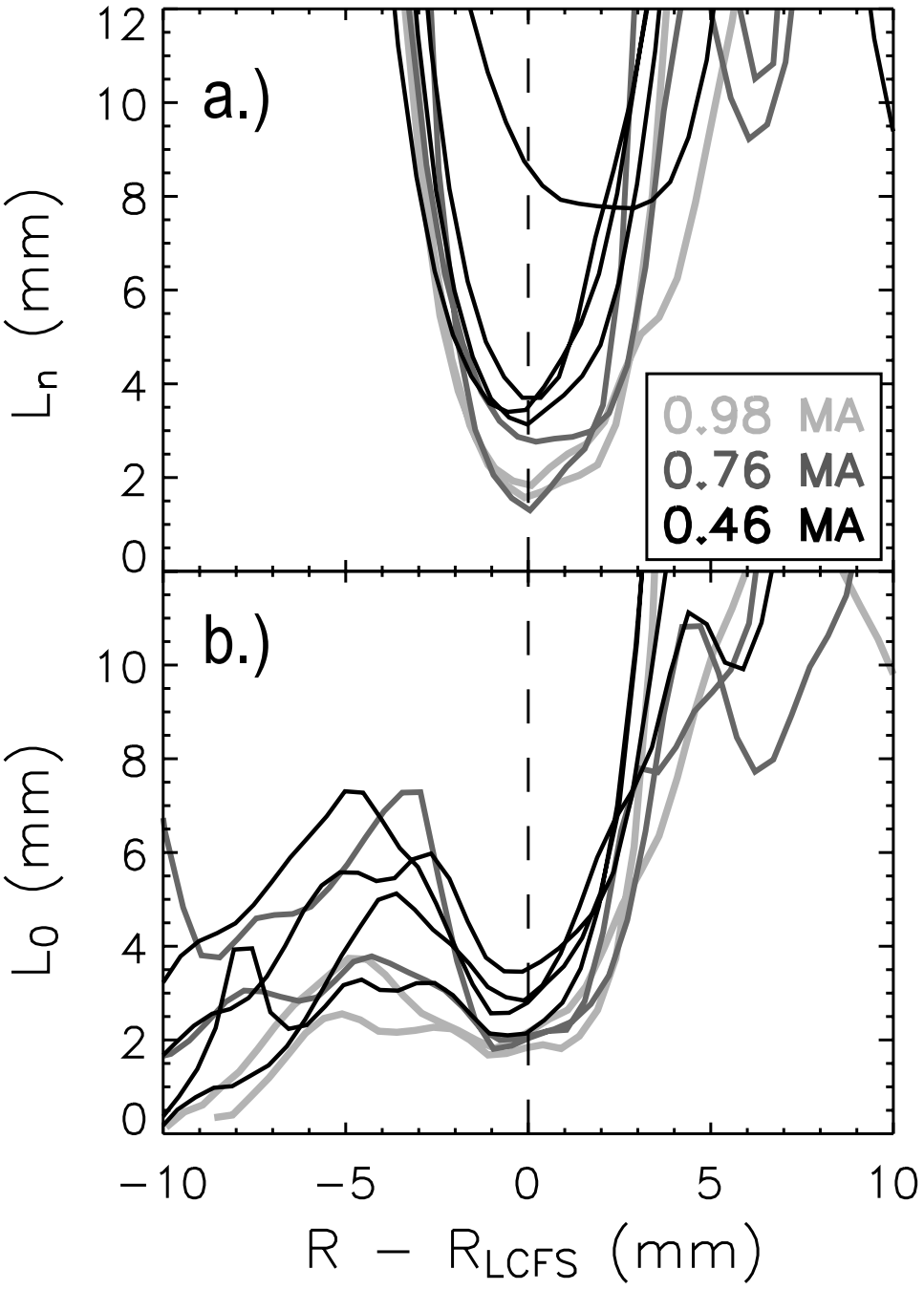

Figure 6-7: Gradient scale lengths of electron density and neutral density in the pedestal at currents of 0.46 MA, 0.76 MA and 0.98 MA. a.) $L_n = |n_e/\nabla n_e|$ b.) $L_0 = |n_D/\nabla n_D|$

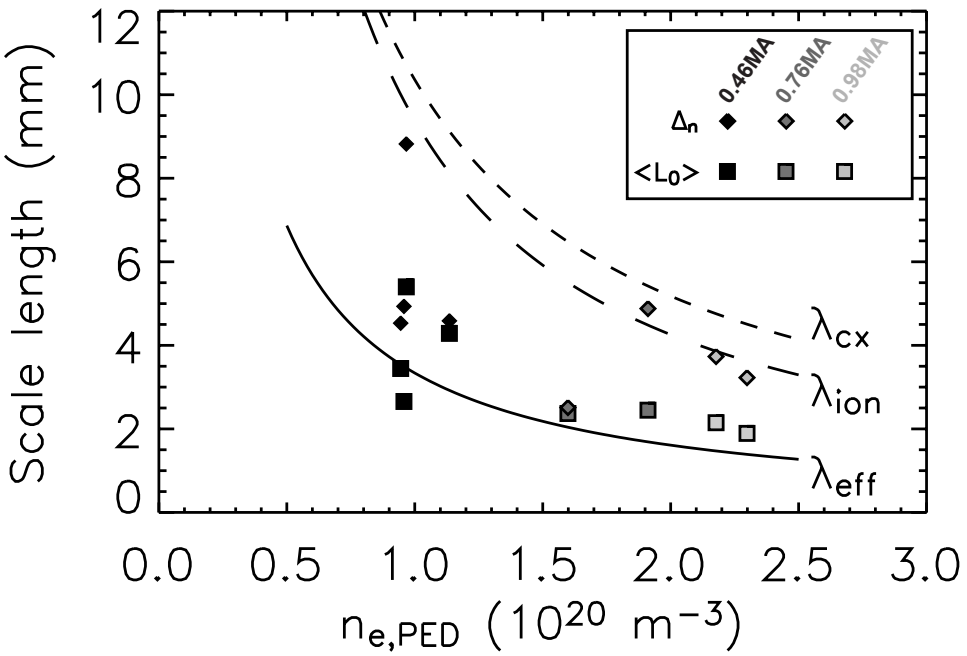

Figure 6-8: Direct comparison of average neutral gradient scale length $\langle L_0 \rangle$ with density pedestal width Δ_n. The maximum values of Δ_n are comparable with estimations of ionization and CX mean free paths. Local n_D scale lengths in the pedestal are more consistent with a smaller effective MFP. Here, $\lambda_{\text{eff}} = v_D/n_e(\langle \sigma v \rangle_{\text{ion}} + 2\langle \sigma v \rangle_{\text{CX}})$.

$\langle \sigma v \rangle_{\text{CX}}$ are relatively constant over the pedestal at the given $T_i \approx T_e$, one would expect the neutral penetration length to scale as v_{D}/n_i. The increase in L_0 inboard of the pedestal may therefore imply an increase in characteristic neutral velocity. This could result from thermal equilibration of D^0 with ions, an effect that can be demonstrated using a kinetic calculation. This will be shown later in this chapter.

The picture emerging from Fig. 6-8 is somewhat reminiscent of the trend observed in DIII-D and plotted in Fig. 2-2. One can ask the question: is this evidence of effective neutral penetration determining the density pedestal width, despite the apparent evidence to the contrary described in Sec. 5.4.1. The answer depends on the plasma transport, which is expected to change considerably when going from high to low current, given the known variation in the QCM and its effect on particle confinement in EDA. Based on the measurements detailed above, it is possible to infer a particle transport coefficient, and relate it to H-mode regime, as follows.

6.1.3 Radial plasma transport

Using the above data set, it is possible to construct profiles of effective diffusivity D_{eff}, assuming transport according to $\Gamma_i = -D_{\text{eff}} \nabla n_i$. This is not meant to imply that the ion transport is purely diffusive in nature; rather, D_{eff} provides a useful metric for evaluating the extent of both diffusive and convective transport. Assuming variation in the radial direction only, S_{ion} can be integrated to yield the ion flux profile $\Gamma_i(R)$. The diffusivity profiles, calculated from $D_{\text{eff}} = -\Gamma_i / \nabla n_e$, are shown in Fig. 6-9a. A well in D_{eff} is present in the pedestal region in all cases, and it is clearly seen to grow deeper as I_P is increased from 0.46 MA to more typical C-Mod currents. Inside the pedestal, values of D_{eff} appear to be in the range of 0.04–0.3 m^2/s, while closer to the LCFS, the minima are typically at 0.02–0.09 m^2/s. The width of the well is approximately 5 mm and has no obvious scaling with current. However, more radial structure could exist farther inside the core plasma, but be unnoticed, given the small values of measured D_α emissivity in this region. In all cases the diffusivity rises to 1 m^2/s or higher just a few millimeters into the SOL.

The trend of decreasing D_{eff} with increasing current is highlighted in Fig. 6-9b, where the diffusivity has been averaged over the pedestal region and plotted against $n_{e,\text{PED}}$. Partcle confinement at 0.5 MA is clearly quite low, nearly reaching L-mode levels. A superficial glance suggests D_{eff} scaling inversely with density, but more usable data would be needed to make a conclusive statement to this effect. In particular, a broader variation of $n_{e,\text{PED}}$ at a fixed I_P would be highly desirable. Repeated attempts have failed to produce significant variation. More data would also be desirable in order to determine whether the apparent drop in D_{eff} while going from 0.76 to 0.98 MA is truly significant.

Systematic errors in R_{LCFS} from EFIT should be addressed, as they have the potential to influence the derived profiles. Indications from Fig. 6-2 are that EFIT may underestimate the size of the plasma at lower I_P. If this is assumed to be the case, then the measured D_α profiles in Fig. 6-6c. should be shifted toward the core plasma in the lower current cases. This would increase the derived neutral density

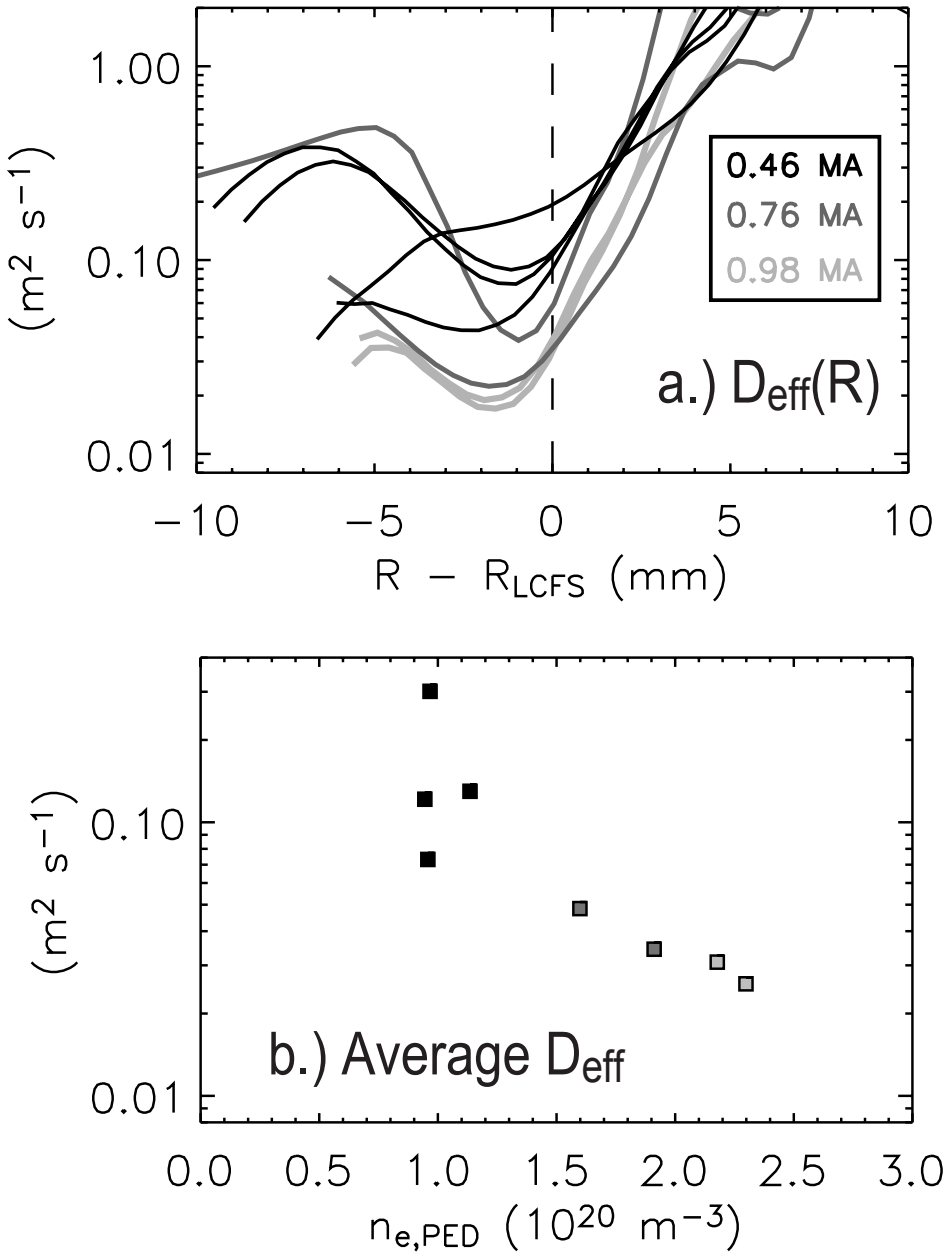

Figure 6-9: Effective diffusivity D_{eff} in the pedestal at varying I_P. a.) Spatially resolved profiles obtained using the density and ionization rate data in Fig. 6-6. b.) D_{eff} averaged over the extent of the pedestal region. There is a substantial drop in particle transport as I_P is increased from 0.46 MA to more typical C-Mod currents.

and ionization rate in the pedestal region, and should preserve the trend in D_{eff}.

Given that the inferred D_{eff} well is similar in width to the pedestal extent and is not obviously correlated with analytical estimates of neutral penetration length, it is reasonable to suspect that Δ_{n_e} is determined by the extent of the region in which plasma transport is suppressed. If this is indeed the case, then a D_{eff} well of fixed width and variable magnitude should yield a pedestal of roughly fixed width and variable gradient. If so, then $n_{e,\text{PED}}$ should scale inversely with average D_{eff}. The implication would then be that increasing I_P raises the pedestal density simply by driving D_{eff} lower.

6.2 Kinetic neutrals and KN1D

The impact of neutral fueling is a crucial point for fully characterizing transport in the pedestal. Experimental measurements of atomic density can be made, as discussed in Sec. 6.1. Additionally, one would like to know more about the neutral temperature and velocity, to fully characterize the interplay of particle and neutral transport. One tool for evaluating the velocity distribution of neutrals is discussed below.

6.2.1 Benefits of a kinetic neutral analysis

Neutrals at the tokamak edge fuel the plasma almost entirely through electron impact ionization, and simple modeling of neutral fueling [57][58] tends to treat neutral species with a fluid analysis, employing ionization as a neutral particle sink. The ionization rate is given by

$$S_{\text{ion}} = n_n n_e \langle \sigma v \rangle_{\text{ion}} \tag{6.1}$$

where the velocity-averaged cross section $\langle \sigma v \rangle_{\text{ion}}$ is a function of T_e only. Thus, neutral temperature does not play a role in the ionization rate, and one need only assume a neutral fluid velocity v_n in determining the MFP to ionization, as in (2.3). It is customary to take for v_n a value consistent with the expected thermal velocity of the neutral species as they pass into the plasma.

Using a fluid analysis for the neutrals is problematic, since such a formulation usually requires that the MFP to interaction be much smaller than the gradient scale length of the medium: $\lambda_{\text{MFP}}/L_n \ll 1$. As has been seen experimentally, these quantities in the C-Mod H-mode edge are of the same order. Thus it is desirable to use a kinetic treatment [150] to analyze the neutrals, retaining information on the velocity distribution of the penetrating neutrals. This allows the proper incorporation of neutral-ion interactions such as charge exchange and elastic scattering, which alter the neutral distribution function even as the neutral density is depleted by ionization.

A Kinetic Neutral 1-D transport code (KN1D) developed by LaBombard [151] was employed for the kinetic analysis of edge neutrals in many experimental cases, providing a complement to the measurements. This code is very useful at returning the full distribution function of neutrals in a slab geometry. It is versatile and fast, and can be run much more quickly than a full Monte Carlo simulation. A brief description of the workings of the algorithm is given below.

6.2.2 KN1D description

KN1D solves for the transport of neutral hydrogen (or deuterium) molecules and atoms through a tokamak plasma edge, taking into account a number of interactions. Neutral populations may experience electron-impact ionization, charge exchange with ions, elastic scattering from ions and collisons with other neutrals. The computational grid is 1-D in space along an axis x that is normal to the LCFS, and 2-D in velocity space, such that the distributions of velocity parallel (v_x) and perpendicular (v_r) to the spatial axis are calculated. The slab geometry is illustrated in Fig. 6-10. Inputs to the code include background profiles of n_i (assumed equal to n_e), T_i and T_e. Recycling from limiter surfaces is modeled, and thus the connection length between limiter surfaces is used as input as well. The gas pressure measured at the vessel wall is specified, and determines the molecular source of H_2 (or D_2). No impurites are considered.

Molecular hydrogen enters from the wall and limiters at room temperature, balancing the outward flux of atomic H. The H_2 dissociates, giving a source of H at the

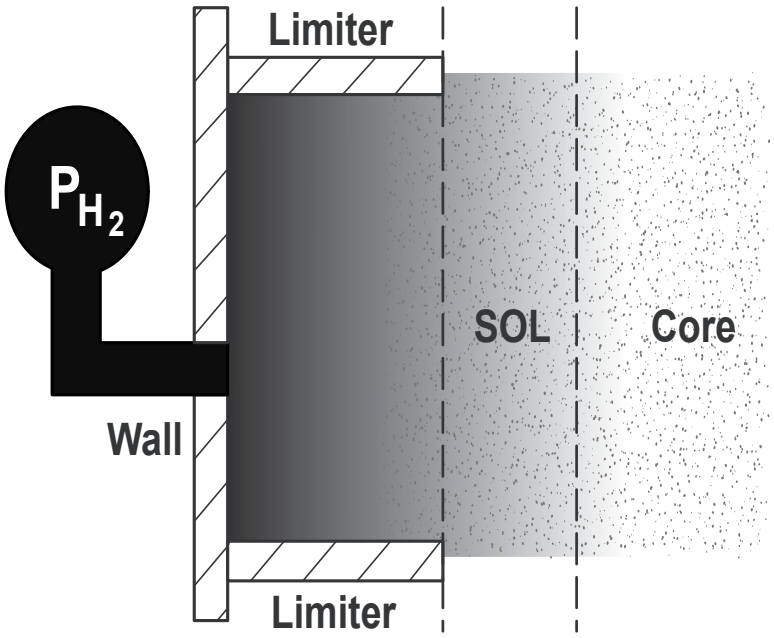

Figure 6-10: Simple picture of KN1D geometry. (Adapted from Ref. 151) Inputs to the code include background profiles of $n_i = n_e$, T_i, T_e, the gas pressure measured at the vessel wall and the connection length between limiter surfaces.

Frank-Condon energy of 3 eV. The distribution functions for molecular and atomic species $f_{\mathrm{H_2}}(v_r, v_x, x)$, $f_{\mathrm{H}}(v_r, v_x, x)$ are evolved by self-consistently solving the Boltzmann equation

$$v_x \frac{\partial f}{\partial x} = \left[\frac{\partial f}{\partial t}\right]_{\mathrm{coll}} + S \tag{6.2}$$

for each species over multiple collision generations. Here $[\partial f/\partial t]_{\mathrm{coll}}$ accounts for the various collisions either species can experience, and S represents the net source. To evaluate $f(v_r, v_x, x)$ for the H_2 and the H, KN1D calls two subroutines iteratively: Kinetic_H2 and Kinetic_H. Convergence is obtained when the molecular flux from the wall is made to match the atomic hydrogen flux to the wall:

$$2\Gamma_{\mathrm{H_2}} = \Gamma_{\mathrm{H}}^{-} \tag{6.3}$$

With the full distribution functions determined, it is straightforward to calculate neutral density n_n, temperature T_n and cross-field bulk velocity $v_{n,x}$ by taking the

appropriate moments.

A sample of typical code input and output is shown in Fig. 6-11. In this sample run on an EDA H-mode in deuterium, measurements from ETS and probes are combined to yield spatially resolved profiles of n_e and T_e extending from over a centimeter inside the LCFS to almost 2 cm beyond the limiter shadow (6-11a–b). T_i is assumed equal to T_e, and the input neutral pressure is taken from a gauge behind the vessel wall. The input flux of D_2 is assumed to enter the domain of computation where the input profiles begin at 0.138 m, at which point molecules are allowed to ionize as well as dissociate and create a source of D^0. The densities of the molecular species (6-11c) stay elevated behind the limiter due to recycling of D_2 from the limiter surfaces, but the density drops precipitously upon entering the SOL, which is free of molecular sources. Thus, the D^0 source from dissociation vanishes. Moving from the far SOL toward the pedestal, plasma density begins to increase, leading to increased collision frequencies. Ionization rate increases, leading to a drop in n_{D}, and both CX and ion-neutral elastic scattering serve to bring T_{D} closer to T_i (6-11d).

The Kinetic_H module, which solves for the atomic distribution function, has undergone some comparisons against the results of Monte Carlo code DEGAS 2 in limited situations. The results of a sample benchmark are discussed in App. A.

6.2.3 Comparison with experiment

Using coefficients from [40], KN1D computes from n_e, T_e and n_{D} profiles of Balmer-α and Lyman-α emissivity, which can be compared with experimental measurements. Such measurements were described in Sec. 1.4.3. A number of limitations exist in the measurements, and in the KN1D model, and these limitations must be considered when evaluating results.

Limitations to comparison

As mentioned previously, there are uncertainties in the mapping of profiles along flux surfaces, as well as the absolute placement of the LCFS by the EFIT reconstruction.

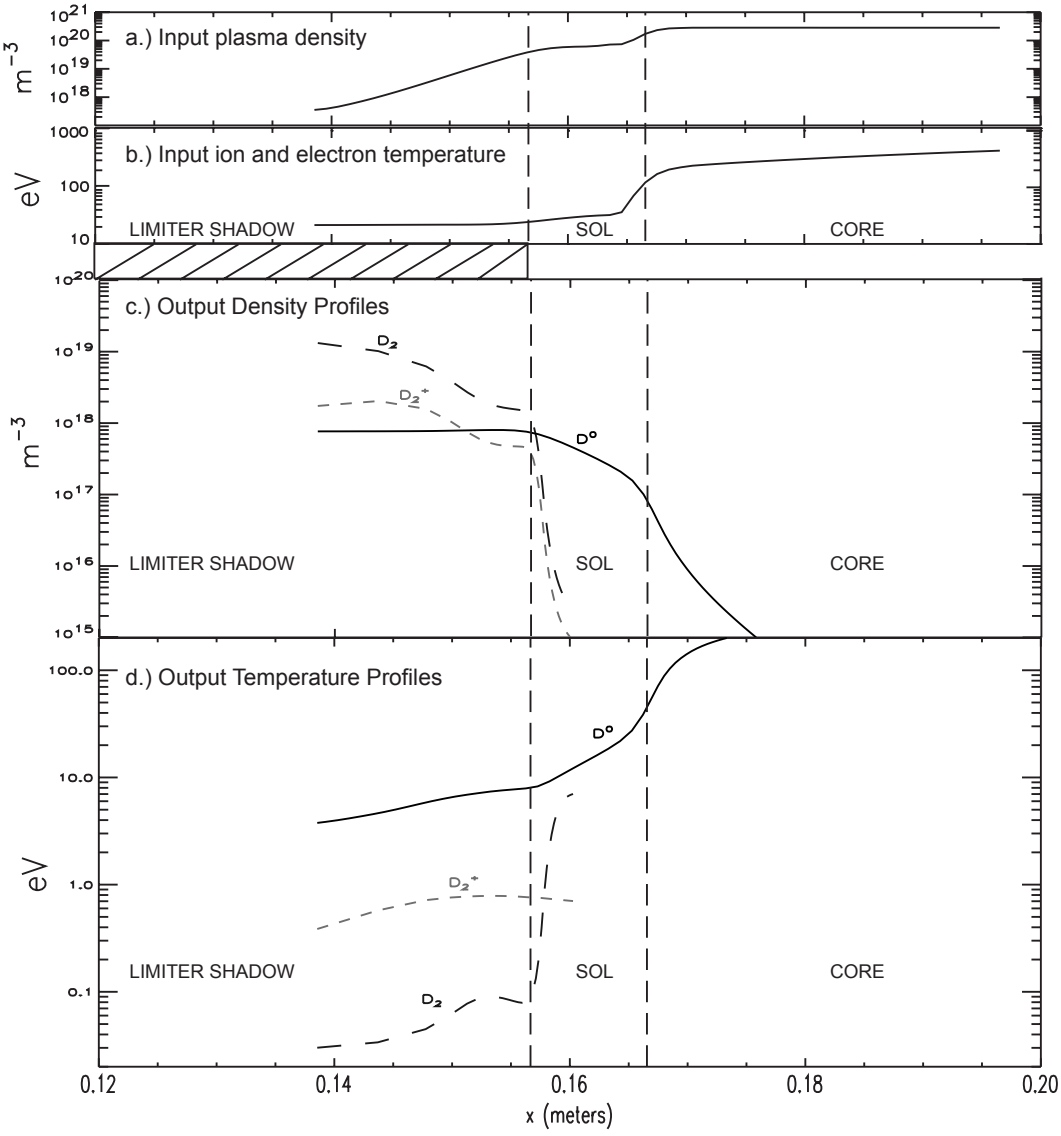

Figure 6-11: Examples of input profiles from a deuterium KN1D run: a.) input $n_i = n_e$, b.) input $T_e = T_i$. The x-axis is distance from the outer vessel wall. The input neutral pressure is the measured value of 0.840 mtorr, and the field line connection length in the limiter shadow is approximated as 0.8 m. c.) and d.) show output density and temperature for the species D_2, D_2^+ and D^0. Molecular populations decay drastically upon emergence from the limiter shadow at $x = 0.157$ m. As plasma density increases, atomic D^0 equilibrates with the ions through collisions, and ionization significantly drops n_D in the pedestal and core plasma.

Another experimental deficiency is the small number of poloidal measurement locations. Edge fueling is generally expected to be poloidal asymmetric, yet a reasonable D_α emissivity profile is obtained only at the outboard midplane. Ly_α emissivity is measured at two poloidal locations, one on the high-field side and one on the low-field side. In addition, due to variation in limiter structures on the low-field side of the tokamak, a significant toroidal variation in neutral density could exist. When modeling plasma and neutrals in the far SOL and in the limiter shadow, one cannot rule out poloidal and toroidal variation in plasma profiles. However, all the local measurements used in the current work (ETS, probes, emissivity inversions, wall pressure) exist at distinct points in θ and Φ. Finally, it is not possible to measure the plasma profiles all the way from the limiter boundary to the wall. Probes and emissivity measurements typically reach only 1–2 cm beyond the edge of the limiter, which Fig. 6-11 shows is over 15 cm from the wall. This forces the KN1D user either to make assumptions about the plasma profiles beyond the range of measurement, or to ignore the plasma there altogether. Because the plasma profiles affect the molecular and atomic penetration toward the plasma, the neutral density achieved at the SOL becomes dependent on these assumptions. For this reason, the limiter-shadow plasma is usually ignored, and the wall pressure is treated as a knob for setting the molecular source that impinges on the region of measured plasma.

The chief limitation of the KN1D model is its simplified treatment of the problem geometry. Because it operates in slab geometry, the KN1D solution of neutral transport can only be considered relevant in a single poloidal location from which the inputs are taken. The ouput of KN1D is extremely sensitive to the shape and magnitude of plasma profiles in the SOL, and so it is important to get these right if one wants an accurate neutral density distribution over the entire SOL. Fortunately, neutral distribution in the SOL is of secondary importance to pedestal studies, as long as the neutral temperature equilibration and neutral penetration scale lengths are accurately computed near the LCFS and farther inboard. Often the input neutral pressure is scaled a certain amount, typically varying from 0.2 to 5, in order to achieve the n_D in the pedestal required to match the measured emissivity.

Modeled SOL profiles

In the absence of good probe data, one can run KN1D relying on ETS only, with some assumptions about radial decay lengths of n_e and T_e in the SOL and limiter shadow (LS). If $R_{\rm LCFS}$ and $R_{\rm LIM}$ are the midplane radial positions of the separatrix and limiter boundary, then profiles are assumed given by

$$n_e = n_{e,\rm LCFS} \exp\left(-\frac{R - R_{\rm LCFS}}{\lambda_{n,\rm SOL}}\right) \tag{6.4}$$

$$T_e = T_{e,\rm LCFS} \exp\left(-\frac{R - R_{\rm LCFS}}{\lambda_{T,\rm SOL}}\right) \tag{6.5}$$

in the SOL ($R_{\rm LCFS} < R_{\rm MID} \leq R_{\rm LIM}$), and

$$n_e = n_{e,\rm LIM} \exp\left(-\frac{R - R_{\rm LIM}}{\lambda_{n,\rm LS}}\right) \tag{6.6}$$

$$T_e = T_{e,\rm LIM} \exp\left(-\frac{R - R_{\rm LIM}}{\lambda_{T,\rm LS}}\right) \tag{6.7}$$

in the LS ($R_{\rm MID} > R_{\rm LIM}$) are used. Adjusting $\lambda_{n,\rm SOL}$, $\lambda_{n,\rm LS}$, $\lambda_{T,\rm SOL}$ and $\lambda_{T,\rm LS}$ alters the neutral density profile and thus the ionization rate and emissivity profiles. When a profile shape is obtained that matches the experiment, the source can be scaled appropriately to match the magnitude globally. Figure 6-12 shows the result of this method, for a low-density H-mode. Here the selected SOL and LS profiles reproduce very well the shape of the D_α outside the LCFS, and a reasonably close match is had inside the pedestal.

6.3 Gas fueling experiments

In order to assess the relative roles played by plasma physics and neutral physics in determining pedestal characteristics, it is desirable to fix, as well as possible, the parameters of one while changing the other. If the physics of neutral penetration are important, then changing the fueling character at constant plasma parameters should affect the plasma pedestal. Such work was pursued on DIII-D (see Sec. 2.3.2), where

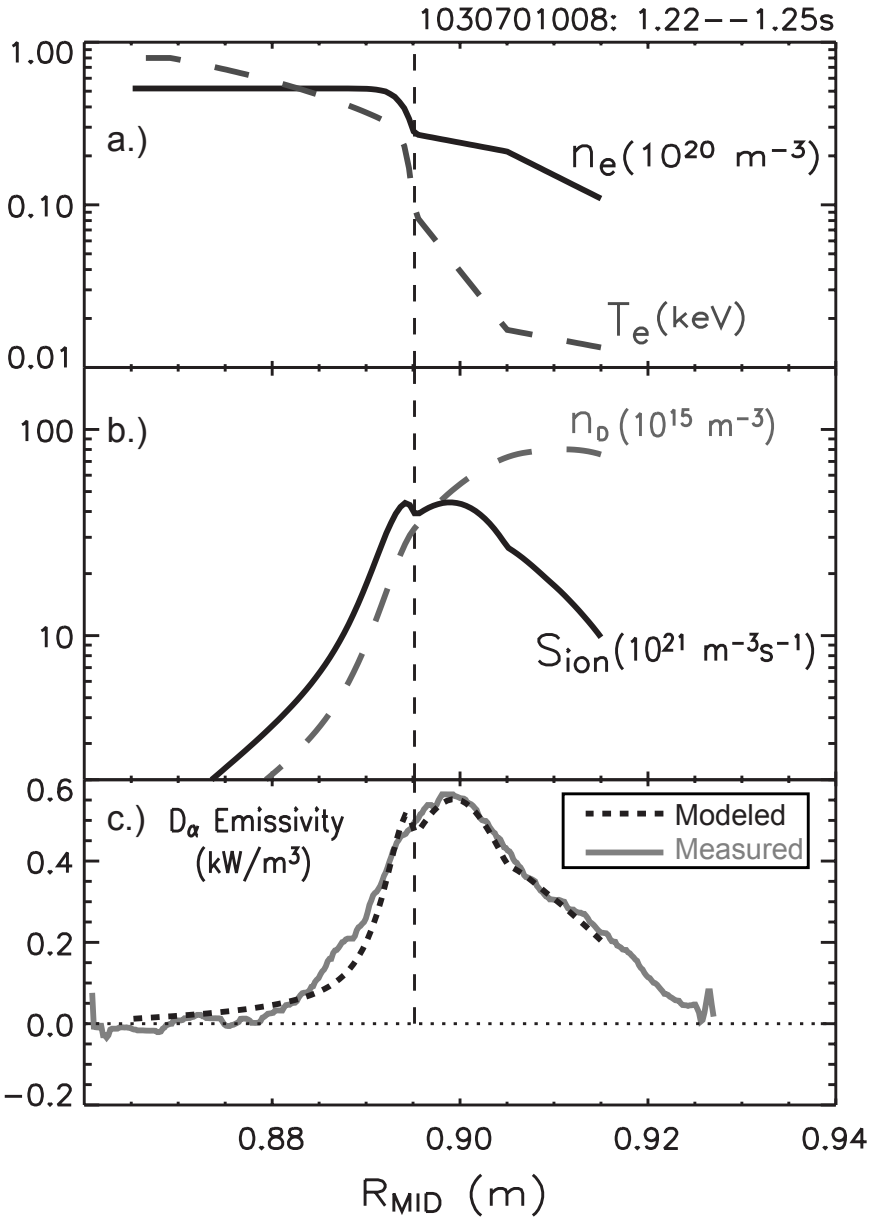

Figure 6-12: Matching output of KN1D with experimental D_α emissivity by adjusting both neutral source rate and decay length parameters outside the LCFS (dashed vertical line). a.) n_e and T_e inside the LCFS are from ETS. For data at larger $R_{\rm MID}$, exponential decay with various scale lengths is assumed: $\lambda_{n,\rm SOL} = 4.0$ cm, $\lambda_{n,\rm LS} = 1.5$ cm, $\lambda_{T,\rm SOL} = 0.6$ cm and $\lambda_{T,\rm LS} = 4.0$ cm. The resulting KN1D run produces b.) a neutral density and ionization rate profile, and also c.) a model D_α profile, which roughly matches in shape the experimental Abel inversion. The measured wall pressure is multiplied by 5.23 to match the D_α magnitudes.

puffing and pumping were used to vary the plasma density and correlate pedestal width to neutral penetration length. Similar work was subsequently attempted on C-Mod, taking advantage of the extensive set of edge diagnostics and computational tools available.

Cryopumping is not yet available on Alcator C-Mod, but various means of gas puffing are available. Plasma fueling is generally done using a fast regulated gas valve. Real-time control is achieved during the discharge using active feedback from the line-integrated density as measured by designated chords of the two-color interferometer (TCI). When generating H-modes, a flat density trace at a given density level is programmed for the flattop phase of the plasma. Typical values for the line-integrated target density are 0.6–1.2$\times 10^{20}$ m^{-2}, which corresponds to a range in average density of 1–2$\times 10^{20}$ m^{-3}. Feedback on the gas valve maintains this desired density in Ohmic and L-mode plasmas, but in H-mode the measured density generally exceeds the programmed density by a considerable margin. Thus, H-mode operation normally proceeds without additional gas fueling, and the plasma is fueled completely by recycling neutrals from the walls. This was the case in discharges previously discussed. The L-mode target density $\bar{n}_{e,L}$ does, however, provides a knob for adjusting the pedestal density in H-mode, while fixing parameters such as I_P, to which n_e is very sensitive. This section describes experiments meant specifically to examine the effects had on H-mode pedestals when varying L-mode density, and also attempts to provide additional fueling after H-mode formation.

6.3.1 L-mode fueling

Scalings derived from experiment in Ch. 5 indicated that at fixed plasma parameters, the value of $n_{e,\mathrm{PED}}$ depends on $\bar{n}_{e,L}$, despite the termination of active fueling upon H-mode formation. Because H-mode pedestal density is expected to be well correlated with neutral flux, the result suggests that the L-mode target density is responsible for setting a persistent fueling boundary condition at the LCFS. The dependence is not especially strong, however, with $n_{e,\mathrm{PED}} \propto \bar{n}_{e,L}^{0.4}$.

Using the scaling for guidance, the target density was varied over as wide a range

as possible while holding other quantities fixed. Typical profiles obtained at three distinct values of $\bar{n}_{e,L}$ are shown in Fig. 6-13. The values of current, field, shaping and input power are approximately the same from discharge to discharge. Qualitatively, the trends determined from the empirical scaling studies are reproduced. The density pedestal rises weakly with increased $\bar{n}_{e,L}$, while $T_{e,\mathrm{PED}}$ drops. The width of the pedestal region does not appear to change.

Pedestal density data as a function of $\bar{n}_{e,L}$ are shown in Fig. 6-14a. Consistent with the scaling of (5.5), doubling the target density resulted in a 30–40% increase in $n_{e,\mathrm{PED}}$. It is impossible to determine a distinct trend in Δ_{n_e} over this narrow range of density. Figure 6-14b shows widths from tanh-fits to time-averaged profiles, with typical error bars. Nothing very conclusive can be said about the width scaling from these data alone.

The Mahdavi model for determining the pedestal width Δ_{n_e} predicts a direct proportionality to the ionization mean free path λ_{ion}. Equations (2.3) and (2.5) can be recast as $\Delta_{n_e} = 2\lambda_{\mathrm{ion}}/E$ and compared with values from the experiment described above. Figure 6-15 shows pedestal widths of 2–4 mm that demonstrate no trend with $n_{e,\mathrm{PED}}$. The Δ_{n_e} here are determined from a tanh-fit to the combined ETS and probe profiles. Also plotted are the ionization MFP, using characteristic neutral temperatures in the pedestal to estimate v_n. (T_n is obtained from by running KN1D with the measured plasma profiles as inputs.) For these discharges, $\lambda_{\mathrm{ion}} \approx 3\text{–}4 \times \Delta_{n_e}$, which would imply a coefficient E of 6–8.

In the Mahdavi model, this factor is given by the ratio of flux expansion at the poloidal location of fueling θ_0 to that at the measurement location θ_m:

$$E = \frac{f(\theta_0)}{f(\theta_m)} = \frac{\frac{dx}{d\xi}|_{\theta=\theta_0}}{\frac{dx}{d\xi}|_{\theta=\theta_m}} \tag{6.8}$$

where x and ξ are coordinates representing radial distance from the LCFS and poloidal flux. To fit this model to the experimental data requires that the fueling be dominantly located in the divertor region, where the flux expansion is considerably larger than that at the ETS locations (see Fig. 3-5). However, on C-Mod, there is strong ev-

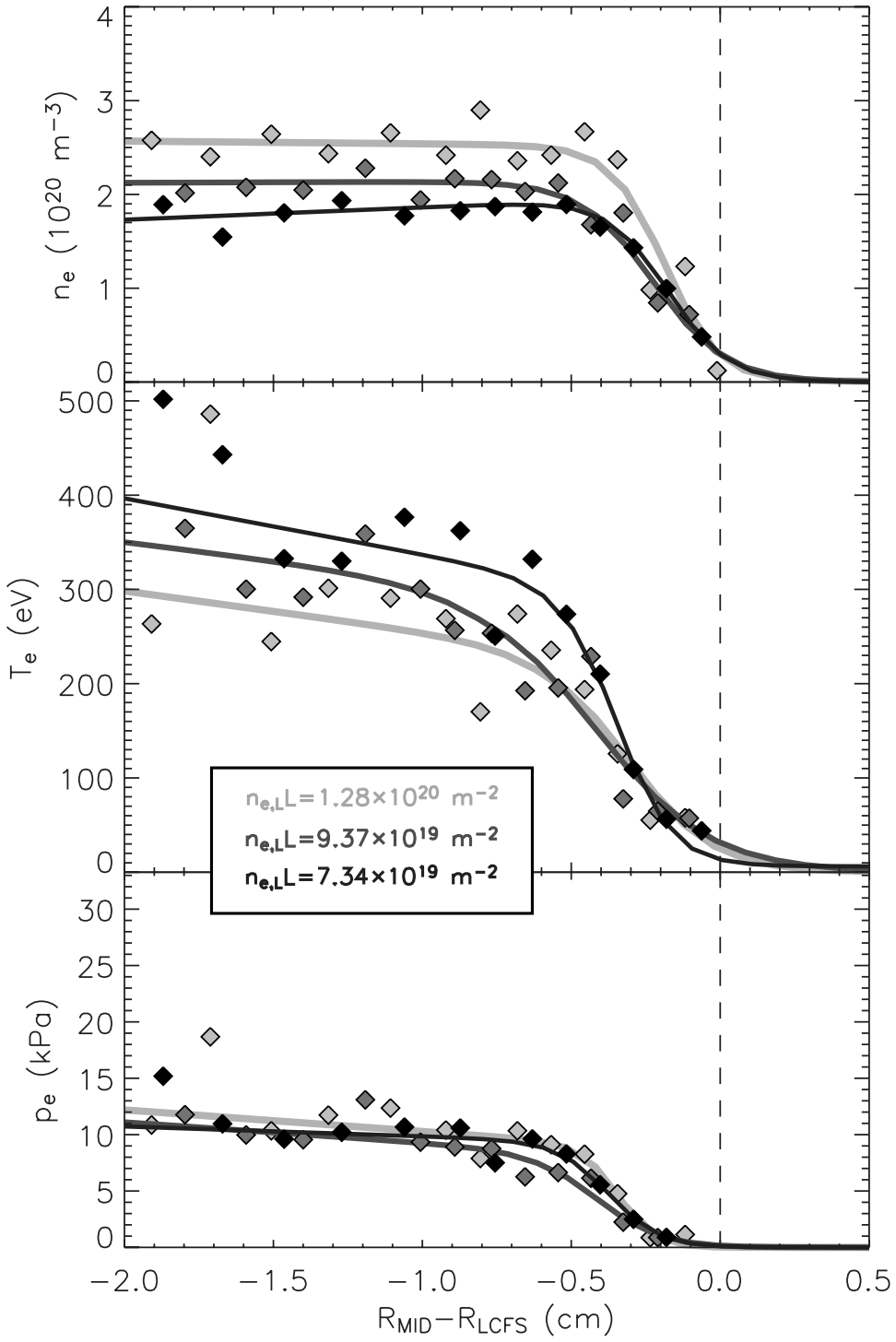

Figure 6-13: Sample profiles of edge n_e, T_e and p_e in a discharge-to-discharge scan of target density. The pedestal values behave as expected, and Δ variation is small.

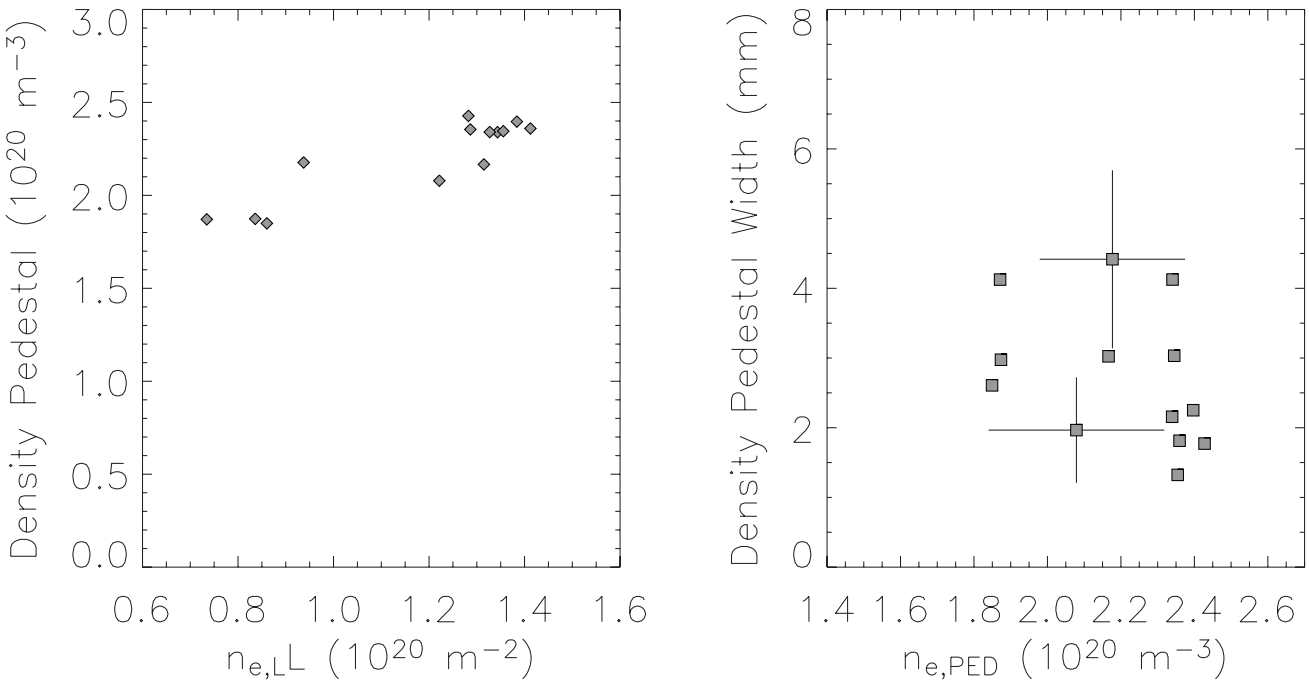

Figure 6-14: No significant variation in Δ_n is obtained when plasma parameters are fixed and target density is scanned. a.) Density pedestal as a function of line-integrated target density in 0.8MA, 5.4T plasmas, with input power regulated such that $T_{e,\mathrm{PED}} \approx 300$eV. The weakness of the scaling provides little useful range in $n_{e,\mathrm{PED}}$. b.) Pedestal width in same discharges, as function of $n_{e,\mathrm{PED}}$. Typical error bars are plotted for two points. Shaping in these discharges was fixed at κ=1.7, δ_U=0.35 and δ_L=0.5.

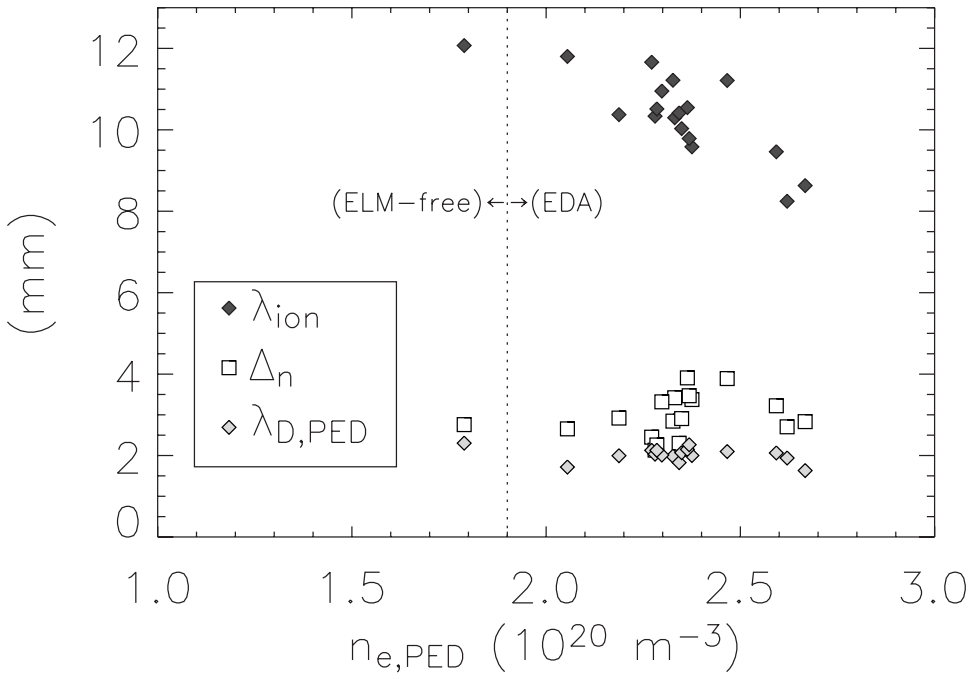

Figure 6-15: Characteristic scale lengths in the pedestal as $n_{e,\mathrm{PED}}$ is varied. The estimated ionization mean free path λ_{ion} goes inversely with plasma density, while the pedestal width Δ_n shows no systematic variation. The n_e data are from combined ETS and probe data. The quantity $\lambda_{\mathrm{D,PED}}$ is the e-folding length of the neutral density in the pedestal as determined from the kinetic neutral code KN1D (see Sec. 6.2).

idence that main chamber recycling is the dominant mode of plasma fueling. [38][152] In addition, the inverse correlation of ionization MFP with $n_{e,\mathrm{PED}}$ is not mirrored in the density width. Unfortunately, experimental diagnosis of the actual neutral penetration length is not available for this data set. However, KN1D was used to compute characteristic scale length of neutral density in the pedestal $\lambda_{\mathrm{D,PED}}$. These quantities, also shown in Fig. 6-15, are similar in magnitude to Δ_n. Taken altogether, these experimental data do not support the simple neutral penetration model of Mahdavi. However, based on these data, it is not possible to rule out a correlation of actual neutral penetration length, which differs considerably from λ_{ion}, with pedestal width.

6.3.2 Puffing into H-mode

Efforts were made to alter the neutral source characteristics in existing H-modes by aggressively fueling with D_2 puffs. By increasing the neutral density, presumably the

neutral flux at the LCFS is increased, resulting in higher core fueling and increased $n_{e,\mathrm{PED}}$. This would allow a further test for the inverse density width scaling. Also, by injecting gas at different locations, the poloidal distribution of the neutral source might be changed sufficiently to allow observations of relative changes in pedestal structure.

Time traces from an aggressively fueled H-mode are shown in Fig. 6-16. In this discharge, standard outboard fueling with feedback from TCI is used to regulate the L-mode target. An EDA H-mode is initiated at $t = 0.66$ s by application of 2.7 MW of ICRF power (6-16a). The plasma density (6-16b), edge temperature (6-16c) and stored energy (6-16d) rise and reach steady-state values in less than 100 ms. At around $t = 0.8$ s, a capillary on the inner wall begins releasing a flow of D_2 into the high-field side SOL. Over the next 0.5 s, the capillary releases approximately 80 torr-L of gas, corresponding to about 3×10^{21} D_2 molecules. The H-mode persists for about 100 ms before the plasma transitions back to a L-mode discharge, into which the inboard fueling continues until $t = 1.3$ s, when the plasma reaches the Greenwald density limit [153] and terminates disruptively. The gas input is evident in a visible image taken from the low-field side and viewing the inner wall. Figure 6-17 shows the camera view before and during the puff. The bright plume visible on the left side of the inner wall indicates the position of the gas capillary. Gas injected at this point tends to be swept along a flux tube, apparently by the ambient plasma flow, resulting in an elongated plume that extends toroidally and down towards the divertor. This strong ion flow pattern in lower single null plasmas has been confirmed using scanning probe measurements at various poloidal locations. [154]

Figure 6-16 shows that the plasma begins to respond to the gas puff at $t = 0.82$ s. Fueling increases, yielding a positive dN/dt, which persists until the H-L transition at $t = 0.92$ s. The concurrent decrease in stored energy is indicative of a falling global temperature, and a T_e drop of roughly 30% is indeed observed at the edge. Because auxiliary input power is stable during the H-mode puffing, core radiated power is dropping, and ohmic power can only increase as temperature drops, the trends point to a large amount of power being transported into the SOL as a result of the puff.

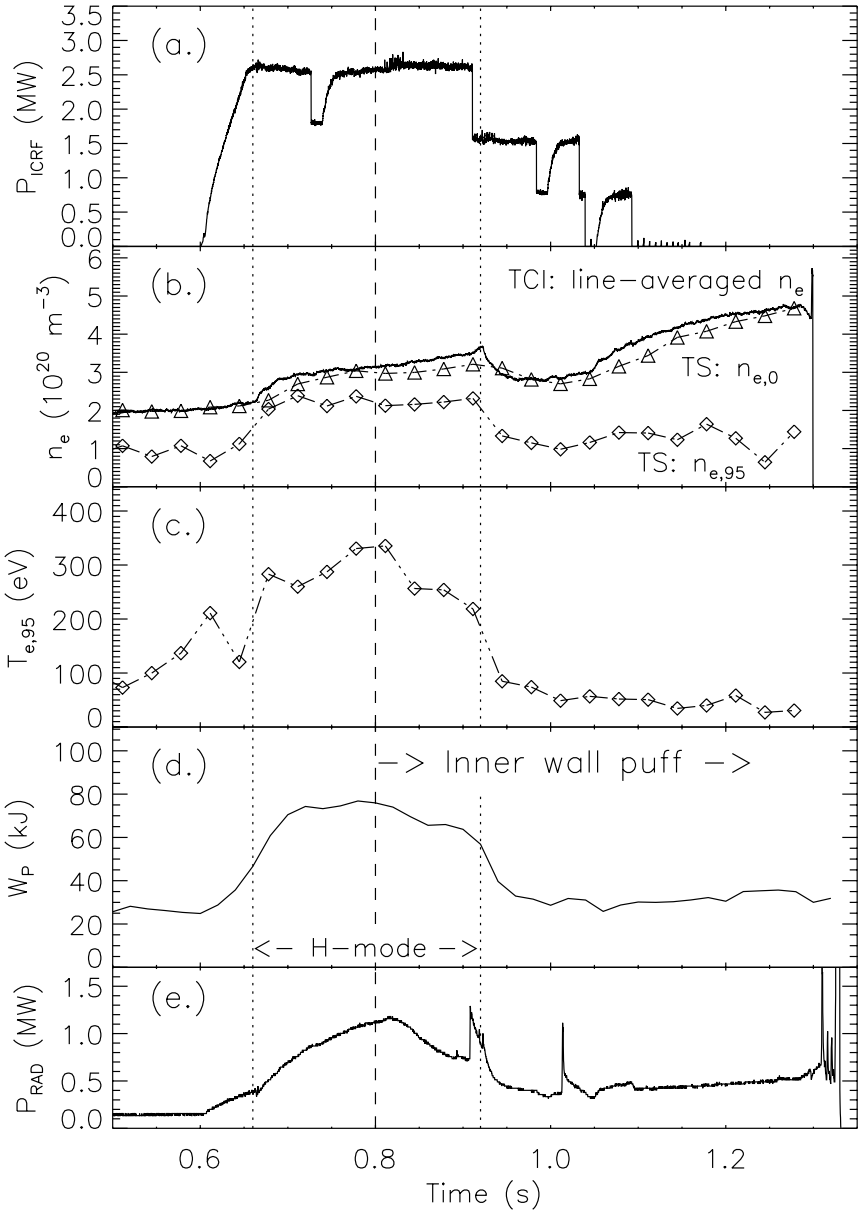

Figure 6-16: H-mode discharge with application of D_2 puff from inner wall. Time traces are a.) ICRF input power, b.) line-averaged density from TCI and both central (triangles) and edge (diamonds) n_e from TS, c.) $T_{e,95}$ from ETS, d.) plasma stored energy and e.) radiated power. Dotted vertical lines mark the L-H and H-L transitions. The dashed vertical line marks the puffing onset. Traces for an outer wall puff look similar.

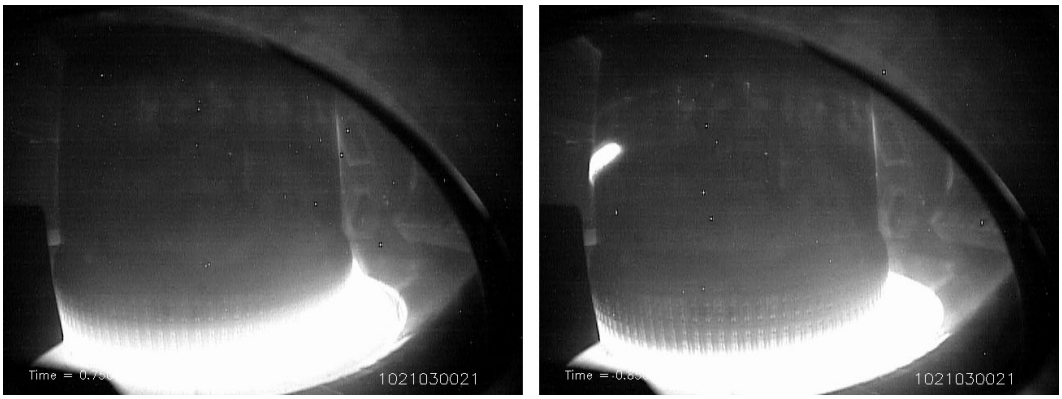

Figure 6-17: Video images of the inner column before and during H-mode D_2 puff. The frame at left is taken 90 ms after the L-H transition and before gas from the inner wall capillary begins flowing. The frame at right is taken approximately 70 ms after the gas puff begins. Neutrals injected into the high-field side SOL typically flow along field lines as they feel a viscous drag due to plasma flow.

Later in the discharge, as RF power is reduced, the L-mode fuels rapidly and the edge continues to cool as the Greenwald limit is approached.

One notable aspect of this H-mode is its relatively slow response to excess gas fueling. Assuming the gas from the capillary is injected uniformly in time, and assuming each D_2 molecule dissociates and ionizes, the expected rate of rise of plasma inventory is $dN/dt = 1.2 \times 10^{22}$ s^{-1}. Based on estimations from TCI measurements, the peak rate-of-rise following initiation of the gas puff is roughly 10–20% of this value, obtained in the L-mode portion of the discharge around $t = 1.05$ s. In the puffed phase of the H-mode, from $t = 0.82$ s to 0.92 s, dN/dt is even lower: approximately 4×10^{20} s^{-1}, based on TCI. Gas injected on the low-field side had an effect on the plasma of similar magnitude. The indication from these data are that aggressive gas puffing is an ineffective knob for bulk plasma fueling while in H-mode. Some of this effect may be due to the high rate of neutral flow parallel to field lines in the SOL. It is probable that significant neutral density is swept into the divertor region, significantly increasing the particle fueling time. Indications are that this effect should be stronger in plasmas with higher levels of input power and perhaps higher edge gradients. [154] Additionally, it is thought that the high density achieved in the C-Mod pedestal may act as an effective screen to additional neutral fueling. This will be addressed in some

detail in the next section.

Because the interferometer measurement is obtained along a chord that passes vertically through the plasma at $R = 68$ cm, it intersects both the core plasma and the SOL. Calculation of the line-averaged density is in practice done by assuming zero density outside the LCFS and dividing by the chord length in the core plasma L_C:

$$\bar{n}_e = \frac{1}{L_C}\int_{(C+S)} n_e dL = \frac{1}{L_C}\int_C n_e dL + \frac{1}{L_C}\int_S n_e dL \tag{6.9}$$

Here the integrals over C and S represent the chord lengths through the core and SOL plasma. Because of the additional contribution from the second term on the right hand side of this expression, this technique for determining the core $\bar{n}_e$ will always overestimate the core $\bar{n}_e$ when finite density exists in the SOL. The fractional error in the estimation can be approximated from the characteristic chord lengths and densities in the core and SOL

$$f_{\bar{n}_e} = \left(\frac{L_S}{L_C}\right)\left(\frac{n_{e,\mathrm{SOL}}}{n_{e,\mathrm{CORE}}}\right) \tag{6.10}$$

and could easily be 10–20% in certain discharges. As a consequence, the $\bar{n}_e$ in Fig. 6-16b is always greater than or equal to the TS central density.

The time behavior of the density shows that, during the puffed H-mode, the relative increase in the central and edge n_e from TS is smaller than the relative increase in $\bar{n}_e$ from TCI. Based on the equation above, the extra increase in the TCI trace is easily attributed to an enhanced n_e in the unconfined plasma. Therefore, the core plasma inside the LCFS appears to be screened from neutral fueling even better than the combined core and SOL. Detailed edge profiles obtained before and during gas puffing confirm this suggestion. The top two panels in Fig. 6-18 show ETS and probe profiles of n_e and T_e measured before and during puffing into H-mode. Regardless of whether the gas is injected on the outboard (left panel) or inboard side (right panel), the height of the n_e pedestal undergoes very little change, while the SOL denities are driven up by a factor of two. Simultaneous with the puff, $T_{e,\mathrm{PED}}$ is seen to drop. The lower panels show profiles of Ly_α emissivity, highly smoothed

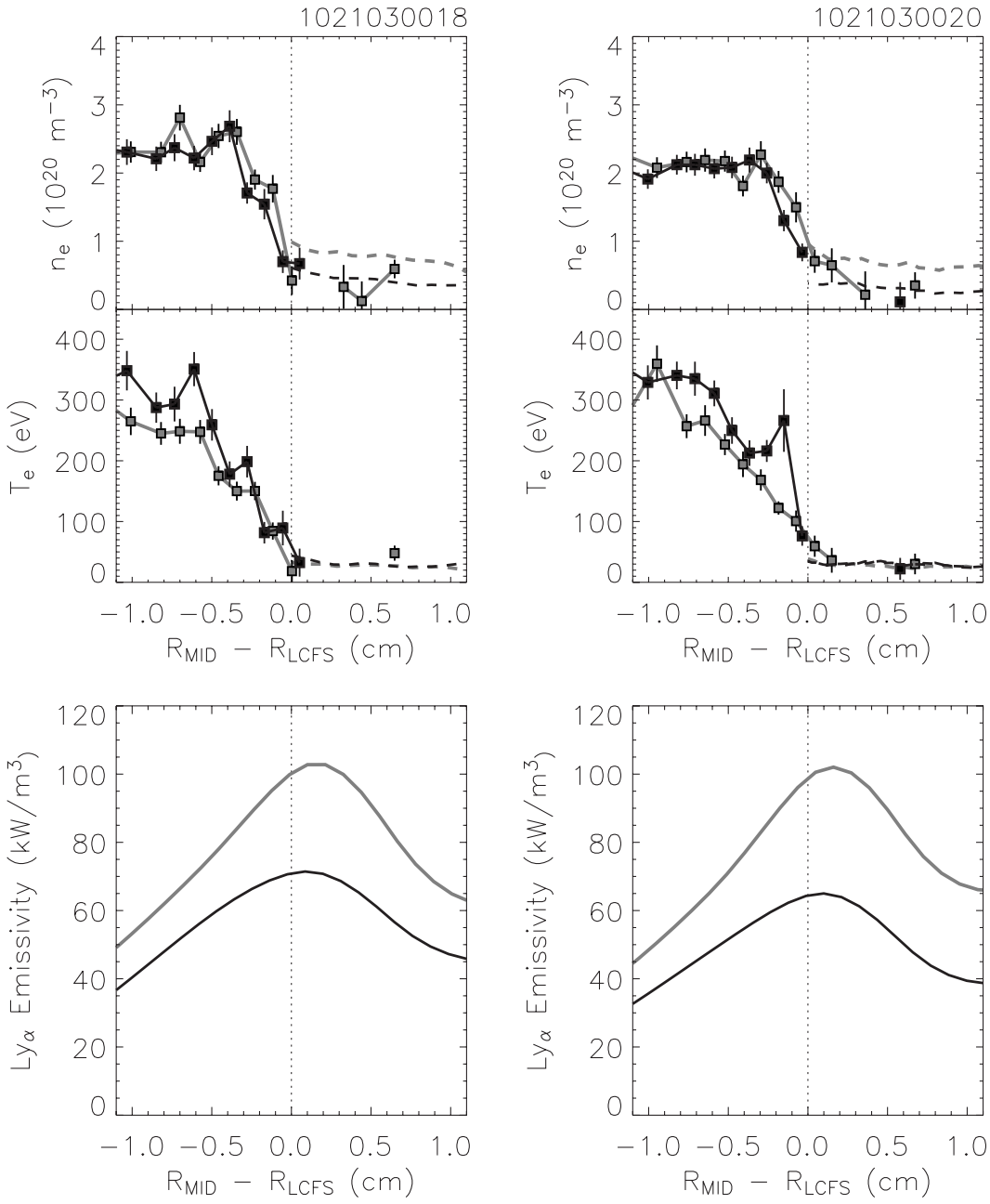

Figure 6-18: Edge profiles in H-mode before (black) and during (gray) gas puffing from distinct poloidal locations. Shown in the upper panels are n_e and T_e from both ETS (squares) and the scanning probe (dashed curves). The lower panels show Ly$_\alpha$ emissivity at the midplane. For discharge 1021030018, the puffing is from the low-field side of the tokamak; for 1021030020, the puff comes from the inner wall. Density and emissivity rise in the SOL, and changes in the pedestals, are independent of puffing location

for clarity, measured at the outboard midplane using the diode array described in Sec. 1.4.3. The edge neutral emissivity responds by nearly doubling, regardless of the poloidal location of the puff.

These measurements indicate that puffing gas into the vessel serves mainly to fill the the SOL with plasma, while having only a small effect on the net core fueling. Despite much higher levels of ionization and plasma density accumulating in the SOL, the H-mode plasma forms an effective barrier to core fueling. This is not to say that the pedestal profiles are unaffected. In fact, Fig. 6-19 shows a shift of the density pedestal toward the SOL during fueling from either inboard or outboard locations. This result is in stark contrast to the Mahdavi model for n_e pedestal formation, which predicts that increasing the neutral flux should result in both a larger value of $n_{e,\mathrm{PED}}$ and a narrower Δ, where Δ is determined from the distance between the pedestal top and the separatrix. In Fig. 6-19, the LCFS is determined from the point at which $T_e \approx 50$ eV, as required from a SOL power balance argument. [134] The Δ, as computed according to the Mahdavi methodology (*i.e.*, the distance between the pedestal top and the LCFS), is reduced by a factor of roughly two during the puff, despite the fact that $n_{e,\mathrm{PED}}$ stays essentially fixed.

Despite the discrepancy with the prediction of the Mahdavi model, it is clear that the pedestal characteristics are changed by the application of excess neutral fueling. Therefore, it is not reasonable to attribute ETB structure entirely to the diffusivity well or any other plasma physics alone. For a better understanding of how neutrals fuel the H-mode edge on C-Mod, a more sophisticated neutral transport model was desired.

6.4 1-D modeling and computation

The qualitative difference in density pedestal scalings and response to fueling in DIII-D and C-Mod prompted consideration of whether the fueling processes are strongly dependent on the overall plasma parameters. In particular, C-Mod operates at a much higher plasma density, and, as previously mentioned, ion-neutral collision

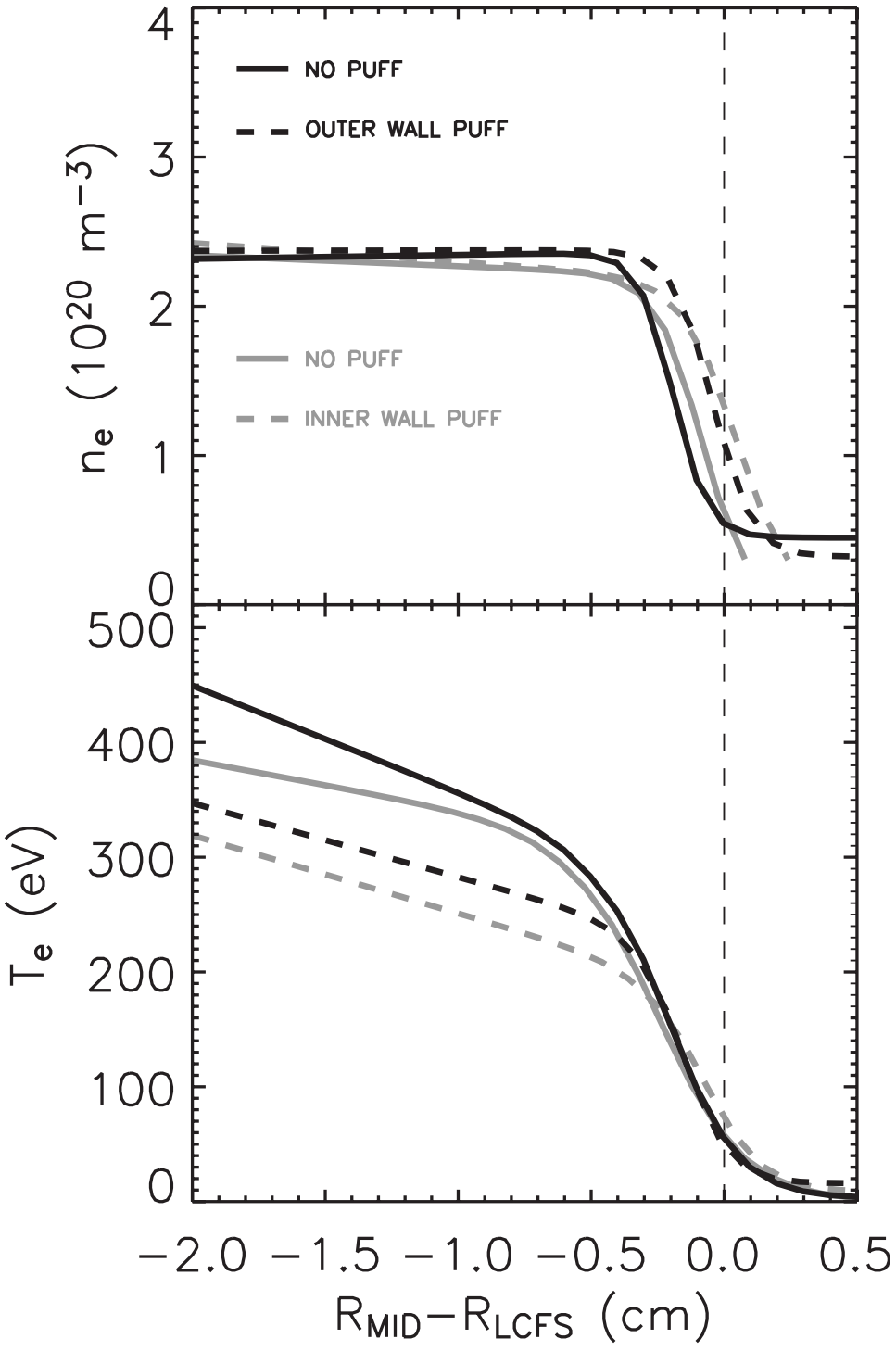

Figure 6-19: Time-averaged tanh-fit ETS profiles in EDA H-modes before and during gas puffing from both outer and inner walls. In the case of fueling from either location, $T_{e,\mathrm{PED}}$ is depressed, and the position of the n_e pedestal shifts outward relative to T_e. Characteristic gradients remain roughly fixed.

times are extremely short. It was concluded that if neutrals equilibrated thermally with ions in the pedestal, then much of the 1-D fluid modeling of Mahdavi *et al.* would lack applicability on C-Mod.

Work was done on C-Mod to expand the prior modeling and to account properly for the effect of charge exchange on the neutral population. The prior work, described in Sec. 2.2.2, assumed radial flux balance was satisfied and introduced an ionization rate to deplete neutrals. The model provided for neither momentum nor energy exchange between ions and neutrals in the pedestal, assuming that the neutrals traversed the pedestal region with velocity characteristic of neutral temperature T_n at the pedestal foot. Kinetic analysis using the KN1D code demonstrated a tendency for strong thermal equilibration between ions and neutrals, as well as an inward increase in the neutral drift velocity, particularly at high densities characteristic of C-Mod. Thus, ion-neutral interactions should not be overlooked.

Mossessian added the mechanism of charge exchange to the prior model and allowed the neutral temperature T_n to evolve in space. [126][155] This gives rise to what can be termed a "warm neutral" model, which can then be used to simulate density pedestals on C-Mod and other machines. The content of the model, and the numerical results from it, will be explained below.

6.4.1 The "warm neutral" model

The constitutive equations of the 1-D fluid model with CX are given as follows. The model is defined on the coordinate x, with $x = 0$ corresponding to the LCFS, and $x > 0$ being inside the core plasma. Subscripts of i and n stand for the ion and neutral species, and a subscript of 0 indicates the value of a given quantity at the LCFS.

Begin by assuming diffusive particle transport, characterized by an effective perpendicular diffusivity $D_\perp$:

$$\Gamma_i = -D_\perp \frac{dn_i}{dx} \tag{6.11}$$

As always, modeling particle transport with a diffusion coefficent is not to suggest

that the governing mechanism behind transport is purely diffusive. Choosing this form is for utility. Continuity relates ion flux Γ_i to the ionization source rate:

$$\frac{d\Gamma_i}{dx} = n_n n_i \langle \sigma v \rangle_{\text{ion}} \tag{6.12}$$

The ion flux is then balanced by the neutral flux:

$$\Gamma_i = -\Gamma_n = -(n_n v_n) \tag{6.13}$$

Plasma boundary conditions are imposed at the separatrix by taking the form of SOL density to be

$$n_{i,\text{SOL}} = n_{i,0} \exp\left(\frac{x}{\lambda_{\text{SOL}}}\right) \tag{6.14}$$

an assumption which is consistent with experimental observation. Also required is continuity of the n_i gradient at the LCFS:

$$\left.\frac{dn_{i,\text{SOL}}}{dx}\right|_0 = \left.\frac{dn_{i,\text{core}}}{dx}\right|_0 \Longrightarrow n_{n,0} v_{n,0} = \frac{D_{\perp,0} n_{i,0}}{\lambda_{\text{SOL}}} \tag{6.15}$$

The model thus far is essentially identical to that of Mahdavi *et al.*, and the equations can be solved analytically to produce the equations in 2.2.2. In this case, v_n and $D_\perp$ are assumed constant, and the resulting n_i pedestal is determined solely by the ionization length of D^0.

To examine the effects of thermal equilibration on the neutral population, and allow finite dv_n/dx, one proceeds to develop a momentum balance relation. This is derived from the Boltzmann equation for the atomic species:

$$v_x \frac{\partial f}{\partial x} = \left.\frac{\partial f}{\partial t}\right|_{\text{coll}} + S(x, v) \tag{6.16}$$

Multiplying by $m_n v_x d\vec{v}$ and integrating over velocity space gives the momentum balance equation for neutrals:

$$\frac{d}{dx}(kT_n n_n) + \frac{d}{dx}(m_n n_n v_n^2) = -m_n(v_n - v_i) n_n n_i \langle \sigma v \rangle_{\text{cx}} - m_n v_n n_n n_i \langle \sigma v \rangle_{\text{ion}} \tag{6.17}$$

The terms on the left represent, separately, the momentum flux divergence associated with the neutral temperature T_n and the drift velocity v_n. The first term on the right hand side represents the momentum source and sink due to charge exchange, and the second term is purely a sink of momentum due to ionization.

Using the reasonable assumptions that $n_n \ll n_i$ and $v_n < v_t$, where v_t is the thermal velocity of the neutrals, one can solve (6.12), (6.13) and (6.17) to obtain equations for the derivatives of neutral drift velocity and density:

$$\frac{dv_n}{dx} = -n_i \frac{\langle \sigma v \rangle_{\rm ion} v_t^2 - \langle \sigma v \rangle_{\rm cx} v_n^2}{v_t^2 - v_n^2} + \frac{v_n}{v_t^2 - v_n^2} \frac{dv_t^2}{dx} \tag{6.18}$$

$$\frac{dn_n}{dx} = n_n n_i v_n \frac{\langle \sigma v \rangle_{\rm ion} - \langle \sigma v \rangle_{\rm cx}}{v_t^2 - v_n^2} - \frac{n_n}{v_t^2 - v_n^2} \frac{dv_t^2}{dx} \tag{6.19}$$

These equations can be numerically integrated to produce n_n and v_n profiles, given appropriate cross-section values and ion densities. The thermal velocity of the neutrals is also needed to close the system of equations. While another level of sophistication could be added by introducing an energy balance equation into the model, it is expedient to utilize a kinetic solution of neutral transport to obtain $v_t = (kT_n/m_n)^{1/2}$. This is done below using KN1D.

To gain some intuitive feel for the physics inside these equations, one can make the further simplifying assumption that $v_n \ll v_t$. Then (6.18) and (6.19) can be written

$$\frac{1}{v_n}\frac{dv_n}{dx} = -\frac{n_i}{v_n}\left(\langle \sigma v \rangle_{\rm ion} - \langle \sigma v \rangle_{\rm cx} \frac{v_n^2}{v_t^2} \right) + \frac{1}{T_n}\frac{dT_n}{dx} \tag{6.20}$$

$$\frac{1}{n_n}\frac{dn_n}{dx} = \frac{n_i v_n}{v_t^2} \left(\langle \sigma v \rangle_{\rm ion} - \langle \sigma v \rangle_{\rm cx} \right) - \frac{1}{T_n}\frac{dT_n}{dx} \tag{6.21}$$

Though the above assumption is not always strictly satisfied, the transformed equations show a trait that is generally true. In many circumstances the $(dT_n/dx)/T_n$ terms in (6.20) and (6.21) tend to contribute significantly to, and even dominate, the right hand sides of the equations. The implication is that a large normalized gradient in T_n drives increased gradients in both v_n and n_n. Obtaining a large T_n gradient can occur easily if an ion temperature pedestal exists in the presence of high plasma

density, a condition well satisfied by the C-Mod edge.

6.4.2 Kinetic input to fluid modeling

As has been shown, KN1D efficiently produces the full velocity distribution of neutrals entering a plasma slab and undergoing ionization, charge exchange and elastic scattering. Given input profiles of plasma density and temperature, KN1D is capable of producing profiles of neutral density, temperature and drift velocity. Figure 6-20 shows sets of profiles from two KN1D runs using model pedestal profiles. In this and all modeling in this section, it is assumed that $T_i = T_e$ and $n_i = n_e$. The n_i and T_i pedestals are chosen to have typical widths of a few millimeters, $T_{i,\mathrm{PED}}$ is held fixed, and $n_{i,\mathrm{PED}}$ is varied by a factor of approximately 3 in order to examine the effects on thermal equilibration of neutrals and ions. Neutral temperature determined by KN1D is shown in 6-20b, compared to the input T_i. T_n more closely approaches T_i in the case of higher plasma density, indicating enhanced kinetic equilibration via ion-neutral interactions. Correspondingly, higher gradients in v_n and n_n are produced by KN1D for larger n_i (6-20c–d). Numerically integrating (6.18) and (6.19) for this case, using the KN1D values of T_n, produces the dashed curves in 6-20d, which agree quite well with the kinetic calculation in the pedestal region.

Density pedestal matching

A suitable application for this fueling model is the exploration of the relative effect of fueling on the determination of pedestal characteristics, for a given plasma transport model. The first step to developing this aspect is the generation of mutually consistent n_n and n_i profiles. A KN1D run for a given set of n_i and T_i profiles will yield several quantities necessary to the solution of the model equations for v_n and n_n. Both $T_n(x)$ and the boundary condition $v_n(0)$ are returned, as well as the $D_\perp$ profile obtained by combining (6.11) and (6.13):

$$D_\perp = (dn_i/dx)^{-1}\,\Gamma_n = (dn_i/dx)^{-1}\,n_n v_n \tag{6.22}$$

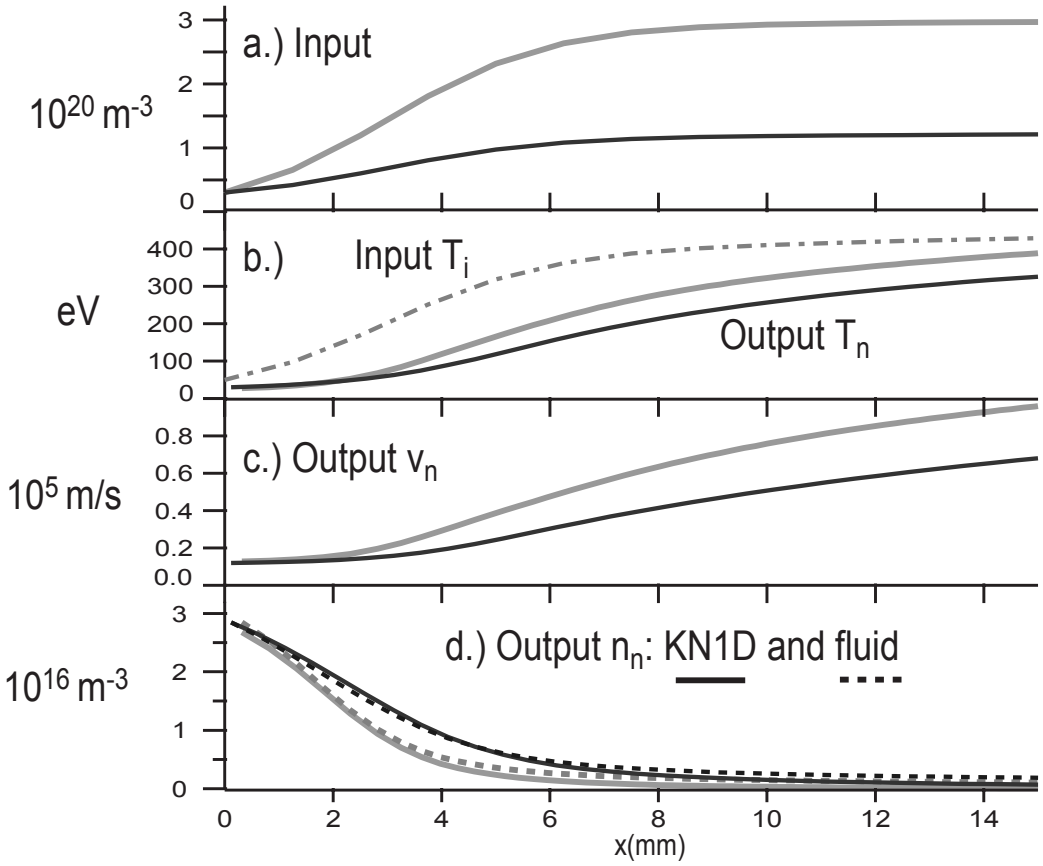

Figure 6-20: KN1D runs using model pedestal profiles with varying $n_{i,\mathrm{PED}}$. a.) Input $n_i = n_e$ for the two cases. b.) Output T_n in either case, alongside the input T_i profile. Temperature equilibration is significantly enhanced at the higher density. c.) Output v_n is also considerably increased at higher n_i. d.) Sharper n_n gradients result in the higher density case, in both KN1D output (solid curves) and in the results of the fluid model, supplemented with the T_n from KN1D (dashed curves). (Adapted from Ref. 155.)

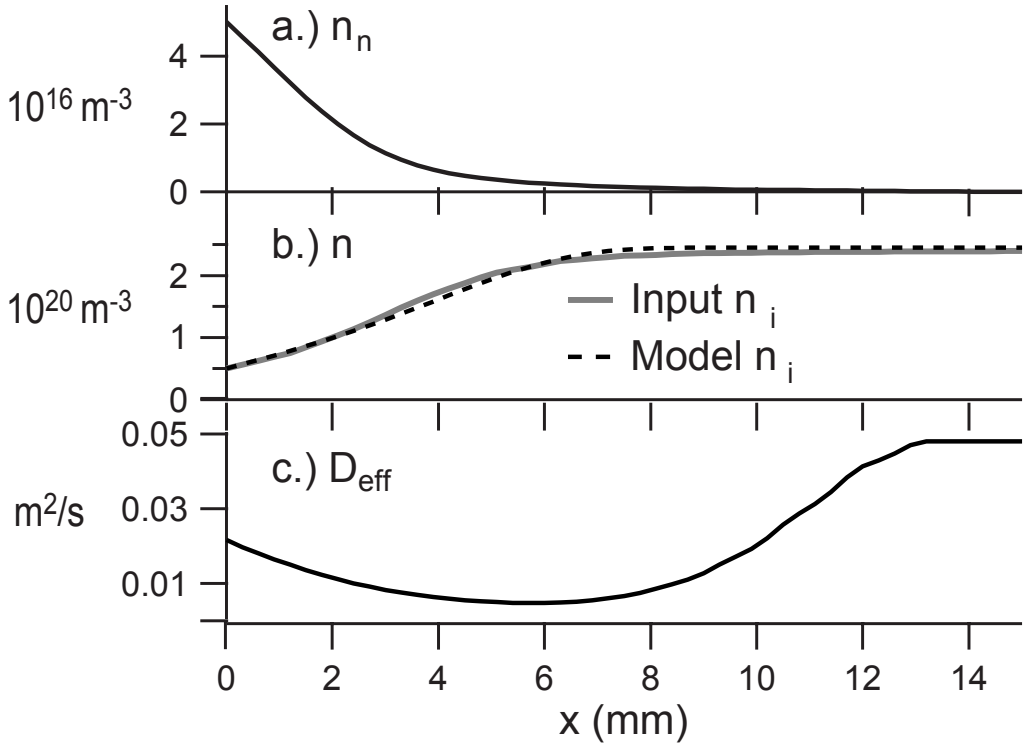

Figure 6-21: Results of matching n_i pedestal with the coupled kinetic-fluid neutral model (Step 1 of Fig. 6-22). a.) Neutral density. b.) Input n_i profile (solid curve) compared with the resulting n_i obtained from solving the model equations (dashed curve). c.) Corresponding effective diffusivity solution. (Adapted from Ref. 155.)

Equations (6.11), (6.18) and (6.19) are then solved, adjusting the values of $n_{n,0}$ and $D_{\perp,0}$ until a good match is had with the originally input n_i profile. Figure 6-21 shows typical results from this method. The agreement between the input and output n_i pedestal is satisfactory, and the magnitude of effective diffusivity is consistent with the wells inferred from measurements in Sec. 6.1.

Impact of increased fueling

Matching the ion pedestal makes up Step 1 of the method illustrated in Fig. 6-22. In Step 2 the effects of perturbations to the neutral fueling rate are investigated. Here an attempt is made to isolate the impact of neutrals from the plasma transport. Fixing the plasma diffusivity and the ion temperature, the model equations are solved again with a perturbed value of $n_n(0)$. Naturally, increasing the neutral density will

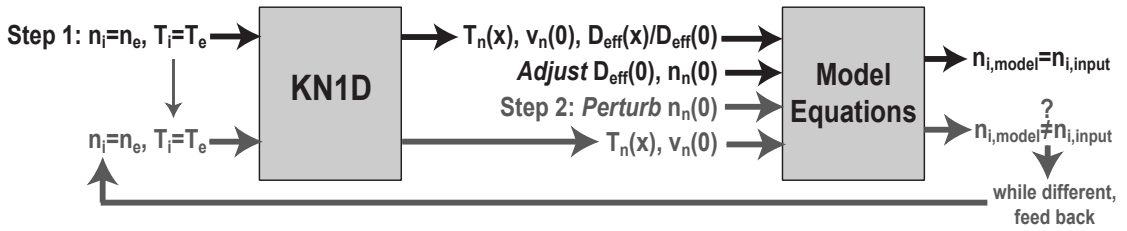

Figure 6-22: Method used to model the effect of neutral fueling changes on the pedestal. Step 1 integrates the fluid equations, given the kinetic results from KN1D, and sets up the diffusivity profile and neutral source needed to produce the model n_i pedestal. Step 2 (dark gray) involves adjusting the neutral source, then iteratively recalculating n_i from the fluid equations and regenerating KN1D results until a new n_i is obtained.

increase neutral flux and change the n_i pedestal solution so that it no longer matches the input profile. Therefore, KN1D has to be rerun with the modified n_i profile to yield new values of $T_n(x)$ and $v_n(0)$ as in Step 1. The solution of the fluid equations, followed by the calculation from KN1D, is repeated iteratively until the resultant n_i profiles converge. Throughout this process, the T_e and T_i profiles remain assumed fixed.

Based on a brief examination of (6.22), one might expect the n_i gradient to increase with neutral fueling. However, at the high densities typical of C-Mod operation, n_n gradients sharpen considerably as density is raised, and overall neutral penetration to the top of the pedestal is changed very little. Figure 6-23(a–d) demonstrates the trends that are observed in a model pedestal with the neutral density at the LCFS increased, and then decreased, by 20%. There are clear increases in the magnitudes of ∇n_n, ∇T_n and ∇v_n in the pedestal as plasma density, and hence atom-ion reaction rates, increases. The rollover in the computed v_n near the top of the pedestal is not consistent with KN1D results, in which v_n continues to rise with increasing x. This is a consequence of the model equations employing constant values of ionization and CX cross-sections, and it can be ignored, since it has no significant effect on the results in the pedestal. Throughout the pedestal region, the pedestal n_i locally increases, but the gradient remains largely unchanged. Furthermore, $n_{i,\mathrm{PED}}$ stays fixed. These results are qualitatively similar to the experimental results observed in the puffed H-

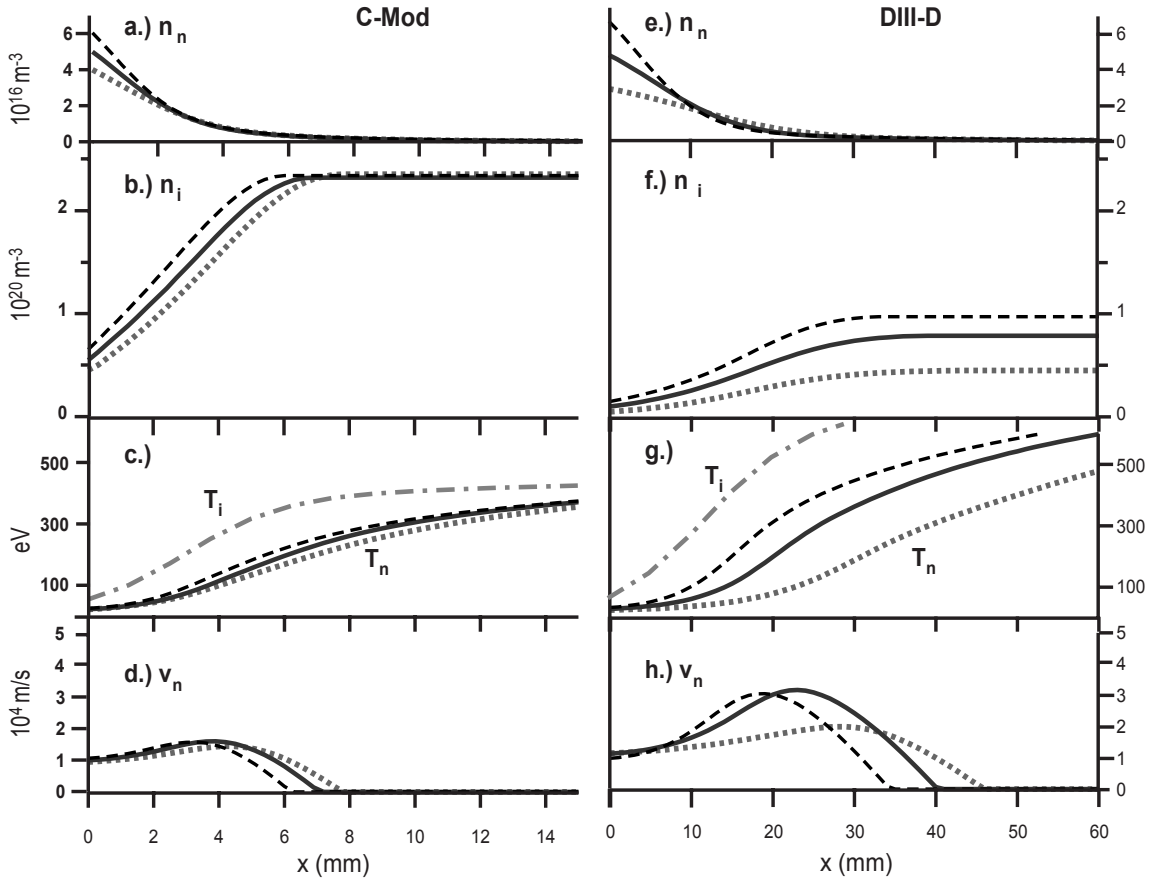

Figure 6-23: Results of perturbations to neutral source at LCFS while fixing plasma transport for both C-Mod and DIII-D, employing the method charted in Fig. 6-22. Plots at left illustrate what occurs when $n_n(0)$ is increased (dashed curves) and decreased (dotted curves) 20% from the nominal value determined by matching the original model n_i. a.) A sharpening of n_n gradient is observed with increasing density, along with b.) locally increased n_i. However, $|\nabla n_i|$ and $n_{i,\mathrm{PED}}$ remain unchanged. c.) shows the final T_n determined from KN1D, and d.) shows the v_n obtained from the fluid model equations. The rollover in v_n near the top of the pedestal is a result of using constant collision rates in the fluid model; no corresponding inflexion is seen in the KN1D results. Panels (e–h.) show the corresponding quantities in a similar exercise using typical DIII-D parameters (note the difference in x scales). In this case, $|\nabla n_i|$ and $n_{i,\mathrm{PED}}$ increase with increasing fueling. Qualitatively, these results agree with experimental observations on either machine. (Adapted from Ref. 155.)

modes discussed in Sec. 6.3.2. Compare specifically with the density pedestals shown in Fig. 6-19.

By contrast, when a larger tokamak operating at lower density is modeled in the same manner, an impact is had on the n_i pedestal when neutral fueling is changed. Fig. 6-23(e–h) show results from perturbing density in a pedestal characteristic of those observed on DIII-D. The major radius is about 2.5 times larger in this machine than in C-Mod, and a similar increase is seen in typical pedestal widths. Considerably smaller densities are also generally had. Raising and lowering $n_n(0)$ has a substantial corresponding effect on $n_{i,\mathrm{PED}}$, as well as ∇_{n_i}. This result is qualitatively similar to experimental results on DIII-D, in which puffing and pumping likewise affected the measured density pedestals (see Sec. 2.3.2). Along with the $n_{i,\mathrm{PED}}$ increase comes an overall increase in the temperature equilibration rate of the neutrals, leading, as in the C-Mod cases, to greater gradients in T_n, v_n and n_n in the pedestal region. Though ∇T_n and ∇v_n appear quite steep in the DIII-D case, their gradient scale lengths are actually longer than in the C-Mod case. (Note the difference in x scales.)

These data can be interpreted in the following way. Because plasma densities in the C-Mod case are high, temperature equilibration happens over a short distance. The equilibration length, and hence the gradient scale lengths of n_n and v_n in the pedestal region respond very little to changes in absolute density. In the DIII-D case, longer equilibration lengths mean that the T_n gradient will not dominate the determination of the n_n and v_n scale lengths. Thus, the pedestals behave as might be expected from 1-D modeling without temperature equilibration factored in. In fact, the lowest density case has a very flat v_n profile, consistent with the simple assumptions of that modeling.

This modeling, of course, has limitations and simplifications that should be considered. As with all fluid modeling on short spatial scales, the relation $\lambda_{\mathrm{MFP}} \ll L$ is not satisfied. This concern is partially addressed by incorporating a kinetic calculation for the ion-neutral thermal equilibration. Also, for n_n and v_n there is reasonable agreement in the region of interest between KN1D and the fluid equations. Another major drawback is the restriction of study to slab geometry, when the tokamak fuel-

ing problem has at least two dimensions (radial and poloidal) and, in which a third (toroidal) may play a role. Nonetheless, the 1-D fluid modeling with finite dT_n/dx gives some insight into the relevance of ion-neutral thermal equilibration in determining pedestal characteristics, and indicates that the problem can not generally be solved by using a simple ionization-based model.

6.5 Conclusions on particle transport

The results of this work on particle transport in the pedestal lead to some interesting conclusions. First, experimental measurements suggest a marked difference in the magnitude of plasma transport as plasma current is varied over a wide range. Much of the enhanced diffusivity that is inferred as I_P is lowered is likely due to the formation and increased effect of the QCM in the EDA edge. However, additional drives to plasma transport, such as enhancement to neoclassical diffusion, cannot be ruled out. Because $n_{e,\mathrm{PED}}$ scales linearly with I_P, and is fairly resistant to changes in other parameters, it is difficult to vary significantly the pedestal density without strongly affecting the plasma radial transport. Thus, evaluating the effect of neutral fueling on the pedestal is difficult experimentally.

The range in $n_{e,\mathrm{PED}}$ that is obtained by varying L-mode target density, while keeping other parameters fixed, allows for comparison with a simple theory of ionization MFP determining pedestal width. Kinetic calculation of neutral penetration in these discharges yields a measure of expected neutral penetration. The computed neutral penetration scale and the pedestal width are of similar magnitude. Both are much smaller than, and do not scale with λ_{ion}. A possible explanation for these results is that the plasma physics governing radial ion and electron transport sets the pedestal width, which in turn determines the radial decay length of the neutral density profile.

The warm neutral model highlights a potential mechanism for limiting the neutral density scale length. In the process of equilibrating with the bulk ions, neutrals feel a bulk acceleration toward the core, and a reduction in density exceeding that which would be given if only ionization were at work. This effect of ion-neutral equilibration

is potentially critical to understanding and predicting ETB structure on any high-density tokamak. Considering that ITER is designed to run closer to characteristic C-Mod densities than those of current larger tokamaks, it may be prudent to include this mechanism in any predictive pedestal model.

The limitations to these experimental and modeling results have been detailed above, and certainly should be addressed further. Additional neutral density data over a wider range of plasma parameters is desired to make more concrete statements about the scaling of transport coefficients, and experimental uncertainties need to be minimized. Additional work should be done to model the fueling process in more than one dimension, and to develop a better physical picture of the processes governing the complex transport phenomena, which are here encapsulated simply as "D_{eff}". The current work serves as a excellent starting point for this future work.

Chapter 7

Final Conclusions and Future Work

The work described in this thesis has contributed to the study of edge transport barriers on tokamaks, a critical topic for the development of fusion reactors as a power source. Because tokamak energy confinement depends strongly on the boundary condition imposed by the edge pedestal, one needs a predictive capability for the pedestal width and height before one can accurately model confinement on a future machine. The complete physical description of transport and stability needed to obtain this predictive capability does not yet exist. However, the continued efforts of modelers and experimentalists throughout the community help to refine existing knowledge and identify promising directions for future research.

7.1 Major contributions to ETB studies

A number of significant contributions to the field of ETB studies were made on Alcator C-Mod during the course of this thesis research, as discussed in Sec. 3.6. Chapters 4 through 6 highlighted some particularly important original work, which is recapitulated below. With the exception of the excellent density pedestal modeling described in Sec. 6.4, the presented analyses are primarily the work of the author. Naturally, though, this research benefited at every step from the assistance of the numerous individuals, specifically acknowledged on p. 5.

7.1.1 Millimeter resolution profile diagnosis

Key results from Chapters 3 and 4

Spurred by the apparently narrow ETB region on C-Mod, the ETS system was deployed in order to measure profiles of T_e and n_e with millimeter spatial resolution. As seen in Ch. 3, the diagnostic was successful, giving an unprecedented midplane radial resolution of 1.3 mm. Profiles were obtained with relatively small uncertainties in a temperature and density range characteristic of the pedestal region ($20 \lesssim T_e[\text{eV}] \lesssim 800$, $0.3 \lesssim n_e[10^{20}\ \text{m}^{-3}] \lesssim 5$). Study of these profiles allowed a thorough phenomenological description of the ETB and surrounding regions.

In Ch. 4, it is shown that supplementing ETS measurements with data obtained from other diagnostics allowed for excellent radial characterization of core, pedestal and SOL profiles. As demonstrated in Fig. 4-1, a richness in radial profile structure can exist in general. Though the bulk of the current work concentrates on the narrow ETB region within a few millimeters of the LCFS, the processes determining the gradient scale lengths in the SOL and in the core region are also of potential importance in determining total energy confinement. Presumably, though, the most critical region to understand is the pedestal region spanned by the ETS measurement. Here the profiles are readily fitted with a standard pedestal shape function for ease of analysis. The examination of a large data set of fitted pedestal parameters reveals typical pedestal widths of 2–6 mm, with $\Delta_T \gtrsim \Delta_n$, on average. The ability to diagnose n_e and T_e profiles with such small scale lengths was absent prior to operation of the ETS. Because the range of measured Δ is significantly above the lower limit of ETS resolution, it is safe to say that the width of the C-Mod pedestal is well characterized.

7.1.2 Pedestal characteristics in H-mode regimes

Further results from Chapter 4

Progress has been made in determining the existence criteria for certain H-mode regimes in terms of pedestal parameters. A particularly significant determination

has been the phase space of ELM-free and EDA H-modes. Because EDA H-modes demonstrate steady-state performance without large ELMs, while still maintaining relatively high energy confinement, the regime has been discussed as an attractive reactor regime. However, EDA can only be useful in this regard if the conditions for its existence are compatible with expected reactor parameters. Thus the current work has attempted to understand the conditions favoring EDA and the associated quasi-coherent mode.

The results of Sec. 4.3.3 show that the presence or absence of the QCM can be related to conditions near the edge, in particular edge density, temperature and safety factor. Results are consistent with both q and and $\nu^\star$ being critical parameters for the existence of EDA. Because the edge pedestal of a burning plasma experiment is expected to have low collisionality, due to very high edge temperature ($T_{e,\mathrm{PED}} >$ 1 keV), the QCM is not highly likely in such a device, and one should expect a future reactor to operate in another regime, such as the ELMy H-mode regime anticipated for ITER. However, there is experimental evidence that pressure gradient plays a comparable role in the presence or absence of the QCM, as illustrated in Fig. 4-7. It is conceivable, given these results, that the QCM physics may be relevant even at low $\nu^\star$, should sufficient pressure gradient exist.

7.1.3 Empirical scalings of the EDA H-mode pedestal

Key results from Chapter 5

A scaling study of pedestal parameters and associated plasma confinement was performed in EDA H-modes by varying operational parameters in controlled experiments. This study was intended both to enhance the understanding of the transport barrier in EDA and to determine relationships between operational parameters and the pedestal that could be compared to those on other tokamaks. As on other machines, core confinement depends strongly on edge conditions. As Ch. 5 shows, W_P scales in a nearly linear fashion with $p_{e,\mathrm{PED}}$, such that empirical confinement scalings to some degree are determined by the scalings of the edge pedestal.

In EDA at fixed plasma shape, the small pedestal width ($\Delta/a \approx 1$–3%) shows little systematic variation with plasma parameters. There are thus no obvious trends with which one can compare to theory, or to the width scalings determined on other experiments. The pedestal width does not appear to be determined by ion orbit loss mechanisms, as has been inferred under certain regimes of operation on JT-60U, DIII-D, JET and ASDEX Upgrade. Nor is there a clear inverse scaling of Δ_n with $n_{e,\mathrm{PED}}$, as would be expected if the density pedestal was determined by the neutral penetration length, as seen on DIII-D. That these scalings are not reproduced readily on C-Mod indicates that the physics setting ETB width can be highly specific to the tokamak in question, and that the physics determining the ETB extent may be quite sophisticated. This finding highlights the need for a more fundamental understanding, as a prerequisite for extrapolating pedestal widths to future machines.

Clear scalings are determined for the pedestal heights and gradients in EDA H-mode. Two of the most striking scalings concern the electron pressure and density pedestals. The p_e pedestal height and gradient both scale as $I_P^2 P_{\mathrm{SOL}}^{1/2}$, exhibiting a dependence on plasma current that is similar to the scalings found on JT-60U, DIII-D, JET and ASDEX Upgrade in the Type I ELMy regime. However, the EDA discharges under study exhibit no ELMs, and analysis has shown them to be stable to the ideal MHD modes responsible for these ELMs. It is possible that the I_P^2 scaling is related to the physics of the QCM, which, as discussed above, exists preferentially at both higher collisionality and normalized pressure gradient α_{MHD}. Next, it is seen that $n_{e,\mathrm{PED}}$ scales linearly with I_P, and more weakly with L-mode target density, indicating that neutral fueling plays a more limited role on setting the edge density than might be expected.

In an interesting departure from the pedestal results obtained on ELMy discharges in JT-60U, DIII-D, JET and ASDEX Upgrade, the pedestal gradients on C-Mod tend to relax as stronger shaping is obtained. Operating at higher triangularity is seen to lower the normalized density pedestal $n_{e,\mathrm{PED}}/I_P$ and pressure gradient $|\nabla p_e|/I_P^2$. Pedestal widths grow as well, and the effect is extremely pronounced when triangularity is scanned dynamically during a discharge.

7.1.4 Neutral fueling in a high density pedestal

Key results from Chapter 6

A number of experiments were initiated to answer questions surrounding the density pedestal, and the relative contributions to its structure from plasma transport and neutral fueling. This work, while still in a somewhat exploratory phase, reveals some potentially important aspects of pedestal physics. These findings ought to be considered in any attempt to build a predictive model for the pedestal on future machines.

First, high resolution profiles of deuterium neutral emissivity were obtained and used in concert with ETS and probe data to determine neutral density and ionization source rates in both the SOL and the pedestal. This made possible well-resolved inferences of neutral penetration length, fueling rate and effective plasma diffusivity through the pedestal and SOL region. As plasma current, and thus q is varied from one discharge to another, changes in profiles are observed which reflect differences in transport. The mid-pedestal D_{eff} increases as the plasmas transition from low-q to high-q, consistent with the QCM gaining strength and producing enhanced particle transport. The D_{eff} well is comparable in width to the density pedestal, and the local neutral density gradient scale lengths L_0 tend to be less than Δ_n, except for $n_{e,\text{PED}} \lesssim 1.5 \times 10^{20}$ m^{-3}, values typically obtained at low values of I_P. The experiment suggests the pedestal width is generally set by the extent of the plasma transport barrier, rather than the extent of neutral penetration, at least at the higher densities characteristic of typical C-Mod operation.

This conclusion is further supported by experimental attempts to change the neutral fueling of plasmas while fixing other discharge parameters such as field, current, and shape. Increasing the programmed target density increases the neutral source rate in L-mode discharges, and allows for satisfactory control of L-mode density. As discussed above, H-mode n_e pedestals achieve a value set largely by the discharge current, with a weaker dependence on the density obtained immediately before the L-H transition. Varying this target density over a wide range introduces a relatively

narrow spread in measured $n_{e,\mathrm{PED}}$, with no systematic variation in Δ_n. Neutral penetration lengths derived from a the kinetic neutral code KN1D are of the same order as, but slightly smaller than, Δ_n in this case, just as was shown in the experimental data taken at various I_P. These kinetic calculations and the experimental diagnosis described above represent an attempt to determine real neutral penetration lengths over a range of pedestal conditions, rather than rely on assumptions from theory.

Attempts to puff gas at the plasma after the H-mode is established show a low fueling rate for the core plasma, and no significant change in the values of $n_{e,\mathrm{PED}}$ or ∇n_e, as would be expected from simple fluid modeling of neutral fueling on the pedestal. A more sophisticated treatment, undertaken by Mossessian, considered momentum balance from charge exchange interactions and allowed for the thermal equilibration of neutrals with the bulk ion population. In this model, CX and elastic collisions between ions and neutrals sharply increase gradients in the neutral thermal velocity, the neutral drift velocity and the neutral density. The modeling suggests a different behavior of density pedestals in tokamaks of high and low density, which qualitatively matches data taken on C-Mod and DIII-D. In the small, high density tokamak, the pedestal height and gradient remain roughly fixed in response to neutral fueling perturbations; in the larger, low density tokamak, these pedestal quantities grow with increased source rate. The indication is that a complete pedestal model should include collisional processes that equilibrate neutrals with ions, particularly when the collision rates are high, as on high density tokamaks such as C-Mod (or ITER).

7.2 Directions for future work

Continued development of ETB research is important for the community at large, and also specifically for the Alcator C-Mod program. Many avenues for additional work can be proposed on C-Mod. Long term recommended steps include the development of improved edge diagnostics; dedicated SOL Thomson scattering and neutral emissivity profiles in multiple poloidal locations are good examples. Measurements

such as these diagnostics would provide would allow for more certain characterization of radial T_e and n_e profiles from core plasma to limiter, and would provide valuable information on the poloidal variation of neutral fueling. In the absence of these diagnostic enhancements, however, a number of short term opportunities for improvement exist.

The physics of the QCM and its effect on plasma transport can be further examined, both experimentally and computationally. Prior experimental shape scans of C-Mod plasmas indicated that having sufficient triangularity was important for EDA access. The character of the QCM at $\delta \gtrsim 0.5$ could be analyzed further, and the existence criteria in terms of edge plasma parameters compared to the results of Sec. 4.3.3, which were determined for discharges at moderate triangularity. Further simulations of the C-Mod H-mode edge can also be performed using 3-D turbulence simulations, as mentioned in Sec. 4.3.2. Plans exist to scan the input pedestal parameters within a series of such simulations; [144] this should verify whether the QCM is being correctly simulated and perhaps determine access conditions to EDA that can be compared with experimental results.

Plans are also afoot to extend the study of pedestal scalings into the broad range of machine parameters available on C-Mod ($0.4 < I_P[\mathrm{MA}] < 2.0$, $2.6 < B_T[\mathrm{T}] < 8.0$), while supplying levels of ICRF heating in the range of 1–5 MW. [156] By doing so, one may determine separate pedestal and confinement scalings for ELM-free H-modes and for discharges exhibiting small ELMs, analagous to the relationships developed for EDA in Ch. 5. This will allow for a systematic comparison across regimes on C-Mod. In addition, ELM-free scalings may provide a better comparison to pedestal scalings on other tokamaks. This experimental plan calls for continued diagnosis of pedestal profiles (ETS), SOL profiles (probes) and neutral emissivity throughout the edge (GPI camera), in order that a more careful analysis of plasma and neutral transport, such as that performed in Ch. 6, can be attempted.

Additional data and modeling are essential to refining the analyses begun in Ch. 6. Fully characterizing the trends in ETB diffusivity will require more experimental data with accurate neutral emissivity diagnostics. Such data are expected to be

collected during the scaling extension experiment described above. There is also room for further experimentation and modeling in the context of H-mode fueling. A quantitative comparison between gas puff modeling results and the experimentally measured edge parameters would be very useful, particularly over a range of pedestal densities. This has the potential to further resolve the relative contributions of plasma physics and neutral fueling to determining pedestal structure. Such work could prove essential to building a complete pedestal model for ITER or any subsequently built tokamak.

Appendix A

Benchmarking KN1D

In order to increase confidence in KN1D solutions to the neutral transport problem, some comparisons were made with the widely used Monte Carlo neutral transport code DEGAS 2. [157][158] By tracking large numbers of particles as they encounter collisions with the background medium, and maintaining energy statistics at each point in the computational grid, DEGAS 2 is capable of producing a binned energy distribution that can be compared with the kinetically computed $f(E_{\rm D})$ from KN1D. Likewise it is easy to compare directly $n_{\rm H}$ and $T_{\rm H}$ computed by both codes. A successful benchmark results when mutually consistent results are obtained from runs in either code with identical geometry and a matching physics model. A relatively simple test case is described below.

The initial test case chosen was a comparison of DEGAS 2 to a 1-D analytic fluid model solution in a dense, low temperature plasma. [159] The DEGAS 2 case was run on a 2-D box with side walls that act as mirrors, and with profile variation only along the length of the box, simulating a slab geometry. This case was well suited for direct comparison with KN1D.

In the DEGAS 2 test case, profiles of plasma density and temperature are specified along the length of the box, with T_i linear between 1 eV at $x = 0$ m and 10 eV at $x = 1$ m. Density is chosen to maintain constant ion pressure: $n_i(x) = p_i/T_i(x)$, where $p_i = 8.5 \times 10^{19}\mathrm{eV/m}^3$. Neutral hydrogen atoms are inserted at $x = 0$ with a temperature of 1 eV. Neutrals are reflected from the $x = 0$ surface, as well as the

side walls, and the $x = 1$ surface is an exit. The analytic solution in [159] neglects viscosity, ionization and recombination, and thus the only reaction considered in the DEGAS 2 simulation is hydrogen-proton charge exchange (CX).

Because the test case includes no H_2 molecules, only the atomic module of KN1D, Kinetic_H, is useful for this benchmark. In order to model the same physics as in the test case, the elastic scattering terms are turned off, as is recombination. Ionization cannot be explicitly toggled off in Kinetic_H; therefore electron temperature is set to 0.2 eV everywhere in order to maintain an insignificant number of ionizations. The initial neutral distribution function is a one-sided 1 eV Maxwellian at $x = 0$, with a positively-directed neutral flux having the same value as the DEGAS 2 case: $\Gamma_0 = 5 \times 10^{18}$ m^{-2}s^{-1}. The standard form of Kinetic_H assumes that the $x = 0$ surface is an exit for neutrals, rather than a mirror, as the DEGAS 2 simulation assumed. Under this assumption, a much higher input flux is required for Kinetic_H to match the DEGAS 2 neutral density, because of the high rate of CX reflection from the plasma slab.

In order to better match the geometry of the DEGAS 2 case, the Kinetic_H code was altered to allow reflection of neutrals at $x = 0$. At the end of each neutral generation, the modified Kinetic_H reflects the portion of f_{H} with $v_x < 0$ about $v_x = 0$ and uses this as input to the subsequent generation. Because particles are not lost from the $x = 0$ surface, the input flux used in the DEGAS 2 simulation is adequate to reproduce the n_{H} profile. This neutral density is simply the numerical integral of the distribution function:

$$n_{\mathrm{H}}(x) = \int\int f_{\mathrm{H}}(v_r, v_x, x)(2\pi v_r) dv_r dv_x \tag{A.1}$$

The following moments are typically taken by KN1D to determine bulk hydrogen velocity $V_{x,\mathrm{H}}$ and temperature T_{H}:

$$V_{x,\mathrm{H}}(x) = \frac{\Gamma_{\mathrm{H}}(x)}{n_{\mathrm{H}}(x)} = \frac{1}{n_{\mathrm{H}}(x)} \int\int v_x f_{\mathrm{H}}(v_r, v_x, x)(2\pi v_r) dv_r dv_x \tag{A.2}$$

$$T_{\mathrm{H}}(x) = \frac{p_{\mathrm{H}}(x)}{n_{\mathrm{H}}(x)} = \frac{1}{n_{\mathrm{H}}(x)} \frac{m_{\mathrm{H}}}{3} \int\int [v_r^2 + (v_x - V_{x,\mathrm{H}})^2] f_{\mathrm{H}}(v_r, v_x, x)(2\pi v_r) dv_r dv_x \quad \text{(A.3)}$$

It can be seen from (A.3) that Kinetic_H subtracts out the x-directed drift velocity before computing the temperature and separately outputs the mean drift and the spread of the neutral distribution function, as though f_{H} were a shifted Maxwellian. However, DEGAS 2 returns an effective neutral temperature that does not subtract the drift term. This can be computed from Kinetic_H results according to

$$T_{\mathrm{H,eff}}(x) = \frac{p_{\mathrm{H,eff}}(x)}{n_{\mathrm{H}}(x)} = \frac{1}{n_{\mathrm{H}}(x)} \frac{m_{\mathrm{H}}}{3} \int\int (v_r^2 + v_x^2) f_{\mathrm{H}}(v_r, v_x, x)(2\pi v_r) dv_r dv_x \quad \text{(A.4)}$$

The direct comparisons of n_{H} and $T_{\mathrm{H,eff}}$ for this test case are shown in Fig. A-1. As neutrals diffuse by CX along the length of the plasma, they gain energy from the ions. $T_{\mathrm{H,eff}}$ increases, and is slightly less than T_i over most of the length of the plasma slab. For $x \lesssim 2$ cm, the effective neutral temperature is higher than T_i, as a result of high energy H returning from downstream CX reactions with hotter ions. An acceleration is felt in the neutral drift, which can be seen immediately from the persistently negative value of dn_{H}/dx. Since neutral flux is constant, this corresponds to a positive $dV_{x,\mathrm{H}}/dx$. The ratio of drift velocity to thermal velocity $v_{t,\mathrm{H}}$ increases from a few percent for $x < 0.5$ m to roughly half near the exit at $x = 1$ m.

As one might expect, results of this KN1D run were sensitive to the CX cross-section chosen as input. While the default CX cross-section in KN1D is taken from a compilation by Janev, *et al.* [160, p272], the DEGAS 2 benchmark employed a more accurate $\langle \sigma v \rangle_{\mathrm{CX}}$ determined by Janev and Smith. [161, p78] To match DEGAS 2, the Janev-Smith formula was compiled in place of the default cross-section, giving the good agreement of Fig. A-1. Using the default cross-sections, which are almost twice as large, the n_{H} gradient from KN1D is systematically larger. Based on these results, subsequent runs with KN1D employed the Janev-Smith cross-section. Obtaining this level of agreement also provided insight into detailed algorithm requirements, such as minimum grid-spacing and convergence criteria.

The results of benchmarking against DEGAS 2 have shown that the process of proton-hydrogen charge exchange is modeled correctly. There are, of course, many

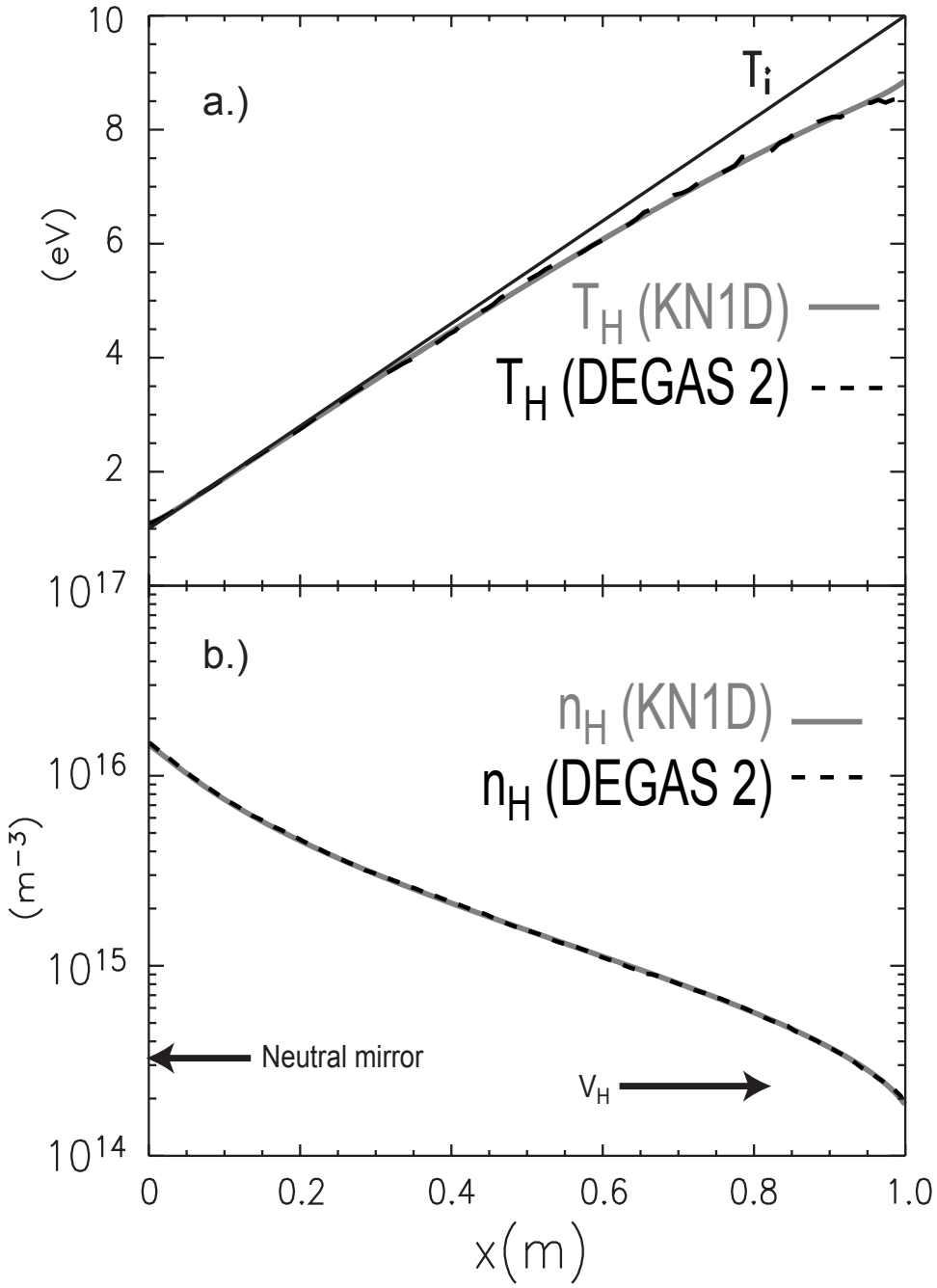

Figure A-1: Comparison of a.) neutral temperature and b.) density in a simple 1-D benchmark of KN1D (solid curves) against DEGAS 2 (dashed curves). Neutrals launched from or reflected from the "mirror" surface at $x = 0$ undergo CX with ions, gaining bulk velocity and equilibrating their temperature with the plasma ions. T_i ranges from 1 to 10 eV as shown, and n_i is such that p_i is constant everywhere.

other important reactions important to the results of a KN1D run, including ionization and elastic scattering of atoms, and a great number of molecular reactions. The implementation of these reactions in KN1D should be evaluated as well.

Bibliography

[1] I. H. Hutchinson *et al.* First results from Alcator-C-MOD. *Phys. Plasmas*, 1(5):1511–1518, May 1994.

[2] Eric Alan Nelson-Melby. *Observations and Theory of Mode-Converted Ion Bernstein Waves in the Alcator C-Mod Tokamak.* PhD thesis, Massachusetts Institute of Technology, Cambridge, Massachusetts, February 2002. Appendix A.

[3] Francis F. Chen. *Introduction to Plasma Physics and Controled Fusion*, volume 1. Plenum Press, New York, second edition, 1984.

[4] Kenro Miyamoto. *Plasma Physics for Nuclear Fusion.* MIT Press, Cambridge, Massachusetts, revised edition, 1987.

[5] Nicholas A. Krall and Alvin W. Trivelpiece. *Principles of Plasma Physics.* San Francisco Press, San Francisco, 1986.

[6] John Wesson. *Tokamaks.* Clarendon Press, Oxford, third edition, 2004.

[7] M. Kotschenreuther *et al.* Quantitative predictions of tokamak energy confinement from first-principles simulations with kinetic effects. *Phys. Plasmas*, 2(6):2381–2389, June 1995.

[8] C. S. Pitcher *et al.* The relation of edge confinement to global confinement in ASDEX Upgrade (Axially Symmetric Divertor Experiment). *Phys. Plasmas*, 4(7):2577–2583, July 1997.

[9] W. Suttrop *et al.* Identification of plasma-edge-related operational regime boundaries and the effect of edge instability on confinement in ASDEX Upgrade. *Plasma Phys. Control. Fusion*, 39(12):2051–2066, December 1997.

[10] T. H. Osborne *et al.* H-mode pedestal characteristics, ELMs, and energy confinement in ITER shape discharges on DIII-D. *Plasma Phys. Control. Fusion*, 40(5):845–850, May 1998.

[11] M. Greenwald *et al.* H mode confinement in Alcator C-Mod. *Nucl. Fusion*, 37(6):793–807, June 1997.

[12] F. Wagner *et al.* Regime of improved confinement and high beta in neutral-beam-heated divertor discharges of the ASDEX tokamak. *Phys. Rev. Lett.*, 49(19):1408–1412, November 1982.

[13] ITER Physics Basis Editors *et al.* Chapter 1: Overview and summary. *Nucl. Fusion*, 39(12):2137–2174, December 1999. ITER Physics Basis Special Issue.

[14] L. L. Lao *et al.* Reconstruction of current profile parameters and plasma shapes in tokamaks. *Nucl. Fusion*, 25(11):1611–1622, November 1985.

[15] Jeffrey P. Friedberg. *Ideal Magnetohydrodynamics*. Plenum, New York, 1987.

[16] H. Zohm. Edge localized modes (ELMs). *Plasma Phys. Control. Fusion*, 38(2):105–128, February 1996.

[17] Y. Lin *et al.* Upgrade of reflectometry profile and fluctuation measurements in Alcator C-Mod. *Rev. Sci. Instrum.*, 70(1):1078–1081, January 1999.

[18] Y. Takase *et al.* Radiofrequency-heated enhanced confinement modes in the Alcator C-Mod tokamak. *Phys. Plasmas*, 4(5):1647–1653, May 1997.

[19] M. Greenwald *et al.* Characterization of enhanced Dα high-confinement modes in Alcator C-Mod. *Phys. Plasmas*, 6(5):1943–1949, May 1999.

[20] M. Greenwald *et al.* Studies of EDA H-mode in Alcator C-Mod. *Plasma Phys. Control. Fusion*, 42(5A):A263–A269, May 2000.

[21] E. Marmar *et al.* Enhanced D-alpha H-mode studies in the Alcator C-Mod tokamak. In *Proceedings of the 18th Fusion Energy Conference*, page EX2/5, Vienna, 2001. International Atomic Energy Agency. IAEA-CN-77.

[22] A. E. Hubbard *et al.* Pedestal profiles and fluctuations in C-Mod enhanced D-alpha H-modes. *Phys. Plasmas*, 8(5):2033–2040, May 2001.

[23] J. A. Snipes *et al.* The quasi-coherent signature of enhanced D_α H-mode in Alcator C-Mod. *Plasma Phys. Control. Fusion*, 43(4):L23–L30, April 2001.

[24] A. Mazurenko *et al.* Experimental and theoretical study of quasicoherent fluctuations in enhanced D_α plasmas in the Alcator C-Mod tokamak. *Phys. Rev. Lett.*, 89(22):225004–1–4, November 2002.

[25] Y. Kamada *et al.* Growth of the edge pedestal in JT-60U ELMy H-mode. *Plasma Phys. Control. Fusion*, 41(11):1371–1379, November 1999.

[26] W. Suttrop *et al.* Effects of type-I edge-localized modes on transport in ASDEX Upgrade. *Plasma Phys. Control. Fusion*, 40(5):771–774, May 1998.

[27] V. P. Bhatnagar *et al.* Edge localized modes and edge pedestal in NBI and ICRF heated H, D and T plasmas in JET. *Nucl. Fusion*, 39(3):353–367, March 1999.

[28] L. Zeng *et al.* Dynamics of pedestal perturbations by ELMs and edge harmonic oscillations in DIII-D. *Plasma Phys. Control. Fusion*, 46(5A):A121–A129, May 2003.

[29] J. W. Hughes *et al.* High-resolution edge Thomson scattering measurements on the Alcator C-mod tokamak. *Rev. Sci. Instrum.*, 72(1):1107–1110, January 2001.

[30] D. A. Mossessian, A. Hubbard, and J. Irby. Performance of Alcator C-Mod core Thomson scattering system. *Rev. Sci. Instrum.*, 70(1):759–762, January 1999.

[31] E. S. Marmar *et al.* High resolution visible continuum imaging diagnostic on the Alcator C-Mod tokamak. *Rev. Sci. Instrum.*, 72(1):940–943, January 2001.

[32] P. J. O'Shea, A. E. Hubbard, and the Alcator C-Mod group. Nine channel polychromator for fast T_e measurements on Alcator C-Mod. In *Proceedings of the Ninth Joint Workshop on Electron Cyclotron Emission and Electron Cyclotron Heating*, pages 393–401, Borrego Springs, California, 1995.

[33] B. LaBombard *et al.* Experimental investigation of transport phenomena in the scrape-off layer and divertor. *J. Nucl. Mater.*, 241–243:149–166, February 1997.

[34] I. H. Hutchinson. *Principles of Plasma Diagnostics.* Cambridge University Press, Cambridge, second edition, 2002.

[35] K. Kadota, M. Otsuka, and J. Fujita. Space- and time-resolved study of impurities by visible spectroscopy in the high-density regime of JIPP T-II tokamak plasma. *Nucl. Fusion*, 20(2):209–212, February 1980.

[36] D. Mossessian *et al.* Measurements and scalings of the H-mode pedestal on Alcator C-mod. *Plasma Phys. Control. Fusion*, 42(5A):A255–A262, May 2000.

[37] Earl Marmar. Personal communication. May 2000.

[38] B. LaBombard *et al.* Cross-field plasma transport and main-chamber recycling in diverted plasmas on Alcator C-Mod. *Nucl. Fusion*, 40(12):2041–2060, December 2000.

[39] A. R. Striganov and N. S. Sventitskii. *Tables of Spectral Lines of Neutral and Ionized Atoms.* IFI/Plenum, New York, 1968. Translated from Russian.

[40] L. C. Johnson and E. Hinnov. Ionization, recombination, and population of excited levels in hydrogen plasmas. *J. Quant. Spectrosc. Radiat. Transf.*, 13(4):333–358, April 1973.

[41] R. L. Boivin *et al.* High resolution measurements of neutral density and ionization rate in the Alcator C-Mod tokamak. *Rev. Sci. Instrum.*, 72(1):961–964, January 2001.

[42] Mark L. Adams. Brief comments on tangential Ly_α optical depths in Alcator C-Mod. Memorandum, December 2002.

[43] Brian LaBombard. Personal communication. 2002.

[44] S. J. Zweben *et al.* Edge turbulence imaging in the Alcator C-Mod tokamak. *Phys. Plasmas*, 9(5):1981–1989, May 2002.

[45] R. J. Groebner. An emerging understanding of H-mode discharges in tokamaks. *Phys. Fluids B*, 5(7):2343–2354, July 1993.

[46] K. H. Burrell. Effects of $E \times B$ velocity shear and magnetic shear on turbulence and transport in magnetic confinement devices. *Phys. Plasmas*, 4(5):1499–1518, May 1996.

[47] V. B. Lebedev, P. H. Diamond, and B. A. Carreras. Transport bifurcation fronts and the H-mode pedestal width problem. *Bull. Am. Phys. Soc.*, 44:275, 1999.

[48] R. L. Boivin *et al.* Effects of neutral particles on edge dynamics in Alcator C-Mod plasmas. *Phys. Plasmas*, 7(5):1919–1926, May 2000.

[49] M. A. Mahdavi *et al.* Physics of pedestal density profile formation and its impact on H-mode density limit in burning plasmas. *Phys. Plasmas*, 42(10):3984–3991, October 2003.

[50] R. J. Groebner *et al.* Study of H-mode threshold conditions in DIII-D. In *Fusion Energy 1996: Proceedings of the 16th International Conference on Fusion Energy*, volume 1, pages 867–873, Vienna, 1997. International Atomic Energy Agency. IAEA-CN-64.

[51] R. J. Groebner and T. N. Carlstrom. Critical edge parameters for H-mode transition in DIII-D. *Plasma Phys. Control. Fusion*, 40(5):673–677, May 1998.

[52] A. E. Hubbard. Physics and scaling of the H-mode pedestal. *Plasma Phys. Control. Fusion*, 42(5A):A15–A35, May 2000.

[53] K. C. Shaing, E. C. Crume, Jr., and W. A. Houlberg. Bifurcation of poloidal rotation and suppression of turbulent fluctuations: A model for the L-H transition in tokamaks. *Phys. Fluids B*, 2(6):1492–1498, June 1990.

[54] K. C. Shaing. Poloidal magnetic field dependence of the edge electric field layer width in the H mode in tokamaks. *Phys. Fluids B*, 4(2):290–291, February 1992.

[55] Kimitaka Itoh and Sanae-I Itoh. The role of the electric field in confinement. *Plasma Phys. Control. Fusion*, 38(1):1–49, January 1996.

[56] W. Engelhardt and W. Feneberg. Influence of an ergodic magnetic limiter on the impurity content in a tokamak. *J. Nucl. Mater.*, 76–77:518–520, September–October 1978.

[57] F. Wagner and K. Lackner. Divertor tokamak experiments. In D. E. Post and R. Behrisch, editors, *Physics of Plasma-Wall Interactions in Controlled Fusion*, volume 131 of *NATO Advanced Science Institutes Series B: Physics*, pages 931–1004. North Atlantic Treaty Organization, Plenum Press (in cooperation with NATO Scientific Affairs Division), 1986.

[58] M. A. Mahdavi *et al.* High performance H mode plasmas at densities above the Greenwald limit. *Nucl. Fusion*, 42(1):52–58, January 2002.

[59] R. J. Groebner *et al.* The role of neutrals in high-mode (H-mode) pedestal formation. *Phys. Plasmas*, 9(5):2134–2140, May 2002.

[60] P. C. Stangeby. On the relative roles of neutral transport and plasma transport in the formation of the density pedestal in magnetically confined plasmas. *J. Phys. D: Appl. Phys.*, 36(22):2784–2797, November 2003.

[61] Weston M. Stacey. Structure of the edge density pedestal in tokamaks. *Phys. Plasmas*, 11(9):4295–4304, September 2004.

[62] F. L. Hinton and G. M. Staebler. Particle and energy confinement bifurcation in tokamaks. *Phys. Fluids B*, 5(4):1281–1288, April 1993.

[63] J. W. Connor, R. J. Hastie, and J. B. Taylor. Shear, periodicity, and plasma ballooning modes. *Phys. Rev. Lett.*, 40(6):396–399, February 1978.

[64] H. R. Wilson and J. W. Connor. Ballooning instabilities, poloidal flow and the temperature pedestal at the tokamak edge. In *Proceedings of the 24th European Physical Society Conference on Controlled Fusion and Plasma Physics*, volume 21A part I of *Europhysics Conference Abstracts*, pages 289–292, Geneva, 1997. European Physcial Society.

[65] H. R. Wilson *et al.* Influence of the plasma edge on tokamak performance. In *Proceedings of the 17th Fusion Energy Conference*, page TH3/2, Vienna, 1999. International Atomic Energy Agency. IAEA-CN-69.

[66] S. I. Braginskii. *Reviews of Plasma Physics*, volume 1, chapter 3, pages 205–311. Consultants Bureau, New York, 1965.

[67] B. N. Rogers and J. F. Drake. Diamagnetic stabilization of ideal ballooning modes in the edge pedestal. *Phys. Plasmas*, 6(7):2797–2801, July 1999.

[68] M. Sugihara *et al.* A model for H mode pedestal width scaling using the International Pedestal Database. *Nucl. Fusion*, 40(10):1743–1755, October 2000.

[69] M. Kotschenreuther et al. First principles calculations of tokamak energy transport. In *Fusion Energy 1996: Proceedings of the 16th International Conference on Fusion Energy*, volume 2, pages 371–383, Vienna, 1997. International Atomic Energy Agency. IAEA-CN-64/D1-5.

[70] A. Kitsunezaki *et al.* JT-60 program. *Fusion Sci. Technol.*, 42(2–3):179–184, September/November 2002. JT-60 Program Review Special Issue.

[71] J. L. Luxon. A design retrospective of the DIII-D tokamak. *Nucl. Fusion*, 42(5):614–633, May 2002.

[72] Albrecht Herrmann and Otto Gruber. Chapter 1: ASDEX Upgrade - Introduction and overview. *Fusion Sci. Technol.*, 44(3):569–577, November 2003. ASDEX Upgrade Review Special Issue.

[73] P.H Rebut, R. J. Bickerton, and B. E. Keen. The Joint European Torus - Installation, 1st results and prospects. *Nucl. Fusion*, 25(9):1011–1022, September 1985.

[74] Y. Kamada *et al.* Fusion plasma performance and confinement studies on JT-60 and JT-60U. *Fusion Sci. Technol.*, 42(2–3):185–254, September/November 2002. JT-60 Program Review Special Issue.

[75] T. Hatae *et al.* Comparison of edge pedestal parameters for JT-60U and DIII-D H-mode plasmas. *Plasma Phys. Control. Fusion*, 42(5A):A283–A288, May 2000.

[76] M. Mori, the JT-60 Team, and the JFT-2M Team. Overview of the recent experimental results in JT-60 and JFT-2M. *Plasma Phys. Control. Fusion*, 36(7A):A39–A49, July 1994.

[77] T. Hatae *et al.* Characteristics of edge pedestal width in JT-60U ELM-free H-mode plasmas. *Plasma Phys. Control. Fusion*, 40(6):1073–1083, June 1998.

[78] Y. Kamada *et al.* Onset condition for ELMs in JT-60U. *Plasma Phys. Control. Fusion*, 38(8):1387–1391, August 1996.

[79] E. J. Doyle *et al.* Modifications in turbulence and edge electric fields at the L-H transition in the DIII-D tokamak. *Phys. Fluids B*, 3(8):2300–2307, August 1991.

[80] P. Gohil, K. H. Burrell, and T. N. Carlstrom. Parametric dependence of the edge radial electric field in the DIII-D tokamak. *Nucl. Fusion*, 38(1):93–102, January 1998.

[81] R. J. Groebner and T. H. Osborne. Scaling studies of the high mode pedestal. *Phys. Plasmas*, 5(5):1800–1806, May 1998.

[82] R. L. Miller *et al.* Ballooning mode stability for self-consistent pressure and current profiles at the H-mode edge. *Plasma Phys. Control. Fusion*, 40(5):753–756, May 1998.

[83] P. B. Snyder *et al.* Characterization of peeling-ballooning stability limits on the pedestal. *Plasma Phys. Control. Fusion*, 46(5A):A131–A141, May 2004.

[84] T. H. Osborne *et al.* The effect of plasma shape on H-mode pedestal characteristics on DIII-D. *Plasma Phys. Control. Fusion*, 42(5A):A175–A184, May 2000.

[85] R. J. Groebner *et al.* Comparison of H-mode barrier width with a model of neutral penetration length. *Nucl. Fusion*, 44(1):204–213, January 2004.

[86] P. Breger *et al.* Plasma-edge gradients in L-mode and ELM-free H-mode JET plasmas. *Plasma Phys. Control. Fusion*, 40(3):347–359, March 1998.

[87] J. Lingertat *et al.* The edge operational space in JET. *J. Nucl. Mater.*, 266-269:124–130, March 1999.

[88] G. Saibene *et al.* The influence of isotope mass, edge magnetic shear and input power on high density ELMy H modes in JET. *Nucl. Fusion*, 39(9):1133–1156, September 1999.

[89] G. Saibene *et al.* Comparison of core and edge characteristics of NB and ICRH ELMy H-modes in JET. In *Proceedings of the 26th Conference on Controlled Fusion and Plasma Physics*, volume 23J of *Europhysics Conference Abstracts*, pages 97–100, Geneva, June 1999. European Physcial Society.

[90] Wolfgang Suttrop *et al.* Chapter 6: H-mode and pedestal physics in ASDEX Upgrade. *Fusion Sci. Technol.*, 44(3):636–649, November 2003. ASDEX Upgrade Review Special Issue.

[91] W. Suttrop *et al.* Effect of plasma shape variation on ELMs and H-mode pedestal properties in ASDEX Upgrade. *Plasma Phys. Control. Fusion*, 42(5A):A97–A102, May 2000.

[92] T. Onjun *et al.* Models for the pedestal temperature at the edge of H-mode tokamak plasmas. *Phys. Plasmas*, 9(12):5018–5030, December 2002.

[93] T. Hatae *et al.* Understanding of H mode pedestal characteristics using the multimachine pedestal database. *Nucl. Fusion*, 41(3):285–294, March 2001.

[94] A. E. Hubbard *et al.* Measurements of the high confinement mode pedestal region on Alcator C-Mod. *Phys. Plasmas*, 5(5):1744–1751, May 1998.

[95] P. C. Stek. *Reflectometry Measurements on Alcator C-Mod.* PhD thesis, Massachusetts Institute of Technology, Cambridge, Massachusetts, March 1997.

[96] I. H. Hutchinson *et al.* Edge transport barrier phenomena in Alcator C-Mod. *Plasma Phys. Control. Fusion*, 41(3A):A609–A616, March 1999.

[97] T. Sunn Pedersen and R. S. Granetz. Edge x-ray imaging measurements of plasma edge in alcator c-mod. *Rev. Sci. Instrum.*, 70(1):586–590, January 1999.

[98] John Sheffield. *Plasma Scattering of Electromagnetic Radiation.* Academic Press, New York, 1975.

[99] N. J. Peacock *et al.* Measurement of the electron temperature by Thomson scattering in Tokamak, T3. *Nature*, 224(5218):488–490, November 1969.

[100] T. Matoba *et al.* Thomson scattering measurements on ohmically heated plasmas in the JFT-2 Tokamak. *Jpn. J. Appl. Phys.*, 18(3):611–619, March 1979.

[101] D. Johnson *et al.* TFTR edge Thomson scattering system. *Rev. Sci. Instrum.*, 57(8, pt.2):1810–1812, August 1986.

[102] H. Salzmann *et al.* The LIDAR thomson scattering diagnostic on JET. *Rev. Sci. Instrum.*, 59(8, pt.2):1451–1456, August 1988.

[103] B. LeBlanc *et al.* The PBX-M Thomson scattering system. *Rev. Sci. Instrum.*, 61(11):3566–3569, November 1990.

[104] T. N. Carlstrom *et al.* The multipulse thomson scattering diagnostic on the diii-d tokamak. *14th IEEE/NPSS Symposium. Fusion Engineering. Proceedings (Cat. No.91CH30355-3)*, pages 1195–1198, 1992.

[105] C. J. Barth *et al.* PROMT: a multiposition Thomson-scattering system for RTP. *Rev. Sci. Instrum.*, 63(10, pt.2):4947–4949, October 1992.

[106] P. Pizzolati *et al.* The Frascati Tokamak Upgrade Thomson scattering system: the optical and spectral analysis equipments. *Rev. Sci. Instrum.*, 63(10, pt.1):4403–4409, October 1992.

[107] T. Yamauchi *et al.* The JFT-2M TV Thomson scattering system. *Jpn. J. Appl. Phys. 1, Regul. Pap. Short Notes*, 31(7):2255–2259, July 1992.

[108] H. Murmann *et al.* The Thomson scattering systems of the ASDEX upgrade tokamak. *Rev. Sci. Instrum.*, 63(10, pt.2):4941–4943, October 1992.

[109] T. Hatae *et al.* First operation results of YAG laser Thomson scattering system on JT-60U. *Fusion Eng. Des.*, 34–35:621–624, March 1997.

[110] Alan W. DeSilva. The evolution of light scattering as a plasma diagnostic. *Contrib. Plasma Phys.*, 40(1):9–22, April 2000.

[111] D. Dimock *et al.* A compact Thomson scattering system. *Rev. Sci. Instrum.*, 68(1):700–703, January 1997.

[112] John David Jackson. *Classical Electrodynamics*. John Wiley & Sons, New York, third edition, 1999.

[113] Continuum. *Operation and Maintenance Manual for the Powerlite 9000 Series Laser*. Santa Clara, CA, October 1993.

[114] Francis A. Jenkins and Harvey E. White. *Fundamentals of Optics*. McGraw-Hill, New York, third edition, 1957.

[115] Reich Watterson and Kuo-in Chen. Status of the Alcator C-MOD scanning two-dimensional Thomson scattering diagnostic. *Rev. Sci. Instrum.*, 61(10):2867–2869, October 1990.

[116] J. W. Hughes *et al.* Thomson scattering upgrades on Alcator C-Mod. *Rev. Sci. Instrum.*, 74(3):1667–1670, March 2003.

[117] A Bregni and L Giudicotti. Background plasma light subtraction by delay line techniques for a Thomson scattering apparatus. *J. Phys. E: Sci. Instrum.*, 15(12):1310–1312, December 1982.

[118] C. L. Hsieh *et al.* Silicon avalanche photodiode detector circuit for Nd:YAG laser scattering. *Rev. Sci. Instrum.*, 61(10):2855–2857, October 1990.

[119] J. A. Stillerman *et al.* MDSplus data acquisition system. *Rev. Sci. Instrum.*, 68(1):939–942, January 1997.

[120] H. Röhr. Rotational Raman scattering of hydrogen and deuterium for calibrating Thomson scattering devices. *Phys. Lett. A*, 81(8):451–453, February 1981.

[121] F. Flora and L. Giudicotti. Complete calibration of a Thomson scattering spectrometer system by rotational Raman scattering in H_2. *Appl. Opt.*, 26(18):4001–4008, September 1987.

[122] C. M. Greenfield *et al.* Real-time digital control, data acquisition, and analysis system for the DIII-D multipulse Thomson scattering diagnostic. *Rev. Sci. Instrum.*, 61(10):3286–3288, October 1990.

[123] Donald W. Marquardt. An algorithm for least-squares estimation of nonlinear parameters. *J. Soc. Ind. Appl. Math.*, 11(2):431–441, June 1963.

[124] Robert Granetz. Personal communication. 2002.

[125] J. W. Hughes *et al.* Observations and empirical scalings of the high-confinement mode pedestal on Alcator C-Mod. *Phys. Plasmas*, 9(7):3019–3030, July 2002.

[126] D. A. Mossessian, J. W. Hughes, and B. LaBombard. On the role of atomic physics in formation of the H-mode pedestal. To be published, 2005.

[127] D. A. Mossessian *et al.* High-confinement-mode edge stability of Alcator C-mod plasmas. *Phys. Plasmas*, 10(5):1720–1726, May 2003.

[128] D. A. Mossessian *et al.* Edge dimensionless identity experiment on DIII-D and Alcator C-Mod. *Phys. Plasmas*, 10(3):689–698, March 2003.

[129] A. E. Hubbard and *et al.* Variation of edge gradients with heat flux across L-H and H-L transitions in Alcator C-Mod. *Plasma Phys. Control. Fusion*, 44(5A):A359–A366, May 2002.

[130] A. E. Hubbard and *et al.* Local threshold conditions and fast transition dynamics of the L-H transition in Alcator C-Mod. *Plasma Phys. Control. Fusion*, 46(5A):A95–A104, May 2004.

[131] B. LaBombard *et al.* Particle transport in the scrape-off layer and its relationship to discharge density limit in Alcator C-Mod. *Phys. Plasmas*, 8(5):2107–2117, May 2001.

[132] R. S. Granetz *et al.* Scaling of H-mode pedestal characteristics in DIII-D and C-Mod. In *Proceedings of the 17th Fusion Energy Conference*, page EX6/2, Vienna, 1999. International Atomic Energy Agency. IAEA-CN-69.

[133] A. E. Hubbard *et al.* Pedestals and confinement in Alcator C-Mod H-modes. In *Proceedings of the 26th Conference on Controlled Fusion and Plasma Physics*, volume 23J of *Europhysics Conference Abstracts*, pages 13–16, Geneva, June 1999. European Physcial Society.

[134] Peter C. Stangeby. *The Plasma Boundary of Magnetic Fusion Devices*. Institute of Physics Publishing, Bristol, 2000.

[135] Alexander Mazurenko. *Phase Contrast Imaging on the Alcator C-Mod Tokamak*. PhD thesis, Massachusetts Institute of Technology, Cambridge, Massachusetts, July 2001.

[136] Yijun Lin. *Experimental Application and Numerical Study of Reflectometry in the Alcator C-Mod Tokamak*. PhD thesis, Massachusetts Institute of Technology, Cambridge, Massachusetts, May 2001.

[137] I. H. Hutchinson *et al.* High-field compact divertor tokamak research on Alcator C-Mod. In *Fusion Energy 1996: Proceedings of the 16th International Conference on Fusion Energy*, volume 1, pages 155–165, Vienna, 1997. International Atomic Energy Agency. IAEA-CN-64.

[138] D. A. Mossessian *et al.* H-mode pedestal characteristics and MHD stability of the edge plasma in Alcator C-Mod. *Plasma Phys. Control. Fusion*, 44(4):423–437, April 2002.

[139] O. Sauter, C. Angioni, and Y. R. Lin-Liu. Neoclassical conductivity and bootstrap current formulas for general axisymmetric equilibria and arbitrary collisionality regime. *Phys. Plasmas*, 6(7):2834–2839, July 1999.

[140] J. W. Connor *et al.* Magnetohydrodynamic stability of tokamak edge plasmas. *Phys. Plasmas*, 5(7):2687–2700, July 1998.

[141] P. B. Snyder *et al.* Edge localized modes and the pedestal: A model based on coupled peelingballooning modes. *Phys. Plasmas*, 9(5):2037–2043, May 2002.

[142] B. N. Rogers, J. F. Drake, and A. Zeiler. Phase space of tokamak edge turbulence, the L-H transition, and the formation of the edge pedestal. *Phys. Rev. Lett.*, 81(20):4396–4399, November 1998.

[143] B. A. Carreras *et al.* Transport effects induced by resistive ballooning modes and comparison with high-β_p ISX-B Tokamak confinement. *Phys. Rev. Lett.*, 50(7):503–506, February 1983.

[144] Maxim Umansky. Personal communication. June 2005.

[145] J. R. Myra *et al.* Resistive modes in the edge and scrape-off layer of diverted tokamaks. *Phys. Plasmas*, 7(11):4622–4631, July 2000.

[146] X. Q. Xu *et al.* Dynamical simulations of boundary plasma turbulence in divertor geometry. *New J. Phys.*, 4:53.1–53.15, 2002.

[147] J. W. Connor and R. J. Hastie. Collisionless and resistive ballooning stability. *Phys. Plasmas*, 6(11):4260–4264, November 1999.

[148] Philip R. Bevington and D. Keith Robinson. *Data Reduction and Error Analysis for the Physical Sciences*. McGraw-Hill, Boston, second edition, 1992.

[149] ITER Physics Expert Group on Confinement and Transport *et al.* Chapter 2: Plasma confinement and transport. *Nucl. Fusion*, 39(12):2175–2250, December 1999. ITER Physics Basis Special Issue.

[150] Michael Tendler and Daniel Heifetz. Neutral particle kinetics in fusion devices. *Fusion Technol.*, 11(2):289–310, March 1987.

[151] Brian LaBombard. KN1D: a 1-D space, 2-D velocity, kinetic transport algorithm for atomic and molecular hydrogen in an ionizing plasma. Research Report PSFC-RR-01-3, Massachusetts Institute of Technology Plasma Science and Fusion Center, Cambridge, Massachusetts, August 2001.

[152] Maxim Umansky. *Transport of particles and energy in the edge plasma of the Alcator C-Mod tokamak*. PhD thesis, Massachusetts Institute of Technology, Cambridge, Massachusetts, October 1999.

[153] Martin Greenwald. Density limits in toroidal plasmas. *Plasma Phys. Control. Fusion*, 44(8):R27–R80, August 2002.

[154] B. LaBombard *et al.* Transport-driven Scrape-Off-Layer flows and the boundary conditions imposed at the magnetic separatrix in a tokamak plasma. *Nucl. Fusion*, 44(10):1047–1066, October 2004.

[155] D. A. Mossessian, J. W. Hughes, and B. LaBombard. One-dimensional modeling of neutral transport in H-mode pedestal region. Poster given at 10th EU-US Transport Task Force Workshop, Varenna, Italy, September 2004. P7.

[156] J. W. Hughes, A. E. Hubbard, and C. S. Chang. Extension of pedestal scalings. Alcator C-Mod Mini-Proposal No. 410, January 2005.

[157] D. Stotler and C. Karney. Neutral gas-transport modeling with DEGAS-2. *Contrib. Plasma Phys.*, 34(2–3):392–397, 1994.

[158] Daren Stotler *et al. User's Guide for DEGAS 2*, November 2001. CVS Revision 1.1.

[159] D. P. Stotler *et al.* DEGAS 2 neutral transport modeling of high density, low temperature plasmas. In *Fusion Energy 1996: Proceedings of the 16th International Conference on Fusion Energy*, volume 2, pages 633–639, Vienna, 1997. International Atomic Energy Agency. IAEA-CN-64.

[160] R. K. Janev *et al. Elementary Processes in Hydrogen-Helium Plasmas: Cross Sections and Reaction Rate Coefficients.* Springer Series on Atoms + Plasmas. Springer-Verlag, New York, 1987.

[161] R. K. Janev and J. J. Smith. *Atomic and Plasma-Material Interaction Data for Fusion*, volume 4. International Atomic Energy Agency, Vienna, 1993.